Parametric Excitation of Coupled Nonlinear Microelectromechanical Systems

Zur Erlangung des akademischen Grades Doktor-Ingenieur (Dr.-Ing.)
Genehmigte Dissertation von Ahmed AbdelMonem Barakat Mosaad aus Kairo, Ägypten.
Tag der Einreichung: 01.11.2022, Tag der Prüfung: 21.12.2022

1. Gutachten: Prof. Dr. Dr. h.c. Peter Hagedorn
2. Gutachten: Prof. Dr. Bernhard Schweizer
Darmstadt, Technische Universität Darmstadt

TECHNISCHE UNIVERSITÄT DARMSTADT

Fachbereich Maschinenbau

Parametric Excitation of Coupled Nonlinear Microelectromechanical Systems

Genehmigte Dissertation von Ahmed AbdelMonem Barakat Mosaad

Tag der Einreichung: 01.11.2022
Tag der Prüfung: 21.12.2022

Darmstadt, Technische Universität Darmstadt

Bitte zitieren Sie dieses Dokument als:
URN: urn:nbn:de:tuda-tuprints-231989
URL: http://tuprints.ulb.tu-darmstadt.de/23198
Jahr der Veröffentlichung auf TUprints: 2023

Dieses Dokument wird bereitgestellt von tuprints,
E-Publishing-Service der TU Darmstadt
http://tuprints.ulb.tu-darmstadt.de
tuprints@ulb.tu-darmstadt.de

Erklärungen laut Promotionsordnung

§ 8 Abs. 1 lit. c PromO

Ich versichere hiermit, dass die elektronische Version meiner Dissertation mit der schriftlichen Version übereinstimmt.

§ 8 Abs. 1 lit. d PromO

Ich versichere hiermit, dass zu einem vorherigen Zeitpunkt noch keine Promotion versucht wurde. In diesem Fall sind nähere Angaben über Zeitpunkt, Hochschule, Dissertationsthema und Ergebnis dieses Versuchs mitzuteilen.

§ 9 Abs. 1 PromO

Ich versichere hiermit, dass die vorliegende Dissertation selbstständig und nur unter Verwendung der angegebenen Quellen verfasst wurde.

§ 9 Abs. 2 PromO

Die Arbeit hat bisher noch nicht zu Prüfungszwecken gedient.

Darmstadt, 01.11.2022

Ahmed A.Barakat Mosaad

Vorwort

Zuallererst bin ich Allah, dem Allmächtigen, zutiefst dankbar, dass Er mir die Fähigkeit und das Wissen gegeben hat, diese Arbeit abzuschließen.

Diese Arbeit wurde in der AG Dynamik und Schwingungen, Fachgebiet Numerische Berechnungsverfahren im Maschinenbau, Fachbereich Maschinenbau an der Technischen Universität Darmstadt angefertigt. Es war eine Reise voller Herausforderungen seit ihrem Beginn im Sommer 2018, durch die ich mich bei allen bedanken möchte, die mir geholfen haben, sie abzuschließen.

In erster Linie bin ich meinem Doktorvater, Prof. Peter Hagedorn, zu großem Dank verpflichtet, da er mich vom ersten Tag an auf persönlicher und wissenschaftlicher Ebene in unvergleichlicher Weise unterstützt hat. Ich habe ihm immer dafür gedankt, dass er unerbittlich und ständig aufmerksam war, um meine Ambitionen zu fördern, mir Unterstützung zu geben und Verständnis für die Umstände zu haben, insbesondere in schwierigen Momenten. Ich möchte mich auch bei Prof. Bernhard Schweizer für die Übernahme des Korreferats dieser Arbeit und für die Diskussion darüber bedanken.

Diese Arbeit wurde durch die Graduiertenschule CE im Centre for Computational Engineering der TU Darmstadt unterstützt. Daher bin ich ihr vor allem für die Ermöglichung der Teilnahme an Konferenzen und Seminaren dankbar. In diesem Zusammenhang möchte ich mich bei Prof. Michael Schäfer für die Aufnahme als Kollegiat in die Graduiertenschule und für die Integration im Fachgebiet FNB bedanken. Auch die Zusammenarbeit mit Dr. Markus Lazanowski und die sehr freundliche Kommunikation mit Carina Schuster schätze ich sehr.

Vielen Dank an meinen Kollegen Artem für seine Hilfe zu Beginn meiner Arbeit, meinen Bürokollegen Alfredo für seine netten Gespräche, Maria Rauck für ihre freundliche Mitarbeit und Michael Fladerer für seine ständige Hilfsbereitschaft. Außerdem war es eine große Freude, mit Zacharias zusammenzuarbeiten, dem ich für seine wertvollen Einblicke und seine freundliche Kooperation dankbar bin. Außerdem danke ich meinen Kollegen bei FNB, insbesondere Stefanie, Jessica, Max, Felix, Arezoo und Iman für die schöne Zeit und die gute Atmosphäre.

Ich möchte mich bei Prof. Thomas Sattel für die Aufnahme meiner experimentellen Studien

in seinem Labor an der TU Ilmenau bedanken, für seine Motivation zu meiner Arbeit und für die freundliche Begrüßung durch ihn und seine Familie. Mein Dank gilt auch seinem Team, insbesondere Robert Reichert für seine wertvollen technischen Hinweise, Hans-Georg Pietscher für seine Kooperation und Björn Wilbertz für seine Hilfe bei den Experimenten.

Ich danke Prof. Eva Weig für die Ermöglichung der Verfassung meiner Dissertation während meines Aufenthalts an der TU München. Vielen Dank auch an Prof. Rubens Sampaio und Dr. Roberta Lima für die freundliche Zusammenarbeit an der PUC Universität, Rio de Janeiro, und für die wertvollen Diskussionen. Ich bedanke mich auch sehr bei Prof. Alois Steindl und Prof. Fadi Dohnal für die einsichtsvollen Gespräche.

Auf persönlicher Ebene möchte ich meinen Eltern meinen aufrichtigen Dank für ihre Ermutigung und ihr Vertrauen in meine Kompetenzen aussprechen. Ein besonderer Dank gilt meinem Vater und meinem Mentor Prof. El-Hakim, deren Rolle meinen wissenschaftlichen Charakter geprägt hat, und denen ich diese Arbeit zu ihrem Gedenken widme. Ich bin dankbar für meine Frau Sarah und meine Kinder, ohne deren Geduld und Ermutigung ich diese Arbeit nicht hätte abschließen können. Ich danke auch meinen Freunden Nour, Hisham und Sherif für ihre Zeit, um Verbesserungsvorschläge für den Text zu geben.

Schließlich danke ich dem Deutschen Akademischen Austauschdienst (DAAD) und dem Ägyptischen Ministerium für Hochschulbildung und Forschung für die finanzielle Unterstützung durch das Stipendienprogramm GERLS und dafür, dass sie mir die Möglichkeit gegeben haben, meine Promotion an der TU Darmstadt durchzuführen.

Ahmed A. Barakat
München, 01.11.2022

Kurzfassung

Das Aufkommen der Halbleiterindustrie in der zweiten Hälfte des letzten Jahrhunderts eröffnete überraschende neue Perspektiven für die Entwicklung dynamisch-mechanischer Systeme. Sie ermöglichte dank der sich ständig weiterentwickelnden Mikrofabrikationsmethoden die Entwicklung von mikroelektromechanischen Systemen (MEMS), gefolgt von ihrem Äquivalent im Nanometerbereich, den NEMS. Heutzutage machen M/NEMS neben elektrischen, optischen und telekommunikativen Komponenten einen großen Teil der Industrie für Miniatursensoren aus. Da diese winzigen dynamischen elektromechanischen Systeme mitunter Kopplungen zwischen Freiheitsgraden sowie Nichtlinearitäten aufweisen, spielt die Theorie der Stabilität dynamischer Systeme eine wichtige Rolle bei ihrem Entwurf und ihrer Umsetzung.

In der Praxis werden Stabilitätsprobleme oft aus zwei verschiedenen Perspektiven angegangen. Die erste, meist bei linearen Systemen, zielt darauf ab, jegliche Instabilitäten zu vermeiden, da diese zerstörerische Folgen für Komponenten in mechanischen, elektrischen und elektronischen Systemen haben könnten. Im Gegensatz dazu zielt die zweite Perspektive bei nichtlinearen Systemen darauf ab, das System in Regionen der Instabilität für die triviale Lösung zu treiben, während nach stabilen stationären nichttrivialen Lösungen der zugrunde liegenden Differentialgleichungen gesucht wird.

Mit dem Aufkommen von Mikro- und Nanosystemen könnte die zweite Perspektive mehr an Bedeutung gewinnen. Das liegt daran, dass diese Systeme unter normalen Betriebsbedingungen ein typisches nichtlineares Verhalten und höhere Amplituden aufweisen können als makroskalige Systeme. Höhere Amplituden ermöglichen in diesem Sinne eine bessere Verstärkung einer Eingangsanregung und damit eine höhere Empfindlichkeit von Miniaturmessgeräten. Sind die Systemparameter zudem zeitperiodisch, könnte sich die triviale Lösung bei den so genannten parametrischen Resonanzen als instabil erweisen. Bekannt als parametrisches Pumpen in Mikro- und Nanosystemen wird die Systemantwort in der Regel bei diesen Resonanzfrequenzen verstärkt.

Aus diesen Gründen konzentriert sich diese Arbeit hauptsächlich auf parametrisch angeregte nichtlineare Systeme. Dennoch wird in dieser Arbeit ein systematischer Denkansatz verfolgt, bei

dem die Ursprünge der Destabilisierung in zeitinvarianten Systemen untersucht werden, bevor eine theoretische Studie über zeitperiodische Systeme im Allgemeinen und zeitperiodische nichtlineare Systeme im Besonderen durchgeführt wird.

In dieser theoretischen Studie wird eine innovative Idee für die M/NEMS-Industrie vorgestellt, nämlich die breitbandige parametrische Verstärkung durch eine bimodale Anregungsmethode. Diese Idee wird dann in Mikrosystemen anhand eines speziellen Beispiels, dem Mikrogyroskop, umgesetzt. Da dieses Gerät im Vergleich zu anderen Trägheitssensoren sehr kostengünstig ist, wird es derzeit weiterentwickelt, um eine höhere Empfindlichkeit und Genauigkeit zu erreichen. Zu diesem Zweck werden die theoretischen Ergebnisse, einschließlich der erwähnten Idee, in diesem Gerät umgesetzt und erweisen sich somit als effektiver Beitrag zu seiner Leistung.

Außerdem wird eine experimentelle Untersuchung an einem analogen Mikrosystem durchgeführt. Durch die experimentelle Studie wird ein elektronisches System eingeführt, um die vorgeschlagene bimodale parametrische Anregungsmethode auf das Mikrosystem anzuwenden. Durch den Vergleich der Stabilitätskarten in Theorie und Experiment wird das theoretische Modell validiert.

Abschließend wird in dieser Arbeit eine theoretische Studie über parametererregte nichtlineare Systeme durchgeführt, dann auf Mikrogyroskopen implementiert und schließlich experimentell validiert. Dadurch setzt diese Arbeit einen ersten Schritt für den Einsatz der vorgeschlagenen Anregungsmethode in der M/NEMS-Industrie.

Abstract

The commencement of the semi-conductor industry in the second half of the last century gave a surprising new outlook for engineered dynamical mechanical systems. It enabled, thanks to the continuously evolving microfabrication methods, the implementation of Micro Electromechanical systems (MEMS) followed by their nano-counterpart or NEMS. Nowadays M/NEMS constitute a massive portion of the small-scaled sensors industry, in addition to electrical, optical and telecommunication components. Since these tiny dynamical electromechanical systems involve sometimes couplings between degrees of freedom as well as nonlinearities, the theory of stability in dynamical systems plays a significant role in their design and implementation.

From a practical point of view, the approach to stability problems often takes two different perspectives. The first one, most commonly in linear systems, aims to avoid any instability which could cause destructive consequences for mechanical structures or for electrical and electronic components. On the contrary in nonlinear systems, the second perspective aims to drive the system into regions of instability for the trivial solution, while searching for stable nontrivial steady-state solutions of the underlying differential equations.

With the advent of micro and nanosystems, the second perspective could acquire increased importance. This is attributed to their capability to exhibit typical nonlinear behavior and higher amplitudes at normal operation conditions, when compared to macroscale systems. Higher amplitudes, in this sense, allows for a better amplification of an input excitation, and thereby higher sensitivity for miniature sensors and measurement devices. In addition, if the system parameters were time-periodic, the trivial solution could turn to be unstable at the so called parametric resonances. Known as parametric pumping in micro and nanosystems, the system's response is usually amplified at these resonance frequencies for higher sensitivity and accuracy.

For these reasons, this work is mainly focused on parametrically excited nonlinear systems. Nevertheless, a systematic approach is followed in this thesis, where the origins of destabilization are surveyed in time-invariant systems before proceeding to carry out a theoretical study on time-periodic systems in general, and time-periodic nonlinear systems in particular.

Through this theoretical study, a novel idea for the M/NEMS industry is presented, namely the broadband parametric amplification using a bimodal excitation method. This idea is then implemented in microsystems, by investigating a particular example, that is the microgyorscope. Given the low-cost of this device in comparison with other inertial sensors, it is being currently enhanced to reach a relatively higher sensitivity and accuracy. To this end, the theoretical findings, including the mentioned idea, are implemented in this device and prove to contribute effectively to its performance.

Moreover, an experimental investigation is carried out on an analogous microsystem. Through the experimental study, an electronic system is introduced to apply the proposed bimodal parametric excitation method on the microsystem. By comparing the stability charts in theory and experiment, the theoretical model could be validated.

In conclusion, a theoretical study is carried out through this work on parametrically excited nonlinear systems, then implemented on microgyroscopes, and finally experimentally validated. Thereby, this work puts a first milestone for the utilization of the proposed excitation method in the M/NEMS industry.

Contents

1 Introduction

The study of motion extends back in history for about three millennia since the start of civilization in Egypt, Mesopotamia and China, motivated by the periodicity of celestial bodies motion, and gravity on earth, among other phenomena. However, the surviving texts in the context of deducing *laws of motion* carried the names of Greek philosophers, as Aristotle and Archimedes, then those of Islamic scholars, as Ibn-Sina (Lat. Avicenna) and Ibn-Bajja (Lat. Avempace), all through the Renaissance scientists Galileo Galilei and Isaac Newton [1, 2], when these laws took finally a correct mathematical form.

The study of dynamical systems started to take its formalism from the works of Hamilton, Lagrange, Jacobi and Poincaré. This study is concerned with any mathematically defined system with state variables that undergo time evolution after being set initially to some initial conditions, or subjected to external excitation. The definition itself implies the time differentiation of the state variables. Time, therefore, provides the basic mathematical structure of a dynamical system, as being the independent variable. However, if the system parameters happen to be time-dependent, a totally different system will then be studied, which is called a *time-varying system*. A special type is *time-periodic* systems, where the time-varying system parameter has a specific periodic time.

Turning from this abstract picture to more physical grounds, we find that the most common dynamical systems in classical mechanics involve *oscillations*, as a result of having an inertia and a restoring force. This essentially means that the mathematical formulation includes second order derivatives.

The dynamical system in this sense could include linear as well as nonlinear terms. Although almost all phenomena are nonlinear in nature, the linear approximation was found in most practical cases to be satisfactory. However, at high amplitudes or special conditions the linearized models lose ground in favor of *nonlinear* models.

Besides time-periodicity and nonlinearity, the dimensionality of the system has a significant influence on its dynamics. Although systems are naturally continuous in classical physics, the discretization in space was found to be of great importance, reducing a partial differential

equation to a set of n ordinary differential equations, thus defining the system's dimensions.

By classifying dynamical systems according to the three aforementioned aspects, that is, time-dependency of system parameters, linearity or nonlinearity, and dimensionality, we find the class of multi-degree-of-freedom (M-DoF), nonlinear, time-periodic systems of great interest. The interest in this class of problems arose due to two different reasons. Firstly, although each of the three aspects of this class was discussed extensively in the literature, but much lesser focus is given to this class specifically, formed by the combination of them. Secondly, this class of problems happens to appear naturally in an important and exponentially increasing branch of applications of dynamical systems, which is micro- and nanosystems [3, 4]. For these reasons a large interest is grown over time to explore this class of problems more thoroughly on one side, and on the other side to consider the implementation of this theoretical work for the development of micro and nanosystems. From a practical point of view, the time-periodicity of system parameters could be understood as *parametric excitation* of the system. Therefore, a compact name for this class of problems is given under the title of parametric excitation of coupled nonlinear microelectromechanical systems, where *coupled* hints at the multi-dimensional systems. Microsystems are specified here, while nanosystems are excluded, since only microsystems were considered in this work, however, the theoretical results can be extended to nanosystems as well.

A large portion of micro- or nanoelectromechanical systems (M/NEMS) can be categorized as sensors and actuators, whose most important key performance indicator is the sensitivity to measured quantities. Thus, numerous *amplification* techniques were introduced to improve the sensitivity of these devices. From this perspective, parametric excitation offers here an important method of amplification, named *parametric amplification*, which gained a significant importance for small-scaled sensors exhibiting oscillatory motion, such as resonators. The connection between parametric excitation and signal amplification comes through the *destabilization* effect of parametric excitation. Therefore, through the analysis of parametrically excited nonlinear MEMS, special attention will be given to the destabilization of the trivial stationary solution, and thereby, to the effect of nontrivial steady-state solutions, in promoting the amplification of the response.

This work, however, will discuss also the destabilization and amplification effects in linear and time-invariant systems, before going through nonlinear time-periodic ones. This approach will help to add more explanation and insights into the targeted class of problems.

1.1 Parametric excitation

The term *parametric excitation* refers to the existence of displacement-dependent or velocity-dependent or sometimes inertia-dependent terms with time-periodic coefficients in the system's differential equations, where the excitation of the system takes place through the system parameters. The behavior of these systems was known to be first discussed by Faraday through his experiments on producing wave motion in fluids by vibrating a membrane or a plate in 1831 [5]. *Faraday waves*, were therefore named after him, and refer to unstable nonlinear standing waves appearing on liquids enclosed in a vibrating container. He observed that these waves have one half the excitation frequency, which is the typical signature of the primary parametric resonance. These were explained afterwards by Lord Rayleigh in 1883 by relating them to the Mathieu equation [6]. Mathieu studied standing waves in fluids, and was interested in putting a theory describing the natural modes of lakes with elliptical boundaries. In 1873 through his study, the well-known equation of motion with parametric excitation was deduced and bore his name, to be the *Mathieu equation*.

In the following decade 1880s, two major developments were introduced. Floquet presented his theory to solve time-periodic differential equations, which can offer a numerical solution. This solution serves as a reference for verifying approximate analytical solutions. The second achievement was Hill's infinite determinants, which were basically intended to solve the three body problem, known as Hill's lunar equation [7]. Through his work, the solar perturbations of the lunar periodic motion lead to differential equations with time-periodic coefficients. Then through the use of the Fourier series to solve it, he could arrive at Hill's infinite determinants, through which the borders of stability could be derived [8]. The well-known stability chart for the Mathieu equation was presented first by Ince in 1927 and by M.J.O. Strutt in 1928 [9], the former was out of a mathematical interest while the latter was to describe the electronic motion in periodic crystal lattices. In this latter research field specifically the prominent Bloch's theorem in quantum mechanics was introduced for the same problem, based on the Floquet theory but expanded in three dimensions [10].

Turning the problem into multi-degree-of-freedom systems, other phenomena can be observed. An overview of the effects of parametric excitation in multi-degree-of-freedom systems is given in Mettler [11]. In the few decades afterwards, articles and monographs were published explaining the instability conditions, and deducing approximate analytical expressions for the stability borders for primary and secondary combination resonances [8, 12, 13, 14]. Theoretical investigations were carried out from different perspectives. The first approach, which started with Mathieu's work itself, is to explore the stability/instability conditions under parametric

excitation in various system configurations, with linear or nonlinear elements [15, 16, 17, 18]. Moreover, an exact solution for the Mathieu equation was always an endeavor. Different studies approached this problem series expansion, such as Laurent series [19]. Another approach, however, is to find stabilizing effects of parametric excitation. This approach stems from the investigation of A.Tondl [20], and introducing the term *anti-resonance* in this context [21]. The formulation of full suppression of self-excited vibrations through parametric excitation was further studied afterwards [21, 22]. This stabilizing effect was brought further by F.Dohnal by deriving approximate analytical expressions for stability boundary curves under synchronous parametric excitation at combination frequencies [23] and extended afterwards by including a second order approximation using the averaging method [24].

Experimentally investigating parametric resonances, on the other hand, dates back to Faraday's and Mathieu's works on standing waves in fluids. In the past decades, several experimental investigations were conducted. Following the previously mentioned classification, one approach is to offer experimental proof for the stabilizing effect of the parametric excitation [25, 26, 27, 28]. Nevertheless, experiments were also conducted to explore the instability regions, sometimes named *Arnold tongues*, in the stability chart. They were conducted in macro systems [29, 30, 31], or in microsystems [32]. In experimental investigations of parametric resonances there is a common contrast between macro and microsystems. In the former case, there exist experimental studies to exhibit parametric resonances for the sake of understanding the phenomenon, such as in [33], but these resonances are rarely considered beneficial in macrosystems. At this scale, it is usually referred to resonances as being detrimental to the structure's health, since the system's nonlinearities can not usually offer enough limitation of amplitudes without causing failure or fatigue, that is why normally a control scheme is presented in order to control the response amplitude [29]. An exceptional study, however, is conducted by Rhoads et al where they investigated the possibility of constructing a macro parametric amplifier in analogy with microsystems [34].

A specific phenomenon receives a special attention in this work, namely, the *broadband destabilization* effect. In his investigations about parametric excitation of M-DoF systems, Cesari [35] in a special case found that instability can be caused at all excitation frequencies, that is when a phase-shift in the parametric excitation coupling terms was included, this was called afterwards as the case of *total instability*. Further contributions to this problem were given by Schmieg [36], who investigated the problem analytically using slowly varying phase and amplitude to determine the stability borderlines. Moreover, he could validate his work experimentally on an analogue electrical circuit. Eicher [18, 12] also considered this case of excitation with a specific focus on the determination of stability borderlines, and their shifting

in the stability chart as a result of including a phase-shift in the excitation terms. Recently, Karev et al [37, 38] included the effect of circulatory and gyroscopic effects in the study of the problem, seeking a better generalization of the problem. A more compact name, namely *asynchronous* parametric excitation [39, 38], is given to this case where the coupling terms in the parametric excitation matrix are phase-shifted. This expression will be used in this work interchangeably with phase-shifted parametric excitation, more specifically when the phase-shift is equal to $\pi/2$.

Investigating this problem in nonlinear systems makes it a more specified problem, since most of the previously mentioned works were on linear systems with some brief calculations after adding nonlinear terms [40, 36]. This, however, did not include several possible cases, such as the inclusion of intrinsic parametric excitation terms or the consideration of nonlinear damping [36]. In a broader field of research, parametrically excited two-degree-of-freedom nonlinear systems we discussed before in the literature [41, 42], however, with less attention to coupling parametric excitation terms (off-diagonal terms in the parametric excitation matrix), much less including a phase-shift between these terms. According to this reviewed literature, it could be concluded that the asynchronous parametric amplification of nonlinear systems was not thoroughly enough discussed in the literature, which makes this point an interesting point of study in this thesis, especially due to its relevance to micro- and nanosystems, which leads us to the next section.

1.2 Nonlinear dynamics of M/NEMS

Micro- and nano-electromechanical systems (M/NEMS) represent an increasingly developing technology that gradually wide-spread to include a wide spectrum of applications, thanks to to the evolving micro-fabrication techniques. They constitute nowadays important elements in electrical, electronic, optical and telecommunication systems. Examples include radio-frequency (RF) components, such as switches and filters, in addition to optical elements, as digital micro-mirrors devices (DMD) and equalizers, not to mention microwave oscillators and photonic crystals, to name a few [43]. In the sensors industry, they stand out in comparison with other technologies in measuring physical or chemical quantities [44]. A great portion of the commercially available accelerometers, micro-gyroscopes, time-keeping oscillators, mass- and force-sensors are based on such devices [45]. This extends to include bio-MEMS used in genomic and protein analysis [46], not to mention imaging technologies, most importantly the atomic force microscope (AFM) [47]. Furthermore, in fundamental science research extensive effort is put to understand atomic, molecular and quantum phenomena using NEMS [48].

Moreover, NEMS started to take part in the continuously growing pursuit of developing quantum technologies since the first signs of quantum-behavior in a nanosystem [49]. Most recently, nanomechanical resonators could play an important role in the transfer of quantum information (a qubit) from the microwave regime into the optical one [50].

Due to the significantly high amplitudes and the used material properties, M/NEMS can exhibit nonlinear phenomena under normal operating conditions. Nonlinear terms in differential equations of physical systems arise out of different origins, such as geometry, elasticity, piezoelectricity, and motion constrains among others. However, in M/NEMS the influence of these forces turns to be of larger significance, in addition to the presence of other forces which were not commonly considered in macrosystems, such as van der Waals, Casimir, and adhesion forces. The greater influence of all the mentioned forces is related to the miniature scale of the system's characteristic dimensions, which can be better explained by non-dimensionalization of the mathematical model [4]. This influence can also be attributed to the strong intercoupling of different forces, since transduction from one type of force field to another does not always have to be linear. An illustrating example is the bimorph actuators, which transforms electrical potential to thermal flow and afterwards to elastic deflection at the same spot simultaneously [51, 52]. In addition, micro and nano devices are sometimes also designed to exhibit a nonlinear behavior for the sake of amplification and enhancement of sensitivity [53].

In M/NEMS, the search for a resonator design with a higher amplification factor Q is steadily increasing [54]. To this end, several nonlinear dynamical phenomena, such as nonlinear modal couplings, internal resonances, sub- and superharmonic resonances are exploited for the sake of obtaining high oscillation amplitudes [55]. On another hand, at millikelvin temperatures nano-oscillators could approach the quantum-ground state level, i.e. the quantization of vibrations states [56]. These efforts lead to the idea of realizing a quantum bit (qubit) based on nanomechanical resonators, which could have significant implications in the development of the widely pursued quantum information systems. This idea relies largely on the anharmonicity of the oscillator which could be achieved by introducing nonlinearities in the system [57].

For better amplification and higher Q factor, parametric resonances are commonly used as mechanical amplifiers in N/MEMS [58], and called *parametric amplifiers*, which refers also to electronic or optical parametric amplifiers. Mechanical amplification in this sense has other advantages than just increasing the sensitivity or the gain of the system. An additional benefit is that they can be superior to electronic counterparts in terms of secondary noise production [59]. Moreover, mechanical parametric amplification provides thermal noise squeezing effect, which could have significant implications in terms of measurement precision at the nanoscale [60].

Thus, parametric excitation in M/NEMS plays an important role to achieve better sensitivity

as well as precision levels. The investigation of parametric excitations in MEMS was first carried out in the well known work by Rugar and Grütter[60], in which they report the *noise squeezing* effect of parametric resonances. Afterwards, a long list of scientists dedicated extensive research to the subject. Turner et al [32] reported detecting five parametric resonances in a torsional MEMS resonator. In the last two decades, the parametric amplification scheme paved its way into different applications, such as mass-sensing [61], inertial sensing [62, 63, 64, 65], microscanners [66] and atomic force microscopy [67].

In conclusion, the nonlinear dynamical behavior is more pronounced in micro and nano-systems than larger scaled systems. In addition, parametric excitation of these systems is a preferable amplification method for the explained reasons. For these reasons, applying the theory of parametrically excited nonlinear systems on M/NEMS would be of significant interest. In this work, the theoretical study is applied on the micro-ring gyroscope. Thus, a review of the previous research work on these devices is given special attention in the next section.

1.2.1 Micro-gyroscopes

MEM gyroscopes are an example of Coriolis Vibratory Gyroscopes (CVG), also called Vibrating Structure Gyroscopes (VSG). They are usually based on two degree of freedom models, representing the drive and sense modes. Different structures were used for these models, which can be sorted into discrete and continuous systems [68]. An example of the former is the vibrating comb gyroscope and of the latter is the micro-ring gyroscope. In both cases the primary/drive mode is actuated by an external force, and coupled to the secondary/sense mode by the gyroscopic Coriolis forces only under the rotation of the ring reference frame. The coupling gyroscopic force is linear in the rotation rate, and acts as an excitation for the secondary/sense mode. The amplitude of the sense mode is then correlated to the rotation rate, and thus the rotation rate could be measured.

Micro-gyroscopes were developed extensively in the last three decades. However, these developments fall short of attaining the performance of other conventional gyroscopes [69]. Being lighter, smaller in size and lower in cost MEM gyroscopes can offer great potential for navigation systems if they acquired the needed performance measures. These measures are mainly the bias stability, the Angle Random Walk (ARW) and the scale-factor (sensitivity). These could be greatly enhanced by decreasing noise and increasing sensitivity [70, 71]. Until recently, researchers sought improvement of MEM gyroscopes to reach the tactical grade (0.1 deg/h Bias Stability) [72, 73]. However, the aim is still to reach the inertial grade ($<$0.01 deg/h) in MEM gyroscopes [73].

A major problem here is that the Coriolis force $F_{coriolis} = 2m\Omega\dot{x}$ is usually very small, where m is the vibrating mass, Ω is the reference frame rate of rotation, that is to be measured, and x is the primary/drive mode displacement. Both the mass m and rotation rate Ω have relatively very small values. Therefore, in order to attain high scale factor (sensitivity) of the measurement a significantly high actuation force is to be used. However, this leads to higher noise due to the electric feedthrough caused by parasitic capacitance [71]. On the other hand, another major problem is the mismatch between the drive and sense modes. That is because if they are untuned, the Coriolis gyroscopic term $F_{coriolis} = 2m\Omega\dot{x}$, resulting from the primary mode oscillation x, will not be in resonance with the secondary/sense natural frequency. Therefore in order to increase the system sensitivity and decrease noise, i.e. increase Signal to Noise Ratio (SNR), several design and control schemes have been introduced in the literature to address both mentioned problems [64, 74, 63].

On the other hand, in designing high Q devices, for attaining high sensitivity, signals would be impaired by mechanical and electronic noises, a main source of which is the electronic amplification of the small value Coriolis force [75]. A mechanical-based amplification can then offer a better solution with respect to noise reduction before the electronic readout interface [74]. In that sense, parametric resonances proved to be significantly advantageous, since they are not damping-dependent and cause noise squeezing [60, 76], which can enhance both ARW and bias stability. Moreover, parametric amplification can spare the need for higher amplitude of forcing elements, this leads to lower electrical feedthrough due to parasitic capacitances [71]. In this way, it is possible to increase the device's sensitivity without impairing the SNR.

In MEM gyroscopes parametric excitations were first considered by Oropeza-Ramos et al [62] for the conventional comb-gyroscopes and by Gallacher et al [64] for micro-ring gyroscopes. To the best of the authors' knowledge, in most of the investigated cases in the literature only one degree of freedom was parametrically excited except for few studies, like the one by the Gallacher team [71] and in the recent one by Zhou et al [77]. However, both contributions did not investigate the coupling between the two parametric excitations. Parametric resonances were investigated as well in gyroscopes that exhibit nonlinear effects, either for the sake of optimizing the parametric amplification [74], or to investigate the possibility of having self-induced parametric amplification [78, 76] or for increasing the bandwidth of amplification [63].

In all the given cases, the parametric amplification is sought in general at the parametric resonance frequencies, and mainly at the primary resonance frequency, which is double the natural frequency. Authors normally differentiate between a parametric resonance and a parametric amplification [67]. While the former describes having an unstable trivial solution,

the latter suggests exciting the system just below instability, both excitation schemes are applied at the parametric resonance frequency. However, in the first case the amplitude is only limited through the nonlinear response, i.e. by having a nontrivial stable solution. For the case of parametric amplification, an important common remark in the literature is that the amplification gain is highly sensitive to the phase shift between the parametric excitation and the drive forcing excitation. Using this observation, either the amplification gain or the suppression of the quadrature errors could be optimized [74, 76].

However, tuning the parametric excitation frequency at the system's resonant frequencies can be also challenging, and the loss of the quality factor, i.e. the sensitivity, can follow a slight mistuning. For this sake, the *broadband destabilization* effect described before could be of major significance. This effect occurs through an asynchronous coupling parametric excitation, which was neither investigated before for nonlinear systems in enough detail as explained, nor was it exploited for microsystems, neither theoretically nor experimentally. Thus, a specific interest arises in this case to investigate this effect in microsystems due to its uniqueness in the theory of parametric excitation, taking the micro-ring gyroscope as a suitable example.

1.3 Problem statement and research objectives

According to the previous review of literature, several research questions could be found, which were either not investigated in enough detail or were not discussed at all.

Firstly, although the theory of parametric excitation or the theory of differential equations with time-periodic coefficients were investigated for about one and half centuries, a lesser effort was given to specific cases for M-DoF systems. More precisely, the broadband destabilization effect appearing through asynchronous coupling parametric excitation, in other words parametric excitation with phase-shifted off-diagonal terms, in two-degree-of-freedom systems were only discussed in a few number of contributions. This indicates that this case is still not adequately covered. This was found to be correct, especially when a nonlinear system is addressed. Moreover, the analytical description of parametric amplification below the onset of instability, named *non-resonant parametric amplification* in this work, was not elaborated before in the literature despite the importance of this effect in parametric amplifiers.

Secondly, micro and nanosystems exhibit a nonlinear behavior more significantly than macro-systems as explained. For these systems, a nonlinear modeling should be highly recommended for a precise description of the system dynamics. Moreover, the implementation of parametric excitation in these systems proved through the past three decades to be of significant value. Therefore, the exploitation of the theory of parametric excitation in nonlinearly modeled micro

and nanosystems should be considered necessary. However, the discussion in the literature on the nonlinear analysis of these systems is far from being comprehensive . On the other hand, the broadband destabilization effect happens to be of major importance in terms of increasing systems' sensitivity and adding flexibility to the tuning of the excitation frequency. Both of these benefits are considered important performance indicators in the sensors industry.

Thirdly, the experimental validation of the aforementioned asynchronous parametric excitation was not implemented before in mechanical systems. In addition, the behavior of the system at the difference combination frequency had never been experimented in any type of systems. Moreover, since this excitation scheme offers instability at non-resonant frequencies, thus, the instability conditions at these frequencies should be also explored.

These unaddressed questions leaves the opportunity to be covered through this work. Therefore, the main research objectives of this work will be:

- Introducing a more detailed investigation of parametrically excited nonlinear systems, while studying the role of asynchronous excitation.
- Presenting an analytical explanation for the parametric amplification in the vicinity of the instability threshold.
- Implementing the discussed theory of parametric excitation in micro-ring gyroscopes using linear and nonlinear modeling.
- Carrying out an experimental investigation to explore the instability conditions of a two-degree-of-freedom microsystem using the discussed theory for the sake of validation.

1.4 Outline

This work can be divided into three major domains of contribution. First, a development in the theory of time-periodic multi-degree-of-freedom systems is introduced and especially when nonlinearities are involved. Secondly, an implementation in a MEMS, namely, micro-ring gyroscope, is provided, again through linear and nonlinear modeling. And finally, an experimental validation of the mostly used mathematical model in this work is presented.

The first domain is presented in chapter 3. However, a preparatory discussion about sources of destabilization in time-invariant systems is presented first in chapter 2, with some newly analyzed problems. A part of section 2.3, was published in an original research paper [79], where a simple circulatory nonlinear system was analyzed explaining how an autonomous nonlinear system could exhibit instability through follower forces.

Through the discussion, a bottom-up approach is followed. This means that the discussion

starts with the simplest form of the equation of motion, explaining the possible sources of instability or destabilization, that is in linear time-invariant single-degree-of-freedom (S-DoF) systems. Then we turn to M-DoF systems and observe the *added* sources of destabilization by increasing the dimensionality. The discussion proceeds to include nonlinear systems looking as well for the added sources of instability. This approach is then extended as well to time-periodic systems in chapter 3. Using this approach, a break-down of the sources of destabilization could be introduced giving a deeper insight into different phenomena.

In chapter 3, the discussion starts with results from previous works about Mathieu equation and proceeds again to M-DoF time-periodic systems giving some more insights into them by applying a numerical analysis using the Floquet theory and an analytical one using the method of normal forms. Section 3.1 was published as a part of an original paper [80]. At the end of this section an analytical study is presented in order to explain the *parametric amplification* which occurs near the border of instability. Afterwards, the discussion follows towards parametrically excited nonlinear M-DoF systems, where the multiple scales method is used to carry out a bifurcation analysis around the resonant frequencies. Through the analysis, some interesting results are presented, giving some understanding of this class of systems before implementing the theory in microsystems. Section 3.2 constitutes most of the original work [81] submitted and being reviewed.

The second domain of this work is concerned with the implementation of the discussed theory in micro-ring gyroscopes. We start our discussion with linear modeling of the micro gyroscope in chapter 4 using Hamilton's principle, then the origin of the intrinsic parametric excitation is calculated. Afterwards, the asynchronous parametric excitation is introduced to the micro gyroscope through a suggested electronic circuit, and the amplification of the system's response was obtained. Most of this chapter is a part of a published original paper [80], with some results published in [82]. The discussion then continues to the case of the nonlinearly modeled micro-ring gyroscope in chapter 5 In this case the autonomous system is first analyzed, i.e. without parametric excitation, and the fixed points were identified. Afterwards a simplified excited model is investigated to obtain some first understanding of the system, since the system's equations are shown to be of high complexity. Afterwards, the system is analyzed again using the method of normal forms in full detail and the resonance curves and limit cycles were obtained. A part of this chapter is published in the original article [83].

Finally, this work is concluded by validating the linear time-periodic system with asynchronous parametric excitation experimentally in chapter 6. This is carried out on a system of two coupled micro-cantilevers. We first introduce the test-rig and the system of measurement, the preliminary experiments were discussed, and the application of the bimodal asynchronous

parametric excitation is explained. The results were discussed afterwards and compared to the mathematical model.

The experimental work was carried out in collaboration with the research team of Prof. Thomas Sattel at the mechatronics department of the Technical University of Ilmenau. The electronic circuit was partly implemented by Hans-Georg Pietscher for the pre-amplification of the micro-cantilevers, in addition he contributed to bring up the setup of the software platform used for measurement and excitation. Moreover, the technical advice of Robert Reichert was also considerably valuable in the phase of electronic circuit implementation. However, the design and implementation of the electronic circuit board used for the parametric excitation, which is the contribution of this work, is accomplished by the author, in addition to the measurement scripts and the carrying out of the experiments.

2 Time-invariant systems

In this chapter, the stability of time-invariant systems will be briefly discussed. Since this work is mainly concerned with parametrically excited nonlinear systems, the understanding of the stability problem in time-invariant systems will serve as a suitable introduction. In this introduction, however, two nonlinear systems will be newly discussed. One is concerned with the coupling between two Duffing oscillators, and the other focuses on the effect of circulatory forces. The latter example can also serve to understand the role of the asymmetry of the stiffness matrix, in a wide sense, in destabilizing the system. The chapter will begin by discussing time-invariant linear systems and proceed with nonlinear systems.

2.1 Time-invariant linear systems

Consider a generic oscillatory system of the form

$$\boldsymbol{M}\ddot{\boldsymbol{q}}(t) + (\boldsymbol{D} + \boldsymbol{G})\,\dot{\boldsymbol{q}}(t) + (\boldsymbol{K} + \boldsymbol{N})\,\boldsymbol{q}(t) = \boldsymbol{f}(t), \tag{2.1}$$

where $\boldsymbol{q}(t), \boldsymbol{f}(t)$ are a time-dependent vectors, $\dot{(\,)} = d/dt$,

$$\begin{aligned} \boldsymbol{M} = \boldsymbol{M}^T, \quad \boldsymbol{D} = \boldsymbol{D}^T, \quad \boldsymbol{K} = \boldsymbol{K}^T, \\ \boldsymbol{G} = -\boldsymbol{G}^T, \quad \boldsymbol{N} = -\boldsymbol{N}^T, \end{aligned}$$

and $\boldsymbol{M}, \boldsymbol{D}, \boldsymbol{K}$ are the mass, damping and stiffness positive-definite symmetric matrices respectively, while $\boldsymbol{G}, \boldsymbol{N}$ are the gyroscopic and circulatory skew-symmetric matrices respectively. These definitions will be maintained throughout the thesis unless otherwise stated.

To discuss the stability of this system's solutions, we define the stability of a solution in the sense of Lyapunov stability. For an autonomous linear or nonlinear system, where $\boldsymbol{f}(t) = 0$, we

rewrite the system in first order to be

$$\dot{\boldsymbol{z}}(t) = \boldsymbol{f}(\boldsymbol{z}), \tag{2.2}$$

where $\boldsymbol{f}(\boldsymbol{z})$ is the system's vector field, then the Lyapunov stability means [84]:

For a fixed point $\boldsymbol{z}^*$, where $\boldsymbol{f}(\boldsymbol{z}^*) = 0$, $\boldsymbol{z}^*$is said to be Lyapunov stable if, given $\epsilon > 0$, there exists a $\delta = \delta(\epsilon) > 0$ such that, for any other solution, $\boldsymbol{y}(t)$ of (2.2), satisfying $|\boldsymbol{z}^*(t_0) - \boldsymbol{y}(t_0)| < \delta$, then $|\boldsymbol{z}^*(t) - \boldsymbol{y}(t)| < \epsilon$ for $t > t_0,\ t_0 \in \mathbb{R}$.

While $\boldsymbol{z}^*$is said to be asymptotically stable if it is Lyapunov stable and there exists a $\delta > 0$ such that, for any other solution, $\boldsymbol{y}(t)$ of (2.2), if $|\boldsymbol{z}^*(t_0) - \boldsymbol{y}(t_0)| < \delta$, then $\lim_{t\to\infty} |\boldsymbol{z}^*(t) - \boldsymbol{y}(t)| = 0$.

In linear systems, as in the case here, this stability definition reduces to the examination of the real parts of the system's eigenvalues. The system is then called Lyapunov stable, if and only if all real parts of the eigenvalues are not positive, and the algebraic and geometric multiplicities of the eigenvalues with vanishing real parts coincide. While the system is asymptotically stable if the real parts of all eigenvalues are strictly negative [85]. However to determine the stability of a fixed point $\boldsymbol{z}^*$ in a nonlinear system, some information could be deduced by linearization. The same stability criterion then applies by *linearization* of the nonlinear system but only if the fixed point is *hyperbolic* according to the *Hartman-Grobman theorem*, that is when no real part of any eigenvalue of the linearized system vanishes. However, if the fixed point is *non-hyperbolic*, the stability of the solution in the linearized system can not be extended to the corresponding stability in the nonlinear system [86], and a nonlinear stability analysis will then be required.

The bottom-up approach explained in the introduction to study the potential sources of system's destabilization in these systems is to be followed here by discussing first a single-degree-of-freedom (S-DoF) system. In this case only mass, damping and stiffness terms will be included, since gyroscopic and circulatory forces can only exist in multi-degree-of-freedom (M-DoF) systems. In a S-DoF system instability is caused by either negative damping or stiffness terms, or by the appearance of secular terms in the trivial solution due to resonance at zero damping.

By adding degrees of freedom to the S-DoF system, the trivial solution could be then destabilized due to the appearance of skew-symmetric couplings existing in $\boldsymbol{G}, \boldsymbol{N}$ matrices. Firstly, the circulatory *non-conservative* forces can destabilize the solution of an undamped system if they were large enough. Briefly, if we consider $\boldsymbol{D} = 0, \boldsymbol{G} = 0, \boldsymbol{f}(t) = 0$ in (2.1), giving

an $\boldsymbol{MKN}$ system, in which

$$\boldsymbol{M} = \begin{bmatrix} 1 & 0 \\ 0 & 1 \end{bmatrix}, \qquad \boldsymbol{K} = \begin{bmatrix} \omega_1^2 & 0 \\ 0 & \omega_2^2 \end{bmatrix}, \qquad \boldsymbol{N} = \begin{bmatrix} 0 & -p \\ p & 0 \end{bmatrix}, \tag{2.3}$$

the characteristic equation becomes

$$\lambda_{1,2}^2 = \frac{-(\omega_1^2 + \omega_2^2)}{2} \pm \frac{1}{2}\sqrt{(\omega_1^2 - \omega_2^2)^2 - 4p^2} \tag{2.4}$$

and the *instability* condition reads

$$4p^2 > (\omega_1^2 - \omega_2^2)^2, \tag{2.5}$$

which means that large non-conservative circulatory forces can cause *flutter* instability [87].

Another destabilization effect occurs by adding positive damping to the this same $\boldsymbol{MKN}$ system. Although damping, in general, is thought of as a stabilizing mechanism, but in this case it destabilizes the system's trivial solution, this phenomenon is called *Ziegler destabilization paradox* [85, 88]. The destabilization paradox occurs as well for a $\boldsymbol{MDGK}$ in the case of having a negative stiffness element in the $\boldsymbol{K}$ matrix and a stabilizing gyroscopic matrix. That means, in the undamped version $\boldsymbol{MGK}$ system, the system's trivial solution is stabilized by the gyroscopic forces, since the negative stiffness terms alone drive the solution into instability. However, if *pervasive* damping is added to this stabilized solution, it looses its stability again [87], yielding another form of the destabilization paradox.

2.2 Time-invariant nonlinear systems

We turn now to discuss the effect of adding nonlinear terms to the system. This changes the system (2.1) into

$$\boldsymbol{M}\ddot{\boldsymbol{q}}(t) + (\boldsymbol{D} + \boldsymbol{G})\,\dot{\boldsymbol{q}}(t) + (\boldsymbol{K} + \boldsymbol{N})\,\boldsymbol{q}(t) + \boldsymbol{f}_{nl}(\boldsymbol{q}, \dot{\boldsymbol{q}}, \boldsymbol{t}) = \boldsymbol{f}(t), \tag{2.6}$$

where the vector $\boldsymbol{f}_{nl}$ represents the added nonlinear terms. We will follow the discussed perspective in highlighting the sources of destabilization by building up the complexity of the system step by step and discovering these sources in each step. In the current case an example

will be discussed for elaboration. Consider the two-degree-of-freedom system

$$\ddot{u}_1 + \omega_1^2 u_1 + \mu_1 \dot{u}_1 + k_1 u_1^3 + \gamma_1 \dot{u}_1^3 - \alpha_1 u_2 = 0, \tag{2.7}$$
$$\ddot{u}_2 + \omega_2^2 u_2 + \mu_2 \dot{u}_2 + k_2 u_2^3 + \gamma_2 \dot{u}_2^3 - \alpha_2 u_1 = F\cos(\Omega_f t), \tag{2.8}$$

where ω_i^2, α_i and μ_i represent the stiffness and damping matrix elements respectively, k_i, γ_i represent the nonlinear terms, and F, Ω_f the forced excitation amplitude and frequency. This system represents two Duffing oscillators with a single linear stiffness coupling element α_i. Without this coupling the system will lose the effect of dimensionality on its behavior.

2.2.1 The multiple scales method

In order to analyze the system's behavior and the stability of its solutions, the multiple scales method is used [41, 89]. A first step is to examine the effect of perturbing the corresponding linear system by adding the small parameter ϵ, that is

$$\ddot{u}_1 + \omega_1^2 u_1 + \epsilon\left(\mu_1 \dot{u}_1 + k_1 u_1^3 + \gamma_1 \dot{u}_1^3 - \alpha_1 u_2\right) = 0, \tag{2.9}$$
$$\ddot{u}_2 + \omega_2^2 u_2 + \epsilon\left(\mu_2 \dot{u}_2 + k_2 u_2^3 + \gamma_2 \dot{u}_2^3 - \alpha_2 u_1\right) = \epsilon F\cos(\Omega_f t), \tag{2.10}$$

then we seek a solution in an expanded form

$$u_1(t;\epsilon) = u_{10}(T_0, T_1) + \epsilon u_{11}(T_0, T_1) + ..., \tag{2.11a}$$
$$u_2(t;\epsilon) = u_{20}(T_0, T_1) + \epsilon u_{21}(T_0, T_1) + ..., \tag{2.11b}$$

where $T_i = \epsilon^i t,\ D_i = \partial/\partial T_i$ and

$$\begin{aligned} \frac{\partial}{\partial t} &= D_0 + \epsilon D_1 + ..., \\ \frac{\partial^2}{\partial t^2} &= D_0^2 + 2\epsilon D_0 D_1 + \dots . \end{aligned} \tag{2.12}$$

Inserting (2.11) and (2.12) in (2.9) and separating according to the order of ϵ gives: for $\boldsymbol{\epsilon^0}$,

$$D_0^2 u_{10} + \omega_1^2 u_{10} = 0, \tag{2.13a}$$

$$D_0^2 u_{20} + \omega_2^2 u_{20} = 0, \tag{2.13b}$$

while for $\boldsymbol{\epsilon^1}$,

$$D_0^2 u_{11} + \omega_1^2 u_{11} = -\mu_1 D_0 u_{10} - k_1 u_{10}^3 - \gamma_1 D_0 u_{10}^3 + \alpha_1 u_{20} + 2 D_0 D_1 u_{10}, \tag{2.14a}$$

$$D_0^2 u_{21} + \omega_2^2 u_{21} = -\mu_2 D_0 u_{20} - k_2 u_{20}^3 - \gamma_2 D_0 u_{20}^3 + \alpha_2 u_{10} + 2 D_0 D_1 u_{20} + F\cos(\Omega_f T_0). \tag{2.14b}$$

Solving (2.13) gives as usual

$$u_{10}(T_0, T_1) = A_1(T_1) e^{i\omega_1 T_0} + \bar{A}_1(T_1) e^{-i\omega_1 T_0}, \tag{2.15a}$$

$$u_{20}(T_0, T_1) = A_2(T_1) e^{i\omega_2 T_0} + \bar{A}_2(T_1) e^{-i\omega_2 T_0}, \tag{2.15b}$$

by inserting this solution in (2.14) we get

$$\begin{aligned} D_0^2 u_{11} + \omega_1^2 u_{11} = &- i e^{i\omega_1 T_0} \mu_1 \omega_1 A_1 - e^{3i\omega_1 T_0} k_1 A_1 + i e^{3i\omega_1 T_0} \gamma_1 \omega_1^3 A_1^3 + e^{i\omega_2 T_0} \alpha_1 A_2 \\ &- 3 e^{i\omega_1 T_0} k_1 A_1^2 \bar{A}_1 - 3 i e^{i\omega_1 T_0} \gamma_1 \omega_1^3 A_1^2 \bar{A}_1 - 2 i e^{i\omega_1 T_0} \omega_1 D_1 A_1 + CC, \end{aligned} \tag{2.16a}$$

$$\begin{aligned} D_0^2 u_{21} + \omega_2^2 u_{21} = &- i e^{i\omega_2 T_0} \mu_2 \omega_2 A_2 - e^{3i\omega_2 T_0} k_2 A_2 + i e^{3i\omega_2 T_0} \gamma_2 \omega_2^3 A_2^3 + e^{i\omega_1 T_0} \alpha_2 A_1 \\ &- 3 e^{i\omega_2 T_0} k_2 A_2^2 \bar{A}_2 - 3 i e^{i\omega_2 T_0} \gamma_2 \omega_2^3 A_2^2 \bar{A}_2 - 2 i e^{i\omega_2 T_0} \omega_2 D_1 A_2 + \frac{1}{2} e^{i\Omega_f T_0} F + CC, \end{aligned} \tag{2.16b}$$

where CC corresponds to the complex conjugates of the right hand side terms.

In view of (2.11), the solution of (2.16) represents the perturbation of the basic harmonic solution (2.15), which therefore includes all the interesting dynamics of the system. Since the main assumption here is that the expansion in (2.11) is converging to an unattainable exact solution, then the terms u_{11}, u_{21} should not be unbounded. This means, all sources of resonances, named *secular terms*, in (2.16) should be eliminated. This procedure puts a limiting condition on the amplitudes of first order correction terms u_{11}, u_{21} in order to adhere to the asymptotic convergence of the solution. This is based on the fact that the nonlinear terms, in addition to the forcing term here, act only as a perturbation of a corresponding linear system.

In order to eliminate the secular terms a distinction should be made between different resonance cases in the system, since for each case different terms appear to be resonant. In the general non-resonant case, that is when Ω_f not near any of the system resonance frequencies, eliminating the secular terms gives differential equations for the amplitudes A_1, A_2, which are

$$2 i \omega_1 D_1 A_1 + i \mu_1 \omega_1 A_1 + 3 k_1 A_1^2 \bar{A}_1 + 3 i \gamma_1 \omega_1^3 A_1^2 \bar{A}_1 = 0, \tag{2.17a}$$

$$2i\omega_2 D_1 A_2 + i\mu_2\omega_2 A_2 + 3k_2 A_2^2\bar{A}_2 + 3i\gamma_2\omega_2^3 A_2^2\bar{A}_2 = 0. \tag{2.17b}$$

It should be noted here, that the forced excitation is considered to be a *weak* one, as a result we notice no effect in the amplitudes equations at non-resonant frequencies. However, if a *hard excitation* is considered, that is not multiplied by the small parameter ϵ, this means rewriting (2.13) and (2.14) to be

$$D_0^2 u_{10} + \omega_1^2 u_{10} = 0, \tag{2.18a}$$

$$D_0^2 u_{20} + \omega_2^2 u_{20} = F\cos(\Omega_f T_0), \tag{2.18b}$$

$$D_0^2 u_{11} + \omega_1^2 u_{11} = -\mu_1 D_0 u_{10} - k_1 u_{10}^3 - \gamma_1 D_0 u_{10}^3 + \alpha_1 u_{20} + 2D_0 D_1 u_{10}, \tag{2.19a}$$

$$D_0^2 u_{21} + \omega_2^2 u_{21} = -\mu_2 D_0 u_{20} - k_2 u_{20}^3 - \gamma_2 D_0 u_{20}^3 + \alpha_2 u_{10} + 2D_0 D_1 u_{20}, \tag{2.19b}$$

then the solution of the zero-order equation will be

$$u_{10}(T_0, T_1) = A_1(T_1)e^{i\omega_1 T_0} + \bar{A}_1(T_1)e^{-i\omega_1 T_0}, \tag{2.20a}$$

$$u_{20}(T_0, T_1) = A_2(T_1)e^{i\omega_2 T_0} + \bar{A}_2(T_1)e^{-i\omega_2 T_0} + \Gamma\cos(\Omega_f T_0), \tag{2.20b}$$

where $\Gamma = F/(\omega_2^2 - \Omega_f^2)$. Then substituting this solution again into (2.19) and eliminating the secular terms yields

$$2i\omega_1 D_1 A_1 + i\mu_1\omega_1 A_1 + 3k_1 A_1^2\bar{A}_1 + 3i\gamma_1\omega_1^3 A_1^2\bar{A}_1 = 0, \tag{2.21a}$$

$$2i\omega_2 D_1 A_2 + i\mu_2\omega_2 A_2 + 3k_2 A_2^2\bar{A}_2 + 3i\gamma_2\omega_2^3 A_2^2\bar{A}_2 + \frac{3\Gamma^2}{2}A_2(k_2 + i\gamma_2\Omega_f^2\omega_2) = 0, \tag{2.21b}$$

which encompasses an additional term when compared to (2.17) corresponding to the effect of the external excitation. This case, however, becomes interesting only for observing the forced excitation effect in the non-resonant case, or in the case of studying sub- and superharmonic resonances.

As a first attempt, we study the case of the unforced Duffing oscillator, i.e. $\Gamma = 0$, by investigating three parameters which are affecting the system dynamics, the linear and nonlinear damping coefficients μ_i, γ_i and the nonlinear stiffness coefficient k_i, especially when they change their sign. However, ω_i is always positive since we assume all the systems studied here to be oscillatory. Another remark about (2.17) and (2.21) is that they do not include any trace of α, this means that the coupling between both degrees of freedom does not affect the non-resonant condition. This means as well that studying any of both degrees of freedom is fairly equivalent

and can be done individually. Thus, in speaking about the autonomous non-resonant case the system reduces to a S-DoF system. This matches with our bottom-up study program here, through which the causes of instability are studied by adding building blocks to the system in the sense of mathematical terms.

The autonomous Duffing equation is studied extensively through the literature, see for instance [41, 90]. But for the sake of this work we will only be interested in the case when the nonlinearity brings an additional source of instability. First, we solve (2.21a) by writing the amplitude A in a polar form

$$A_1(T_1) = a_1(T_1)e^{i\phi_1(T_1)}, \tag{2.22}$$

where a and ϕ are real functions of T_1.

Substituting (2.22) in (2.21a) and separating real and imaginary parts gives

$$-2\omega_1 a\phi_1' = 0, \qquad 2\omega_1 a_1' + \mu_1\omega_1 a_1 + 3\gamma_1\omega_1^3 a_1^3 = 0, \tag{2.23}$$

where the prime dictates a time-differentiation where there is only one time scale in this equation. Here we find clearly that we have nontrivial steady state amplitudes a_1, namely, by setting $a_1' = 0$ we get

$$\mu_1\omega_1 a_1 + 3\gamma_1\omega_1^3 a_1^3 = 0, \tag{2.24}$$

which means that the possible steady state values of a_1 are

$$a_1^* = 0, \qquad a_1^* = \sqrt{\frac{-\mu_1}{3\gamma_1\omega_1^2}} \tag{2.25}$$

where the second value exists only if μ_1 and γ_1 have opposite signs. To examine the stability of these solutions, we plug them in the differential equation (2.23), linearize around the fixed point and calculate the eigenvalues. For any fixed point from (2.25), let $a_1 = a_1^* + \delta a_1$, after linearization this gives

$$\delta a_1' + (\mu_1 + 9\gamma_1\omega_1^2 a_1^{*2})\delta a_1 = 0. \tag{2.26}$$

If the nontrivial value of a_1^* in (2.25) is inserted, this gives a negative damping with the eigenvalue $\lambda = 2\mu_1$. This means, if the system has a positive linear damping $\mu_1 > 0$ but a negative nonlinear damping γ_1, an unstable limit cycle is obtained due to a subcritical Hopf bifurcation. Thus, if a perturbation is initiated outside the limit cycle, the perturbed amplitude δa_1 and thus the perturbed solution $u_1 = a_1\cos(\omega_1 t + \phi_1)$ will grow forever, even if the system has a positive linear damping $\mu_1 > 0$. This instability is of pure *nonlinear* origin, and could not be deduced by linear analysis [90].

Although we started our analysis with a non-autonomous system, we could see that assuming a *weak* force reduced the system into an autonomous one at non-resonant frequencies. However, a different result is obtained for the same assumption but while *detuning* the excitation frequency around the natural frequency of the second degree of freedom, that is

$$\Omega_f = \omega_2 + \epsilon\sigma, \tag{2.27}$$

where σ is the detuning parameter. By plugging (2.27) in (2.16), this yields

$$2i\omega_1 D_1 A_1 + i\mu_1\omega_1 A_1 + 3k_1 A_1^2\bar{A}_1 + 3i\gamma_1\omega_1^3 A_1^2\bar{A}_1 = 0, \tag{2.28a}$$

$$2i\omega_2 D_1 A_2 + i\mu_2\omega_2 A_2 + 3k_2 A_2^2\bar{A}_2 + 3i\gamma_2\omega_2^3 A_2^2\bar{A}_2 - \frac{1}{2}Fe^{i\sigma T_1} = 0. \tag{2.28b}$$

Again the amplitudes will be written in polar form

$$A_1(T_1) = a_1(T_1)e^{i\phi_1(T_1)}, \tag{2.29a}$$

$$A_2(T_1) = a_2(T_1)e^{i\phi_2(T_1)}, \tag{2.29b}$$

then by substituting in (2.28) and separating real and imaginary parts give

$$\omega_1 a_1' + \frac{1}{2}\mu_1\omega_1 a_1 + \frac{3}{8}\gamma_1\omega_1^3 a_1^3 = 0 \tag{2.30a}$$

$$\omega_1 a_1\phi_1' - \frac{3}{8}k_1 a_1^3 = 0 \tag{2.30b}$$

$$\omega_2 a_2' + \frac{1}{2}\mu_2\omega_2 a_2 + \frac{3}{8}\gamma_2\omega_2^3 a_2^3 - \frac{1}{2}F\sin(\sigma T_1 - \phi_2) = 0, \tag{2.30c}$$

$$\omega_2 a_2\phi_2 - \frac{3}{8}k_2 a_2^3 + \frac{1}{2}F\cos(\sigma T_1 - \phi_2) = 0 \tag{2.30d}$$

Since the arguments of the trigonometric functions are composed of two terms which are functions of the independent variable T_1, a change of coordinates would be necessary in order to find the stationary solutions of this system. By letting $\phi_1 = \sigma T_1 - \theta_1$ and $\phi_2 = \sigma T_1 - \theta_2$ we find

$$\omega_1 a_1' + \frac{1}{2}\mu_1\omega_1 a_1 + \frac{3}{8}\gamma_1\omega_1^3 a_1^3 = 0 \tag{2.31a}$$

$$\omega_1 a_1(\sigma - \theta_1') - \frac{3}{8}k_1 a_1^3 = 0 \tag{2.31b}$$

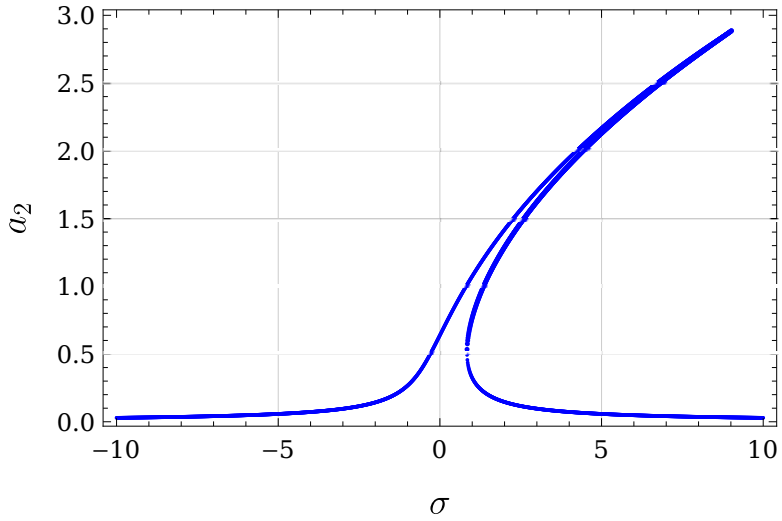

Figure 2.1: Resonance curve of Duffing oscillator according to (2.32), where $\omega_2 = \sqrt{3}, \mu_2 = 0.2, k_2 = 5, F = 1$ and $\gamma_2 = 0$.

$$\omega_2 a_2' + \frac{1}{2}\mu_2\omega_2 a_2 + \frac{3}{8}\gamma_2\omega_2^3 a_2^3 - \frac{1}{2}F\sin(\theta_2) = 0, \tag{2.31c}$$

$$\omega_2 a_2(\sigma - \theta_2') - \frac{3}{8}k_2 a_2^3 + \frac{1}{2}F\cos(\theta_2) = 0 \tag{2.31d}$$

then by setting $a_2' = 0$ and $\theta_2' = 0$ we get the steady-state solutions. The equations show how the two degrees of freedom are uncoupled, which means that the coupling stiffness terms have no effect. Finally, the two last equations are solved for a_2 to give the resonance equation

$$\begin{aligned}&(48F^2k_2 + 128\sigma(\mu_2^2 + 4\sigma^2)\omega_2^3)a_2^2 - 48(k_2(\mu_2^2 + 12\sigma^2)\omega_2^2 - 4\gamma_2\mu_2\sigma\omega_2^5)a_2^4 \\ &+ 72(3k_2^2\sigma\omega_2 - k_2\gamma_2\mu_2\omega_2^4 + \gamma_2^2\sigma\omega_2^7)a_2^6 - 27k_2(k_2^2 + \gamma_2^2\omega_2^6)a_2^8 - 128F^2\sigma\omega_2 = 0.\end{aligned} \tag{2.32}$$

By plotting the resonance equation in Fig. 2.1, it shows the typical Duffing resonance curve for a S-DoF system. The first degree of freedom, however, behaves as an unforced Duffing oscillator as discussed before. This means that no coupling exists between both degrees of freedoms and thus no energy transfer.

2.2.2 1:1 Internal resonance

Another nonlinear phenomenon that could cause response amplification or destabilization of solutions is the internal resonance. To illustrate this phenomenon it will be assumed that the natural frequencies of the system are nearly equal, i.e. $\omega_1 \simeq \omega_2$. This case has a particular

importance in some microsystems. A typical example would be the micro-ring gyroscope, which due to its axis-symmetry exhibits a degenerate first natural frequency, thus having two eigenfunctions or modes for the same frequency. In practice this degeneracy is broken due to fabrication limitations, but both natural frequencies remain similar. This particular example will be discussed in chapters 4 and 5.

To analyze this case, we return again to (2.16) but with a new resonance condition. We will assume having the second DoF tuned at resonance, that is

$$\Omega_f = \omega_2 + \epsilon\sigma_1, \tag{2.33}$$

while the first DoF has a similar natural frequency as discussed before, this means

$$\omega_1 = \omega_2 + \epsilon\sigma_2. \tag{2.34}$$

By plugging these resonance conditions into (2.16), and in order to eliminate the secular terms, we get the following solvability conditions

$$2i\omega_1 e^{i\sigma_2 T_1}\omega_1 A_1' + i\mu_1\omega_1 e^{i\sigma_2 T_1}\omega_1 A_1 + 3e^{i\sigma_2 T_1}k_1 A_1^2\bar{A}_1 + 3ie^{i\sigma_2 T_1}\gamma_1\omega_1^3 A_1^2\bar{A}_1 - \alpha_1 A_2 = 0, \tag{2.35a}$$

$$2i\omega_2 A_2' + i\mu_2\omega_2 A_2 + 3k_2 A_2^2\bar{A}_2 + 3i\gamma_2\omega_2^3 A_2^2\bar{A}_2 - \frac{1}{2}Fe^{i\sigma T_1} - \alpha_2 e^{i\sigma_2 T_1}A_1 = 0. \tag{2.35b}$$

Here we can see the appearance of the coupling terms $\alpha_1 A_2, \alpha_2 A_1$ for the first time through our analysis. As before, we put the amplitudes in polar form

$$A_1 = \frac{1}{2}a_1 e^{i\phi_1}, \tag{2.36a}$$

$$A_2 = \frac{1}{2}a_2 e^{i\phi_2}, \tag{2.36b}$$

then inserting them into the solvability conditions and separating real and imaginary parts gives

$$\omega_1 a_1\phi_1' - \frac{3}{8}k_1 a_1^3 + \frac{1}{2}\alpha_1 a_2\cos(\sigma_2 T_1 + \phi_1 - \phi_2) = 0 \tag{2.37a}$$

$$\omega_1 a_1' + \frac{1}{2}\mu_1\omega_1 a_1 + \frac{3}{8}\gamma_1\omega_1^3 a_1^3 + \frac{1}{2}\alpha_1 a_2\sin(\sigma_2 T_1 + \phi_1 - \phi_2) = 0 \tag{2.37b}$$

$$\omega_2 a_2\phi_2' - \frac{3}{8}k_2 a_2^3 + \frac{1}{2}\alpha_2 a_1\cos(\sigma_2 T_1 + \phi_1 - \phi_2) + \frac{1}{2}F\cos(\sigma_1 T_1 - \phi_2) = 0 \tag{2.37c}$$

$$\omega_2 a_2' + \frac{1}{2}\mu_2\omega_2 a_2 + \frac{3}{8}\gamma_2\omega_2^3 a_2^3 - \frac{1}{2}\alpha_2 a_1\sin(\sigma_2 T_1 + \phi_1 - \phi_2) - \frac{1}{2}F\sin(\sigma_1 T_1 - \phi_2) = 0 \tag{2.37d}$$

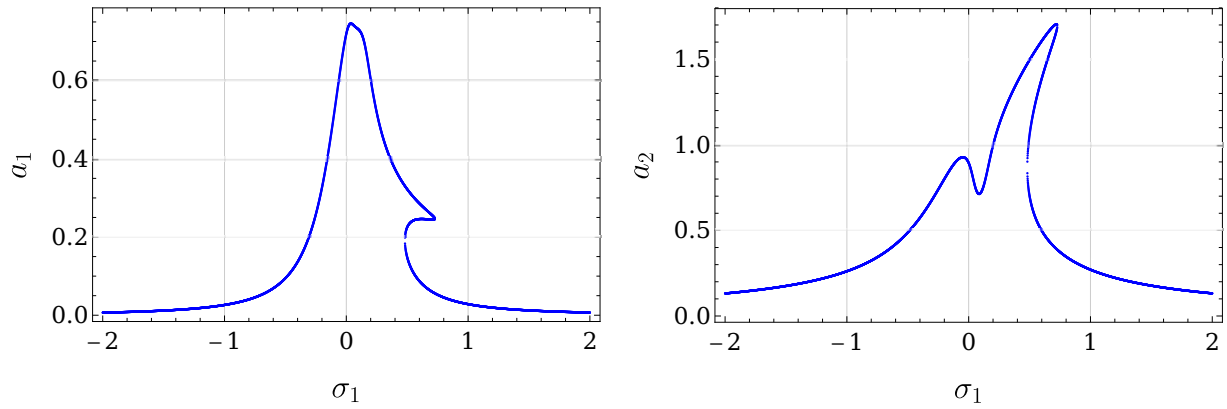

(a) a_1 (b) a_2

Figure 2.2: Resonance curves of a_1 and a_2 under 1:1 internal resonance according to (2.38), where $\omega_1 = 0.97, \omega_2 = 0.95, k_1 = 0.3, k_2 = 0.6, \alpha_1 = 0.2, \alpha_2 = 0.4, \mu_1 = 0.2, \mu_2 = 0.3, F = 0.5, \gamma_1 = \gamma_2 = 0$ and $\sigma_2 = 0.02$.

Following the same procedure as before, we define $\delta_2 = \sigma_2 T_1 + \phi_1 - \phi_2$ and $\delta_1 = \sigma_1 t_1 - \phi_2$. For the sake of stationary solutions we set then $a_1' = 0, a_2' = 0$, while $\phi_1' = \sigma_1 - \sigma_2, \phi_2' = \sigma_1$ which lead to $\delta_1' = \delta_2' = 0$. Solving the four algebraic equations yields two coupled resonance equations

$$\begin{aligned} &a_1^2\left(64(\mu_1^2+4(\sigma_1-\sigma_2)^2)(\sigma_1-\sigma_2)\omega_1^3+24k_1\alpha_1^2a_2^2\right)+64\alpha_1^2(\sigma_2-\sigma_1)\omega_1a_2^2\\ &+\left(-24k_1(\mu_1^2+12(\sigma_1-\sigma_2)^2)\omega_1^2+96\gamma_1\mu_1(\sigma_1-\sigma_2)\omega_1^5\right)a_1^4\\ &+36\left(3k_1^2(\sigma_1-\sigma_2)\omega_1-k_1\gamma_1\mu_1\omega_1^4+\gamma_1^2(\sigma_1-\sigma_2)\omega_1^7\right)a_1^6-\frac{27}{2}k_1(k_1^2+\gamma_1^2\omega_1^6)a_1^8=0, \end{aligned} \tag{2.38a}$$

$$\begin{aligned} &-256F^2\alpha_1^2a_2^2+256\alpha_1^2(\mu_2^2+4\sigma_1^2)\omega_2^2a_2^4+384\alpha_1^2\omega_2(-2k_2\sigma_1+\gamma_2\mu_2\omega_2^3)a_2^6+144\alpha_1^2(k_2^2+\gamma_2^2\omega_2^6)a_2^8\\ &+a_1^2\left(512\alpha_1\alpha_2(\mu_1\mu_2+4\sigma_1(\sigma_2-\sigma_1))\omega_1\omega_2a_2^2+384\alpha_1\alpha_2\omega_1(2k_2(\sigma_1-\sigma_2)+\gamma_2\mu_1\omega_2^3)a_2^4\right)\\ &+a_1^4\left(256\alpha_2^2(\mu_1^2+4(\sigma_1-\sigma_2)^2)\omega_1^2+384\alpha_1\alpha_2(2k_1\sigma_1+\gamma_1\mu_2\omega_1^3)\omega_2a_2^2+288\alpha_1\alpha_2(\gamma_1\gamma_2\omega_1^3\omega_2^3-k_1k_2)a_2^4\right)\\ &+384\alpha_2^2\omega_1(2k_1(\sigma_2-\sigma_1)+\gamma_1\mu_1\omega_1^3)a_1^6+144\alpha_2^2(k_1^2+\gamma_1^2\omega_1^6)a_1^8=0. \end{aligned} \tag{2.38b}$$

Through Fig. 2.2 a typical resonance curve for internal resonances is depicted. The spacing between the two peaks in each figure relies on the detuning parameter σ_2. By increasing σ_2 one of the peaks keeps increasing and the other decreases until the first one disappears at a large detuning between the two frequencies. Moreover, at some value of σ_2 a bifurcation occurs and an isolated branch (*isola*) in each of the resonance frequency curves appears, which is shown in Fig. 2.3. Through these figures multiple solutions appear at some excitation frequencies, some of them are isolated from other solutions which causes a sudden jump in amplitude by

varying the excitation frequency. Both multi-stability and jumps could be beneficial as well as detrimental with respect to different applications.

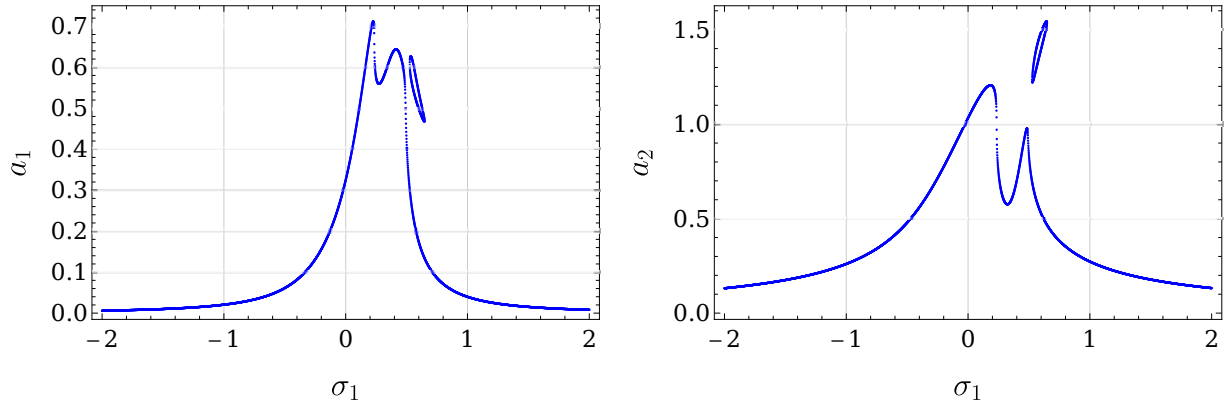

(a) a_1 (b) a_2

Figure 2.3: Resonance curves and isolas of a_1 and a_2 under 1:1 internal resonance according to (2.38), where $\omega_1 = 0.97, \omega_2 = 0.95, k_1 = 0.3, k_2 = 0.6, \alpha_1 = 0.2, \alpha_2 = 0.4, \mu_1 = 0.2, \mu_2 = 0.3, F = 0.5, \gamma_1 = \gamma_2 = 0$ and $\sigma_2 = 0.3$.

2.3 Circulatory forces: an example

Another source of instability is discussed in this section, where circulatory forces are considered again but in a more elaborate nonlinear case. Circulatory forces (also named follower or non-conservative positional forces) grasped the attention of the academic community since the famous work of Ziegler [91]. These *non-potential positional* forces were found to cause instability of the trivial solution in the system under certain conditions [92, 93]. In addition, they were found to have a practical significance in several applications extending from the phenomenon of intense angular self-oscillations of a carriage wheel to the squealing brakes and the self-excited vibrations in paper calenders [85].

Since most mechanical systems can be reduced to lumped-parameter systems, a basic understanding of the phenomenon can be attained from the simplest possible mechanical system, i.e. two degree-of-freedom (2-DoF) mass-spring system. In an attempt to investigate the effect of circulatory forces in its simplest case, in [87] a 2-DoF system was presented, which will be further analyzed in this section.

Fig.2.4 shows a 2-DoF system composed of a point mass supported by two orthogonal springs and pressed against a rotating disc underneath, which causes a frictional force acting on the point mass in the direction of relative velocity. The contact between the point mass and the

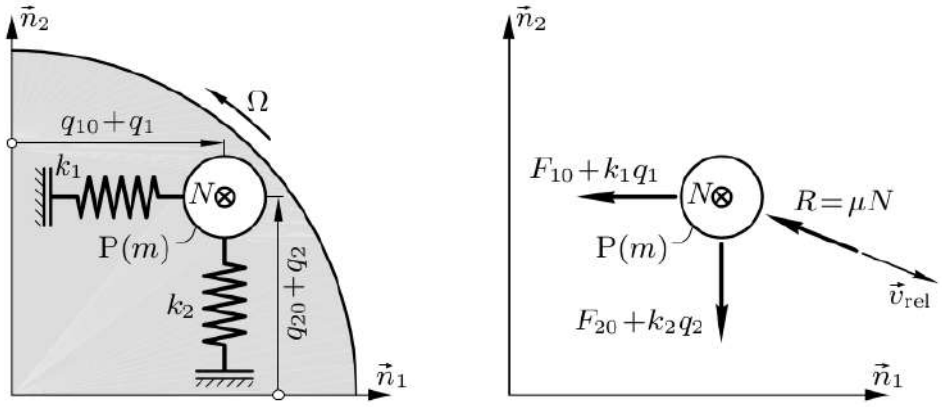

Figure 2.4: Point mass on a rotating disc (left), free-body diagram (right), courtesy of P. Hagedorn [87]

disc is assumed to be always slipping, without any sticking.

The equations of motion will be derived according to the free-body diagram shown in Fig. 2.4 [87]. The disturbing force here is the frictional force R applied on the point mass due to its slip-friction with the rotating disc, which is calculated in vector form to be

$$\vec{R} = -\mu N \frac{\vec{v}_{rel}}{|\vec{v}_{rel}|}, \tag{2.39}$$

where $\vec{v}_{rel}$ is the velocity of the point mass P with respect to the rotating disc. We define P^* to be the point on the rotating disc in contact with P. Thus, to calculate $\vec{v}_{rel}$ as follows

$$\begin{aligned} \vec{v}_{rel} = \vec{v}|_P - \vec{v}|_{P^*} &= [\dot{q}_1\vec{n}_1 + \dot{q}_2\vec{n}_2] - [-(q_{20}+q_2)\Omega\,\vec{n}_1 + (q_{10}+q_2)\Omega\,\vec{n}_2] \\ &= (\dot{q}_1 + (q_{20}+q_2)\Omega)\,\vec{n}_1 + (\dot{q}_2 - (q_{10}+q_1)\Omega)\,\vec{n}_2. \end{aligned} \tag{2.40}$$

Applying Newton's second law on the point mass, and separating into the two orthogonal directions gives

$$m\ddot{q}_1 + (F_{10}+k_1q_1) = -\mu N \frac{(\dot{q}_1 + (q_{20}+q_2)\Omega)}{\sqrt{(\dot{q}_1 + (q_{20}+q_2)\Omega)^2 + (\dot{q}_2 - (q_{10}+q_1)\Omega)^2}}, \tag{2.41a}$$

$$m\ddot{q}_2 + (F_{20}+k_2q_2) = -\mu N \frac{(\dot{q}_2 - (q_{10}+q_1)\Omega)}{\sqrt{(\dot{q}_1 + (q_{20}+q_2)\Omega)^2 + (\dot{q}_2 - (q_{10}+q_1)\Omega)^2}}, \tag{2.41b}$$

where the spring forces at the stationary point $q_1 = q_{10}, q_2 = q_{20}$ can be calculated to be

$$F_{10} = -\mu N \frac{q_{20}\Omega}{\sqrt{q_{20}^2\Omega^2 + q_{10}^2\Omega^2}}, \qquad F_{20} = \mu N \frac{q_{10}\Omega}{\sqrt{q_{20}^2\Omega^2 + q_{10}^2\Omega^2}}.$$

2.3.1 Nonlinear analysis

We start with non-dimensionalization of the system to reduce the system to its simplest form and identify the influencing parameters. We introduce the non-dimensional time τ and the normalized displacement u_i to be

$$\tau = \Omega t \quad u_i = \frac{q_i}{a}, \qquad i = 1, 2 \tag{2.42}$$

then the differentiation with respect to time gives

$$\begin{aligned} u' &= \frac{du}{d\tau} = \frac{du}{dt}\frac{dt}{d\tau} = \frac{1}{a\Omega}\dot{q}, \\ u'' &= \frac{d^2u}{d\tau^2} = \frac{d^2u}{dt^2}\frac{d^2t}{d\tau^2} = \frac{1}{a\Omega^2}\ddot{q}. \end{aligned} \tag{2.43}$$

For simplicity we will set our coordinates so that $q_{10} = q_{20} = a$, in this case the equations of motion become

$$ma\Omega^2 u_1'' + (F_{10} + k_1 a u_1) = -\mu N \frac{a\Omega u_1' + (a + a u_2)\Omega}{\sqrt{(a\Omega u_1' + (a + a u_2)\Omega)^2 + (\dot{q_2} - (a\Omega u_2' - (a + a u_1)\Omega)^2}}, \tag{2.44a}$$

$$ma\Omega^2 u_2'' + (F_{20} + k_2 a u_2) = -\mu N \frac{a\Omega u_2' - (a + a u_1)\Omega}{\sqrt{(a\Omega u_1' + (a + a u_2)\Omega)^2 + (\dot{q_2} - (a\Omega u_2' - (a + a u_1)\Omega)^2}}, \tag{2.44b}$$

where

$$F_{10} = -F_{20} = -\frac{\mu N}{\sqrt{2}} \tag{2.45}$$

Dividing by $ma\Omega^2$ leads to

$$u_1'' + (-\eta + \bar{k}_1 u_1) = -\sqrt{2}\eta \frac{u_1' + (1 + u_2)}{\sqrt{(u_1' + (1 + u_2))^2 + (u_2' - (1 + u_1))^2}}, \tag{2.46a}$$

$$u_2'' + (\eta + \bar{k}_2 u_2) = -\sqrt{2}\eta \frac{u_2' - (1 + u_1)}{\sqrt{(u_1' + (1 + u_2))^2 + (u_2' - (1 + u_1))^2}}, \tag{2.46b}$$

where

$$\bar{k_i} = \frac{k_i}{m\Omega^2}, \qquad \eta = \frac{\mu N}{\sqrt{2} m a \Omega^2}. \tag{2.47}$$

In order to determine the solutions of the system and their stability, (2.46) is then rewritten in four dimensional first-order system

$$v_1' - v_2 = 0, \tag{2.48a}$$

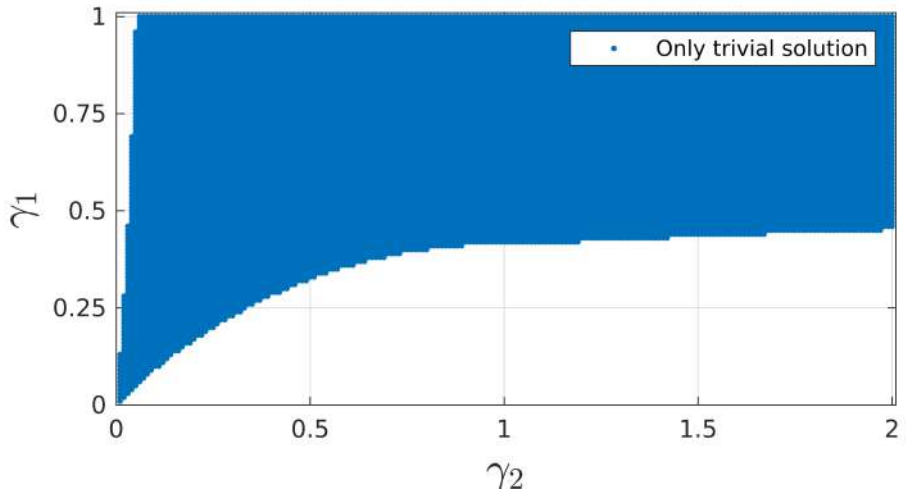

Figure 2.5: The trivial and nontrivial fixed points in the parameter space $\gamma_1 - \gamma_2$, see (2.50)

$$v_2' + \bar{k}_1 v_1 + \sqrt{2}\eta \frac{v_2 + (1 + v_3)}{\sqrt{(v_2 + (1 + v_3))^2 + (v_4 - (1 + v_1))^2}} - \eta = 0, \tag{2.48b}$$

$$v_3' - v_4 = 0, \tag{2.48c}$$

$$v_4' + \bar{k}_2 v_3 + \sqrt{2}\eta \frac{v_4 - (1 + v_1)}{\sqrt{(v_2 + (1 + v_3))^2 + (v_4 - (1 + v_1))^2}} + \eta = 0, \tag{2.48d}$$

then by setting $v_1' = v_2' = v_3' = v_4' = 0$ to find the stationary points we get

$$\bar{k}_1 v_{1st} + \sqrt{2}\eta \frac{1 + v_{3st}}{\sqrt{(1 + v_{3st})^2 + (1 + v_{1st})^2}} - \eta = 0, \tag{2.49a}$$

$$\bar{k}_2 v_{3st} - \sqrt{2}\eta \frac{1 + v_{1st}}{\sqrt{(1 + v_{3st})^2 + (1 + v_{1st})^2}} + \eta = 0. \tag{2.49b}$$

and $v_{2st} = v_{4st} = 0$, where the index st means stationary.

The equations (2.49) allow another simplification by dividing by η to give

$$\gamma_1 v_{1st} + \sqrt{2} \frac{1 + v_{3st}}{\sqrt{(1 + v_{3st})^2 + (1 + v_{1st})^2}} - 1 = 0, \tag{2.50a}$$

$$\gamma_2 v_{3st} - \sqrt{2} \frac{1 + v_{1st}}{\sqrt{(1 + v_{3st})^2 + (1 + v_{1st})^2}} + 1 = 0, \tag{2.50b}$$

with only two parameters γ_1, γ_2.

First, we study the existence of nontrivial stationary solutions by varying the parameters γ_1, γ_2. This could be depicted in the parameter space $\gamma_1 - \gamma_2$ in Fig. 2.5 . In this figure we can

identify at each pair of parameters whether we have only the trivial stationary solution, shown in blue, or if at least a nontrivial stationary solution exists which is shown in white.

An example of the nontrivial stationary points is shown in Fig. 2.6, where v_{1st} of the fixed points is depicted with respect to γ_1. This serves as vertical cross sections in Fig. 2.5 at two different γ_2 values. By calculating the eigenvalues for all nontrivial solutions, it was found that at least one stable fixed point is present.

In order to verify the stability of the nontrivial solution, direct numerical integration is applied on the original system of differential equations (2.48) and a projection of the phase space in the $v_1 - v_3$ plane is plotted in Fig. 2.7. It can be shown that the positive and negative values of the nontrivial fixed points v_{1st} are stable. Moreover, a stable limit cycle could also be found, which relates to flutter instability discussed before in section 2.1. We proceed by studying the stability of the trivial solution. To this end we calculate the Jacobian matrix of the system (2.48), that is

$$\boldsymbol{J} = \begin{bmatrix} 0 & 1 & 0 & 0 \\ -\bar{k_1} + \dfrac{\sqrt{2}\eta\psi_1\psi_2}{\Psi} & -\dfrac{\sqrt{2}\eta\psi_2^2}{\Psi} & -\dfrac{\sqrt{2}\eta\psi_2^2}{\Psi} & \dfrac{-\sqrt{2}\eta\psi_1\psi_2}{\Psi} \\ 0 & 0 & 0 & 1 \\ \dfrac{\sqrt{2}\eta\psi_1^2}{\Psi} & -\dfrac{\sqrt{2}\eta\psi_1\psi_2}{\Psi} & -\bar{k_2} - \dfrac{\sqrt{2}\eta\psi_1\psi_2}{\Psi} & -\dfrac{\sqrt{2}\eta\psi_1^2}{\Psi} \end{bmatrix} \tag{2.51}$$

where

$$\Psi = \left(\psi_1^2 + \psi_2^2\right)^{3/2}, \quad \psi_1 = (1 + v_2 + v_3), \quad \psi_2 = (1 + v_1 - v_4).$$

At the fixed point $\boldsymbol{v}_{st} = \mathbf{0}$ we have

$$\Psi = 2^{3/2}, \quad \psi_1 = 1, \quad \psi_2 = 1, \tag{2.52}$$

which lets the evaluation of the Jacobian to be

$$\boldsymbol{J}|_{\boldsymbol{v}=\mathbf{0}} = \begin{bmatrix} 0 & 1 & 0 & 0 \\ -\bar{k_1} + \dfrac{\eta}{2} & -\dfrac{\eta}{2} & -\dfrac{\eta}{2} & \dfrac{-\eta}{2} \\ 0 & 0 & 0 & 1 \\ \dfrac{\eta}{2} & \dfrac{-\eta}{2} & -\bar{k_2} - \dfrac{\eta}{2} & -\dfrac{\eta}{2} \end{bmatrix} \tag{2.53}$$

The Jacobian matrix here contains three system parameters $\bar{k}_1, \bar{k}_2$ and η. By setting $\eta = 1$ and varying the other two parameters, this gives us an indication about trivial solution stability

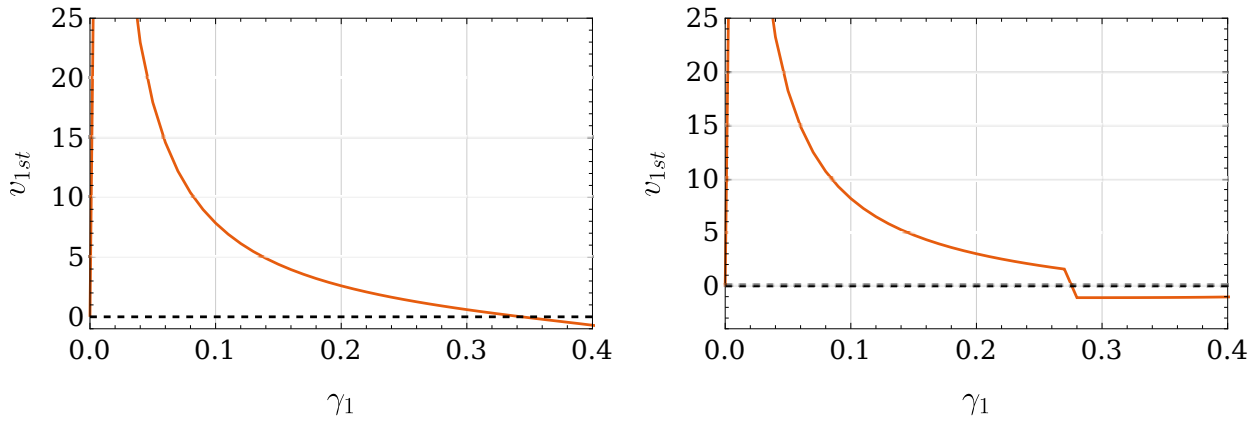

(a) $\gamma_2 = 1.1$ (b) $\gamma_2 = 2$

Figure 2.6: The stationary solutions of v_1 with respect to γ_1 at two different γ_2 values.

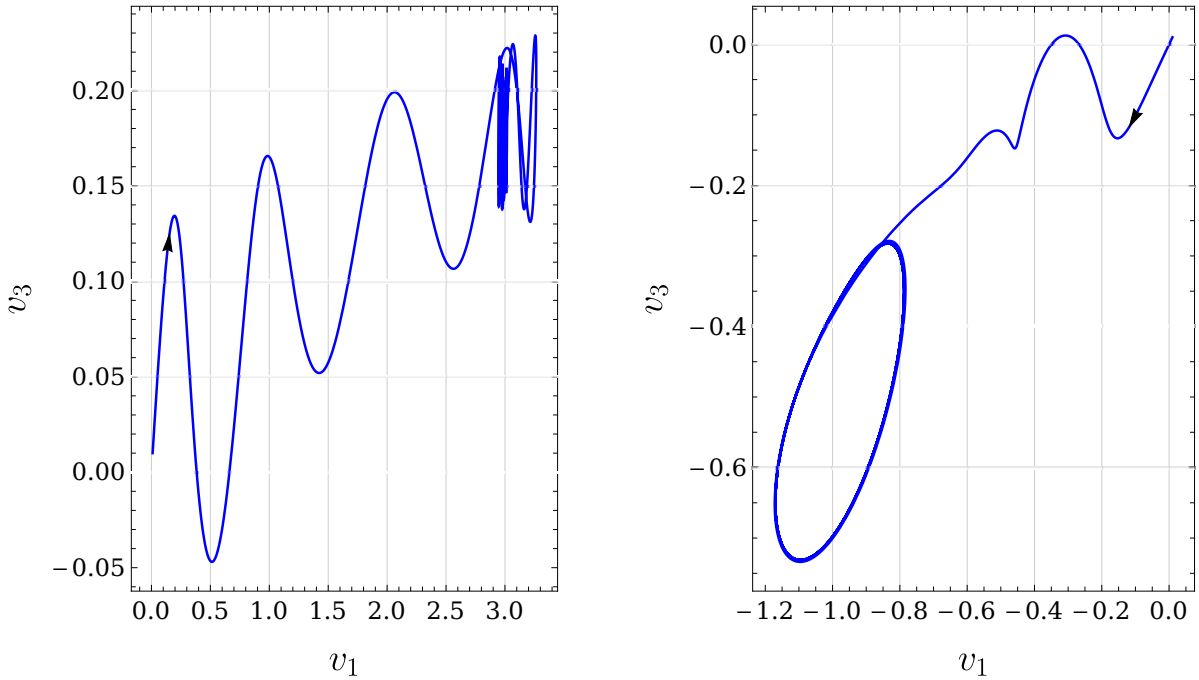

(a) $\gamma_1 = 0.2, \gamma_2 = 2$ (b) $\gamma_1 = 0.4, \gamma_2 = 2$

Figure 2.7: Time trajectories of the system variables near the trivial solution in the projection v_1-v_3 of the phase space.

for the ratio between excitation and system stiffness, which is corresponding to γ_i in (2.50) . The same approach will be used analytically in the next subsection.

Using this approach the eigenvalues of the Jacobian could then be calculated at each evaluated pair of $(\bar{k}_1, \bar{k}_2)$, which gives the required information on the trivial solution stability at each point of the parameter space ($\bar{k}_1$-$\bar{k}_2$).

The real parts of the eigenvalues are calculated, and the maximum real part is checked whether it is positive, thus indicating instability according to the definition of stability discussed in section 2.1. In Fig. 2.8 the maximum real part of the eigenvalues at each point of the parameter space is shown in terms of a color spectrum appearing in the legend on the top of the figure. The true blue color represents a stable solution, whereas all other colors represent the instability of the trivial solution at different levels.

Some observations could be made from this figure. First, although the slip-only friction is normally attributed to damping the system, we find here a totally different picture. The frictional force does contribute to the damping mechanism but it induces *circulatory* forces as well. This could be noticed from the Jacobian matrix (2.53) by observing the two elements

$$J_{23} = \frac{\partial f_2}{\partial v_3} = \frac{\partial f_2}{\partial q_2} = -\frac{\eta}{2}, \quad J_{41} = \frac{\partial f_4}{\partial v_1} = \frac{\partial f_4}{\partial q_1} = \frac{\eta}{2}, \tag{2.54}$$

where f_i is the vector field for the degree of freedom i. These two elements represent the system's circulatory forces by definition. Since in our case the damping coefficients and stiffnesses are positive, therefore, there is no reason for instability in our case except for the existence of the circulatory forces.

Secondly, we observe that as long as $\bar{k}_1 \simeq \bar{k}_2$ the trivial solution is stable, and for regions of significantly dissimilar stiffnesses the trivial solution is greatly destabilized.

And thirdly, by comparing Fig. 2.8 with Fig. 2.5 we find that the trivial solution is destabilized in some parts, for instance where $\bar{k}_2 < 0.5$, where no nontrivial solution exists. That means at these parts the system has no stable solution.

In conclusion, the system shows its propensity to instability even though the mechanical system from the first sight seems to have no peculiarities to exhibit instability. Thereby, this system could illustrate the influence of circulatory forces remarkably in such a simple mechanical system.

In addition, this gives some insight about the effect of losing the symmetry of the stiffness matrix. Since any asymmetric real matrix can be decomposed to the sum of symmetric and skew-symmetric matrices, circulatory forces then hint at losing (breaking) the symmetry of the stiffness matrix in a wide sense, i.e. displacement-proportional matrix. A detailed explanation

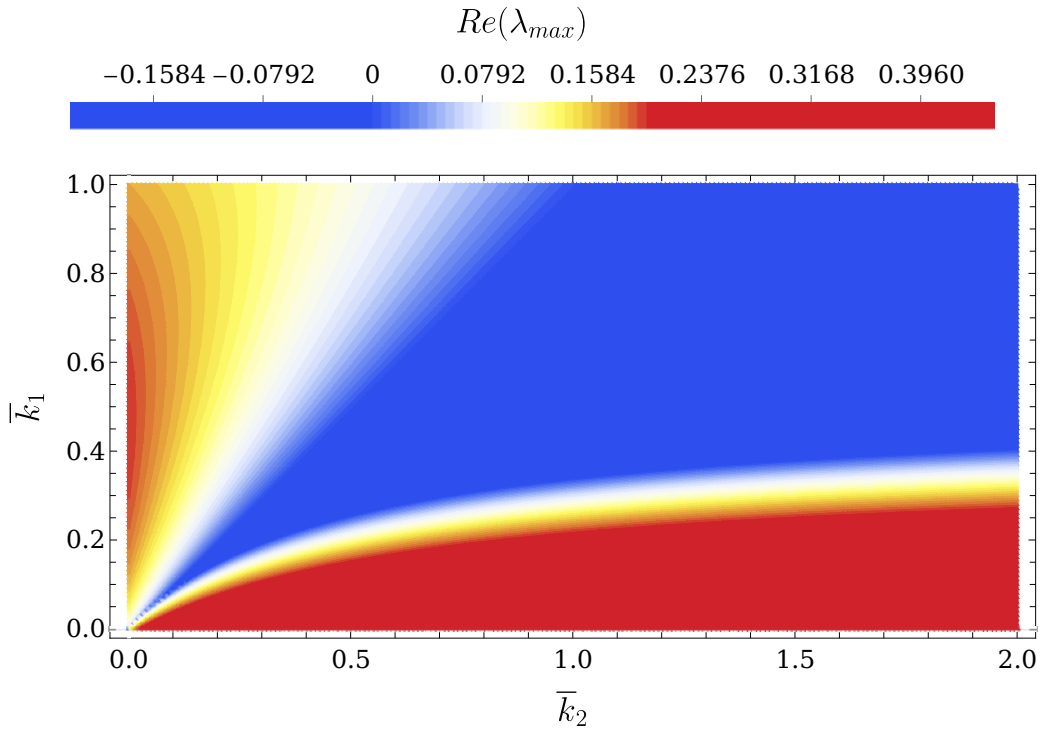

Figure 2.8: Maximum real part of the eigenvalues for the trivial fixed point in the parameter space $\bar{k}_1$-$\bar{k}_2$, see (2.53).

of the conditions of instability in these systems can be found in [94]. This occurs as well when the stiffness matrix becomes time-dependent as a parametric excitation, as will be explained in chapter 3. In this case, if the symmetry of the parametric excitation matrix is lost by adding a phase-shift in its off-diagonal terms, we observe a significantly special case, that is the asynchronous parametric excitation, which will be given special attention in the next chapters.

2.3.2 Linearized system

Up to this point the stability of different system solutions was studied numerically. An analytical approach will then be conducted to understand the stability of system's trivial solution. In order to do that, we linearize the system around the trivial solution to be

$$\begin{aligned} u_1'' + \bar{k}_1 u_1 + \frac{\eta}{2}[u_1' + u_2' + (u_2 - u_1)] = 0, \\ u_2'' + \bar{k}_2 u_2 + \frac{\eta}{2}[u_1' + u_2' + (u_2 - u_1)] = 0. \end{aligned} \tag{2.55}$$

It can be represented in matrix form as

$$\boldsymbol{M}\boldsymbol{u}'' + \boldsymbol{D}\boldsymbol{u}' + (\boldsymbol{K} + \boldsymbol{N})\boldsymbol{u} = \boldsymbol{0} \tag{2.56}$$

where

$$\begin{aligned} \boldsymbol{M} &= \begin{bmatrix} 1 & 0 \\ 0 & 1 \end{bmatrix}, \qquad \boldsymbol{D} = \frac{\eta}{2}\begin{bmatrix} 1 & 1 \\ 1 & 1 \end{bmatrix}, \\ \boldsymbol{K} &= \begin{bmatrix} \bar{k}_1 - \frac{\eta}{2} & 0 \\ 0 & \bar{k}_2 + \frac{\eta}{2} \end{bmatrix}, \qquad \boldsymbol{N} = \begin{bmatrix} 0 & \frac{\eta}{2} \\ -\frac{\eta}{2} & 0 \end{bmatrix}. \end{aligned} \tag{2.57}$$

For the ansatz

$$u_1(t) = U_1 e^{\lambda t}, \tag{2.58a}$$

$$u_2(t) = U_2 e^{\lambda t}, \tag{2.58b}$$

we find the characteristic equation to be

$$\lambda^4 + \eta\lambda^3 + [\bar{k}_1 + \bar{k}_2]\lambda^2 + \frac{\eta}{2}[\bar{k}_1 + \bar{k}_2]\lambda + \frac{\eta}{2}[\bar{k}_1 - \bar{k}_2] + \bar{k}_1\bar{k}_2 = 0. \tag{2.59}$$

Due to the relative complexity of the characteristic equation, we study as a first attempt the special case of $\bar{k}_1 = \bar{k}_2$. In this case the characteristic equation becomes

$$\lambda^4 + \eta\lambda^3 + 2\bar{k}\lambda^2 + \eta\bar{k}\lambda + \bar{k}^2 = 0. \tag{2.60}$$

with the roots

$$\lambda_{1,2} = \frac{1}{2}[-\eta \pm \sqrt{\eta^2 - 4\bar{k}}] \qquad \lambda_{3,4} = \pm i\sqrt{\bar{k}}. \tag{2.61}$$

The first two eigenvalues show an upper limit of zero for the real part, when $\bar{k} << \eta$, while the last two eigenvalues have no real parts. This means, that if the system stiffnesses are exactly equal, the trivial solution proves to be stable or *marginally* stable for any given frictional force η. This complies very well with the previous numerical study conducted. In Fig. 2.8 all the real parts of the system's eigenvalues are either negative or zero when $\bar{k}_1 = \bar{k}_2$

In the general case, however, we use the Routh-Hurwitz criterion to obtain the stability of the trivial solution. The criterion states that for the characteristic equation

$$a_0\lambda^4 + a_1\lambda^3 + a_2\lambda^2 + a_3\lambda + a_4 = 0 \tag{2.62}$$

the condition for all roots to have negative real parts, thereby asymptotic stability, is that all the inequalities [95, 96]

$$\begin{aligned} C_1 : \Delta_1 = a_1 > 0, \quad C_2 : \Delta_2 = a_1 a_2 - a_0 a_3 > 0 \\ C_3 : \Delta_3 = a_3 \Delta_2 - a_1^2 a_4 > 0, \quad C_4 : \Delta_4 = a_4 \Delta_3 > 0 \end{aligned} \tag{2.63}$$

The criterion in our case states that if the inequalities

$$C_1 : \eta > 0, \tag{2.64a}$$

$$C_2 : \frac{\eta}{2}(\bar{k}_1 + \bar{k}_2) > 0, \tag{2.64b}$$

$$C_3 : \frac{\eta^2}{4}(\bar{k}_1 - \bar{k}_2)\left[(\bar{k}_1 - \bar{k}_2) - 2\eta\right] > 0, \tag{2.64c}$$

$$C_4 : \frac{\eta}{2}[\bar{k}_1 - \bar{k}_2] + \bar{k}_1 \bar{k}_2 > 0 \tag{2.64d}$$

are satisfied, this would be a sufficient and necessary condition that each eigenvalue has a negative real part.

In our mechanical system, $\bar{k}_{1,2}$ and η are always positive, which means that the first two inequalities are always satisfied. However, for the last two inequalities we differentiate between two cases, $\bar{k}_1 > \bar{k}_2$ or $\bar{k}_2 > \bar{k}_1$. For $\bar{k}_1 > \bar{k}_2$ the last inequality is always satisfied, however the third one will not if $\eta > \frac{(\bar{k}_1 - \bar{k}_2)}{2}$.

In the other case, $\bar{k}_2 > \bar{k}_1$, we rewrite the third inequality in the form

$$(\bar{k}_2 - \bar{k}_1)\left[(\bar{k}_2 - \bar{k}_1) + 2\eta\right] > 0, \tag{2.65}$$

which is obviously satisfied. To study the last inequality in this case, we divide it with $\bar{k}_1 \bar{k}_2$, yielding

$$\frac{\eta}{2}[\frac{1}{\bar{k}_1} - \frac{1}{\bar{k}_2}] < 1. \tag{2.66}$$

But because $\frac{1}{\bar{k}_1} - \frac{1}{\bar{k}_2}$ in the case $\bar{k}_2 > \bar{k}_1$ is always positive, this means that the inequality will not be satisfied if

$$\frac{1}{\bar{k}_1} - \frac{1}{\bar{k}_2} > \frac{2}{\eta}. \tag{2.67}$$

In summary, the trivial solution does not include negative real parts in two different cases,

that is

$$\eta \begin{cases} > \dfrac{\bar{k}_1 - \bar{k}_2}{2}, & \bar{k}_1 > \bar{k}_2 \\ > \dfrac{2\bar{k}_1\bar{k}_2}{\bar{k}_2 - \bar{k}_1}, & \bar{k}_1 < \bar{k}_2, \end{cases} \tag{2.68}$$

which means, that satisfying the inequalities (2.68) either leads to the instability of the trivial solution according to the linear analysis, or to a zero real part.

By close observation of the *instability* conditions for the trivial solution in (2.68) we can see that instability can not occur for exactly equal stiffnesses, which was proved before in the special case $\bar{k}_1 = \bar{k}_2$, and supported by the previous numerical calculation of the system's exponents. And secondly, if the frictional force could exceed the difference between both stiffness values, the trivial solution turns to be unstable. This case could only happen if the stiffnesses are away from equality and when their values are quite small. This same observation could be made again from Fig. 2.8 and its succeeding discussion.

2.4 Conclusion

In summary, several observations could be obtained by analysing time-invariant systems. In the system of coupled two Duffing oscillators, although the system is relatively simple, the one-to-one internal resonance could initiate strange behaviors, such as an isola. This case specifically is important for the next chapters, since this type of internal resonance appear in systems with degenerate natural frequencies, which is the case for the axis-symmetric micro-gyroscope. In the other example, circulatory forces were found to influence the dynamics of the system, either linear or nonlinear if they were large enough with respect to system stiffness coefficients. Moreover, in the nonlinear system they were found to cause a destabilization of the trivial solution even when no nontrivial solution exists, which is a divergence case. For some values of system parameters, they could even initiate a limit cycle in the absence of external excitation or negative damping. Moreover, circulatory forces corresponds to having a skew-symmetric displacement-proportional matrix, in other words, it corresponds to introducing an asymmetry in the stiffness matrix. For time-periodic stiffness matrices, discussed in the next chapters, their symmetry could be lost by adding a phase-shift to the off-diagonal terms leading to other destabilization phenomena. These aspects and sources of instability should be noted through our bottom-up approach to help in understanding more complex systems.

3 Time-periodic systems

In this chapter, the analysis of dynamical systems proceeds towards time-periodic systems, where the sources of destabilization of solutions and the amplification of the system's response are discussed. Time-periodic systems are a specific type of time-varying systems of differential equations, where their coefficients are time-periodic. This time-periodicity allows for using the well-known *Floquet* theory to analyze the stability of these systems' solutions. The difference between these systems and their corresponding ones with constant coefficients requires a different measure of stability. Stability can no longer be determined by the real parts of the system's eigenvalues. However, in the Floquet formulation of the problem we arrive at a quite similar stability condition using the system's *characteristic exponents* due to Lyapunov [97].

The motivation for studying these systems dates back to the nineteenth century in the works of Faraday, Lord Rayleigh and Mathieu in explaining natural phenomena [5]. However, nowadays many practical applications make use of parametric excitation in obtaining better performance. This proves to be of significant importance in microsystems [58], which constitute the main application discussed in this thesis.

Using the same approach as the previous chapter, we start by discussing linear time-periodic systems, in general, and the asynchronous parametric excitation in particular using the method of normal forms. The discussion extends to the case of forced parametrically excited systems, where both forced and parametric excitations exist. This type of systems was discussed in the literature for decades [8], however, not for the asynchronous excitation case. Moreover, the correspondence between the destabilization of the trivial fixed point and the amplification of the response is discussed.

Finally, we arrive at time-periodic nonlinear systems, where the multiple scales method is used to analyze the possible nontrivial solutions and the corresponding bifurcations at resonant frequencies. In this way, this chapter gives an overall picture on the dynamics of M-DoF time-periodic linear and nonlinear systems under asynchronous excitation, which also serves as a theoretical background for the following chapters.

3.1 Linear time-periodic systems

Here we confine ourselves to the linear M-DoF system

$$\boldsymbol{M}\ddot{\boldsymbol{q}} + (\boldsymbol{D} + \boldsymbol{G})\,\dot{\boldsymbol{q}} + (\boldsymbol{K} + \boldsymbol{C}(t))\,\boldsymbol{q} = \boldsymbol{f}(t). \tag{3.1}$$

where

$$\boldsymbol{M} = \begin{bmatrix} 1 & 0 \\ 0 & 1 \end{bmatrix}, \qquad \boldsymbol{D} = \begin{bmatrix} \delta_{11} & \delta_{12} \\ \delta_{21} & \delta_{22} \end{bmatrix}, \qquad \boldsymbol{G} = \gamma \begin{bmatrix} 0 & 1 \\ -1 & 0 \end{bmatrix}, \qquad \boldsymbol{f}(t) = \begin{bmatrix} f_1(t) \\ f_2(t) \end{bmatrix}.$$

$$\boldsymbol{K} = \begin{bmatrix} \omega_1^2 & 0 \\ 0 & \omega_2^2 \end{bmatrix}, \qquad \boldsymbol{C}(t) = \begin{bmatrix} \xi_{11}\cos(\Omega_p t + \zeta_{11}) & \xi_{12}\cos(\Omega_p t + \zeta_{12}) \\ \xi_{21}\cos(\Omega_p t + \zeta_{21}) & \xi_{22}\cos(\Omega_p t + \zeta_{22}) \end{bmatrix},$$

This linear equation considers a certain type of systems with periodically time-varying coefficients known as *parametrically excited systems*, where $\boldsymbol{C}(t)$ is the parametric excitation matrix, with amplitudes ξ_{ij}, frequency Ω_p and phases ζ_{ij}. Here the time-periodicity appears only in displacement proportional terms, or in the stiffness matrix in a wide sense. Time-periodic inertia or time-periodic velocity proportional coefficients are not included, and constant circulatory forces are not considered.

In this case, the stability analysis of the trivial fixed point can not be carried out by evaluating the real parts of the eigenvalues, since the system is non-autonomous. Instead, a solution can be sought for by linearizing around a periodic solution [98]. Moreover, the fact that the time-dependent coefficients have a period time T simplifies the problem as will be discussed afterwards.

Studying the stability of a periodic solution can be carried out with the help of the Poincaré map. This could be visualized by considering the time variable in (3.13) to be an additional degree of freedom. In this case, a hyperplane could be placed at T-periods along this new coordinate, and the vector flow could be traced by its intersection with this plane. If the time coordinate is turned to be polar, such that the angular coordinate will be $\theta = 2\pi t/T \ (mod\, 2\pi)$, we have only one hyperplane and vector flow will intersect it at every period T, this hyperplane is the Poincaré map. Thus we obtain a discretization for the system, and the stability turns from being studied around a periodic solution to be studied around a fixed point on the Poincaré map [99]. This is very similar to the approach of the Floquet theory, where the stability of the trivial solution is then determined around this fixed point [100].

3.1.1 Floquet theory

According to the previous discussion, Floquet theory is introduced here to determine the stability of time-periodic linear systems. First, the M-DoF system (3.1) with $f = 0$ is converted into a first order four dimensional system leading to

$$\dot{\boldsymbol{z}} = \boldsymbol{A}(t)\boldsymbol{z}. \tag{3.2}$$

According to Floquet ansatz, the fundamental matrix $\boldsymbol{Z}(t)$ can be written as

$$\boldsymbol{Z}(t) = \boldsymbol{P}(t)e^{\boldsymbol{B}t}, \tag{3.3}$$

where each of $\boldsymbol{Z}$, $\boldsymbol{P}$, $\boldsymbol{B}$ is an $n \times n$ matrix, $\boldsymbol{P}(t) = \boldsymbol{P}(t+T)$, and $\boldsymbol{B}$ is constant. By translating $\boldsymbol{Z}(t)$ in time with the periodic time T, (3.3) gives

$$\begin{aligned} \boldsymbol{Z}(t+T) &= \boldsymbol{P}(t+T)e^{\boldsymbol{B}(t+T)} \\ &= \boldsymbol{P}(t)e^{\boldsymbol{B}t}e^{\boldsymbol{B}T} \\ &= \boldsymbol{Z}(t)\boldsymbol{C}, \end{aligned} \tag{3.4}$$

which means that a translation by a time-period is only a linear transformation by the constant matrix C, called the *monodromy matrix*. This matrix describes the time evolution of the system solutions represented by the fundamental matrix $\boldsymbol{Z}(t)$, and thus carries the information about the stability of the system's solutions.

According to Floquet, the stability of the trivial solution can be obtained numerically by choosing the initial conditions

$$\boldsymbol{Z}(0) = I_{4\times4}, \tag{3.5}$$

where $I_{4\times4}$ is the identity matrix of the size four.

The system's fundamental matrix $\boldsymbol{Z}(t)$ is then calculated, which for the given initial conditions constitute the monodromy matrix when $t = T = \frac{2\pi}{\Omega_p}$, since according to (3.4)

$$\boldsymbol{C} = \boldsymbol{Z}(\frac{2\pi}{\Omega_p}), \qquad \text{since} \quad \boldsymbol{Z}(T) = \boldsymbol{Z}(0)\boldsymbol{C} \tag{3.6}$$

By evaluating the eigenvalues of this matrix, we obtain the *Floquet characteristic multipliers* μ, which represent the eigenvalues of the Poincaré map generated by the section orthogonal to the periodic solution [100]. Then

$$\nu_i = \frac{1}{T}\ln(\mu_i). \tag{3.7}$$

are the system's *Floquet characteristic exponents*, and their real parts are found to be *Lyapunov characteristic exponents* [101].

The same criterion of stability of a fixed point explained in section 2.1 can be extended here for the periodic solution of a non-autonomous system. If all Lyapunov exponents are negative, which means that all Floquet multipliers are inside the unit circle of the complex plane, the solution is said to be asymptotically stable. While if any Lyapunov exponent is positive, which means that any Floquet multiplier lies outside the unit circle, the system is said to be unstable. Moreover for nonlinear systems, if none of the Floquet multipliers associated with a non-hyperbolic solution lies outside the unit circle, in other words if none of the Lyapunov exponents is positive, then a nonlinear analysis is necessary to determine the stability [99].

The Floquet theorem implies also that (3.2) can be transformed by

$$\boldsymbol{z}(t) = \boldsymbol{P}(t)\boldsymbol{y}(t) \tag{3.8}$$

which gives

$$\dot{\boldsymbol{y}} = \boldsymbol{P}^{-1}(\boldsymbol{A}\boldsymbol{P} - \dot{\boldsymbol{P}})\boldsymbol{y}, \tag{3.9}$$

but since

$$\boldsymbol{P}(t) = \boldsymbol{Z}(t)e^{-\boldsymbol{B}t} \tag{3.10}$$

then

$$\begin{aligned} \dot{\boldsymbol{P}} &= \dot{\boldsymbol{Z}}e^{-\boldsymbol{B}t} - \boldsymbol{B}\boldsymbol{Z}e^{-\boldsymbol{B}t} \\ &= \boldsymbol{A}\boldsymbol{P} - \boldsymbol{P}\boldsymbol{B} \end{aligned} \tag{3.11}$$

finally

$$\dot{\boldsymbol{y}} = \boldsymbol{B}\boldsymbol{y} \tag{3.12}$$

which is a linear system with constant coefficients. From this result we understand that the transformation by a T-periodic operator in (3.8) changes the problem into a linear system with constant coefficients in (3.12). This is called *Lyapunov reducibility theorem* as a result of *Floquet-Lyapunov transformation* [14].

3.1.2 Parametrically excited systems

Following the same bottom-up approach as previously discussed, the first insights about parametrically excited systems could be obtained by reducing this system into a S-DoF one,

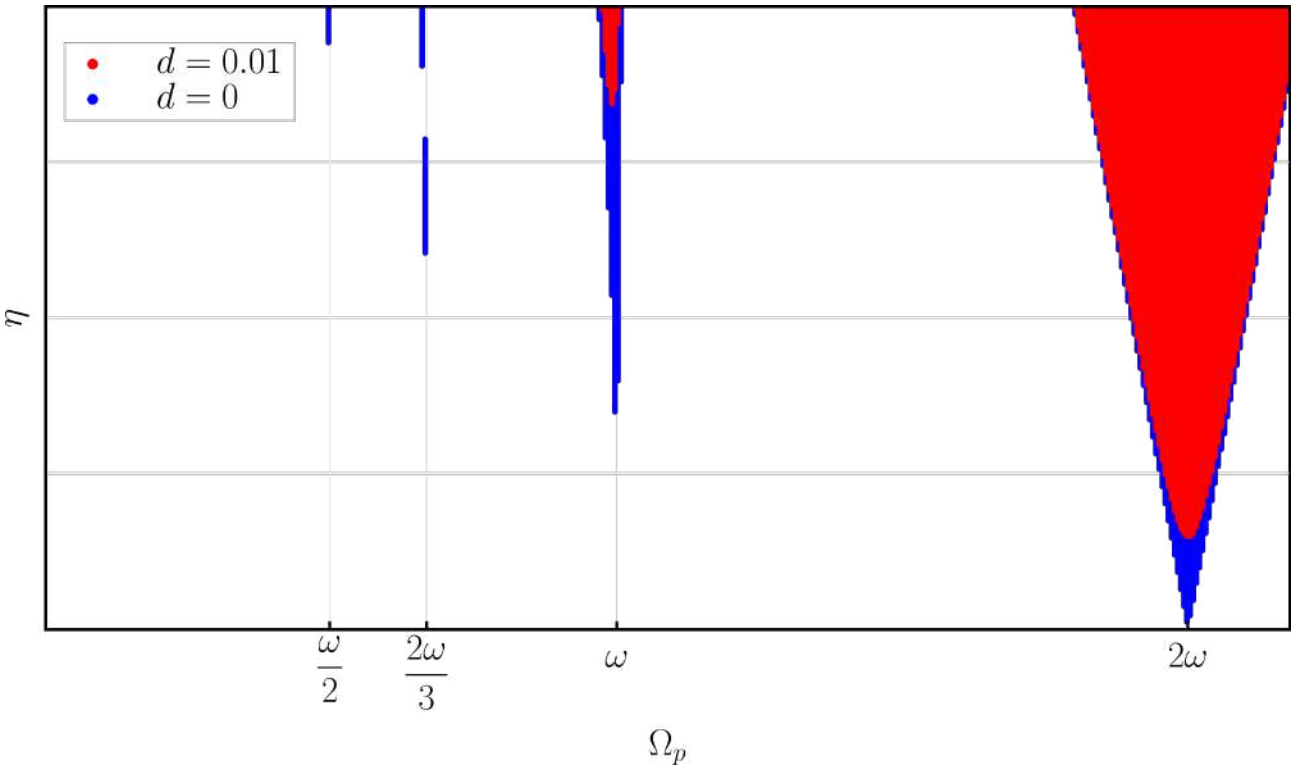

Figure 3.1: Stability chart of Mathieu equation (3.13) for two damping coefficients $d = 0, d = 0.01$

which is the *Mathieu-Hill* equation [8]

$$m\ddot{q} + d\dot{q} + (k + \xi cos(\Omega_p t))q = 0. \tag{3.13}$$

Although the equation seems to be simple, an exact closed-form solution could not be attained [102]. Therefore in order to study the dynamics in this system either approximate analytical methods are used or a numerical integration is carried out.

In the linear case we are interested in studying the stability of the trivial fixed point for different system parameters. Here we vary only the parametric excitation parameters: amplitude ξ and frequency Ω_p. By examining the stability of the trivial fixed point using Floquet theory as explained before, we could depict the result at each point in the parameter space Ω_p-ξ which is known as *the stability chart*.

In Fig. 3.1 the stability chart of Mathieu equation (3.13) is depicted for two cases, when there is no damping, i.e. $d = 0$, and when a small damping $d = 0.01$ is included. Only the instability points are shown in the stability diagram, where the red points correspond to the damped case and the blue ones to the undamped. Few observations could be made. First, we observe

the destabilization of the trivial fixed point at frequencies $\Omega_p = 2\omega/n$, where $\omega = \sqrt{k/m}$ and $n \in \mathbb{N}$, in separated regions called *instability tongues* or *Arnold's tongues*. This result is obtained numerically, analytically using Hill's infinite determinants [8] or using perturbation and averaging methods [103]. Secondly, the existence of damping causes the instability tongues to shrink upwards. And finally, the primary resonance region is much larger than the others, and its corresponding singularity in the solution has the largest influence on the solution.

We conclude that adding a time-periodic term in simple mass-spring-damper system adds another sort of instability to the system. In accordance with the approach used in this thesis to address the problem of stability in different systems, we then proceed by adding other dimensions and finally by adding nonlinearities.

3.1.3 Bimodal parametric excitation

The instability due to parametric resonance is then extended to M-DoF systems. In these systems, however, this kind of instability not only occurs at $\Omega_p = 2\omega_i/n$, which are called here primary parametric resonances, but also at *combination or secondary resonances*, i.e. at $\Omega_p = |\omega_i \pm \omega_j|/n$, where $i = 1, 2, n \in \mathbb{N}$. Moreover, we discuss also the possibility of destabilizing the trivial solution at *non-resonant* frequencies as well. To discuss these phenomena we are concerned with the two-degree of freedom system

$$\boldsymbol{M}\ddot{\boldsymbol{q}} + (\boldsymbol{D} + \boldsymbol{G})\,\dot{\boldsymbol{q}} + (\boldsymbol{K} + \boldsymbol{C}(t))\,\boldsymbol{q} = 0, \tag{3.14}$$

which is the same as (3.1) but without forced excitation, i.e. $\boldsymbol{f} = 0$.

In order to illustrate the effect of increased dimensionality, as we did in time-invariant systems, as well as the effect of the coupling terms in $\boldsymbol{C}(t)$

$$\boldsymbol{C}(t) = \begin{bmatrix} \xi_{11}\cos(\Omega_p t + \zeta_{11}) & \xi_{12}\cos(\Omega_p t + \zeta_{12}) \\ \xi_{21}\cos(\Omega_p t + \zeta_{21}) & \xi_{22}\cos(\Omega_p t + \zeta_{22}) \end{bmatrix}. \tag{3.15}$$

We consider three types of special cases. In the first case (*system I*), the off-diagonal terms are canceled, i.e. $\xi_{12} = 0, \xi_{21} = 0$, whilst in *system II*, the matrix is fully populated but all terms are in-phase, i.e. $\xi_{12} \neq 0, \xi_{21} \neq 0, \zeta_{ij} = 0$, and finally in *system III* the matrix is the same as in system II but includes a phase shift between the off-diagonal terms, i.e. $\xi_{12} \neq 0, \xi_{21} \neq 0, \zeta_{21} = -\pi/2, \zeta_{11} = \zeta_{12} = \zeta_{22} = 0$. This last case is called *asynchronous parametric excitation* through this work.

According to section 3.1.1, the system's trivial solution is unstable if at least one Lyapunov

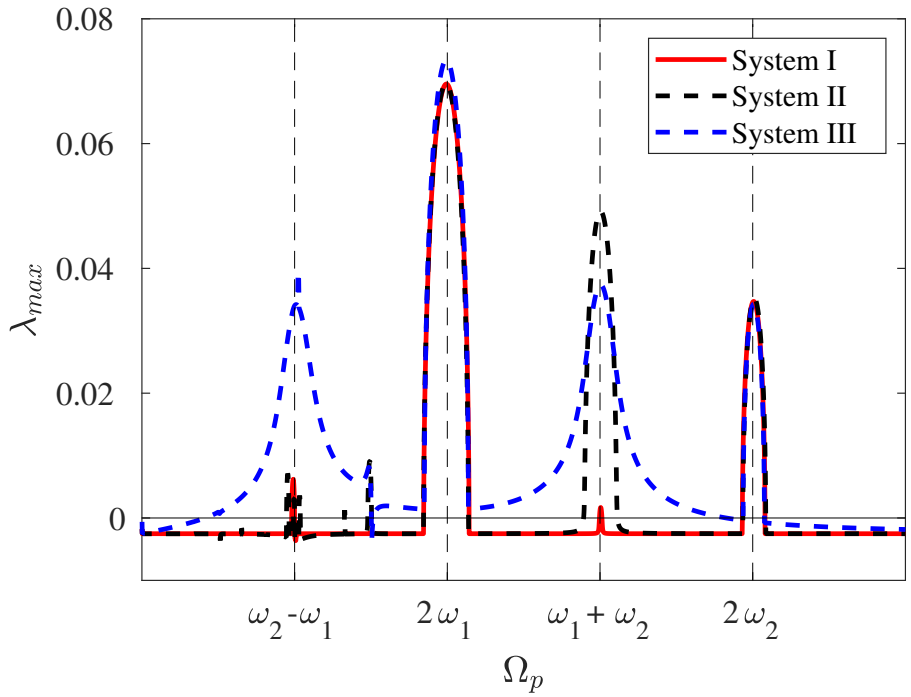

Figure 3.2: The effect of coupling terms of $\boldsymbol{C}(t)$. System I: $\xi_{12} = \xi_{21} = 0$, system II: $\xi_{12} = \xi_{21} = \xi, \zeta_{11} = \zeta_{12} = \zeta_{21} = \zeta_{22} = 0$, system III: $\xi_{12} = \xi_{21} = \xi, \zeta_{11} = \zeta_{21} = \zeta_{22} = 0, \zeta_{12} = -\pi/2$. For all systems: $\xi_{11} = \xi_{22} = \xi, \xi = 0.3, \gamma = 0.1, \delta_{11} = 0.01, \delta_{22} = 0.005, \delta_{12} = \delta_{21} = 0, \omega_1 = 1, \omega_2 = 2$.

exponent λ_i is positive. Thus, we search for the maximum exponent

$$\lambda_{max} = max(\frac{1}{T} \ln |\mu|), \tag{3.16}$$

where μ is the Floquet characteristic multiplier of the monodromy matrix, see (3.7). Then the maximum Lyapunov exponent is calculated for given system parameters and at each parametric excitation frequency Ω_p in a defined interval.

Fig. 3.2 shows how the coupling terms can affect the system's stability. That is, without any coupling terms, i.e. for system I, instability occurs mainly at the parametric resonance frequencies, i.e. $\Omega_p = \frac{\omega_i \pm \omega_j}{n}$, $n \in \mathbb{N}$. For system II, we obtain a similar behavior but with an increased tendency of instability at the combination resonance frequencies, i.e. $\Omega_p = \omega_1 \pm \omega_2$.

However, in system III, the phase shift $\zeta_{21} = -\pi/2$ causes a significantly different behavior. In this case the system exhibits instability at *non-resonant* frequencies, which leads to a *broadband* destabilizing effect, for instance in the interval $[\omega_2 - \omega_1, \omega_2 + \omega_1]$. This follows the analysis by Karev [37, 38], where the condition for *global* effects, e.g. the explained *broadband* destabilization, was given as $\zeta_{12} - \zeta_{21} \neq \pi m, m \in \mathbb{Z}$. This is indeed our case, since $\zeta_{12} - \zeta_{21} = \pi/2$.

In order to elaborate on this idea, Fig. 3.3 shows the instability regions in the parameter space Ω_p-ξ. As shown in the figure, the trivial solution in a broad frequency band and when $\xi > 0.27$ is unstable due to the proposed parametric excitation method, and specifically due to the presence of the phase shift between the coupling off-diagonal terms. This differs from the case of synchronous $\boldsymbol{C}(t)$, i.e. systems I and II, in which we can not achieve broadband instability at small excitation amplitude ξ.

The variation in the system's eigenvalues, and specifically the increase of the maximum eigenvalue in a broad frequency band could be understood as a *negative-damping* effect, which potentially implies an amplification of the system's forced response under the given parametric excitation frequency. Hence, we conclude from this section, that through this proposed method of excitation, a parametric amplification can be acquired not only at *resonant frequencies* as reported before in the literature [67], but also at *non-resonant frequencies*. This will be further discussed in section 3.1.6.

Having this effect on a broad band of frequencies can be promising in different ways for the micro sensors technology. Firstly, the tuning of the parametric excitation frequency is less sensitive. Secondly, this can allow for a potential noise squeezing effect [60] also in the broad frequency band. Moreover, since the change in the system's eigenvalues with respect to the excitation frequency is not abrupt but gradual and continuous, we can think of a frequency Ω_p tuning of the amplification gain instead of tuning it through the parametric excitation amplitude ξ_{ij}.

3.1.4 The method of normal forms

In order to discuss the stability of the micro-ring gyroscope, an analytical method, namely the *normal form method*, is used. This method is explained in different sources on nonlinear mechanics, a brief exposition can be found in [104, 84] and a more detailed one can be found in [105, 106, 107], where the last reference is followed in our calculations.

As in the numerical Floquet calculations we start from the first-order four dimensional system (3.2). However, since the system is not autonomous, we rewrite the time-periodic coefficients as additional variables, changing the system from non-autonomous linear system into an autonomous nonlinear one. In addition, some dummy variables are also introduced for the sake of having more representative and insightful analytical expressions at the end.

Applying these to (3.14) after excluding the external forcing gives

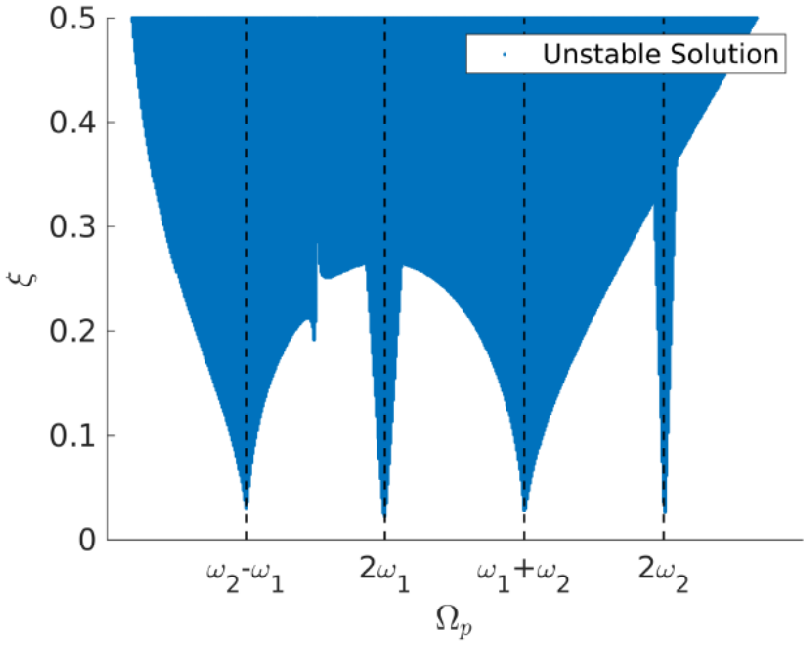

Figure 3.3: Stability chart of system (3.14) in the parameter space Ω_p-ξ where $\xi_{12} = \xi_{21} = \xi, \zeta_{11} = \zeta_{21} = \zeta_{22} = 0, \xi_{11} = \xi_{22} = \xi, \gamma = 0.1, \delta_{11} = 0.01, \delta_{22} = 0.005, \delta_{12} = \delta_{21} = 0, \omega_1 = 1, \omega_2 = 2$, and $\zeta_{21} = -\pi/2$

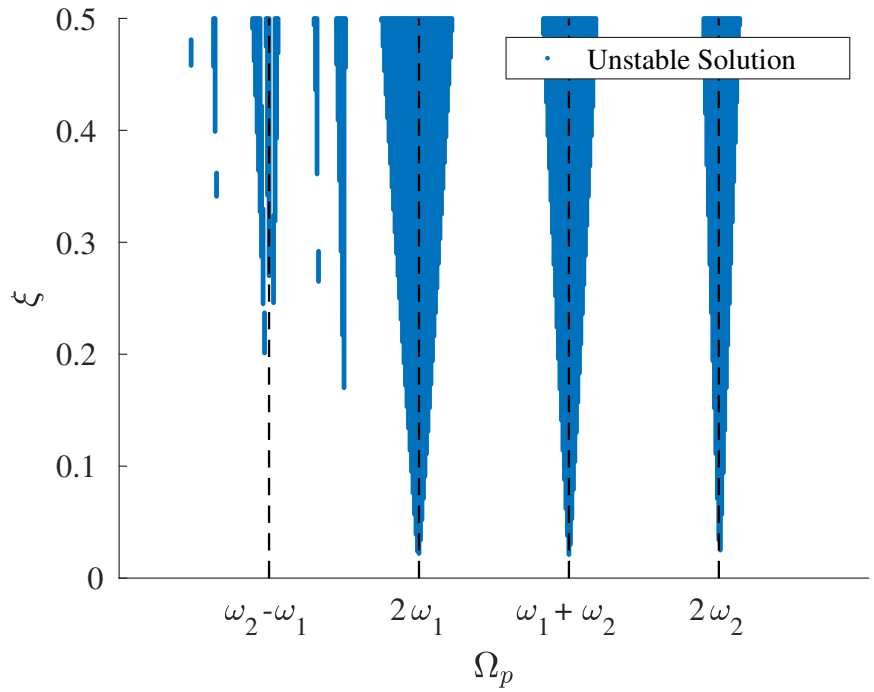

Figure 3.4: Stability chart of system (3.14) in the parameter space Ω_p-ξ, same parameter values as Fig. 3.3, except for $\zeta_{21} = 0$

$$\dot{z}_1 = z_2, \tag{3.17a}$$

$$\dot{z}_2 = \left[-\omega_1^2 - \frac{1}{2}\xi_{11}\left(e^{i\zeta_{11}}z_5 + e^{-i\zeta_{11}}z_6\right)\right] z_1 - \frac{1}{2}\xi_{12}\left(e^{i\zeta_{12}}z_5 + e^{-i\zeta_{12}}z_6\right) z_3 - \left(\delta_{11}z_2 + (\delta_{12}+\gamma)z_4\right) z_7, \tag{3.17b}$$

$$\dot{z}_3 = z_4, \tag{3.17c}$$

$$\dot{z}_4 = -\frac{1}{2}\xi_{21}\left(e^{i\zeta_{21}}z_5 + e^{-i\zeta_{21}}z_6\right) z_1 - \left[\omega_2^2 + \frac{1}{2}\xi_{22}\left(e^{i\zeta_{22}}z_5 + e^{-i\zeta_{22}}z_6\right)\right] z_3 - \left((\delta_{21}-\gamma)z_2 + \delta_{22}z_4\right) z_7, \tag{3.17d}$$

$$\dot{z}_5 = i\Omega_p z_5, \tag{3.17e}$$

$$\dot{z}_6 = -i\Omega_p z_6, \tag{3.17f}$$

$$\dot{z}_7 = 0, \tag{3.17g}$$

where

$$z_1 = q_1, \quad z_2 = \dot{q}_1, \quad z_3 = q_2, \quad z_4 = \dot{q}_2, \quad z_5 = e^{i\Omega_p t}, \quad z_6 = -e^{i\Omega_p t}, \quad z_7 = 1.$$

A linear transformation

$$\boldsymbol{x} = \boldsymbol{R}\boldsymbol{z} \tag{3.18}$$

is applied, such that in the new coordinates the equations are transformed into

$$\dot{\boldsymbol{x}} = \widetilde{\boldsymbol{f}}(\boldsymbol{x}) = \boldsymbol{\Lambda}\boldsymbol{x} + \widetilde{\boldsymbol{F}}_2(\boldsymbol{x}) + \widetilde{\boldsymbol{F}}_3(\boldsymbol{x}) + \ldots \tag{3.19}$$

where Λ is the Jordan form and $\widetilde{\boldsymbol{F}}_i$ are the nonlinear terms of monomials of order i in x.

The essence of the normal form method is to apply a nonlinear transformation resulting in the minimal amount of nonlinear terms in the transformed system, i.e. the *normal form*. This is done through the nonlinear near-identity transformation

$$\boldsymbol{x} = \widetilde{\boldsymbol{g}}(\boldsymbol{y}) = \boldsymbol{y} + \widetilde{\boldsymbol{G}}_2(\boldsymbol{y}) + \widetilde{\boldsymbol{G}}_3(\boldsymbol{y}) + \ldots \tag{3.20}$$

to obtain the normal form

$$\dot{\boldsymbol{y}} = \widetilde{\boldsymbol{h}}(\boldsymbol{x}) = \boldsymbol{\Lambda}\boldsymbol{y} + \widetilde{\boldsymbol{H}}_2(\boldsymbol{y}) + \widetilde{\boldsymbol{H}}_3(\boldsymbol{y}) + \ldots \tag{3.21}$$

then by inserting (3.21) and (3.20) in (3.19) we get the partial differential equation

$$\frac{\partial \widetilde{\boldsymbol{g}}(\boldsymbol{y})}{\partial \boldsymbol{y}} \widetilde{\boldsymbol{h}}(\boldsymbol{y}) = \widetilde{\boldsymbol{f}}(\widetilde{\boldsymbol{g}}(\boldsymbol{y})). \tag{3.22}$$

Then (3.22) is solved for $\widetilde{\boldsymbol{G}}_i$, so that we obtain $\widetilde{\boldsymbol{H}}_i$ with the minimum possible nonlinear terms. Next we define each monomial in the form $y_1^{m_1} y_2^{m_2} y_3^{m_3} ... y_7^{m_7}$. Using (3.22) we find a condition for each monomial in each differential equation, by which the monomial is transferred from $\widetilde{\boldsymbol{f}}(\boldsymbol{x})$ to $\widetilde{\boldsymbol{h}}(\boldsymbol{y})$ without being eliminated, otherwise, i.e. if the condition is not met, this monomial can be eliminated and thereby simplifying the resulting normal form $\widetilde{\boldsymbol{h}}(\boldsymbol{y})$. This condition is called a *resonance condition* which by solving (3.22) reads

$$\lambda_j = \sum_{i=1}^{7} m_i \lambda_i, \quad j \in \{1, 2, .., 7\}. \tag{3.23}$$

where j corresponds to the differential equation $\dot{z}_j = f(z)$ and the sum on the right hand side is calculated for each monomial in row j of the matrix $\widetilde{\boldsymbol{h}}$. Then for the given case, (3.23) reads

$$\lambda_j = (m_1 - m_2)\omega_1 + (m_3 - m_4)\omega_2 + (m_5 - m_6)\Omega_p, \qquad \lambda_j \in \{\omega_1, -\omega_1, \omega_2, -\omega_2, \Omega_p, -\Omega_p, 0\}. \tag{3.24}$$

Since the resonance condition depends on system eigenvalues, the transferred monomials from $\widetilde{\boldsymbol{f}}$ to $\widetilde{\boldsymbol{h}}$ depend on the *resonances* taken into consideration. That means, we have always the choice to consider all excitation frequencies or to exclude some or all resonance frequencies. However, including all the resonance frequencies leads to higher complexity of the normal form, and sometimes to the impossibility of transforming the normal form into polar coordinates, which are normally convenient in the final representation of the system.

After proceeding with the mentioned calculations, the dummy variables are substituted with their original forms

$$y_5 = e^{i\Omega_p t}, \quad y_6 = e^{-i\Omega_p t}, \quad y_7 = 1, \tag{3.25}$$

then finally we arrive at the normal form (3.21) after excluding the terms higher than the third order.

Since we expect periodic solutions, a transformation in the polar coordinates should usually simplify the end expressions and give more insight into the response amplitudes. This is done through the transformation

$$y_1 = \frac{1}{2}\omega_1 e^{i(\phi_1(t) + \frac{1}{2}\Omega_p t)}\, r_1(t), \tag{3.26a}$$

$$y_2 = \frac{1}{2}\omega_1 e^{-i(\phi_1(t)+\frac{1}{2}\Omega_p t)}\, r_1(t), \tag{3.26b}$$

$$y_3 = \frac{1}{2}\omega_2 e^{i(\phi_1(t)+\frac{1}{2}\Omega_p t)}\, r_2(t), \tag{3.26c}$$

$$y_4 = \frac{1}{2}\omega_2 e^{-i(\phi_1(t)+\frac{1}{2}\Omega_p t)}\, r_2(t). \tag{3.26d}$$

In the present case, the normal form method is applied at all given frequencies except for the combined and difference resonance frequencies $\Omega_p = \omega_1 \pm \omega_2$, which means that the primary resonances $\Omega_p = 2\omega_i,\ i = 1, 2$ are included in the analysis. Moreover, it is assumed that the system does not include coupling damping terms, i.e. $\delta_{21} = \delta_{12} = 0$ and that the only non-zero phase shift in the parametric excitation matrix would be ζ_{21}, i.e. $\zeta_{11} = \zeta_{22} = \zeta_{12} = 0$. This leads to

$$\begin{aligned}\dot{r}_1 = \Bigg[&-\frac{1}{2}\delta_{11} + \frac{\xi_{21}\xi_{12}\Omega_p \sin(\zeta_{21})}{2(\Omega_p^2 - (\omega_1-\omega_2)^2)(\Omega_p^2 - (\omega_1+\omega_2)^2)} + \frac{\xi_{12}\gamma\cos(2\phi_1)}{4(\omega_1^2-\omega_2^2)} \\ &+ \frac{\gamma\xi_{21}(\Omega_p-\omega_1)\cos(\zeta_{21}-2\phi_1)}{4\omega_1(\Omega_p-(\omega_1-\omega_2))(\Omega_p-(\omega_1+\omega_2))} + \frac{1}{16\Omega_p\omega_1^2}\xi_{11}\left(\delta_{11}(\Omega_p+2\omega_1)\cos(2\phi_1) - 4\Omega_p\omega_1\sin(2\phi_1)\right)\Bigg] r_1,\end{aligned} \tag{3.27a}$$

$$\begin{aligned}\dot{r}_2 = \Bigg[&-\frac{1}{2}\delta_{22} - \frac{\xi_{21}\xi_{12}\Omega_p \sin(\zeta_{21})}{2(\Omega_p^2 - (\omega_1-\omega_2)^2)(\Omega_p^2 - (\omega_1+\omega_2)^2)} + \frac{\xi_{21}\gamma\cos(\zeta_{21}-2\phi_2)}{4(\omega_1^2-\omega_2^2)} \\ &+ \frac{\gamma\xi_{12}(\Omega_p-\omega_2)\cos(2\phi_2)}{4\omega_2(\Omega_p-(\omega_2-\omega_1))(\Omega_p-(\omega_1+\omega_2))} + \frac{1}{16\Omega_p\omega_2^2}\xi_{22}\left(\delta_{22}(\Omega_p+2\omega_2)\cos(2\phi_2) - 4\Omega_p\omega_2\sin(2\phi_2)\right)\Bigg] r_2,\end{aligned} \tag{3.27b}$$

while $\dot{\phi}_1 = f(\phi_1), \dot{\phi}_2 = f(\phi_2)$.

The last expressions can be simplified to include only the first two terms in each equation of (3.27) if the primary resonances are not to be included.

In order to verify our results, equations (3.27) will be compared to the numerical results obtained before by the Floquet method before. The comparison is depicted in Fig. 3.5. Here we can see a very good agreement between both of them including at the primary resonances $\Omega_p = 2\omega_i,\ i = 1, 2$. As expected, the mismatch between both methods appears only at the combination and difference resonances.

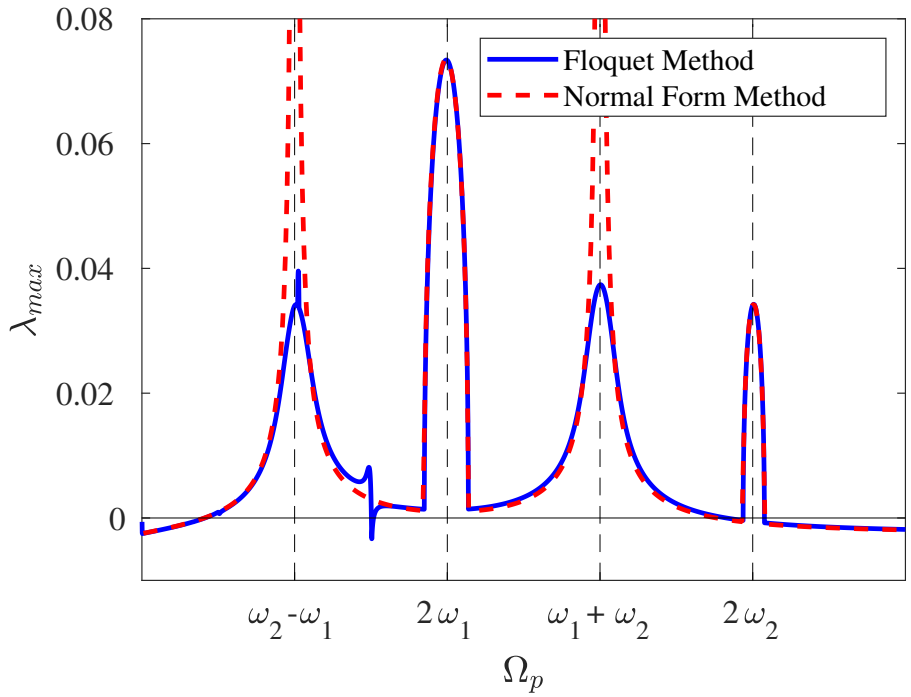

Figure 3.5: Comparison of the results of the normal form method to the numerical Floquet method for the values of λ_{max} w.r.t Ω_p where $\xi_{12} = \xi_{21} = \xi, \zeta_{21} = -\pi/2, \zeta_{11} = \zeta_{21} = \zeta_{22} = 0, \xi_{11} = \xi_{22} = \xi, \gamma = 0.1, \delta_{11} = 0.01, \delta_{22} = 0.005, \delta_{12} = \delta_{21} = 0, \omega_1 = 1$ and $\omega_2 = 2$.

3.1.5 Simplified analytical expression

Given that the normal form shows an appropriate representation of the system dynamics, we shall use a further simplified version of (3.27) for the sake of better understanding.

First by excluding all resonances from our normal form transformation, and moreover by assuming that all the parametric excitation terms have the same amplitude, i.e. $\xi_{11} = \xi_{12} = \xi_{21} = \xi_{22} = \xi$, we get

$$\dot{r}_1 = \left[-\frac{1}{2}\delta_{11} + \frac{\xi^2\Omega_p \sin(\zeta_{21})}{2(\Omega_p^2 - (\omega_1 - \omega_2)^2)(\Omega_p^2 - (\omega_1 + \omega_2)^2)}\right] r_1, \tag{3.28a}$$

$$\dot{r}_2 = \left[-\frac{1}{2}\delta_{22} - \frac{\xi^2\Omega_p \sin(\zeta_{21})}{2(\Omega_p^2 - (\omega_1 - \omega_2)^2)(\Omega_p^2 - (\omega_1 + \omega_2)^2)}\right] r_2. \tag{3.28b}$$

The coefficients of the transformed system variables r_1 and r_2 are in our case the determinants of stability, since they represent the real parts of the eigenvalues of the transformed system,

represented by

$$\lambda_1 = -\frac{1}{2}\delta_{11} + \left[\frac{\xi^2\Omega_p \sin(\zeta_{21})}{2\left[\Omega_p^2 - (\omega_1-\omega_2)^2\right]\left[\Omega_p^2 - (\omega_1+\omega_2)^2\right]}\right], \tag{3.29a}$$

$$\lambda_2 = -\frac{1}{2}\delta_{22} - \left[\frac{\xi^2\Omega_p \sin(\zeta_{21})}{2\left[\Omega_p^2 - (\omega_1-\omega_2)^2\right]\left[\Omega_p^2 - (\omega_1+\omega_2)^2\right]}\right]. \tag{3.29b}$$

A major goal in this discussion is to determine the effect of the parametric excitation parameters (ξ, Ω_p) on system stability. By investigating the dependency of the maximum real eigenvalue $\lambda_{max} = max(\lambda_1, \lambda_2)$ on the parametric excitation frequency, as shown in Fig. 3.5, we find that there is a region of frequencies between $\Delta\omega = \omega_2 - \omega_1$ and $\Sigma\omega = \omega_2 + \omega_1$ where the value of the maximum eigenvalue can be controlled for stabilization or destabilization, and becomes remarkable when the natural frequencies are large and their difference is small. In this region the value of maximum eigenvalue reaches a local maximum or a local minimum according to the value of ξ as can be seen in Fig. 3.6. This band of frequencies is of special importance to the case of microsystems, since in this case the sum of eigenfrequencies $\Sigma\omega$ is relatively large (in the order of $(\mathcal{O}(10^5)Hz)$) and the difference between them $\Delta\omega$ is relatively small $(\mathcal{O}(10^3)Hz)$. Therefore in order to find the local maximum/minimum, λ is differentiated with respect to Ω_p and the expression is equated to zero. A more special case occurs in micro gyroscopes, where the ring is usually designed to be symmetric, while the asymmetry appears due to limited fabrication precision. However even if the undamped natural frequencies are dissimilar, as seen in Fig. 3.6, we have $\Delta\omega << \Sigma\omega$ by at least one order of magnitude. This assumption leads to a simplification for the value of the local minimum/maximum of λ_{max}, this value we shall notate as λ^*.

Starting with the differentiation of λ with respect to Ω_p and equating to zero, we find

$$\Omega_p^2 = \frac{\Delta\omega^2 + \Sigma\omega^2}{6} \pm \frac{1}{6}\sqrt{(\Delta\omega^2 + \Sigma\omega^2)^2 + 12\Delta\omega^2\Sigma\omega^2}, \tag{3.30}$$

where $\Delta\omega = \omega_2 - \omega_1$ and $\Sigma\omega = \omega_2 + \omega_1$ as explained previously. Then following the assumption $\Delta\omega << \Sigma\omega$, we get

$$\Omega^* \simeq \frac{1}{\sqrt{3}}\Sigma\omega, \tag{3.31}$$

where Ω^* represents the parametric excitation frequency at the local minimum of the maximum eigenvalue . Applying this result to (3.29), we find the local extremum of λ_{max} to be

$$\lambda^* \simeq max(\frac{-\delta_{11}}{2} - \delta\lambda, \frac{-\delta_{22}}{2} + \delta\lambda), \qquad \delta\lambda = \frac{3\sqrt{3}}{4}\frac{\xi^2 \sin(\zeta_{21})}{\Sigma\omega^3}. \tag{3.32}$$

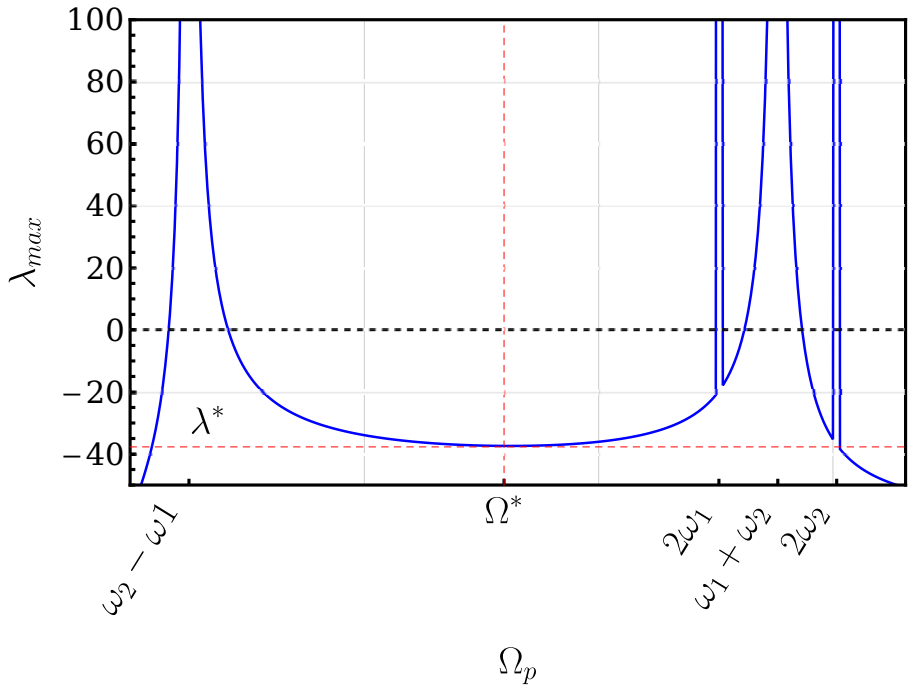

Figure 3.6: Maximum Lyapunov exponent λ_{max} against parametric excitation frequency Ω_p for a system with large and similar natural frequencies $\omega_1 = 2\pi \times 100krad/sec, \omega_2 = 2\pi \times 120krad/sec$, displaying the local minimum at λ^* and Ω^*.

This approximation can give us a better insight into how the system is near to instability given the system parameters. This was found to be sufficiently accurate, under the assumption $\Delta\omega << \Sigma\omega$.

From (3.32) we can infer that the destabilization of the system is highly affected by the ratio $\frac{\xi^2}{\Sigma\omega^3}$. This means that in order to attain a destabilization effect at non-resonant frequencies of such a system with high eigenfrequencies, we need comparably a high excitation amplitude. Then the fraction of $\delta\lambda$ can be designed in the damping order of magnitude $\mathcal{O}(\delta_{ij})$ for the sake of having a better tuning for the excitation amplitude with respect to the corresponding device's response.

In conclusion, by investigating the system (3.14) for stability, different conditions were found to cause destabilization of the trivial solution. The nontrivial solutions do not exist in this case due to the assumed linearity. Other aspects of this investigation are considered in [38]. However, a specific case was focused on, namely, when the coupling parametric excitation terms were phase-shifted with $\pi/2$, where a broadband destabilization was elaborated, especially for micro- and nanosystems with axis-symmetric geometry.

In terms of microsystems, as explained before, the key indicator to be discussed here is *sensitivity*, whose enhancement in our excitation method occurs due to *parametric amplification*.

Up to this point, we could prove how the trivial solution could be destabilized, but to translate this into amplification, the addition of a forced excitation is then necessary.

3.1.6 Parametric amplification

As previously explained in the introduction, we seek to increase the system's response amplitude through parametric excitation, this is one of the main goals of this thesis. This leads directly to an enhancement of the sensitivity of micro or nano-sensor systems. Two main types of enhancement are targeted, one is through *non-resonant parametric amplification* which is amplifying the forced response of the system in a pramateric non-resonant case while assuming system's linearity. Thus, the amplification occurs *outside* the instability regions of the stability chart (see Figs.3.3, 3.4), i.e. without parametric resonance, since driving a linear system into instability of its trivial solution means an unbounded response. The second method is through *parametric resonance* allowing for *resonant parametric amplification*, through which we look for a nontrivial solution with a higher amplitude, and thereby an amplified response [67].

So far we are interested in a linearly modeled system. The response of nonlinear systems will discussed in the next section.

Therefore, in order to investigate the *non-resonant parametric amplification* case, the system should have two types of excitation, that is, the forced excitation which gives the drive of the system, and the parametric excitation which destabilizes the system for the sake of amplification. This means we are willing to explain the connection between *destabilization* of the trivial solution of the autonomous system and the *amplification* of the system response after the addition of the external forced excitation.

To this end, we put the system (3.1) in a perturbed form, that is

$$\begin{aligned} u_1'' + \omega_1^2 u_1 + \epsilon[\mu_1 u_1' + \eta_{11} u_1 \cos(\Omega_p t) + \eta_{12} u_2 \cos(\Omega_p t)] &= \epsilon F_0 \sin(\Omega_f t) \\ u_2'' + \omega_2^2 u_2 + \epsilon[\mu_2 u_2' + \eta_{21} u_1 \cos(\Omega_p t + \zeta) + \eta_{22} u_2 \cos(\Omega_p t)] &= 0, \end{aligned} \tag{3.33}$$

where only the first degree of freedom is forced excited with $F_0 \sin(\Omega_f t)$ and the parametric excitation matrix is fully populated with a phase-shift at one of its off-diagonal terms, that is

$$\boldsymbol{C}(t) = \begin{bmatrix} \eta_{11} \cos(\Omega_p t) & \eta_{12} \cos(\Omega_p t) \\ \eta_{21} \cos(\Omega_p t + \zeta) & \eta_{22} \cos(\Omega_p t) \end{bmatrix}.$$

The multiple scales method is then used to analyze the system response under *weak* excitation up to the second order. The solution will be then perturbed according to

$$u_1(t;\epsilon) = u_{10}(T_0,T_1,T_2) + \epsilon u_{11}(T_0,T_1,T2) + \epsilon^2 u_{12}(T_0,T_1,T_2) + ..., \tag{3.34a}$$

$$u_2(t;\epsilon) = u_{20}(T_0,T_1,T_2) + \epsilon u_{21}(T_0,T_1,T_2) + \epsilon^2 u_{22}(T_0,T_1,T_2) + ..., \tag{3.34b}$$

where $T_i = \epsilon^i t$ and

$$\begin{aligned} \frac{\partial}{\partial t} &= D_0 + \epsilon D_1 + \epsilon^2 D_2..., \\ \frac{\partial^2}{\partial t^2} &= D_0^2 + 2\epsilon D_0 D_1 + \epsilon^2(D_1^2 + D_0 D_2), \end{aligned} \tag{3.35}$$

where $D_i^n = \partial^n / \partial^n T_i$.

Inserting (3.34) and (3.35) in (3.33) and separating according to the order of ϵ gives: for $\boldsymbol{\epsilon^0}$,

$$D_0^2 u_{10} + \omega_1^2 u_{10} = 0, \tag{3.36a}$$

$$D_0^2 u_{20} + \omega_2^2 u_{20} = 0, \tag{3.36b}$$

while for $\boldsymbol{\epsilon^1}$,

$$D_0^2 u_{11} + \omega_1^2 u_{11} = -\mu_1 D_0 u_{10} - \eta_{11} u_{10}\cos(\Omega_p t) - \eta_{12} u_{20}\cos(\Omega_p t) - 2D_0 D_1 u_{10} + F_0 \sin(\Omega_f T_0), \tag{3.37a}$$

$$D_0^2 u_{21} + \omega_2^2 u_{21} = -\mu_2 D_0 u_{20} - \eta_{21} u_{10}\cos(\Omega_p t + \zeta) - \eta_{22} u_{20}\cos(\Omega_p t) - 2D_0 D_1 u_{20}, \tag{3.37b}$$

and finally for $\boldsymbol{\epsilon^2}$,

$$\begin{aligned} D_0^2 u_{12} + \omega_1^2 u_{12} &= -\mu_1(D_0 u_{11} + D_1 u_{10}) - \eta_{11} u_{11}\cos(\Omega_p t) - \eta_{12} u_{21}\cos(\Omega_p t) \\ &\quad - D_1^2 u_{10} - 2D_0 D_2 u_{10} - 2D_0 D_1 u_{11}, \end{aligned} \tag{3.38a}$$

$$\begin{aligned} D_0^2 u_{22} + \omega_2^2 u_{22} &= -\mu_2(D_0 u_{211} + D_1 u_{20}) - \eta_{21} u_{11}\cos(\Omega_p t + \zeta) - \eta_{22} u_{21}\cos(\Omega_p t) \\ &\quad - D_1^2 u_{20} - 2D_0 D_2 u_{20} - 2D_0 D_1 u_{21}. \end{aligned} \tag{3.38b}$$

The zeroth order differential equations (3.36) gives the solution

$$u_{10}(T_0,T_1,T_2) = A_1(T_1,T_2)e^{i\omega_1 T_0} + \bar{A}_1(T_1,T_2)e^{-i\omega_1 T_0}, \tag{3.39a}$$

$$u_{20}(T_0,T_1,T_2) = A_2(T_1,T_2)e^{i\omega_2 T_0} + \bar{A}_2(T_1,T_2)e^{-i\omega_2 T_0}, \tag{3.39b}$$

then inserting this solution in (3.37) gives

$$
\begin{aligned}
D_0^2 u_{11} + \omega_1^2 u_{11} = &-A_1 \left(\frac{1}{2}\eta_{11} e^{i(\omega_1 - \Omega_p)T_0} + \frac{1}{2}\eta_{11} e^{i(\omega_1 + \Omega_p)T_0} + i\mu_1\omega_1 e^{i\omega_1 T_0} \right) \\
&- A_2 \left(\frac{1}{2}\eta_{12} e^{i(\omega_1 - \Omega_p)T_0} + \frac{1}{2}\eta_{12} e^{i(\omega_1 + \Omega_p)T_0} \right) - 2i\omega_1 e^{i\omega_1 T_0} D_1 A_1 \qquad (3.40a) \\
&+ \frac{i}{2} F_0 (e^{-i\Omega_f T_0} - e^{i\Omega_f T_0}) + CC, \\
D_0^2 u_{21} + \omega_2^2 u_{21} = &-A_2 \left(\frac{1}{2}\eta_{22} e^{i(\omega_1 - \Omega_p)T_0} + \frac{1}{2}\eta_{22} e^{i(\omega_1 + \Omega_p)T_0} + i\mu_2\omega_2 e^{i\omega_2 T_0} \right) \\
&- A_1 \left(\frac{1}{2}\eta_{21} e^{i(\omega_1 - \Omega_p)T_0 - i\zeta} + \frac{1}{2}\eta_{21} e^{i(\omega_1 + \Omega_p)T_0 + i\zeta} \right) - 2i\omega_2 e^{i\omega_2 T_0} D_1 A_2 + CC. \qquad (3.40b)
\end{aligned}
$$

Since the amplification problem is defined at the maximum possible amplitude, the forced excitation will be tuned here around its frequency $\Omega_f \simeq \omega_1$. To consider that in our calculation a detuning parameter σ_f is introduced such that

$$\Omega_f = \omega_1 + \epsilon\sigma_f. \qquad (3.41)$$

As explained before in section 2.2.1 we eliminate the secular terms and then obtain the solvability conditions

$$2i\omega_1 D_1 A_1 + i\mu_1\omega_1 A_1 + \frac{i}{2} F_0 e^{i\sigma_f T_1} = 0, \qquad (3.42a)$$

$$2i\omega_2 D_1 A_2 + i\mu_2\omega_2 A_2 = 0, \qquad (3.42b)$$

giving the amplitude solutions

$$A_1(T_1, T_2) = \frac{-e^{i\sigma_f T_1} F_0}{2(\mu_1\omega_1 + 2i\sigma_f\omega_1)} + e^{-\mu_1 T_1/2} B_1(T_2), \qquad (3.43a)$$

$$A_2(T_1, T_2) = e^{-\mu_2 T_1/2} B_2(T_2), \qquad (3.43b)$$

where the amplitudes correspond to the ordinary homogeneous and particular solutions of a forced damped linear system. After eliminating the secular terms, the differential equations of

the first order read

$$D_0^2 u_{11} + \omega_1^2 u_{11} = -A_1 \left(\frac{1}{2}\eta_{11} e^{i(\omega_1 - \Omega_p)T_0} + \frac{1}{2}\eta_{11} e^{i(\omega_1 + \Omega_p)T_0} \right) - A_2 \left(\frac{1}{2}\eta_{12} e^{i(\omega_1 - \Omega_p)T_0} + \frac{1}{2}\eta_{12} e^{i(\omega_1 + \Omega_p)T_0} \right) + CC, \tag{3.44a}$$

$$D_0^2 u_{21} + \omega_2^2 u_{21} = -A_2 \left(\frac{1}{2}\eta_{22} e^{i(\omega_1 - \Omega_p)T_0} + \frac{1}{2}\eta_{22} e^{i(\omega_1 + \Omega_p)T_0} \right) - A_1 \left(\frac{1}{2}\eta_{21} e^{i(\omega_1 - \Omega_p)T_0 - i\zeta} + \frac{1}{2}\eta_{21} e^{i(\omega_1 + \Omega_p)T_0 + i\zeta} \right) + CC. \tag{3.44b}$$

Solving (3.44) yields both homogeneous and particular solutions

$$u_{11} = u_{11h} + u_{11p}, \quad u_{21} = u_{21h} + u_{21p}, \tag{3.45}$$

the latter gives, however, information about the amplification. Thus, we display here only the particular solution at resonance $\sigma_f = 0$ for convenience, that is

$$u_{11p}|_{\sigma_f=0} = \frac{F_0 \eta_{11}}{\mu_1 \omega_1 \Omega_p ((2\omega_1)^2 - \Omega_p^2)} \left(\Omega_p \cos(\omega_1 t) \cos \Omega_p t + 2\omega_1 \sin(\omega_1 t) \sin \Omega_p t \right), \tag{3.46a}$$

$$u_{21p}|_{\sigma_f=0} = \frac{-F_0 \eta_{21}}{2\mu_1 \omega_1} \left(\frac{\cos((\Omega_p - \omega_1)t + \zeta)}{(\Omega_p - (\omega_1 - \omega_2))(\Omega_p - (\omega_1 + \omega_2))} + \frac{\cos((\Omega_p + \omega_1)t + \zeta)}{(\Omega_p + (\omega_1 - \omega_2))(\Omega_p + (\omega_1 + \omega_2))} \right). \tag{3.46b}$$

Here we see obviously the effect of parametric excitation, as an amplifier, on the first-order correction u_{11}, u_{21}. For more elaboration, we extract the amplitude of the correction terms to the first order in each degree of freedom as

$$|U_{11p}| = \frac{F_0 \eta_{11}}{\mu_1 \omega_1 \Omega_p ((2\omega_1)^2 - \Omega_p^2)}, \quad |U_{21p}| = \frac{-F_0 \eta_{21}}{\mu_1 \omega_1 (\Omega_p^2 - (\omega_1 - \omega_2)^2)(\Omega_p^2 - (\omega_1 + \omega_2)^2)}, \tag{3.47}$$

which is plotted against the parametric excitation frequency Ω_p in Fig. 3.7.

Through these expressions and the corresponding figures we can understand the effect of *non-resonant parametric amplification*. The shown steady-state amplitudes are totally governed by the parametric excitation, specifically, if $\eta_{ij} = 0$ the whole response vanishes. This should not cause a confusion with our understanding about the steady-state response of a forced excited system, in which the solution has a steady state amplitude in absence of any parametric excitation, since we are discussing only the correction terms u_{11}, u_{21}. However, as shown before in (3.43), the typical steady-state amplitude for a forced linear system does exist. Secondly,

we could obviously see, that the amplitudes U_{11p}, U_{21p} are amplified even at *non-resonant* frequencies, i.e. not only at parametric resonance frequencies. Although this solution is a first-order correction to the basic solution, it can have an effect on the homogeneous part of the basic solution afterwards, as will be explained.

We proceed with the analysis by inserting (3.39),(3.43) and (3.45) in (3.38) and extracting the secular terms to give the solvability conditions

$$2ie^{-\mu_1 T_1/2}\omega_1 D_2 B_1 + \frac{e^{-\mu_1 T_1/2}}{4(4\omega_1^2-\Omega_p^2)}\left(\mu_1^2(\Omega_p^2-4\omega_1^2)+\eta^2(-2+\frac{e^{i\zeta}(4\omega_1^2-\Omega_p^2)}{(\Omega_p+\omega_1-\omega_2)(\Omega_p+\omega_1+\omega_2)}\right.$$
$$\left.+\frac{e^{-i\zeta}(4\omega_1^2-\Omega_p^2)}{(-\Omega_p+\omega_1-\omega_2)(-\Omega_p+\omega_1+\omega_2)})\right)B_1 - \frac{F_0 e^{i(\sigma_f T_1-\zeta)}}{8(\mu_1+2i\sigma_f)\omega_1}\left(\frac{e^{2i\zeta}\eta^2}{(\Omega_p+\omega_1-\omega_2)(\Omega_p+\omega_1+\omega_2)}\right.$$
$$\left.+\frac{\eta^2}{(-\Omega_p+\omega_1-\omega_2)(-\Omega_p+\omega_1+\omega_2)}+e^{i\zeta}(4i\mu_1\sigma_f-4\sigma_f^2-\frac{2\eta^2}{4\omega_1^2-\Omega_p^2})\right)=0 \tag{3.48a}$$

$$2i\omega_2 D_2 B_2 + \left(\frac{-2\eta^2+\mu_2^2(\Omega_p^2-4\omega_2^2)}{4\omega_2^2-\Omega_p^2}+(\frac{e^{-i\zeta}\eta^2}{(\Omega_p+\omega_2-\omega_1)(\Omega_p+\omega_1+\omega_2)}\right.$$
$$\left.-\frac{e^{i\zeta}\eta^2}{(\Omega_p+\omega_1-\omega_2)(-\Omega_p+\omega_1+\omega_2)})\right)B_2=0 \tag{3.48b}$$

Solving these solvability conditions with the ansatz $B_1(T_2)=B_{10}e^{\lambda_1 T_2},\ B_2(T_2)=B_{20}e^{\lambda_2 T_2}$ gives

$$B_1(T_2) = B_{10}e^{(\Lambda-i\Theta_1)T_2}, \tag{3.49a}$$
$$B_2(T_2) = B_{20}e^{(-\Lambda+i\Theta_2)T_2}, \tag{3.49b}$$

where

$$\begin{aligned}\Theta_1 &= \frac{1}{8\omega_1}(\mu_1^2+\frac{2\eta^2}{4\omega_1^2\Omega_p^2}-\frac{2\eta^2(\omega_1^2-\omega_2^2+\Omega_p^2)\cos(\zeta)}{(\Omega_p^2-(\omega_1-\omega_2)^2)(\Omega_p^2-(\omega_1+\omega_2)^2)})\\ \Theta_2 &= \frac{1}{8\omega_2}(-\mu_2^2-\frac{2\eta^2}{4\omega_2^2\Omega_p^2}-\frac{2\eta^2(\omega_1^2-\omega_2^2-\Omega_p^2)\cos(\zeta)}{(\Omega_p^2-(\omega_1-\omega_2)^2)(\Omega_p^2-(\omega_1+\omega_2)^2)})\\ \Lambda &= \frac{\eta^2\Omega_p\sin(\zeta)}{2((\Omega_p^2-(\omega_1-\omega_2)^2)(\Omega_p^2-(\omega_1+\omega_2)^2))}\end{aligned} \tag{3.50}$$

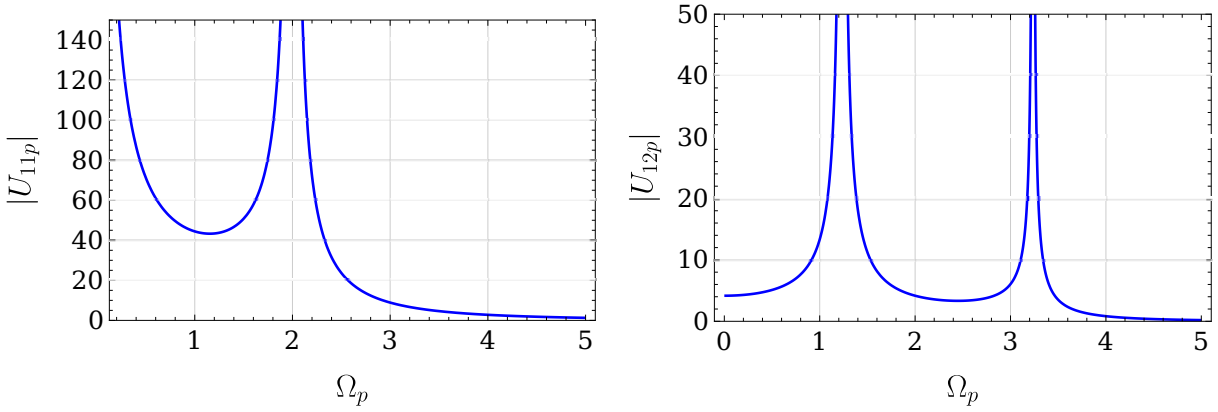

(a) $|U_{11p}|$ (b) $|U_{21p}|$

Figure 3.7: Amplitudes of the first approximation solution $|\Lambda_{11p}|, |\Lambda_{21p}|$ with respect to the parametric excitation frequency Ω_p, where $\omega_1 = 1, \omega_2 = \sqrt{5}, \mu_1 = 0.15, F_0 = 1, \eta_{ij} = 10, \zeta = -\pi/2$.

and finally the solution of (3.33) to the first order approximation gives

$$\begin{aligned} u_{10} &= B_{10}\, e^{(\frac{-\mu_1}{2}+\Lambda)} e^{i(\omega_1-\Theta_1)t} - \frac{F_0}{2\omega_1(\mu_1 + 2i(\Omega_f - \omega_1))}\, e^{i\Omega_f t} + CC, \\ u_{20} &= B_{20}\, e^{(\frac{-\mu_2}{2}-\Lambda)} e^{i(\omega_2+\Theta_1)t} + CC, \end{aligned} \tag{3.51}$$

where perturbation parameter is set to one, $\epsilon = 1$, and B_{10}, B_{20} are constants determined by initial conditions. A closer look at the real part of the homogeneous solution in both degrees of freedom, that is

$$\Lambda_1 = \frac{-\mu_1}{2} + \Lambda = \frac{-\mu_1}{2} + \left[\frac{\eta^2 \Omega_p \sin(\zeta)}{2\left[\Omega_p^2 - (\omega_1 - \omega_2)^2\right]\left[\Omega_p^2 - (\omega_1 + \omega_2)^2\right]} \right], \tag{3.52a}$$

$$\Lambda_2 = \frac{-\mu_2}{2} - \Lambda = \frac{-\mu_2}{2} - \left[\frac{\eta^2 \Omega_p \sin(\zeta)}{2\left[\Omega_p^2 - (\omega_1 - \omega_2)^2\right]\left[\Omega_p^2 - (\omega_1 + \omega_2)^2\right]} \right], \tag{3.52b}$$

we find them exactly the same as derived in 3.29 using the method of normal forms, and $\Lambda_{1,2}$ are the Lyapunov exponents of this system. This is not much surprising, since the only difference between both problems is the additional forced excitation, which is added to the final solution of this system as a particular solution. However, this proves formally the effect of *destabilization* of the solution in the *amplification* of the forced response u_{10}, u_{20}.

The stability of the trivial solution is then governed by the maximum value of Λ_1 and Λ_2, that is

$$\Lambda_{max} = max(\Lambda_1, \Lambda_2), \tag{3.53}$$

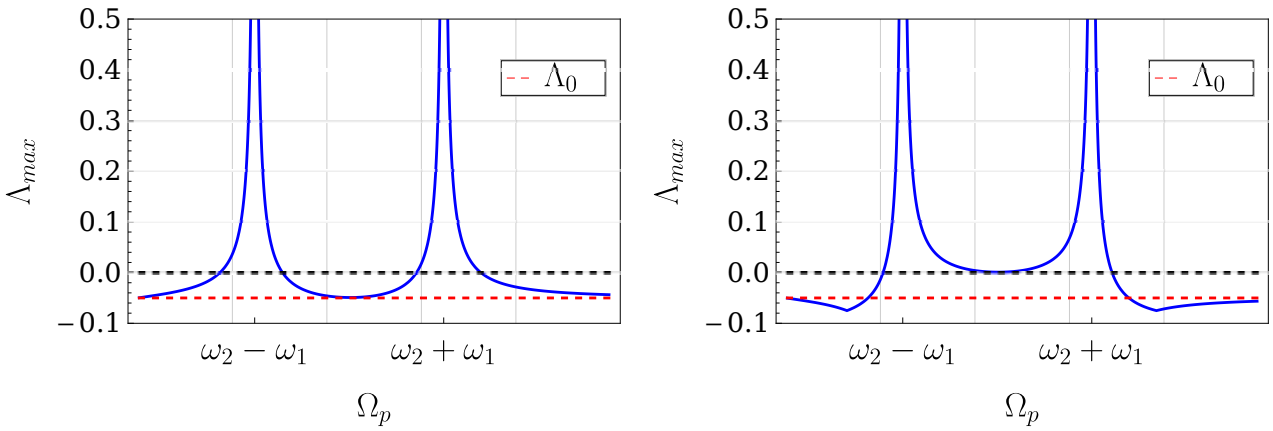

(a) $\zeta = \pi/2$ (b) $\zeta = -\pi/2$

Figure 3.8: Λ_{max} against Ω_p for two phase-shift values

which is plotted against the parametric excitation frequency for two different phase-shifts ζ in Fig. 3.8. We define Λ_0 as Λ_{max} when $\eta = 0$, i.e. at no parametric excitation. In this way, we can identify the destabilization effect for both phase-shift values. As we can see through the figure, $\zeta = -\pi/2$ causes a destabilization for a broad frequency band between $\omega_2 - \omega_1$ and $\omega_2 + \omega_1$. It must be noted here that our discussion concerning the destabilization effect influences the homogeneous solution of (3.51) only, which is a transient response. Therefore, this does not explain why should the whole solution be amplified. Since this amplification effect is well-known experimentally [108], an suggestive explanation is proposed here. We consider the case when $\Lambda_{1,2}$ are near zero, in this case the transiency turns out to be very slow, and have a near-steady-state response, therefore, the harmonic part of the homogeneous solution takes an amplitude B_{10} or B_{20} which depends on the initial conditions, including the perturbing solutions u_{11} and u_{21}, which depend on both the parametric excitation and the forced excitation amplitude as well. This means that driving the system exponent near the zero value allows other perturbations to add to the whole response. This collective response then adds to the particular solution in u_{10}. This could also explain why this effect occurs only in the vicinity of instability, in other words, just under the instability tongue in the stability chart [108]. In order to simulate the amplification effect a time-integration is carried out at three different parametric excitation amplitudes, away from instability, near instability, and in instability and plotted in Fig. 3.9. Here we can see clearly the existence of a critical value of $\eta = 0.94$ at which amplification is observed, and only a slight increase in η to 0.95 causes instability. The critical value lies at the border of instability for the given system parameters and parametric excitation frequency. This critical value could be calculated using the approximate solution (3.52) to be 0.9. This discrepancy is attributed to the analytical approximation. Moreover, the system

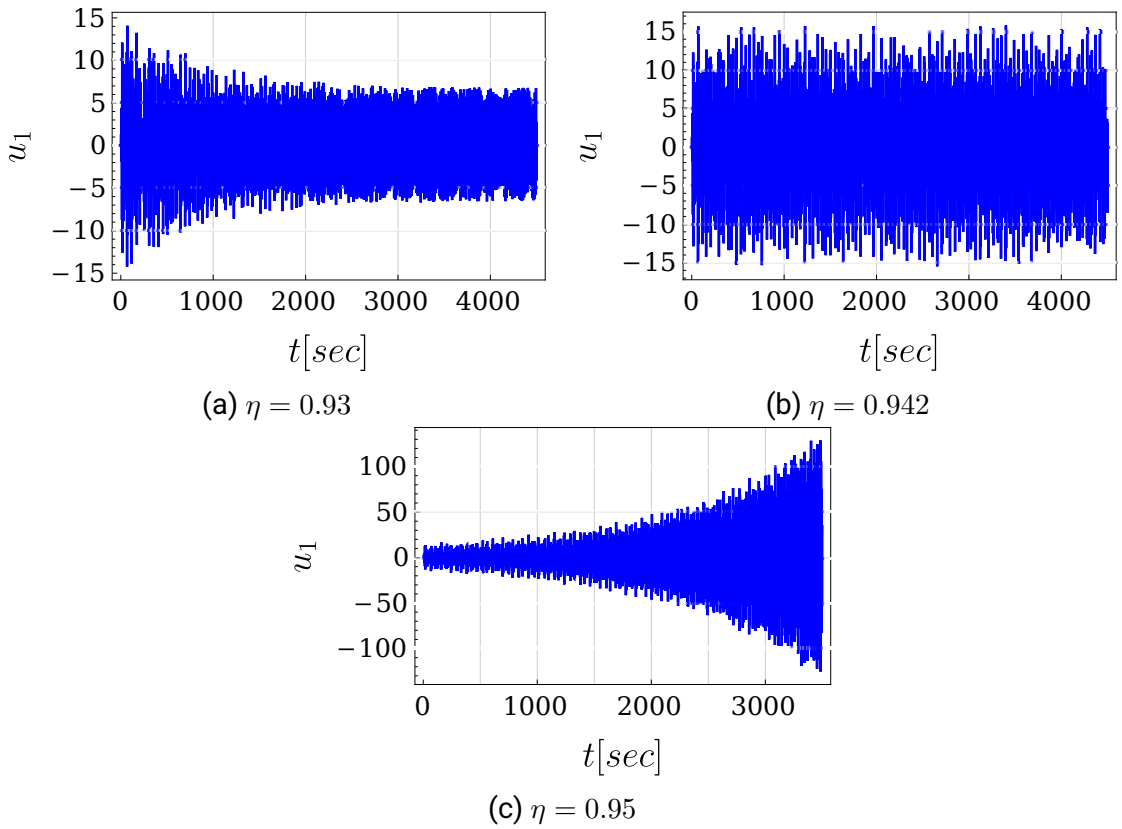

Figure 3.9: Integrated time response of u_1 where $\omega_1 = 1, \omega_2 = \sqrt{5}, \mu_1 = 0.1, \mu_2 = 0.2, F_0 = 1, \Omega_f = 1, \zeta = -\pi/2, \Omega_p = 2.5$.

is time-integrated at various excitation frequencies in the broadband destabilization interval and in each time a critical value is obtained, below which an amplification of the response is observed, and which is near to the critical value calculated using the approximate analytical method. This completes our verification for the hypothesis that the destabilization of the trivial solution corresponds to an amplification of the system's response.

3.2 Nonlinear time-periodic systems

The analysis proceeds further with a nonlinear version of the previously discussed parametrically excited system. In this case, in order to achieve the amplification of the system's response under the parametric resonance, then the study will be focused on the dynamics inside the instability regions of the trivial stationary solution, and thereby this would be called a *resonant parametric amplification* as discussed before in section 3.1.6. Similar two-degree of freedom systems were previously investigated with different analytical methods, using multiple scales, normal

form or averaging methods [42, 15, 109, 110]. However, since the asynchronous parametric excitation was not given appropriate attention until recently, the investigation of this excitation case in presence of nonlinearities was only found in [40], in which the parametric excitation was not fully populated, and only combination resonances were considered with dissimilar natural frequencies. In this work, the asynchronous parametric excitation is considered in a two DoF system, with a fully populated excitation matrix. Moreover, the nontrivial solutions are discussed at all resonant frequencies, and a more detailed bifurcation analysis is carried out.

Thus, we consider a perturbed two DoF nonlinear system

$$\begin{aligned} u_1'' + \omega_1^2 u_1 + \epsilon[\mu_1 u_1' + \gamma_1 u_1^3 + \alpha_1 u_1'^3 + \eta_{11} u_1 \cos(\Omega_p t) + \eta_{12} u_2 \cos(\Omega_p t)] = 0 \\ u_2'' + \omega_2^2 u_2 + \epsilon[\mu_2 u_2' + \gamma_2 u_2^3 + \alpha_2 u_2'^3 + \eta_{21} u_1 \cos(\Omega_p t + \zeta) + \eta_{22} u_2 \cos(\Omega_p t)] = 0 \end{aligned} \tag{3.54}$$

with cubic stiffness and damping nonlinearities having the coefficients γ_i and α_i , $i = 1, 2$, respectively, and having natural frequencies ω_1, ω_2. Without the given parametric excitation, the two DoF would be rather uncoupled, the coupling is then achieved through the parametric excitation terms, which have the coefficients η_{12} and η_{21}, where the latter includes a phase shift ζ. In addition the system includes conventional parametric excitation terms as well with coefficients η_{ii}, $i = 1, 2$. Here there is no forced excitation, that is, the system is purely parametrically excited. All terms but the linear oscillator terms are considered to be small, which is indicated by the perturbation arbitrary parameter $\epsilon << 1$.

3.2.1 Perturbation analysis

The method of multiple scales [41, 89] is used to analyze the given problem up to the first order. One seeks an expansion in the form

$$u_1(t;\epsilon) = u_{10}(T_0, T_1) + \epsilon u_{11}(T_0, T_1) + ..., \tag{3.55a}$$

$$u_2(t;\epsilon) = u_{20}(T_0, T_1) + \epsilon u_{21}(T_0, T_1) + ..., \tag{3.55b}$$

where $T_i = \epsilon^i t,\ D_i = \partial/\partial T_i$ and

$$\begin{aligned} \frac{\partial}{\partial t} &= D_0 + \epsilon D_1 + ..., \\ \frac{\partial^2}{\partial t^2} &= D_0^2 + 2\epsilon D_0 D_1 + ... \end{aligned} \tag{3.56}$$

Inserting (3.55) and (3.56) in (3.54) and separating according to the order of ϵ gives: for $\boldsymbol{\epsilon^0}$,

$$D_0^2 u_{10} + \omega_1^2 u_{10} = 0, \tag{3.57a}$$

$$D_0^2 u_{20} + \omega_2^2 u_{20} = 0, \tag{3.57b}$$

while for $\boldsymbol{\epsilon^1}$,

$$D_0^2 u_{11} + \omega_1^2 u_{11} = -\mu_1 D_0 u_{10} - \gamma_1 u_{10}^3 - \alpha_1 D_0 u_{10}^3 - \eta_{11} u_{10} \cos(\Omega_p t) - \eta_{12} u_{20} \cos(\Omega_p t) - 2 D_0 D_1 u_{10}, \tag{3.58a}$$

$$D_0^2 u_{21} + \omega_2^2 u_{21} = -\mu_2 D_0 u_{20} - \gamma_2 u_{20}^3 - \alpha_2 D_0 u_{20}^3 - \eta_{21} u_{10} \cos(\Omega_p t + \zeta) - \eta_{22} u_{20} \cos(\Omega_p t) - 2 D_0 D_1 u_{20}. \tag{3.58b}$$

Solving (3.57) gives

$$u_{10}(T_0, T_1) = A_1(T_1) e^{i\omega_1 T_0} + \bar{A}_1(T_1) e^{-i\omega_1 T_0}, \tag{3.59a}$$

$$u_{20}(T_0, T_1) = A_2(T_1) e^{i\omega_2 T_0} + \bar{A}_2(T_1) e^{-i\omega_2 T_0}, \tag{3.59b}$$

where the amplitudes A_1, A_2 represent the slow-scale variables, which will exhibit the system's stability in the further calculations, while the exponential expressions represent the fast-scale periodic solution.

Inserting (3.59) in (3.58) gives

$$\begin{aligned} D_0^2 u_{11} + \omega_1^2 u_{11} = & -\gamma_1 (A_1^3 e^{i3\omega_1 T_0} + 3 A_1^2 \bar{A}_1 e^{i\omega_1 T_0}) - \alpha_1 (-i\omega_1^3 A_1^3 e^{i3\omega_1 T_0} + i3\omega_1^3 A_1^2 \bar{A}_1 e^{i\omega_1 T_0}) \\ & - \frac{1}{2} \eta_{11} A_1 (e^{i(\omega_1 - \Omega_p) T_0} + e^{i(\omega_1 + \Omega_p) T_0}) - \frac{1}{2} \eta_{12} A_2 (e^{i(\omega_2 - \Omega_p) T_0} + e^{i(\omega_2 + \Omega_p) T_0}) \\ & - i2\omega_1 D_1 A_1 e^{i\omega_1 T_0} - i\mu_1 \omega_1 A_1 e^{i\omega_1 T_0} + CC, \end{aligned} \tag{3.60a}$$

$$\begin{aligned} D_0^2 u_{21} + \omega_1^2 u_{21} = & -\gamma_2 (A_2^3 e^{i3\omega_2 T_0} + 3 A_2^2 \bar{A}_2 e^{i\omega_2 T_0}) - \alpha_2 (-i\omega_2^3 A_2^3 e^{i3\omega_2 T_0} + i3\omega_2^3 A_2^2 \bar{A}_2 e^{i\omega_2 T_0}) \\ & - \frac{1}{2} \eta_{21} A_1 (e^{i(\omega_1 - \Omega_p) T_0 - i\zeta} + e^{i(\omega_1 + \Omega_p) T_0 + i\zeta}) - \frac{1}{2} \eta_{22} A_2 (e^{i(\omega_2 - \Omega_p) T_0} + e^{i(\omega_2 + \Omega_p) T_0}) \\ & - i2\omega_2 D_1 A_2 e^{i\omega_2 T_0} - i\mu_2 \omega_2 A_2 e^{i\omega_2 T_0} + CC, \end{aligned} \tag{3.60b}$$

where CC stands for the complex conjugates of the preceding terms in each equation.

Since equations (3.60) have secular terms, which contain $e^{\pm i\omega_i T_0}$, thus, all particular solutions of u_{11} and u_{12} are unstable, which contradicts being a finer correction in (3.55). Therefore, the secular terms must vanish. However, these terms are to be known depending on the frequency interval chosen for the solution, whether it is away from resonance frequencies or nearly tuned

to them. For this reason, the following sections will represent the different cases according to the resonant conditions. First, we will study the cases of primary parametric resonance for one degree of freedom, since the primary resonance at the other frequency will give the same behavior. Then we will turn to the interesting case of having 1:1 internal resonance between both DoFs, while one of them being excited parametrically as well. And finally, the nontrivial solutions, or limit cycles, are found at the summation and difference combination frequencies.

3.2.2 Primary parametric resonance

For this case we introduce a detuning parameter, which leads to secular or small-divisor terms in (3.60), that is

$$\Omega_p = 2\omega_1 + \epsilon\sigma_p, \tag{3.61}$$

where $\sigma_p = \mathcal{O}(1)$ is the detuning parameter for the primary parametric resonance. Inserting (3.61) in (3.60) and equating secular terms to zero yields

$$i2\omega_1 D_1 A_1 + i\mu_1\omega_1 A_1 + 3\gamma_1 A_1^2\bar{A}_1 + i3\alpha_1\omega_1^3 A_1^2\bar{A}_1 + \frac{1}{2}\eta_{11}\bar{A}_1 e^{i\sigma_p T_1} = 0, \tag{3.62a}$$

$$i2\omega_2 D_1 A_2 + i\mu_2\omega_2 A_2 + 3\gamma_2 A_2^2\bar{A}_2 + i3\alpha_2\omega_2^3 A_2^2\bar{A}_2 = 0. \tag{3.62b}$$

Since these equations contain complex variables A_1, A_2, a transformation in polar coordinates is suggested as follows,

$$A_1(T_1) = \frac{1}{2}a_1(T_1)e^{i\phi_1(T_1)}, \quad A_2(T_1) = \frac{1}{2}a_2(T_1)e^{i\phi_2(T_1)}. \tag{3.63}$$

Substituting (3.63) in (3.62) and separating real and imaginary terms gives

$$\omega_1 D_1 a_1 + \frac{1}{2}\mu_1\omega_1 a_1 + \frac{3}{8}\alpha_1\omega_1^3 a_1^3 + \frac{1}{4}\eta_{11}a_1\sin(\theta_1) = 0, \tag{3.64a}$$

$$\frac{1}{2}\omega_1 a_1(D_1\theta_1 - \sigma_p) + \frac{3}{8}\gamma_1 a_1^3 + \frac{1}{4}\eta_{11}a_1\cos(\theta_1) = 0, \tag{3.64b}$$

$$\omega_2 D_1 a_2 + \frac{1}{2}\mu_2\omega_2 a_2 + \frac{3}{8}\alpha_2\omega_2^3 a_2^3 = 0, \tag{3.64c}$$

$$\omega_2 a_2 D_1\theta_2 - \frac{3}{8}\gamma_2 a_2^3 = 0, \tag{3.64d}$$

where $\theta_1 = \sigma_p T_1 - 2\phi_1$ and $\theta_2 = \phi_2$. Steady state solutions of the system (3.54) are obtained by calculating the fixed points of (3.64), that is, $D_1 a_i = 0$ and $D_1\theta_i = 0$, for $i = 1, 2$. Thus, the

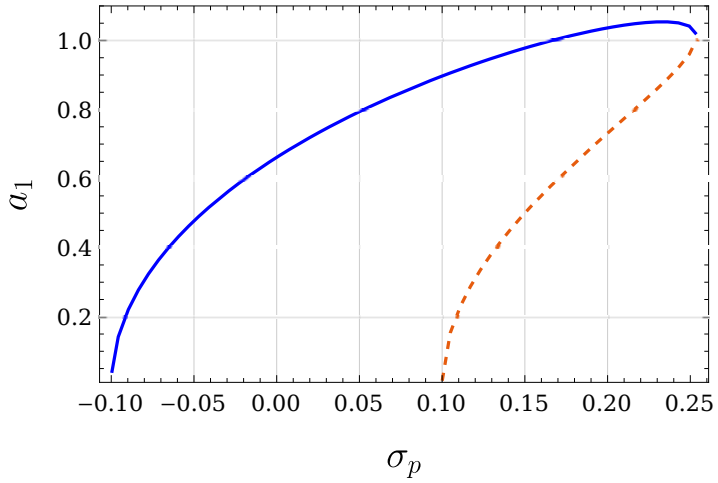

Figure 3.10: Frequency-response curve at the primary parametric resonance of the first DoF

fixed points are

$$\frac{1}{2}\mu_1\omega_1 a_1 + \frac{3}{8}\alpha_1\omega_1^3 a_1^3 + \frac{1}{4}\eta_{11} a_1 \sin(\theta_1) = 0, \tag{3.65a}$$

$$-\frac{1}{2}\omega_1 a_1 \sigma_p + \frac{3}{8}\gamma_1 a_1^3 + \frac{1}{4}\eta_{11} a_1 \cos(\theta_1) = 0, \tag{3.65b}$$

$$\frac{1}{2}\mu_2\omega_2 a_2 + \frac{3}{8}\alpha_2\omega_2^3 a_2^3 = 0, \tag{3.65c}$$

$$\frac{3}{8}\gamma_2 a_2^3 = 0. \tag{3.65d}$$

Obviously, the steady state amplitude of the second oscillator a_2 vanishes, while that of the first one a_1 is given by the resonance equation

$$-9(\gamma_1^2 + \alpha_1^2\omega_1^6)a_1^5 + 24(\gamma_1\sigma_p\omega_1 - \alpha_1\mu_1\omega_1^4)a_1^3 + (4\eta_{11}^2 - 16(\mu_1^2 + \sigma_p^2)\omega_1^2)a_1 = 0. \tag{3.66}$$

Thereby, either we have a trivial solution

$$a_1 = 0$$

or

$$a_1 = \pm\sqrt{\frac{2}{3}}\sqrt{\frac{2\gamma_1\sigma_p\omega_1 - 2\alpha_1\mu_1\omega_1^4 \pm \sqrt{-8\alpha_1\gamma_1\mu_1\sigma_p\omega_1^5 + \gamma_1^2(\eta_{11}^2 - 4\mu_1^2\omega_1^2) + \alpha_1^2\omega_1^6(\eta_{11}^2 - 4\sigma_p^2\omega_1^2)}}{\gamma_1^2 + \alpha_1^2\omega_1^6}}. \tag{3.67}$$

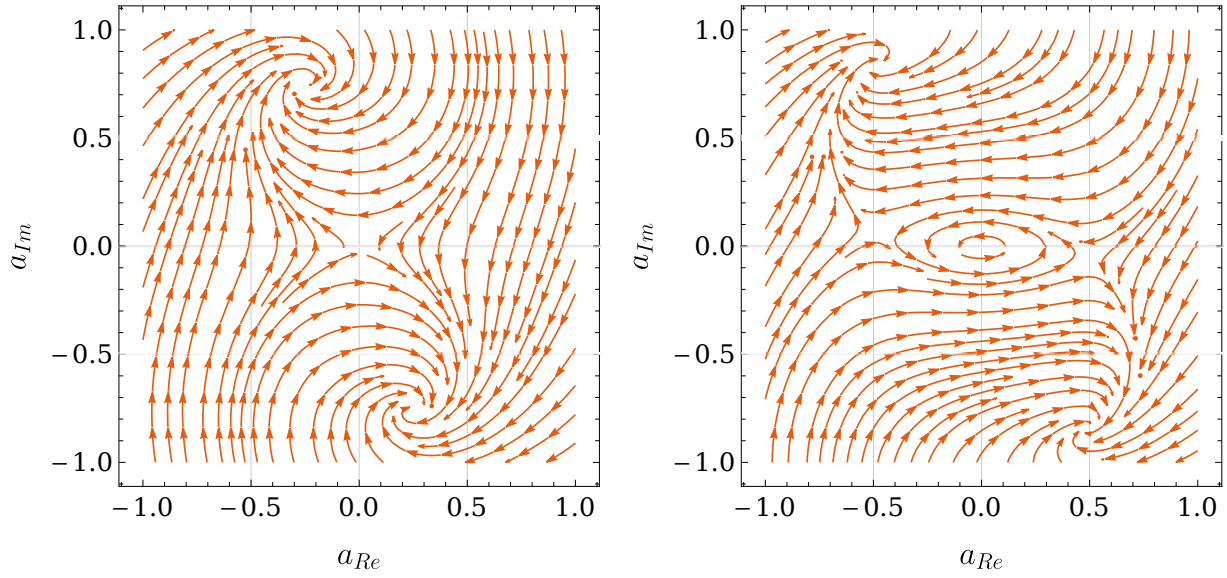

(a) Before bifurcation point, $\sigma_p < 0.1$ (b) After bifurcation point, $\sigma_p > 0.1$

Figure 3.11: Phase plot for the complex plane of the $a_1(T_1)$

The frequency-response curve corresponding to the nontrivial solution (3.67) is presented in Fig. 3.10 for the parameter values $\omega_1 = 1, \mu_1 = 0, \gamma_1 = 0.07, \alpha_1 = 0.03$ and $\eta_{11} = 0.2$. A nonlinear resonance behavior is exhibited, and a stable limit cycle is born after a bifurcation at $\sigma_p = -0.1$. Although the system incorporates Duffing-type nonlinearities, the nontrivial solution here differs substantially from that of a forced Duffing oscillator with regard of the type of excitation. At the point ($\sigma_p = 0.1$) another bifurcation occurs, where a smaller unstable limit cycle appears in addition to the stable one in another interval $\sigma_p \in]0.1, 0.25[$. The phase portrait before and after the bifurcation point is represented in Fig. 3.11 in complex phase space of the slow variable a_1, where A_1 is represented in complex form

$$A_1 = (a_{Re} - ia_{Im})e^{\frac{1}{2}i\sigma_p T_1} \tag{3.68}$$

instead of the polar one used in the analysis. This is depicted as having a saddle trivial fixed point in the first interval and a stable focus. While in the second interval, the stable focus is replaced by a saddle and another stable focus, whilst the trivial solution turns to be stable again. Thus in the second interval two stable solutions exist, at the trivial fixed point and a nontrivial one.

Further insight could be drawn from this analysis by setting the detuning parameter $\sigma_p = 0$ and at the same time cancelling the linear damping, i.e. $\mu_1 = 0$. In this case the nontrivial

solution (3.67) reduces to

$$a_1 = \Gamma = \left(\frac{4\eta_{11}^2}{9(\gamma_1^2 + \alpha_1^2 \omega_1^6)} \right)^{1/4}, \tag{3.69}$$

which will be called Γ for further analysis. As we see in this expression the amplitude of the oscillation is determined mainly by the parametric excitation amplitude η_{11} and the nonlinear terms γ_1, α_1. Here it can be clearly stated that in the case of the absence of any of them we will be left with only the trivial fixed point. Although it might seem to contradict the fact that the unforced Duffing oscillator has nontrivial solutions even without any parametric excitation, the main difference here is that the linear damping was set to zero [90]. The Γ value is considered here to represent a nontrivial solution without perturbing with the linear damping and the detuning of the excitation frequency. The effect of perturbing this solution with varying both of them will be studied next.

Substituting the value of Γ back in (3.66), while keeping the detuning parameter $\sigma_p = 0$ but allowing the linear damping μ_1 to vary, gives

$$a_1^5 + \Gamma^4 \left(\frac{6\alpha_1 \mu_1 \omega_1^2}{\eta_{11}^2} \right) a_1^3 + \Gamma^4 \left(\frac{4\mu_1^2 \omega_1^2}{\eta_{11}^2} - 1 \right) a_1 = 0, \tag{3.70}$$

solving this resonance equation gives again

$$a_1 = 0 \tag{3.71}$$

or

$$a_1^4 + \Gamma^4 \left(\frac{6\alpha_1 \mu_1 \omega_1^2}{\eta_{11}^2} \right) a_1^2 + \Gamma^4 \left(\frac{4\mu_1^2 \omega_1^2}{\eta_{11}^2} - 1 \right) = 0, \tag{3.72}$$

which is clearly a quadratic equation in a_1. Using combined parameters and rewriting it gives

$$a_1^4 + \Gamma^4 \Xi_1 a_1^2 + \Gamma^4 \Xi_2 = 0, \tag{3.73}$$

which has a solution of

$$a_1^2 = \frac{-\Gamma^4 \Xi_1}{2} \pm \frac{1}{2} \sqrt{\Gamma^8 \Xi_1^2 - 4\Gamma^4 \Xi_2}. \tag{3.74}$$

For relatively high excitation amplitudes with respect to system parameters, we find the combined parameters Ξ_1, Ξ_2 and Γ to have values smaller than one. In this case Ξ_2 will dominate the solution. And in order to have a real-valued a_1, i.e. positive-valued a_1^2, Ξ_2 must then be negative. Thus a real valued a_1 can only take place if positive square root solution was selected

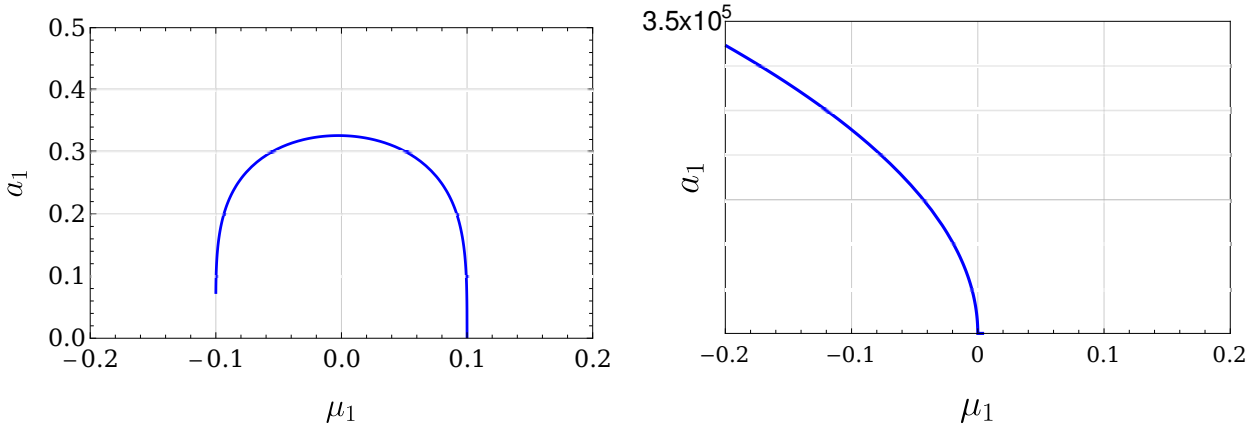

(a) $\eta_{11} = 0.2$ (b) $\eta_{11} = 0.01$

Figure 3.12: Nontrivial solution by varying the system linear damping μ_1, while $\sigma_p = 0$. Other parameter values read $\omega_1 = 1, \gamma_1 = 0.07, \alpha_1 = 0.03$

and if $\Xi_2 < 0$. Reading the Ξ_2 term from (3.72) and applying this condition yields

$$-\frac{\eta_{11}}{2\omega_1} < \mu_1 < \frac{\eta_{11}}{2\omega_1}, \tag{3.75}$$

which could be confirmed by numerically solving (3.72) and plotting the solution in Fig.3.12(a).

However, if the excitation amplitudes were relatively small, causing the combined parameters values to be larger than one, we find Ξ_1 to be dominating. In this case, a real-valued a_1 is only possible for $\mu_1 < 0$, as shown in the same figure.

The plotted solution in Fig. 3.12 corresponds to the solution of the main resonance equation at $\sigma_p = 0$ in Fig. 3.10, where only a stable solution exists. However if another value of σ_p was chosen which includes an unstable solution as well, this should give another dimension to the problem. Thereby, by returning to (3.66) it can be written in

$$a_1^4 + \Gamma^4 \left(\Xi_1 - \frac{6\gamma_1\omega_1}{\eta_{11}^2}\sigma_p \right) a_1^2 + \Gamma^4 \left(\Xi_2 + \frac{4\omega_1^2}{\eta_{11}^2}\sigma_p^2 \right) = 0, \tag{3.76}$$

which gives the admissible amplitude values shown in Fig.3.13 by varying the linear damping μ_1 again. The figure shows isolated stable and unstable steady-state solutions. This is particularly interesting, since the variation of the linear damping could cause an abrupt increase or decrease in the amplitude of the response at a bifurcation point. This high sensitivity of the response at the bifurcation point could be of a significant importance for systems, where high sensitivity is pursued using a bifurcation control scheme.

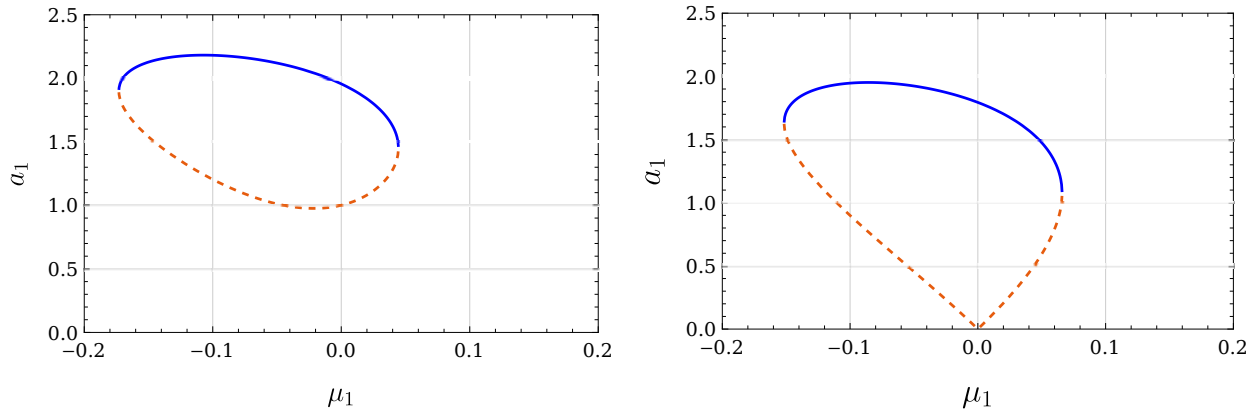

(a) $\sigma_p = 0.15$ (b) $\sigma_p = 0.1$

Figure 3.13: Nontrivial solution by varying the system linear damping μ_1 at two different values for the detuning parameter σ_p. Other parameter values read $\omega_1 = 1, \gamma_1 = 0.07, \alpha_1 = 0.03, \eta_{11} = 0.2$.

3.2.3 Internal resonance under parametric excitation

The case of 1:1 internal resonance stands to be relevant for systems involving degenerate or similar eigenvalues $\omega_1 \simeq \omega_2$. This happens to be the case for structures with axis-symmetric geometry. A motivating example is the micro-ring gyroscope, which will be analyzed afterwards in chapters 4 and 5. It was also shown in section 3.1.5 that the degeneracy of eigenvalues or even the nearness to one another leads to a large broadband effect between the difference and summation combination frequencies. In the nonlinear case, however, another phenomenon could take place, which is the internal resonance, provided that one eigenfrequency is in the vicinity of the other, this would only occur when the ring's geometry is highly symmetric around the axis.

In this case we introduce an additional detuning parameter σ_{in} where

$$\omega_2 = \omega_1 + \epsilon\sigma_{in}, \tag{3.77}$$

while the previous one (3.61) remains effective. Returning to (3.60) and this time inserting both (3.61) and (3.77) gives the solvability conditions

$$i2\omega_1 D_1 A_1 + i\mu_1\omega_1 A_1 + 3(\gamma_1 + i\alpha_1\omega_1^3)A_1^2\bar{A}_1 + \frac{1}{2}\eta_{11}\bar{A}_1 e^{i\sigma_p T_1} + \frac{1}{2}\eta_{12}\bar{A}_2 e^{i(\sigma_p-\sigma_{in})T_1} = 0, \tag{3.78a}$$

$$i2\omega_2 e^{i\sigma_{in}T_1} D_1 A_2 + i\mu_2\omega_2 e^{i\sigma_{in}T_1} A_1 + 3(\gamma_2 + i\alpha_2\omega_2^3)A_2^2\bar{A}_2 e^{i\sigma_{in}T_1} + \frac{1}{2}\eta_{21}\bar{A}_1 e^{i\sigma_p T_1 + i\zeta} + \frac{1}{2}\eta_{22}\bar{A}_2 e^{i(\sigma_p-\sigma_{in})T_1} = 0. \tag{3.78b}$$

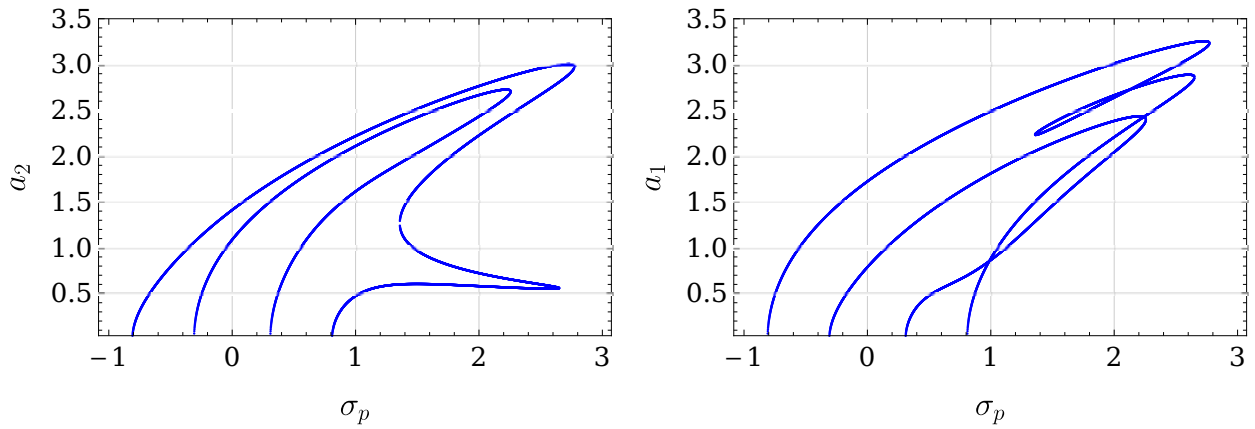

(a) a_2 (b) a_1

Figure 3.14: Nontrivial solutions for a_1 and a_2 by detuning σ_p in case of tuned 1:1 internal resonance, where $\omega_i = 1, \mu_i = 0, \gamma_i = 0.1, \alpha_i = 0.02, \eta_{11} = \eta_{12} = \eta_{21} = 1, \eta_{22} = 0$ and $\sigma_{in} = 0$, for $i = 1, 2$.

In order to investigate the exchange of energy when only one DoF is parametrically excited, we put $\eta_{22} = 0$, while the phase shift is firstly not taken into consideration, i.e. $\zeta = 0$. As previously done, we insert (3.63) in (3.78) then separate real and imaginary parts to yield

$$\omega_1 a_1 D_1\phi_1 - \frac{3}{8}\gamma_1 a_1^3 - \frac{1}{4}\eta_{12} a_2 \cos(\theta_1) - \frac{1}{4}\eta_{11} a_1 \cos(\theta_2) = 0, \tag{3.79a}$$

$$\omega_1 D_1 a_1 + \frac{1}{2}\mu\omega_1 a_1 + \frac{3}{8}\alpha_1\omega_1^3 a_1^3 - \frac{1}{4}\eta_{12} a_2 \sin(\theta_1) + \frac{1}{4}\eta_{11} a_1 \cos(\theta_2) = 0, \tag{3.79b}$$

$$\omega_2 a_2 D_1\phi_2 - \frac{3}{8}\gamma_2 a_2^3 - \frac{1}{4}\eta_{21} a_1 \cos(\theta_1) = 0, \tag{3.79c}$$

$$\omega_2 D_1 a_2 + \frac{1}{2}\mu_2\omega_2 a_2 + \frac{3}{8}\alpha_2\omega_2^3 a_2^3 - \frac{1}{4}\eta_{21} a_1 \sin(\theta_1) = 0, \tag{3.79d}$$

where $\theta_1 = \phi_1 + \phi_2 + (\sigma_{in} - \sigma_p)T_1$ and $\theta_2 = -2\phi_1 + \sigma_p T_1$.

The steady state solutions are then sought when

$$\begin{aligned} &D_1 a_1 = 0, \quad D_1 a_2 = 0, \text{ and} \\ &D_1\theta_1 = 0 \text{ and } D_1\theta_2 = 0, \quad \text{or} \quad D_1\phi_1 = \sigma/2 \text{ and } D_1\phi_2 = \sigma/2 - \sigma_i, \end{aligned} \tag{3.80}$$

which when substituted in (3.79) and solved for a_1 and a_2 give the two resonance equations

$$9(\gamma_2^2 + \alpha_2^2\omega_2^6)a_2^6 + 24\omega_2(-\gamma_2\sigma_p + 2\gamma_2\sigma_{in} + \alpha_2\mu_2\omega_2^3)a_2^4 + 16\omega_2^2(\mu_2^2 + (\sigma_p - 2\sigma_{in})^2)a_2^2 - 4\eta_{21}^2 a_1^2 = 0, \tag{3.81a}$$

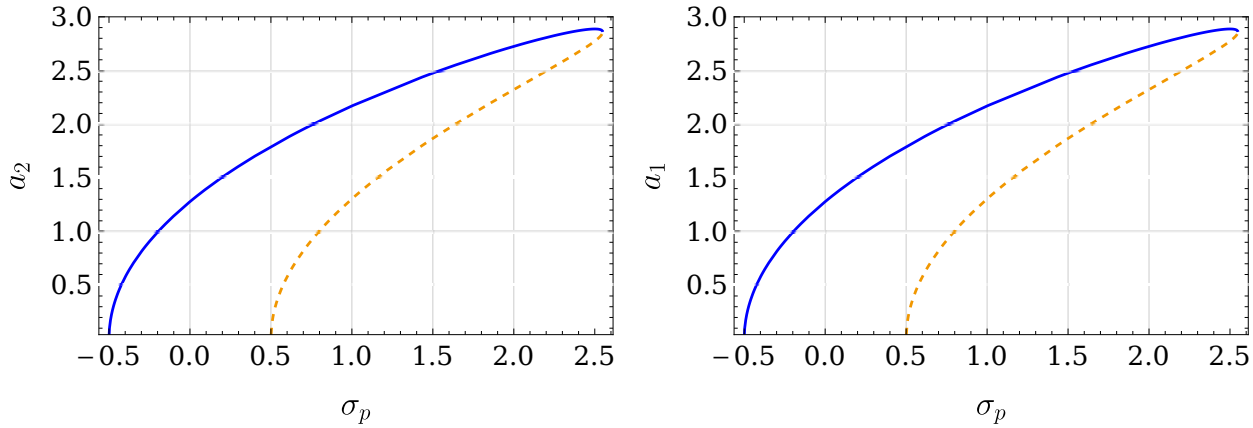

(a) a_2 (b) a_1

Figure 3.15: Nontrivial solutions for a_1 and a_2 by detuning σ_p in case of tuned 1:1 internal resonance, where , where $\omega_i = 1, \mu_i = 0, \gamma_i = 0.1, \alpha_i = 0.02, \eta_{12} = \eta_{21} = 1, \eta_{22} = 0, \sigma_{in} = 0$ and $\eta_{11} = 0$, for $i = 1, 2$.

$$
\begin{aligned}
&9\eta_{21}^2(\gamma_1^2 + \alpha_1^2\omega_1^6)a_1^7 + 24\eta_{21}^2(\alpha_1\mu_1\omega_1^4 - \gamma_1\sigma_p\omega_1)a_1^5 + a_1^3\left[-4\eta_{21}^2(\eta_{11}^2 - 4(\mu_1^2 + \sigma_p^2)\omega_1^2)\right.\\
&\left.+24\eta_{12}\eta_{21}(\gamma_1(\sigma_p - 2\sigma_{in}) - \alpha_1\mu_2\omega_1^3)\omega_2 a_2^2 - 18\eta_{12}\eta_{21}(\gamma_1\gamma_2 + \alpha_1\alpha_2\omega_1^3\omega_2^3)a_2^4\right] \qquad (3.81b)\\
&+ 4\eta_{12}\eta_{21}a_1\left[(\eta_{12}\eta_{21} - 8(\mu_1\mu_2 + \sigma_p(\sigma_p - 2\sigma_{in}))\omega_1\omega_2)a_2^2 + 6\omega_1(\gamma_2\sigma_p - \alpha_2\mu_1\omega_2^3)a_2^4\right] = 0.
\end{aligned}
$$

Figure(3.14) depicts the frequency-response curves for the amplitudes of both degrees of freedom, which were calculated by solving (3.81) while detuning σ_p. These values represent a perfectly symmetrical system ($\sigma_{in} = 0$) with zero linear damping. The resonance curves show the typical "M" shape due to the internal resonance, moreover, the hardening nonlinear stiffness causes all curves to bend to the right. In addition, multiple nontrivial points could be calculated by detuning the excitation frequency. This results in a complex phase space containing various fixed points at a given excitation frequency, which therefore requires a careful stability analysis in future work. However, when the external parametric excitation η_{11} is turned off, the internal resonance's typical behavior vanishes (see Fig.3.15), and the frequency-response curves show only stable and unstable limit cycles similar to the case of primary parametric resonance discussed before. Nevertheless, a distinction should be made here between this case and the case of parametric resonance by observing the solvability conditions in both cases, i.e. in (3.62) and (3.78). In the case of primary resonance we have only one excitation source, which is η_{11}. The energy, however, could not be transferred to the second degree of freedom, due to the absence of internal resonance. In the case discussed here we do have three excitation sources, η_{11}, η_{12} and η_{21}. If the first one is turned off, the other two remain effective, causing a transfer of energy at the primary resonance frequency. These coupling excitation terms will show up again to be influencing the system's behavior under

combination resonance, as will be discussed afterwards. Furthermore, while having zero η_{11} and η_{22}, we have a cross parametric resonance through η_{12} and η_{21}. This leads to the response depicted in Fig.3.15.

3.2.4 Combination parametric resonances

Summation parametric resonance

We apply the same analysis as before for the case of combination parametric resonances, where the parametric excitation frequency is in the neighborhood of the summation or the difference frequencies, that is $\Omega_p \simeq |\omega_1 \pm \omega_2|$. Beginning with the summation resonance we introduce the detuning parameter σ_s, where

$$\Omega_p = \omega_1 + \omega_2 + \epsilon\sigma_s, \tag{3.82}$$

then as before, the resonance condition (3.82) is then inserted in (3.60), to give the solvability conditions

$$i2\omega_1 D_1 A_1 + i\mu_1\omega_1 A_1 + 3\gamma_1 A_1^2\bar{A}_1 + i3\alpha_1\omega_1^3 A_1^2\bar{A}_1 + \frac{1}{2}\eta_{12}\bar{A}_2 e^{i\sigma_s T_1} = 0, \tag{3.83a}$$

$$i2\omega_2 D_1 A_2 + i\mu_2\omega_2 A_2 + 3\gamma_2 A_2^2\bar{A}_2 + i3\alpha_2\omega_2^3 A_2^2\bar{A}_2 + \frac{1}{2}\eta_{21}\bar{A}_1 e^{i(\sigma_s T_1+\zeta)} = 0. \tag{3.83b}$$

Putting the amplitudes $A_1(T_1), A_2(T_1)$ in polar form according to (3.63), substituting in (3.83) and separating real and imaginary terms gives

$$D_1 a_1 = -\frac{1}{2}\mu_1 a_1 - \frac{3}{8}\alpha_1\omega_1^2 a_1^3 - \frac{1}{4\omega_1}\eta_{12} a_2 \sin(\theta_1) \tag{3.84a}$$

$$D_1 a_2 = -\frac{1}{2}\mu_2 a_2 - \frac{3}{8}\alpha_2\omega_2^2 a_2^3 - \frac{1}{4\omega_2}\eta_{21} a_1 \sin(\theta_1)\cos(\zeta) - \frac{1}{4\omega_2}\eta_{21} a_1 \cos(\theta_1)\sin(\zeta) \tag{3.84b}$$

$$D_1\theta_1 = \sigma_s - \frac{3\gamma_1 a_1^2}{8\omega_1} - \frac{3\gamma_2 a_2^2}{8\omega_2} - \frac{1}{4\omega_2}\eta_{21}\frac{a_1}{a_2}\cos(\theta_1)\cos(\zeta) + \frac{1}{4\omega_2}\eta_{21}\frac{a_1}{a_2}\sin(\theta_1)\sin(\zeta) - \frac{1}{4\omega_1}\eta_{12}\frac{a_2}{a_1}\cos(\theta_1), \tag{3.84c}$$

$$D_1\theta_2 = \frac{3\gamma_2 a_2^2}{8\omega_2} + \frac{1}{4\omega_2}\eta_{21}\frac{a_1}{a_2}\cos(\theta_1)\cos(\zeta) - \frac{1}{4\omega_2}\eta_{21}\frac{a_1}{a_2}\sin(\theta_1)\sin(\zeta), \tag{3.84d}$$

where $\theta_1 = \sigma_s T_1 - \phi_1 - \phi_2$ and $\theta_2 = \phi_2$. Steady-state solutions are then obtained by calculating the fixed points of (3.84), that is when $D_1 a_i = 0$ and $D_1\theta_i = 0$, for $i = 1, 2$. However, in this case the effect of the asynchronicity of the parametric excitation, i.e. the presence of the phase shift ζ, heavily influences the nontrivial solutions and limit cycle oscillations. Therefore, we present the nontrivial solutions in two different cases, synchronous $\zeta = 0$ and asynchronous

$\zeta = -\pi/2$. This latter particular phase-shift is chosen according to our analysis of the trivial solution discussed before.

If $\zeta = 0$, then the fixed points of equations (3.84) could be determined from

$$-\frac{1}{2}\mu_1 a_1 - \frac{3}{8}\alpha_1\omega_1^2 a_1^3 - \frac{1}{4\omega_1}\eta_{12} a_2 \sin(\theta_1) = 0 \tag{3.85a}$$

$$-\frac{1}{2}\mu_2 a_2 - \frac{3}{8}\alpha_2\omega_2^2 a_2^3 - \frac{1}{4\omega_2}\eta_{21} a_1 \sin(\theta_1) = 0 \tag{3.85b}$$

$$\sigma_s - \frac{3\gamma_1 a_1^2}{8\omega_1} - \frac{3\gamma_2 a_2^2}{8\omega_2} - \left(\frac{1}{4\omega_2}\eta_{21}\frac{a_1}{a_2} + \frac{1}{4\omega_1}\eta_{12}\frac{a_2}{a_1}\right)\cos(\theta_1) = 0, \tag{3.85c}$$

while under asynchronous excitation, $\zeta = -\pi/2$, the equations read

$$-\frac{1}{2}\mu_1 a_1 - \frac{3}{8}\alpha_1\omega_1^2 a_1^3 - \frac{1}{4\omega_1}\eta_{12} a_2 \sin(\theta_1) = 0 \tag{3.86a}$$

$$-\frac{1}{2}\mu_2 a_2 - \frac{3}{8}\alpha_2\omega_2^2 a_2^3 + \frac{1}{4\omega_2}\eta_{21} a_1 \cos(\theta_1) = 0 \tag{3.86b}$$

$$\sigma_s - \frac{3\gamma_1 a_1^2}{8\omega_1} - \frac{3\gamma_2 a_2^2}{8\omega_2} - \frac{1}{4\omega_2}\eta_{21}\frac{a_1}{a_2}\sin(\theta_1) - \frac{1}{4\omega_1}\eta_{12}\frac{a_2}{a_1}\cos(\theta_1) = 0. \tag{3.86c}$$

From these equations it can be observed that only the η_{21} excitation terms are changed. Furthermore, although the modulation equations (3.84) were in four variables, only three of them influence the vector fields excluding θ_2, which lead to three algebraic equations in three variables to determine the fixed points.

Stability analysis

In order to determine the stability of the obtained nontrivial steady-state solutions, the solution is perturbed using

$$a_1(T_1) = a_{10} + \Delta a_1(T_1), \quad a_2(T_1) = a_{20} + \Delta a_2(T_1), \quad \theta_1(T_1) = \theta_{10} + \Delta\theta_1(T_1), \tag{3.87}$$

compactly written

$$\boldsymbol{z}(T_1) = \boldsymbol{z_0} + \boldsymbol{\Delta z}(T_1), \tag{3.88}$$

which is then inserted in the modulation equations (3.84) to give

$$\boldsymbol{\Delta \dot{z}} = \frac{\partial \boldsymbol{f}(\boldsymbol{\Delta z}, \boldsymbol{z_0})}{\partial \boldsymbol{\Delta z}}|_{\boldsymbol{\Delta z}=\boldsymbol{z_0}} + NLT, \tag{3.89}$$

where $\boldsymbol{J} = \frac{\partial \boldsymbol{f}(\boldsymbol{\Delta z}, \boldsymbol{z_0})}{\partial \boldsymbol{\Delta z}}|_{\boldsymbol{\Delta z}=\boldsymbol{0}}$ is the Jacobian matrix evaluated at the fixed point and NLT represents the nonlinear terms.

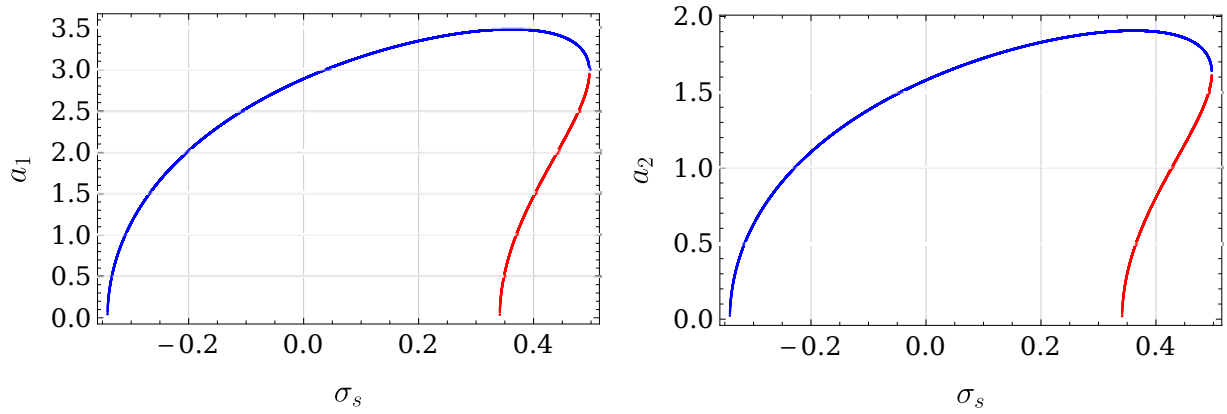

(a) a_1 (b) a_2

Figure 3.16: Nontrivial solutions for a_1 and a_2 by detuning σ_s about the summation frequency, when $\omega_1 = 1, \omega_2 = \sqrt{5}, \gamma_i = 0.07, \alpha_i = 0.03, \eta_{ij} = 1,\ i, j = 1, 2$ and $\zeta = 0$.

After eliminating the nonlinear terms, the linearized system presents an eigensystem with the eigenvectors being tangent to the system's nonlinear manifolds. The stability of the fixed point of the nonlinear system can be deduced from the eigenvalues of the linearized system, as long as the fixed point is hyperbolic according to Hartman-Grobman theorem [86]. In this view, if all the eigenvalues at the investigated fixed point have negative real parts, the fixed point and the corresponding solution are considered asymptotically stable. While the existence of a single positive eigenvalue implies the instability of the solution. However, if the largest eigenvalue is strictly zero, then the stability of the solution cannot be determined by a linear analysis [99].

In this synchronous excitation case, the steady-state solutions are deduced by solving the equations (3.85), then the stability of each fixed point is determined as previously discussed and the result is then plotted in Fig. 3.16, where the blue and red points represent stable and unstable limit cycles respectively. The parametric resonance curve is shown to be similar to primary resonances (see Fig. 3.10), where the amplitude of the second degree of freedom a_2 is lower than the first one a_1.

In the other case, when $\zeta = -\pi/2$, the fixed points of (3.84) are determined through solving (3.86). The resonance curves in this case are then depicted in Fig. 3.17. In this figure, it can be observed that all the nontrivial solutions, or limit cycles, are found to be stable for the given detuning interval. However, the resonance curves of both degrees of freedom have different profiles. Furthermore, detuning the excitation frequency has opposite effects on the amplitudes of the limit cycles of both degrees of freedom; by positive detuning a_2 exhibits higher amplitude than a_1, while by negative detuning the opposite occurs.

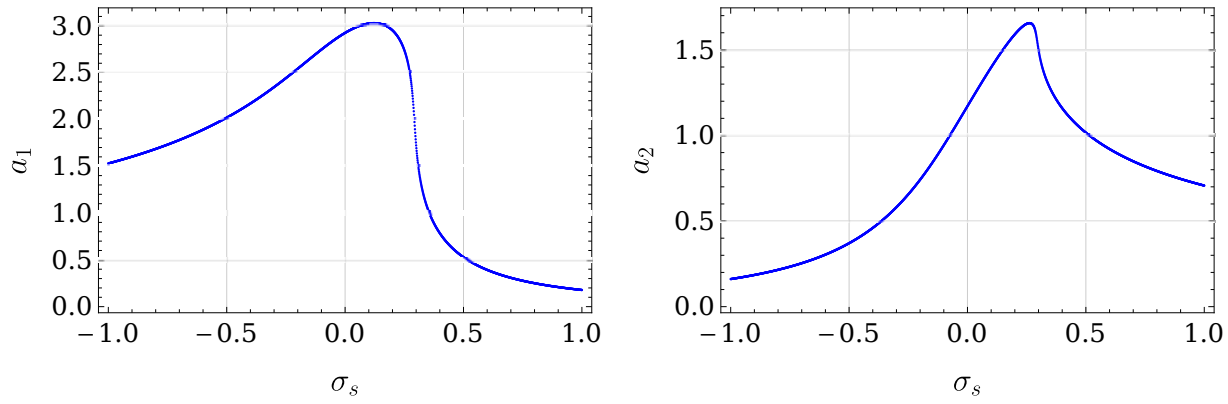

(a) a_1 (b) a_2

Figure 3.17: Nontrivial solutions for a_1 and a_2 by detuning σ_s about the summation frequency, when $\omega_1 = 1, \omega_2 = \sqrt{5}, \gamma_i = 0.07, \alpha_i = 0.03, \eta_{ij} = 1,\ i, j = 1, 2$ and $\zeta = -\pi/2$

Difference parametric resonance

The perturbation analysis is carried out for the difference parametric resonance case, where the parametric excitation frequency is in the neighborhood of the difference frequency or $\Omega_p \simeq |\omega_2 - \omega_1|$. In this case the parametric excitation frequency is detuned through

$$\Omega_p = \epsilon\sigma_d + (\omega_2 - \omega_1), \tag{3.90}$$

where σ_d is the detuning parameter, and ω_2 is assumed to be larger than ω_1 without loss of generality. By inserting this condition again into (3.60) the solvability conditions become

$$i2\omega_1 D_1 A_1 + i\mu_1\omega_1 A_1 + 3\gamma_1 A_1^2\bar{A}_1 + i3\alpha_1\omega_1^3 A_1^2\bar{A}_1 + \frac{1}{2}\eta_{12}A_2 e^{-i\sigma_d T_1} = 0, \tag{3.91a}$$

$$i2\omega_2 D_1 A_2 + i\mu_2\omega_2 A_2 + 3\gamma_2 A_2^2\bar{A}_2 + i3\alpha_2\omega_2^3 A_2^2\bar{A}_2 + \frac{1}{2}\eta_{21}A_1 e^{i(\sigma_d T_1+\zeta)} = 0. \tag{3.91b}$$

Before indulging into the procedure of finding the nontrivial solutions, we can observe the differences in the solvability conditions between summation and difference resonances. By comparing (3.91) and (3.83), we can obviously see that all terms are the same in both equations except for the coupling term in each equation, which causes a vast difference in the end results.

Following the same procedure as before, the modulation equations are found to be

$$D_1 a_1 = -\frac{1}{2}\mu_1 a_1 - \frac{3}{8}\alpha_1\omega_1^2 a_1^3 - \frac{1}{4\omega_1}\eta_{12}a_2\sin(\theta_1) \tag{3.92a}$$

$$D_1 a_2 = -\frac{1}{2}\mu_2 a_2 - \frac{3}{8}\alpha_2\omega_2^2 a_2^3 + \frac{1}{4\omega_2}\eta_{21}a_1\sin(\theta_1)\cos(\zeta) - \frac{1}{4\omega_2}\eta_{21}a_1\cos(\theta_1)\sin(\zeta) \tag{3.92b}$$

$$D_1\theta_1 = -\sigma_d - \frac{3\gamma_1 a_1^2}{8\omega_1} + \frac{3\gamma_2 a_2^2}{8\omega_2} + \frac{1}{4\omega_2}\eta_{21}\frac{a_1}{a_2}\cos(\theta_1)\cos(\zeta) + \frac{1}{4\omega_2}\eta_{21}\frac{a_1}{a_2}\sin(\theta_1)\sin(\zeta) - \frac{1}{4\omega_1}\eta_{12}\frac{a_2}{a_1}\cos(\theta_1), \tag{3.92c}$$

$$D_1\theta_2 = \frac{3\gamma_2 a_2^2}{8\omega_2} + \frac{1}{4\omega_2}\eta_{21}\frac{a_1}{a_2}\cos(\theta_1)\cos(\zeta) + \frac{1}{4\omega_2}\eta_{21}\frac{a_1}{a_2}\sin(\theta_1)\sin(\zeta), \tag{3.92d}$$

where in this case we put $\theta_1 = (\phi_2 - \phi_1) - T_1\sigma_d$ and $\theta_2 = \phi_2$. The modulation equations are then separated into real and imaginary parts, and solved to obtain the steady-state solutions when $D_1\theta_1 = 0, D_1\theta_2 = 0, D_1 a_1 = 0$ and $D_1 a_2 = 0$. The resulting equations are again given in two cases. Thus for the synchronous excitation case $\zeta = 0$, they yield

$$-\frac{1}{2}\mu_1 a_1 - \frac{3}{8}\alpha_1\omega_1^2 a_1^3 - \frac{1}{4\omega_1}\eta_{12}a_2\sin(\theta_1) = 0 \tag{3.93a}$$

$$-\frac{1}{2}\mu_2 a_2 - \frac{3}{8}\alpha_2\omega_2^2 a_2^3 + \frac{1}{4\omega_2}\eta_{21}a_1\sin(\theta_1) = 0 \tag{3.93b}$$

$$-\sigma_d - \frac{3\gamma_1 a_1^2}{8\omega_1} + \frac{3\gamma_2 a_2^2}{8\omega_2} + \frac{1}{4\omega_2}\eta_{21}\frac{a_1}{a_2}\cos(\theta_1) - \frac{1}{4\omega_1}\eta_{12}\frac{a_2}{a_1}\cos(\theta_1) = 0, \tag{3.93c}$$

while if the parametric excitation is asynchronous, i.e. $\zeta = -\pi/2$, this gives

$$-\frac{1}{2}\mu_1 a_1 - \frac{3}{8}\alpha_1\omega_1^2 a_1^3 - \frac{1}{4\omega_1}\eta_{12}a_2\sin(\theta_1) = 0 \tag{3.94a}$$

$$-\frac{1}{2}\mu_2 a_2 - \frac{3}{8}\alpha_2\omega_2^2 a_2^3 + \frac{1}{4\omega_2}\eta_{21}a_1\cos(\theta_1) = 0 \tag{3.94b}$$

$$-\sigma_d - \frac{3\gamma_1 a_1^2}{8\omega_1} + \frac{3\gamma_2 a_2^2}{8\omega_2} - \frac{1}{4\omega_2}\eta_{21}\frac{a_1}{a_2}\cos(\theta_1) - \frac{1}{4\omega_1}\eta_{12}\frac{a_2}{a_1}\cos(\theta_1) = 0, \tag{3.94c}$$

By solving the equations in the synchronous excitation case, an interesting result is observed: nontrivial solutions do not exist. This comes inline with our stability analysis of the trivial solution, where no resonance was found at the difference combination frequency, instead an anti-resonance could be detected. According to this observation, a correspondence between the stability of the trivial solution and the existence of the nontrivial ones can be proposed.

By solving the equations (3.94) the nontrivial solutions (limit cycles) are calculated, their stability is investigated and plotted in Fig. 3.18. The resonance curves are shown to be significantly similar and mirrored around the zero detuning parameter when compared to those calculated around the summation resonance. This result should be related to the difference in the solvability conditions (3.83) and (3.91) where the excitation terms in each case are found to be the complex conjugate of the corresponding ones in the other case.

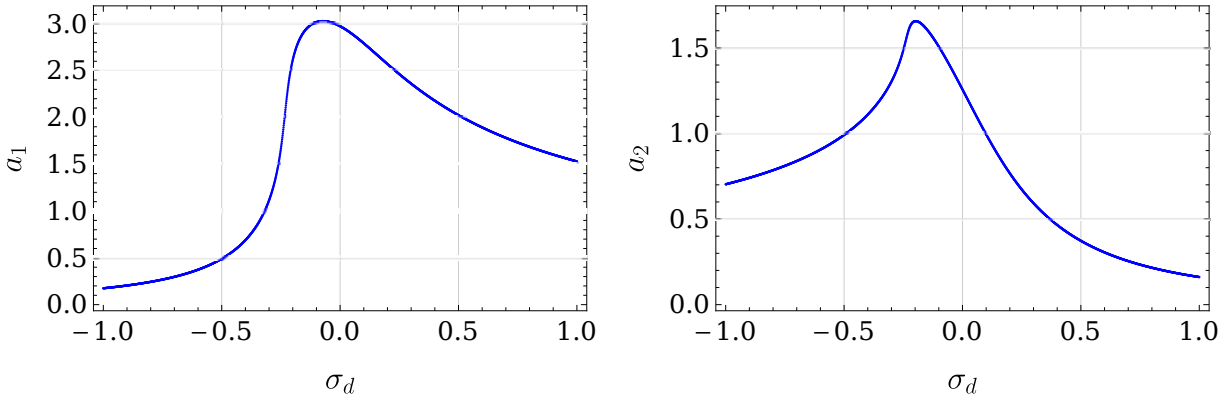

(a) a_1 (b) a_2

Figure 3.18: Nontrivial solutions for a_1 and a_2 by detuning σ_d about the difference frequency, when $\omega_1 = 1, \omega_2 = \sqrt{5}, \gamma_i = 0.07, \alpha_i = 0.03, \eta_{ij} = 1,\ i, j = 1, 2$ and $\zeta = -\pi/2$.

3.3 Conclusion

Through the presented work in this chapter several observations could be summarized. Firstly, the broadband destabilization effect was proved numerically and analytically for linear systems with asynchronous coupling parametric excitation. This effect can be obviously seen in the stability chart in Fig. 3.3. The shape of the instability region in this chart will be observed repeatedly in the next chapters, where the asynchronous excitation is applied on different examples. Accordingly, the topology shown in Fig. 3.3 can be considered typical for this type of excitation.

Secondly, a direct correspondence between the destabilization of the trivial solution and the amplification of the response could be elaborated analytically for linear systems which is a non-resonant parametric amplification in this case. This was explained in the vicinity of the border of instability, which confirms the experimental observations reported in numerous previous works. This relies on the fact that the maximum real part of the system's eigenvalues approach zero, thereby, causing the transient homogeneous solution to be nearly steady. In this way, the initial conditions of the homogeneous solution will be perturbed by higher order corrections deduced according to the multiple scales method. But since these correction terms are influenced by the broadband destabilization effect, therefore, this could be transferred to the main solution to the first order of approximation. This could be verified numerically as well using direct numerical integration of the original system.

Thirdly, nonlinear time-periodic systems exhibit several types of instability. Destabilization in these systems occurs due to different reasons. Resonances and transfer of energy between coupled degrees of freedom contribute to this destabilization, moreover, the addition of a

phase-shift between the coupling parametric excitation terms changes the nontrivial solutions. Through the variation of the linear damping coefficient at the primary parametric resonance, the nontrivial solutions seemed to be limited in domain, but more interestingly it could cause isolated steady-state solutions as well when the excitation frequency is correctly adjusted in a region of multiple limit cycles. In addition, the case of internal resonance shows an influence of each excitation term. Even when the intrinsic excitation terms (diagonal terms in the parametric excitation matrix) are turned off, the coupling excitation terms could cause a cross excitation in both degrees of freedom. At combination resonances, the nontrivial steady-state solutions were obtained, where the asynchronous excitation is shown to have a major effect. In particular, the inclusion of the phase shift between the off-diagonal parametric excitation terms leads to the occurrence of parametric resonance and existence of limit cycles at the difference combination frequency. In addition, the stable and unstable limit cycles existing in the vicinity of the summation combination frequency under synchronous parametric excitation change into only stable ones under asynchronous excitation.

In conclusion, all these observations in addition to those obtained for time-invariant systems form a theoretical background about the behavior of dynamical systems when subjected to different sources of destabilization. In time-invariant systems it was shown that the introduction of asymmetry in the stiffness matrix due to circulatory forces could lead to instability. This happens as well in time-periodic systems, since the inclusion of a phase-shift between the off-diagonal terms introduces an asymmetry to the parametric excitation matrix. Through asynchronous parametric excitation, it is shown in this chapter that the trivial solution could be destabilized at a broad band of frequencies. Moreover, this is linked to a broadband parametric amplification through an analytical study. In addition, this asynchronicity showed an important effect on the nontrivial steady-state solutions at combination resonance frequencies.

All these observations show the significance of the discussed methods of excitation in dynamical systems especially for those of high natural frequencies as discussed in section 3.1.5, which is a characteristic of micro and nanosystems. In the next two chapters, micro-ring gyroscopes are modeled and their dynamical behavior under asynchronous bimodal parametric excitation is studied, where the previous theoretical observations were found significantly beneficial. Moreover, the same excitation method is realized afterwards experimentally and presented in chapter 6.

4 Micro-ring gyroscopes: a linear model

In this chapter, we start applying the discussed theoretical results in the previous chapters on a microsystem, namely, the micro-ring gyroscope. The gyroscope is modeled both linearly and nonlinearly, the first case is presented in this chapter, while the next chapter is concerned with the nonlinear model. Micro-ring gyroscopes are found to be an appropriate application for the theoretical study previously discussed. This is related to being experimented under parametric pumping in various previous works, as well as having an axis-symmetrical geometry that emphasizes the broadband destabilization effect.

After introducing the principles of vibrating structure gyroscopes, a mechanical analysis of the micro-ring gyroscope using Hamilton's principle is first given. Then the system is discretized using Galerkin's method, and the electrostatic excitation terms are derived theoretically. We propose an electronic circuit for implementing the phase-shifted coupling of the bimodal parametric excitation. The two-degree of freedom system is then numerically analyzed using Floquet's method, and the broadband amplification effect is discussed. The normal form method is used to obtain a semi-analytical solution in order to give more insight into the dynamical behavior. Finally the proposed method of excitation is applied on a typical micro-ring gyroscope presented before in the literature, which was experimentally investigated. At the end, we show how this excitation method can be advantageous to the micro-sensors technology.

4.1 Vibrating structure gyroscopes

Vibrating structure gyroscopes are inertial sensors to measure the angular rate. They share the name gyroscope with gimbal-gyroscopes, not because of the existence of gyroscopic coupling, which exists only in a three dimensional system, but since they induce gyroscopic terms in the system. Moreover, they are used, like gimbal gyroscopes in measuring the angular rate and orientation of their reference frame. In order to explain this, consider a two-degree-of-freedom system shown in Fig. 4.1. If the rotation rate $\Omega = 0$, both degrees of freedom are uncoupled. That means, if the first degree of freedom is excited by a force F_a, the other degree

of freedom stays unmoved. The coupling occurs only when the frame rotates. In this case the two-degree-of-freedom model with respect to the rotating frame takes the form

$$\begin{aligned} m\ddot{x} + c_x\dot{x} + k_x x &= F_a + 2m\Omega_z\dot{y}, \\ m\ddot{y} + c_y\dot{y} + k_y y &= -2m\Omega_z\dot{x}, \end{aligned} \tag{4.1}$$

where m is the mass of the lumped mass vibrating in two orthogonal directions x, y, while $c_{x,y}, k_{x,y}$ are the damping and stiffness coefficients respectively. Only the first degree of freedom is excited by F_a. The two equations are coupled due to *Coriolis* forces which are inertial forces initiated with respect to the rotating frame, and energy is transferred from the first degree of freedom to the second one. Since the Coriolis force is the only force acting on the second degree of freedom, then, the amplitude y could be easily correlated to it, and therefore correlated to the rotation rate Ω_z. Through this correlation the rotation rate can be evaluated.

Commercially this type of vibrating gyroscopes, using a lumped mass, is the common type of micro-gyroscopes typically used in mobile phones. However, other more expensive types do exist, which are used in more sophisticated applications for navigation due to their higher sensitivity and reliability such as micro-ring gyroscopes [111]. In this thesis, the micro-ring gyroscope is studied, which is based on an elastic ring vibrating only in-plane.

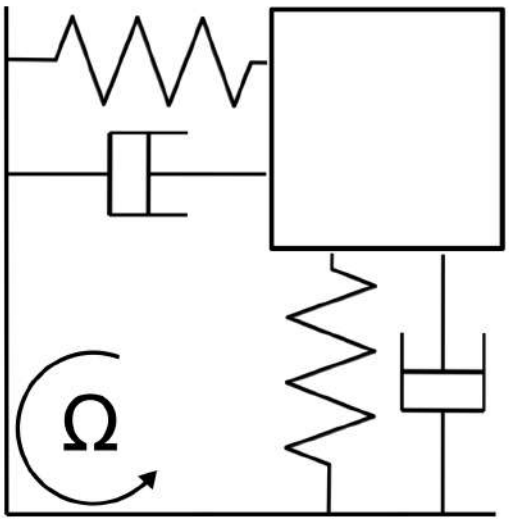

Figure 4.1: Principle of a vibratory structure gyroscope

4.2 Parametric in-plane vibrations in thin elastic inextensible rings

We start the analysis with the basic theoretical development of the micro-ring structure and the effect of parametric and forced excitations on its vibrations. Next, we shift the attention to the micro-ring gyroscopes. Through this approach we seek to develop a generic theoretical framework for parametrically excited micro-ring gyroscopes, while preserving two things; firstly, not referring the reader to external literature in the theory of elasticity or the theory of vibrations, and secondly, not relying on ad-hoc physical assumptions, in order to have a model for micro-ring gyroscopes strictly based on a mathematical derivation.

4.2.1 Determination of the free ring's natural frequencies

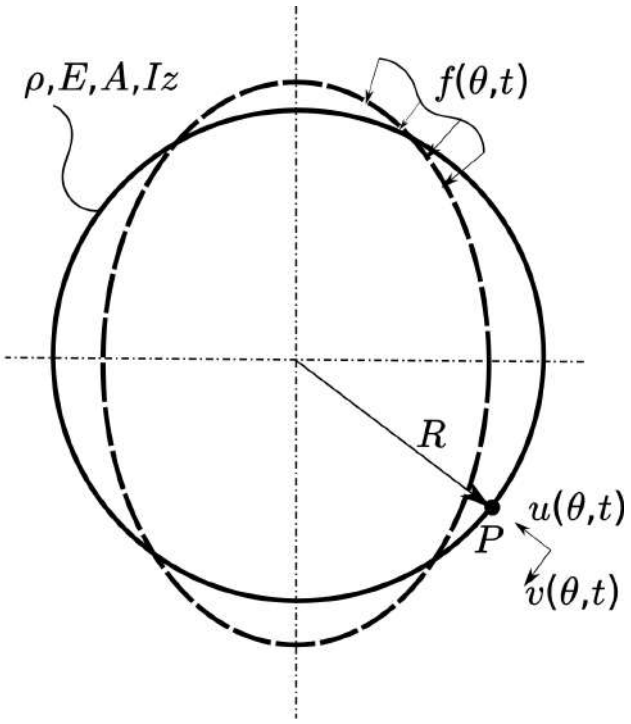

Figure 4.2: Ring in-plane deformation

Beginning with the theory of thin elastic rings, the in-plane vibrations of an elastic ring are illustrated in Fig 4.2. Every infinitesimal element has two degrees of freedom in the plane of vibration. Their displacements are described in local polar coordinates through the variables $u(t,\theta)$ and $v(t,\theta)$. The ring is first analyzed with a given generic external force acting in the radial direction.

A generic equation of motion will be sought for the shown system, which provides the base for all following analyses. The system is investigated through Hamilton's principle leading to the ring's partial differential equation (PDE) and its solution.

The kinetic energy for the ring is

$$T = \frac{1}{2}\rho A R \int_0^{2\pi} \langle \boldsymbol{v}, \boldsymbol{v} \rangle \, d\theta, \tag{4.2}$$

where $\boldsymbol{v} = [\dot{u}, \dot{v}]$ represents the velocity of each infinitesimal element, A is the cross sectional area, R the radius of the ring centerline and ρ the ring's uniform density. Regarding the strain energy, it is assumed that the ring is elastic and that Hook's law applies, which means $\sigma = E\epsilon$, where σ is the stress at a point, ϵ the strain and E Young's modulus for an isotropic material. Therefore the elastic energy is

$$U = \frac{ER}{2} \int_0^{2\pi} \int_A \epsilon^2 \, dA \, d\theta. \tag{4.3}$$

Here ϵ represents the normal (longitudinal) strain along the ring centerline, which can be calculated, for small strains, from the relation

$$\epsilon = \frac{1}{R}[-u + \frac{\partial v}{\partial \theta} - \frac{x}{R}\frac{\partial}{\partial \theta}(v + \frac{\partial u}{\partial \theta})], \tag{4.4}$$

where x represents the distance of a typical element of the ring from the centroidal axis [112]. The last equation follows the *Bernoulli-Euler hypothesis* [113], in which the straight lines (or the plane) perpendicular to the tangent to the ring centerline remain straight and perpendicular to its tangent line after deformation. A last assumption in this hypothesis is the inextensionality of the centerline, which means that $\epsilon = 0$ at $x = 0$, this gives

$$u = \frac{\partial v}{\partial \theta}, \tag{4.5}$$

which eliminates the first two terms in the strain expression, which represent the extensional strain in the ring.

By inserting (4.4) with (4.5) in (4.3), we obtain

$$U = \frac{EI_z}{2R^3} \int_0^{2\pi} (u + \frac{\partial^2 u}{\partial \theta^2})^2 d\theta, \tag{4.6}$$

which represents the strain energy due to in-plain bending.

Finally, the work done by two orthogonal external distributed forces $f_u(\theta,t), f_v(\theta,t)$, i.e. in both u and v coordinates, is expressed as

$$W_{nc} = \int_0^{2\pi} \left[R f_u(\theta,t) u + R f_v(\theta,t) v \right] d\theta, \tag{4.7}$$

where f_u and f_v are the forces per unit length. The variation of the kinetic energy is

$$\delta T = \rho A R \int_0^{2\pi} \frac{\partial^2}{\partial t^2} \left(\frac{\partial^2 v}{\partial \theta^2} - v \right) \delta v d\theta, \tag{4.8}$$

while that of potential energy is

$$\delta U = -\frac{EI}{R^3} \int_0^{2\pi} \left(\frac{\partial^2 v}{\partial \theta^2} + 2\frac{\partial^4 v}{\partial \theta^4} + \frac{\partial^6 v}{\partial \theta^6} \right) \delta v \, d\theta, \tag{4.9}$$

and for the work done by the external force the variation will be

$$\delta W_{nc} = R \int_0^{2\pi} \left[f_v - \frac{\partial f_u}{\partial \theta} \right] \delta v \, d\theta. \tag{4.10}$$

Inserting all terms in Hamilton's principle

$$\int_{t_1}^{t_2} \left(\delta T - \delta U + \delta W_{nc} \right) dt = 0 \tag{4.11}$$

yields the well known equation of motion for a free undamped elastic inextensible thin ring [114, 112]

$$\frac{EI}{\rho A R^4} \left(\frac{\partial^2 v}{\partial \theta^2} + 2\frac{\partial^4 v}{\partial \theta^4} + \frac{\partial^6 v}{\partial \theta^6} \right) + \frac{\partial^2}{\partial t^2} \left(\frac{\partial^2 v}{\partial \theta^2} - v \right) + \frac{1}{\rho A} \left[f_v - \frac{\partial f_u}{\partial \theta} \right] = 0, \tag{4.12}$$

with

$$v(0,t) = v(0+2\pi,t). \tag{4.13}$$

As a first step, we solve this partial differential equation (PDE) for $f(\theta,t) = 0$ (or $f_v, f_u = 0$), in order to get the system natural frequencies and vibration modes.

We first look for the solutions of the type

$$v(\theta,t) = V(\theta) q(t). \tag{4.14}$$

By substituting into (4.12), and separating the temporal and spatial variables we get

$$\frac{d^2V(\theta)}{d\theta^2} + 2\frac{d^4V(\theta)}{d\theta^4} + \frac{d^6V(\theta)}{d\theta^6} - \frac{\omega^2\rho AR^4}{EI}\left[\frac{d^2V(\theta)}{d\theta^2} - V(\theta)\right] = 0, \tag{4.15}$$

$$V^{(n)}(0,t) = V^{(n)}(2\pi,t), \quad n = 0,1,2,3, \tag{4.16}$$

and

$$\ddot{q}(t) + \omega^2 q(t) = 0. \tag{4.17}$$

The eigenfunctions of (4.15) along with (4.16) are obviously $\sin(n\theta)$ and $\cos(n\theta)$, $n\epsilon\mathbb{N}$. Substituting them into (4.15) gives the corresponding eigenvalues

$$\omega_n^2 = \frac{EIn^2(n^2-1)^2}{AR^4\rho(n^2+1)}. \tag{4.18}$$

where $n = 0$ and $n = 1$ correspond to the ring's rotational and translational rigid body modes respectively.

A general solution for the tangential displacement is therefore given by

$$v(\theta,t) = (K + Lt) + \sum_{\infty}^{n=1} \left(A_n \sin(\omega_n t) + B_n \cos(\omega_n t)\right)\left(S_n \sin(n\theta) + C_n \cos(n\theta)\right). \tag{4.19}$$

4.3 Forced and parametric excitation

So far a general solution for the partial differential equation of the inextensible ring was found, but the main aim is to model the micro-ring gyroscope. To this end we assume that the whole system of the ring and its supports rotate at a given constant but small speed of rotation with respect to an inertial reference frame.

For this sake, we add a constant speed rotation of the ring reference frame which will alter the kinetic energy expression as follows. Returning to (4.2), we define now the tangential displacement in the non-inertial rotating frame to be

$$\boldsymbol{v} = [\dot{u},\dot{v}]^T + \boldsymbol{\Omega} \times [u,v]^T, \tag{4.20}$$

where $\boldsymbol{\Omega} = \Omega_z \hat{\boldsymbol{e}}_{\boldsymbol{z}}$ represents the rate of rotation of the ring body fixed frame around the axis

$\hat{e}_z$ normal to the ring plane. In this case the kinetic energy is

$$T = \frac{1}{2}\pi\rho AR\int_0^{2\pi}\left[\dot{u}^2+\dot{v}^2+\Omega_z^2(u^2+v^2)+2\Omega_z(u\dot{v}-\dot{u}v)\right]d\theta. \tag{4.21}$$

Using the expressions of potential energy and external work done as previously stated in (4.6) and (4.7), Hamilton's principle gives

$$\int_{t_1}^{t_2}\int_0^{2\pi}\left[\frac{EI}{R^3}\left(\frac{\partial^2 v}{\partial\theta^2}+2\frac{\partial^4 v}{\partial\theta^4}+\frac{\partial^6 v}{\partial\theta^6}\right)+\rho AR\left(\frac{\partial^2}{\partial t^2}\left(\frac{\partial^2 v}{\partial\theta^2}-v\right)-\Omega_z^2\left(\frac{\partial^2 v}{\partial\theta^2}-v\right)-4\Omega_z\frac{\partial^2 v}{d\theta dt}\right)+R\left(f_v-\frac{\partial f_u}{\partial\theta}\right)\right]\delta v\,d\theta dt=0, \tag{4.22}$$

with the essential boundary condition $v^{(n)}(0,t)=v^{(n)}(2\pi,t)$.

This leads to the partial differential equation of this system

$$\frac{EI}{\rho AR^4}\left(\frac{\partial^2 v}{\partial\theta^2}+2\frac{\partial^4 v}{\partial\theta^4}+\frac{\partial^6 v}{\partial\theta^6}\right)+\left(\frac{\partial^2}{\partial t^2}\left(\frac{\partial^2 v}{\partial\theta^2}-v\right)-\Omega_z^2\left(\frac{\partial^2 v}{\partial\theta^2}-v\right)-4\Omega_z\frac{\partial^2 v}{d\theta dt}\right)+\frac{1}{\rho A}\left(f_v-\frac{\partial f_u}{\partial\theta}\right)=0. \tag{4.23}$$

Here f_u and f_v represent the external distributed (per unit length) load in radial and tangential directions respectively. These loads can be thought of as being a forced excitation, parametric excitation, damping or external support. In this case we will be interested in obtaining the differential equation for an excited rotating ring gyroscope with elastic support. Therefore, we will assume having a radial parametric force as well as a forced excitation force

$$f_{u1}=F_{ex}(\theta,t)+F_p(\theta,t)\,u=F_{ex}(\theta,t)+F_p(\theta,t)\,\frac{\partial v}{\partial\theta}, \tag{4.24}$$

as well as an elastic support in both radial and tangential directions

$$f_{u2}=-k_u u,\quad f_{v2}=-k_v v. \tag{4.25}$$

This leads to the PDE for a parametrically and externally excited elastic inextensible ring elastically supported with respect to a constant-speed rotating frame in the form

$$\frac{EI}{\rho A R^4}\left(\frac{\partial^2 v}{\partial\theta^2}+2\frac{\partial^4 v}{\partial\theta^4}+\frac{\partial^6 v}{\partial\theta^6}\right)+\left(\frac{\partial^2}{\partial t^2}\left(\frac{\partial^2 v}{\partial\theta^2}-v\right)-\Omega_z^2\left(\frac{\partial^2 v}{\partial\theta^2}-v\right)-4\Omega_z\frac{\partial^2 v}{d\theta dt}\right)$$
$$+\frac{1}{\rho A}\left((k_u-F_p)\frac{\partial^2 v}{\partial\theta^2}-\frac{\partial F_p}{\partial\theta}\frac{\partial v}{\partial\theta}-k_v v\right)=\frac{1}{\rho A}\frac{\partial F_{ex}}{\partial\theta}. \quad (4.26)$$

Galerkin's method is used to discretize the system by the ansatz

$$v(\theta,t)=\langle\mathbf{\Phi}(\theta),\boldsymbol{q}(t)\rangle, \quad (4.27)$$

where

$$\mathbf{\Phi}(\theta)=[\sin(2\theta)\quad\cos(2\theta)\quad\sin(3\theta)\quad\cos(3\theta)\ ...], \quad (4.28)$$

and

$$\boldsymbol{q}(t)=[q_1(t)\quad q_2(t)\quad q_3(t)\quad q_4(t)\quad ...], \quad (4.29)$$

where $\mathbf{\Phi}(\theta)$ represents a vector of the system eigenfunctions (mode shapes) starting from the first vibration mode, i.e. when $n=2$ in the general solution (see (4.19)), while $\boldsymbol{q}(t)$ is a vector of the unknown modal coordinates. This can be also represented in the general form

$$v(\theta,t)=\sum_{i=1}^{N}\phi_i(\theta)q_i(t). \quad (4.30)$$

We specify our attention to the case of a discretized two degree of freedom system representing the first two elastic degenerate modes, which are found to be spatially shifted by 45°, this means

$$v(\theta,t)\simeq\sin(2\theta)q_1(t)+\cos(2\theta)q_2(t). \quad (4.31)$$

The external forced and parametric excitations should be assumed in a general form in order to obtain the system's ordinary differential equations (ODEs). Simulating these forces, however, requires taking into consideration that these forces are applied only at the electrodes, therefore they are discontinuous with respect to θ.

This was found to be mathematically complicated if compared to another approach. In the following approximate approach we model the external forces as a power series of the trigonometric shape functions $\Phi(\theta)$ while preserving the angular distribution by choosing the

argument of each function to be 2θ. This leads to

$$F_p = \sum_{k=1}^{\infty} F_{p1-k}(t)\sin^k(2\theta) + F_{p2-k}(t)\cos^k(2\theta), \tag{4.32}$$

while the forced excitation will be represented as

$$F_{ex} = \sum_{k=1}^{\infty} -F_{e1-k}(t)\cos^k(2\theta) + F_{p2-k}(t)\sin^k(2\theta). \tag{4.33}$$

Inserting (4.30) into (4.26) leads to

$$\begin{aligned}
&\sum_{i=1}^{N}\left[-\left(\phi_i'' - \phi_i\right)\right]\ddot{q}_i + \sum_{i=1}^{N}\left[4\Omega_z\phi_i'\right]\dot{q}_i + \sum_{i=1}^{N}\left[\frac{1}{\rho A}F_p\phi_i''\right]q_i + \sum_{i=1}^{N}\left[\frac{1}{\rho A}F_p'\phi_i'\right]q_i \\
&+ \sum_{i=1}^{N}\left[-\frac{EI}{\rho A R^4}\left(\phi_i'' + 2\phi_i^{IV} + \phi_i^{VI}\right) + \Omega_z^2\left(\phi_i'' - \phi_i\right) - \frac{1}{\rho A}\left(k_u\phi_i'' - k_v v\phi_i\right)\right]q_i = \frac{1}{\rho A}F_{ex}'.
\end{aligned} \tag{4.34}$$

(4.34) is then multiplied by any of the base functions ϕ_j and integrated over the domain to give N equations ϕ_i ($i = 1, 2, ...N$)

$$\begin{aligned}
&\sum_{i=1}^{N}\left[-\int_0^{2\pi}\left(\phi_i'' - \phi_i\right)\phi_j d\theta\right]\ddot{q}_i + \sum_{i=1}^{N}\left[\int_0^{2\pi} 4\Omega_z\phi_i'\phi_j d\theta\right]\dot{q}_i \\
&+ \sum_{i=1}^{N}\left[\int_0^{2\pi}\frac{1}{\rho A}F_p\phi_i''\phi_j d\theta\right]q_i + \sum_{i=1}^{N}\left[\int_0^{2\pi}\frac{1}{\rho A}F_p'\phi_i'\phi_j d\theta\right]q_i \\
&+ \sum_{i=1}^{N}\left[\int_0^{2\pi} -\frac{EI}{\rho A R^4}\left(\phi_i'' + 2\phi_i^{IV} + \phi_i^{VI}\right)\phi_j + \Omega_z^2\left(\phi_i'' - \phi_i\right)\phi_j - \frac{1}{\rho A}\left(k_u\phi_i'' - k_v v\phi_i\right)\phi_j d\theta\right]q_i \\
&= \left[\int_0^{2\pi}\frac{1}{\rho A}F_{ex}'\phi_j d\theta\right].
\end{aligned} \tag{4.35}$$

Then (4.31), (4.32) and (4.33) are inserted to get the final discretized system. We found that, using (4.32) and (4.33) results in non vanishing terms for the components with even powers $k \in 2, 4, 6, ...$ in case of the parametric forces, while only the odd powers $k \in 1, 3, 5, ...$ remain in case of the forced excitation forces. For the case of $k \to \infty$, angular distributed point

forces are simulated. Applying that, we get

$$\sum_{i}^{2} m_{ij}\ddot{q}_i + \sum_{i}^{2} g_{ij}\dot{q}_i + \sum_{i}^{2} \kappa_{ij} q_i + \sum_{i}^{2} c_{ij}(t) q_i = f_j(\theta, t), \tag{4.36}$$

or in matrix form

$$\boldsymbol{M}\ddot{\boldsymbol{q}} + \boldsymbol{G}\dot{\boldsymbol{q}} + \boldsymbol{K}\boldsymbol{q} + \boldsymbol{C}(t)\boldsymbol{q} = \boldsymbol{f}. \tag{4.37}$$

where

$$\boldsymbol{M} = \begin{bmatrix} 1 & 0 \\ 0 & 1 \end{bmatrix}, \qquad \boldsymbol{G} = \frac{8}{5}\Omega \begin{bmatrix} 0 & 1 \\ -1 & 0 \end{bmatrix}, \qquad \boldsymbol{f} = \frac{1}{2\rho A} \begin{bmatrix} F_{e1}(t) \\ F_{e2}(t) \end{bmatrix}.$$

$$\boldsymbol{K} = \left(\frac{36EI}{5\rho A R^4} - \Omega^2 + \frac{1}{5\rho A}\left[4k_u + k_v\right] \right) \begin{bmatrix} 1 & 0 \\ 0 & 1 \end{bmatrix}, \qquad \boldsymbol{C}(t) = \frac{-2}{5\pi\rho A} \begin{bmatrix} F_{p1}(t) & 0 \\ 0 & F_{p2}(t) \end{bmatrix}$$

Here we showed that a self-excited parametric excitation of each mode is possible by choosing the correct spatial distribution of the electrodes to correspond to the ring anti-nodes. This can be extended by an external control circuit into having a fully populated $\boldsymbol{C}(t)$ matrix, that is, having coupling terms

$$\boldsymbol{C}(t) = \frac{-2}{5\pi\rho A} \begin{bmatrix} F_{p11}(t) & F_{p12}(t) \\ F_{p21}(t) & F_{p22}(t) \end{bmatrix},$$

or in other words a coupled bimodal parametric excitation. However, the implementation of this matrix will be then through an external electronic circuit. This means that without such a circuit, the coupling terms are not feasible under the construction presented in this section in correspondence to Fig. 4.2. Moreover by considering a damping matrix $\boldsymbol{D}$ we arrive at

$$\boldsymbol{M}\ddot{\boldsymbol{q}} + (\boldsymbol{D} + \boldsymbol{G})\,\dot{\boldsymbol{q}} + (\boldsymbol{K} + \boldsymbol{C}(t))\,\boldsymbol{q} = \boldsymbol{f}. \tag{4.38}$$

4.3.1 Determination of the excitation terms

Till now we assumed having a general expression of excitation according to (4.10) and then it was specified by (4.24), but we did not derive yet these expressions (i.e. F_p and F_{ex}) according to the underlying physics.

We start by applying the electrostatic force through any electrode (see Fig. 4.3), and returning to (4.11), the work done is to be considered. For the given case, a micro-ring is assumed to be excited by an electrostatic force through distributed electrodes around the ring. Taking one

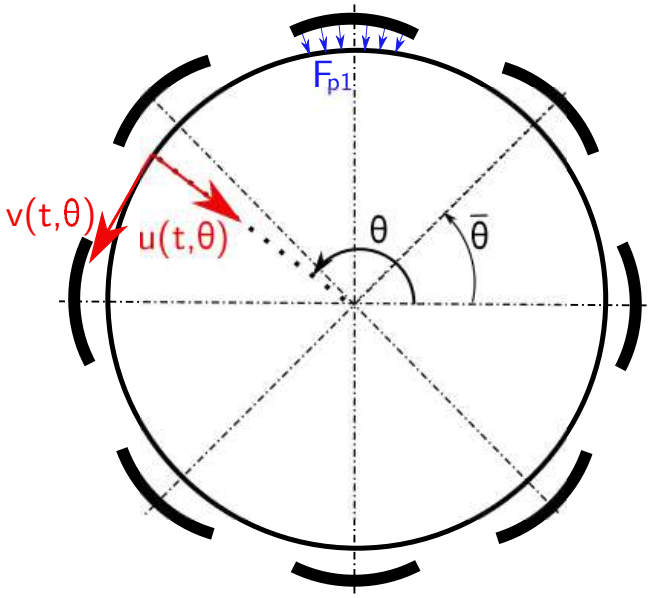

Figure 4.3: Applying electrostatic force F_{p1}

electrode for convenience, The virtual work of the electrostatic force can be then computed as

$$\delta W = \frac{\partial E_e}{\partial u}\delta u(t,\theta), \tag{4.39}$$

where E_e is the electrostatic energy stored between the micro-ring and the electrode.

The electrostatic energy is introduced as

$$E_e = \frac{1}{2}\frac{\epsilon_e A_e}{d}V^2(\theta,t), \tag{4.40}$$

where ϵ_e is the permittivity, A_e is the surface area of the circular segment normal to the electric field, d is the separating distance between the electrode and the ring and V is the applied voltage.

Since an inplane vibration is assumed, the distance d is a function of the radial displacement u, while the surface area A_e is $bRd\theta$. Putting this together gives

$$E_e = \frac{1}{2}\epsilon_e bRV^2(\theta,t)\int_{-\alpha+\bar{\theta}_k}^{\alpha+\bar{\theta}_k}\frac{1}{d}d\theta, \tag{4.41}$$

where b is the ring thickness and $d = d_0 - u$. Without loss of generality, let $F(\theta,t) = \frac{1}{2}\epsilon_e bRV^2(\theta,t)$. Expanding $\frac{1}{d} = \frac{1}{d_0-u}$ with respect to u up to the second order in u leads to

$$E_e = \frac{F(\theta,t)}{d_0}\int_{-\alpha+\bar{\theta}_k}^{\alpha+\bar{\theta}_k}\left[1+\frac{u}{d_0}+\frac{u^2}{d_0^2}\right]d\theta. \tag{4.42}$$

According to (4.39), the virtual work done by the electrostatic force is then

$$\delta W = \frac{F(\theta,t)}{d_0^2}\int_{-\alpha+\bar{\theta}_k}^{\alpha+\bar{\theta}_k}\left[1+\frac{2u}{d_0}\right]\delta u d\theta \tag{4.43}$$

Changing the displacement variable from u to v gives

$$\delta W = \int_{-\alpha+\bar{\theta}_k}^{\alpha+\bar{\theta}_k}\left[\frac{F(\theta,t)}{d_0^2}+\frac{2F(\theta,t)}{d_0^3}\frac{\partial v}{\partial\theta}\right]\frac{\partial\delta v}{\partial\theta}d\theta. \tag{4.44}$$

Integrating by parts gives

$$\delta W = \left[\left(\frac{F(\theta,t)}{d_0^2}+\frac{2F(\theta,t)}{d_0^3}\frac{\partial v}{\partial\theta}\right)\delta v\right]_{-\alpha+\bar{\theta}_k}^{\alpha+\bar{\theta}_k} - \int_{-\alpha+\bar{\theta}_k}^{\alpha+\bar{\theta}_k}\left[\frac{1}{d_0^2}\frac{\partial F}{\partial\theta}+\frac{2}{d_0^3}\frac{\partial F}{\partial\theta}\frac{\partial v}{\partial\theta}+\frac{2}{d_0^3}F\frac{\partial^2 v}{\partial\theta^2}\right]\delta v d\theta \tag{4.45}$$

By comparing (4.45) with the partial differential equation of the whole system (4.26) we can now understand the effect of the electrostatic force on the investigated micro-ring. We can see that the integral part of (4.45) comprises three different terms, an external excitation term that does not depend on the displacement

$$R\frac{\partial F_{ex}}{\partial\theta} = \frac{1}{d_0^2}\frac{\partial F}{\partial\theta} = \frac{\epsilon_e bR}{2d_0^2}\frac{\partial V^2(\theta,t)}{\partial\theta},$$

that means the external force symbol in (4.26) is found to be

$$F_{ex}(\theta,t) = \frac{1}{2d_0^2}\epsilon_e bV^2(\theta,t), \tag{4.46}$$

and comparing the other two terms as well gives the parametric force as

$$F_p(\theta,t) = \frac{1}{d_0^3}\epsilon_e bV^2(\theta,t), \tag{4.47}$$

which asserts the observation by Rhoads et al [58] that all micro/nanoresonators with variable gap electrostatic actuators inherently induce parametric excitation.

By comparing the Hamilton's principle (4.22) used for deriving the PDE (4.26) with the expression of the virtual work (4.45), however, another important remark should be added.

In (4.45) the integral operates on a limited domain $[-\alpha+\bar{\theta}_k, +\alpha+\bar{\theta}_k]$, whilst in (4.22) it is on the whole circle. The usual way of handling this is through discretizing the integral, this however would involve a lot of complications. Another solution is introduced in (4.32) and (4.33), whereby the force is distributed but through trigonometric functions which can be treated easily through Galerkin's method. However, these force distributions represent only an approximation for the discontinuously distributed forces for the sake of simplifying the mathematical work and without losing generality as well.

Thus, we can rewrite the discretized system as

$$\boldsymbol{M}\ddot{\boldsymbol{q}} + (\boldsymbol{D}+\boldsymbol{G})\,\dot{\boldsymbol{q}} + (\boldsymbol{K}+\boldsymbol{C}(t))\,\boldsymbol{q} = \boldsymbol{f}. \tag{4.48}$$

where

$$\boldsymbol{M} = \begin{bmatrix} 1 & 0 \\ 0 & 1 \end{bmatrix}, \qquad \boldsymbol{G} = \frac{8}{5}\Omega \begin{bmatrix} 0 & 1 \\ -1 & 0 \end{bmatrix}, \qquad \boldsymbol{f} = \frac{\epsilon b}{2d_0^2\rho A} \begin{bmatrix} V_1^2(\theta,t) \\ V_2^2(\theta,t) \end{bmatrix}.$$

$$\boldsymbol{K} = \left(\frac{36EI}{5\rho A R^4} - \Omega^2 + \frac{1}{5\rho A}\left[4k_u + k_v\right] \right) \begin{bmatrix} 1 & 0 \\ 0 & 1 \end{bmatrix}, \qquad \boldsymbol{C}(t) = \frac{-2\epsilon b}{5\pi d_0^3 \rho A} \begin{bmatrix} V_1^2(\theta,t) & 0 \\ 0 & V_2^2(\theta,t) \end{bmatrix}.$$

4.4 Modal coupling

4.4.1 Motivation

So far we have modeled the micro ring gyroscope as a discrete two-degree of freedom system, but which is subjected to uncoupled parametric excitation, that means, $\boldsymbol{C}(t)$ did not have any off diagonal terms. However, introducing off diagonal terms, hence modal coupling, brings new and different phenomena, which are the main contribution of this work to the field of micro sensors. Through the publications mentioned in the introduction, it was found that "global effects"for the parametric excitation can be found, i.e. not confined to the parametric resonances or anti-resonances [37, 38].

To the best of the authors' knowledge, this was not studied before in the field of micro sensors and transducers. We shall begin by exploring the effect of adding coupling terms in the parametric excitation matrix. In doing so we will use in this section arbitrary values, which do not correspond to gyroscopes, for the sake of illustration. After explaining the phenomena in the next section, a practical example is given.

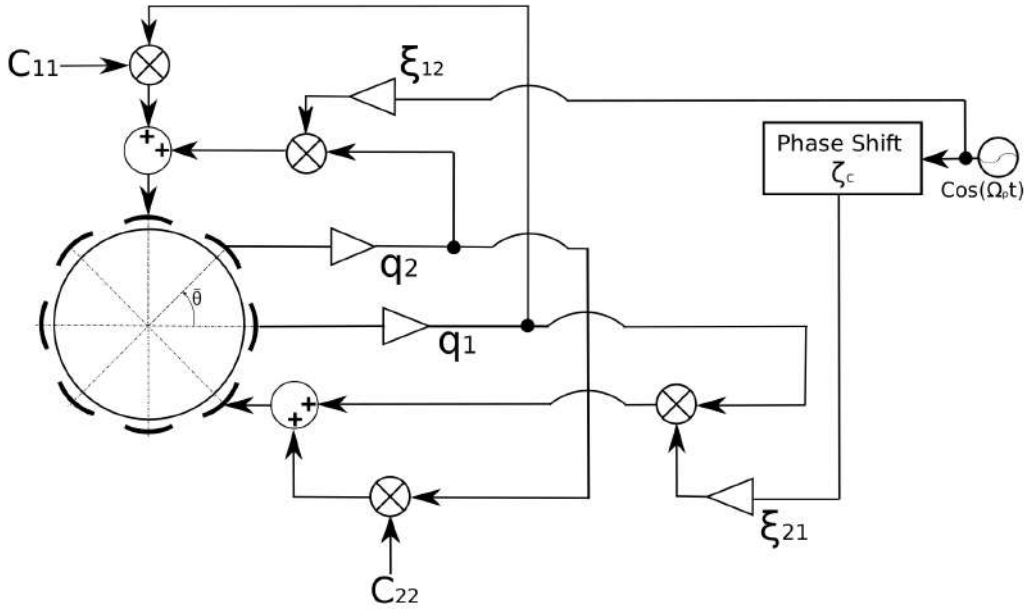

Figure 4.4: A proposed electronic circuit for inducing coupling terms in the parametric excitation matrix. C_{ij} represent the elements of the parametric excitation matrix, while ξ_{ij} represent only the amplitudes of the corresponding terms.

4.4.2 Electronic implementation

The proposed amplification method can be implemented by adding an electronic circuit. As seen from section 4.3.1, the coupling terms are feasible only by introducing an external coupling element. To this end, we propose the electronic circuit shown in Fig. 4.4.

As explained before, the two orthogonal modes of the micro ring are shifted by $\bar{\theta} = 45°$. In Fig. 4.4 eight electrodes are depicted, where each two interact with a vibration mode. For instance, let the antinodes of the first mode be at angles $\bar{\theta} = 0°, 90°, 180°, 270°$, while those for the second mode are shifted by $45°$. Hence, we consider the electrode at $\bar{\theta} = 0°$ as a sense electrode for the first mode, while that for the second mode to be at $\bar{\theta} = 45°$. The remaining two electrodes connected to the circuit represent two of the drive electrodes.

As shown in the figure the displacement signals are acquired through buffer amplifiers [115], then multiplied by a periodic signal $C_{ij} = \xi_{ij}\cos(\Omega_p t + \zeta_{ij})$ before being fed into the corresponding drive electrode. Returning to (4.48), the parametric excitation matrix components for the shown system in Fig. 4.4 will be

$$\boldsymbol{C}(t) = \begin{bmatrix} C_{11}(t) & C_{12}(t) \\ C_{21}(t) & C_{22}(t) \end{bmatrix}. \tag{4.49}$$

Moreover, since we have concluded in section 3.1.3 that the required broadband effect requires a phase shift between C_{12} and C_{21}, applied here as shown in Fig. 4.4 using a phase shifter or an all-pass filter with a phase shift ζ_c between these two input signals.

In this way, the model turns to be exactly the same one presented before in section 3.1.3. Therefore, we use the method discussed there to analyze the stability of the trivial solution. Recalling the results using the normal form method we arrive at the Lyapunov exponents in their simplified form to be

$$\lambda_1 = -\frac{1}{2}\delta_{11} + \left[\frac{\xi^2 \Omega_p \sin(\zeta_{21})}{2\left[\Omega_p^2 - (\omega_1 - \omega_2)^2\right]\left[\Omega_p^2 - (\omega_1 + \omega_2)^2\right]}\right], \tag{4.50a}$$

$$\lambda_2 = -\frac{1}{2}\delta_{22} - \left[\frac{\xi^2 \Omega_p \sin(\zeta_{21})}{2\left[\Omega_p^2 - (\omega_1 - \omega_2)^2\right]\left[\Omega_p^2 - (\omega_1 + \omega_2)^2\right]}\right]. \tag{4.50b}$$

These results prove the possibility of achieving destabilization at parametric non-resonant frequencies. Since the main goal is to have a higher amplification, this correspondence between destabilization of the solution and amplification of response will be elaborated in the following section using data of a realistic micro-ring-gyroscope. However, a mathematical explanation for this correspondence is given before in section 3.1.6.

4.5 Parametric excitation of a realistic micro-gyroscope

Finally, we discuss the dynamic performance of a parametrically excited micro-ring gyroscope using realistic values extracted from [65].

The authors in that paper use a ring of radius 4 mm, width 175 μm and thickness 100 μm. The capacitive gap was measured to be around 6.4 microns and the Q factor of the two vibratory modes is 45000. The system was excited by a voltage about 1 V. The undamped natural frequencies were around 16,500 Hz or 103,672.5 rad/s.

From this data the coefficients of our model were calculated to be

$$\omega_1 = 105\, krad/s, \quad \delta_{11} = 2.5, \quad \gamma = 0.015, \quad \xi = 3.75 \times 10^5.$$

where the remaining parameters are chosen to be

$$\omega_2 = 110\, krad/s, \quad \delta_{22} = 3, \quad \zeta_{21} = -\pi/2.$$

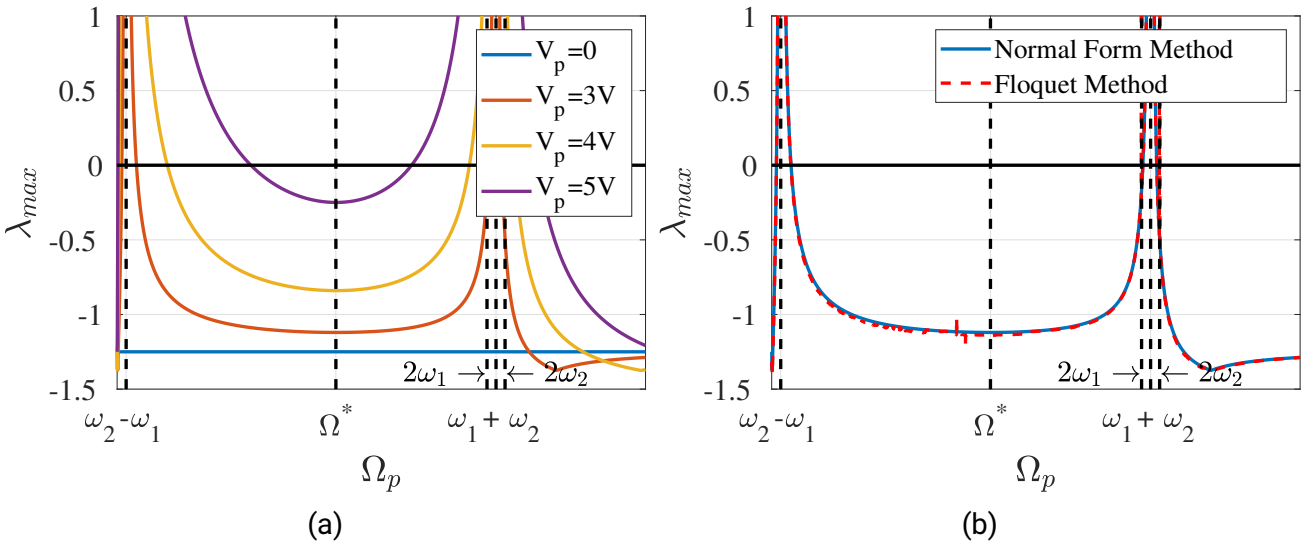

Figure 4.5: (a) Lyapunov exponent against the parametric excitation frequency Ω_p for various excitation amplitudes V_p, (b) Comparing the results between Flocquet method of the untransformed system and the system's normal form at $V_p = 3V$

However, the system described in this paper differs from the one in [65], in that the cited paper did not use a coupled 2 DoF system, but rather only a parametric excitation of a single DoF system. Secondly, and most importantly, in [65] the parametric excitation amplitude was kept at a very low level, so that the parametric amplification could occur only in case of a parametric resonance 2:1. In our case, we tend to have a broader range of amplification at other frequencies using the global effects explained before. This requires the use of a higher value of parametric excitation.

Increasing the parametric excitation amplitude can be obtained practically either through increasing the applied voltage to as high as 10-15 V or by decreasing the capacitance gap from 6 microns to nearly 1 micron, or by tuning both. Choosing a capacitive gap of about 3 microns we get a parametric excitation amplitude of

$$\xi = 3.5 \times 10^6 V_p^2 \tag{4.51}$$

where V_p is the drive voltage amplitude (see (4.47)). The excitation method described in section 4.4.2 is used for the micro ring in order to amplify the gyroscope's forced response.

Fig. 4.5 shows the broadband effects of the parametric excitation on the system's maximum eigenvalue. In case of no coupling in the parametric excitation matrix, i.e. parametrically exciting the two degrees of freedom independently, we do not get any destabilization effect except for the regions of regular parametric resonance, at double the system's undamped

natural frequency. But in our case, after enforcing a coupling parametric excitation between both degrees of freedom, we get the shown effect in a broad range of frequencies. The values of λ^* at Ω^* frequency here represent the analytically calculated local minimum of system's maximum eigenvalue (see Eq. 3.32) at a given voltage, i.e. at a given parametric excitation amplitude. These values were deduced in section 3.1.5 to act as a measure of the system's propensity to destabilization, since they represent the local minimum of Lyapunov exponent in the interval of frequencies exhibiting the broadband destabilization effect.

The figures show clearly how this method of parametric excitation can lead to a destabilization effect in the frequency range $\omega_2 - \omega_1$ to $\omega_2 + \omega_1$ with a minimum at λ^*. This can allow for an obvious advantage for the parametric pumping of the micro gyroscope. That is because the destabilization effect, or the increase of the maximum eigenvalue, leads to a negative damping effect. This is advantageous since damping can not be easily controlled in these systems. But in our case the control of the parametric excitation voltage can allow such an effect.

According to various references [67, 65, 74] the parametric pumping (amplification) of the system forced response is significant before reaching the instability limit, this is especially true when the external force f_1 is phase shifted with $\pi/2$ with respect to the parametric excitation function [67, 76], in our case C_{11}. In order to measure the amplification value, the system response is calculated using direct integration while being parametrically excited at Ω^* and having a forced excitation for the primary mode of vibration $q_1(t)$ at its natural frequency ω_1. Returning to the discretized model of the micro-ring gyroscope (4.48) and by assuming $\delta_{12} = \delta_{21} = 0$, $\zeta_{11} = \zeta_{12} = \zeta_{22} = 0$ and $\xi_{ij} = \xi,\ i, j \in \{1, 2\}$ we get

$$\boldsymbol{M}\ddot{\boldsymbol{q}} + (\boldsymbol{D} + \boldsymbol{G})\,\dot{\boldsymbol{q}} + (\boldsymbol{K} + \boldsymbol{C}(t))\,\boldsymbol{q} = \boldsymbol{f}. \tag{4.52}$$

where

$$\boldsymbol{M} = \begin{bmatrix} 1 & 0 \\ 0 & 1 \end{bmatrix}, \qquad \boldsymbol{D} = \begin{bmatrix} \delta_{11} & 0 \\ 0 & \delta_{22} \end{bmatrix}, \qquad \boldsymbol{G} = \gamma \begin{bmatrix} 0 & 1 \\ -1 & 0 \end{bmatrix}, \qquad \boldsymbol{f} = \begin{bmatrix} f_1 \\ 0 \end{bmatrix}.$$

$$\boldsymbol{K} = \begin{bmatrix} \omega_1^2 & 0 \\ 0 & \omega_2^2 \end{bmatrix}, \qquad \boldsymbol{C}(t) = \xi \begin{bmatrix} \cos(\Omega_p t) & \cos(\Omega_p t) \\ \cos(\Omega_p t + \zeta_{21}) & \cos(\Omega_p t) \end{bmatrix}.$$

The amplitude of the time response (named $\hat{q}_{1amp}$) is then calculated for different values of parametric excitation voltage (see 4.51) and compared to the amplitude of the system's forced

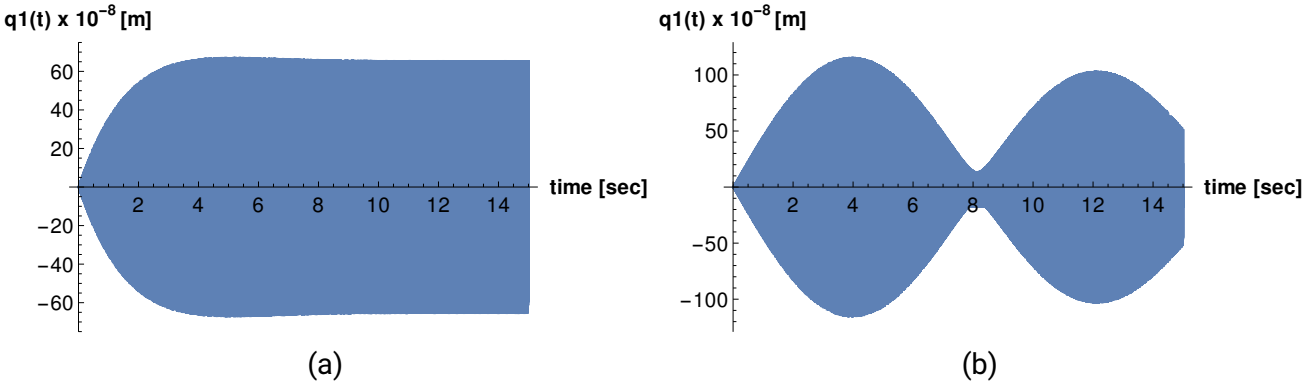

Figure 4.6: Response of the primary mode $q_1(t)$ for the system parameters $\gamma = 0.015, \zeta = -\pi/2, \delta_{11} = 2.5, \delta_{22} = 3, \omega_1 = 105\ krad/s, \omega_2 = 110\ krad/s$ at the external excitation frequency $\Omega_f = \omega_1$ and the parametric excitation frequency $\Omega_p = \Omega^* \simeq 124\ krad/sec$, for two different excitation voltages (a) $V_p = 4.5V$ and (b)$V_p = 5.25V$, where the latter is just below the onset of instability.

response without parametric excitation $\hat{q}_{10}$ through the relation

$$Gain = \frac{\hat{q}_{1amp}}{\hat{q}_{10}}. \tag{4.53}$$

The response $q_1(t)$ of 4.52 is shown in Fig. 4.6 at $\Omega_p = \Omega^*$ and for two different excitation voltages $V_p = 4.5,\ 5.25V$, referring to Fig. 4.5a. It can be seen that the response near the onset of instability shows a *beating phenomenon*, which is exhibited in parametrically excited systems under certain frequency conditions [95]. Moreover, this phenomenon can be also attributed to our analysis in section 3.1.6, since near instability we have two oscillating terms with different frequencies. The amplification through voltage control is depicted in Fig. 4.7, where the last point in the graph represents the last value before the onset of the system's instability. The amplification gain, however, does not show very high values when compared to amplifying the system at the parametric resonance frequencies [67]. But another advantage becomes obvious, that is the possible tuning of parametric excitation frequency across a broad frequency range.

4.6 Conclusion

A new excitation method for micro-ring gyroscopes is introduced for the first time in this chapter. Here we used a previously discussed coupled bimodal excitation scheme, through which a broadband destabilization of the system's trivial solution can be obtained, and therefore, a

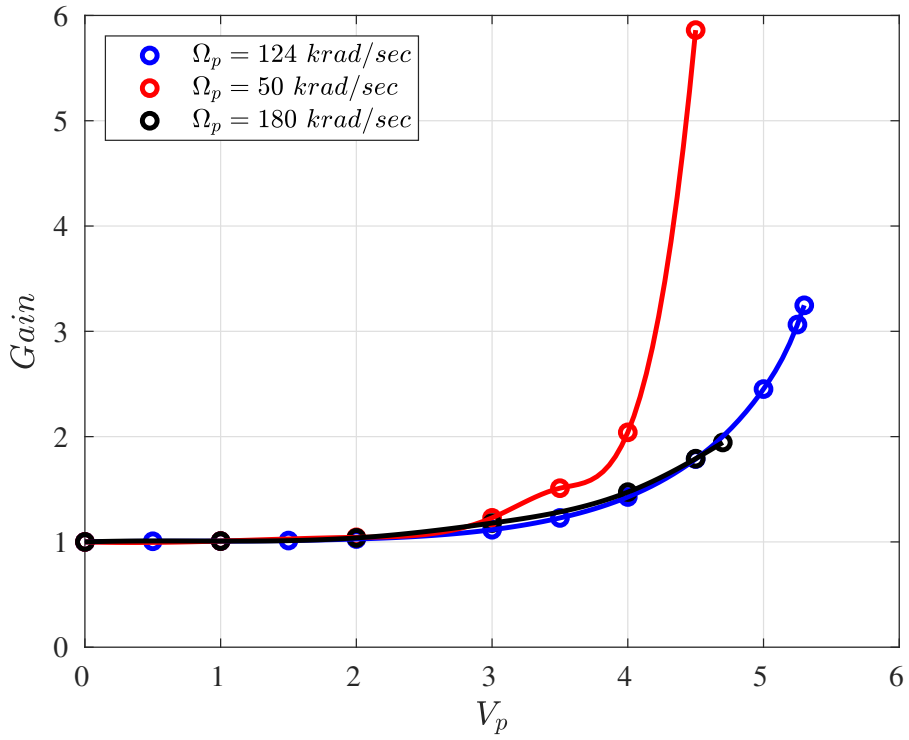

Figure 4.7: Amplification of the primary mode response through increasing the parametric excitation voltage, calculated by direct integration. The system parameters are $\gamma = 0.015, \zeta = -\pi/2, \delta_{11} = 2.5, \delta_{22} = 3, \omega_1 = 105\ krad/s, \omega_2 = 110\ krad/s$. The external excitation is at resonance with ω_1, while the system is parametrically excited at three different frequencies shown in the figure, which all lie within the frequency band $[\omega_2 - \omega_1, \omega_2 + \omega_1]$.

broad band amplification of the drive mode. As shown in section 4.3, parametric self-excitation can only be achieved for the diagonal terms of the parametric excitation matrix, however, using the proposed electronic circuit the coupling terms can be introduced.

As discussed, this was essential in order to obtain the broadband amplification effect. Finally, it was shown using realistic values of a micro-ring gyroscope, that the amplification at *non-resonant* frequencies is practically possible. Since in this way much more flexible conditions can be used to obtain a parametric amplification, we believe, that this new excitation method can add a significant advantage to the parametric excitation methods used in micro gyroscopes and the whole micro sensors technology.

5 Micro-ring gyroscopes: a nonlinear model

In this chapter, the previously presented micro-ring gyroscope is studied again without assuming the linearity of elastic or electrostatic forces. Given the presence of nonlinearities due to elasticity, geometry or electromechanical coupling, the system is analyzed accordingly and Lagrange's equations of motion are deduced. Since the system is now nonlinear, not only the trivial solution is studied, additionally, nontrivial solutions are investigated, and possible bifurcations are considered. This is accomplished first for the autonomous case, where no excitation is involved. Afterwards, a stability analysis of the system's solutions is carried out. As a first attempt, the system is simplified and the resonance curve under only forced excitation is obtained using the method of normal forms. Then, the original nonlinear system is investigated in full after applying the bimodal asynchronous parametric excitation scheme described in the previous chapters. In this case, the dynamics of the system are investigated at the primary resonance frequencies.

5.1 Introduction

The nonlinear behavior is proven to be dominant for the dynamics of most of micro- electromechanical resonators [4, 3]. Micro-gyroscopes are no exception under resonance or instability. This fact becomes of special importance when the system is parametrically excited [67]. At the frequency of parametric resonance, either primary or secondary, we can choose between operating under the threshold of instability (below the instability tongue), or in the region of instability itself. The first alternative allows an approximated linear behavior, while that would not normally be the case for the second alternative. As operating inside the parametric instability region, using *resonant parametric amplification* as explained in section 3.1.6, can offer higher amplification gains, a study for the micro-ring gyroscope in the nonlinear regime is then required.

Nonlinear dynamic analysis as well as experimentation for conventional micro gyroscopes are found in the works of Sharma et al [74] and Oropeza-Ramos [62]. Where for the latter a

hardening Duffing effect is noticed when operating in the instability region, thereby allowing for nonlinear modal coupling, which provided a wide-spectrum amplification for the sense mode in case of a frequency mismatch between drive and sense modes.

The presence of nonlinear behavior in micro ring gyroscopes due to nonlinear elasticity or large strains is also reported in different works of Gallacher's team [116, 65] and Nitzan et al [117, 76, 118]. However, a nonlinear analysis for the micro-ring gyroscope dynamics was first presented in the paper by Polunin and Shaw [78], which was followed by further sensitivity analysis by Liang et al [119]. Notwithstanding, other nonlinear effects in micro ring gyroscopes are reported and analyzed in other works, however, due to electrostatic and/or capacitive nonlinearities [120, 121].

Hence, our scope now is the dynamics of micro-rings undergoing large displacements under parametric resonance, which leads us to the study of the nonlinear elasto-dynamics of inextensible rings. The condition of inextensibility is chosen since it is found that the radial expansion is of negligible order of magnitude [78].

5.2 Nonlinear elastic model

Starting from the classic nonlinear theory of shells due to Donnell [122], Chu [123] studied the nonlinear vibrations of thin cylindrical shells by including nonlinear terms in strain-displacement relations. By considering only flexural vibrations and assuming a thin shell thickness, he found the circumferential strain to be

$$\epsilon_{\theta\theta} = \frac{1}{R}\left[\frac{\partial v}{\partial \theta} + u\right] + \frac{1}{2R^2}\left(\frac{\partial u}{\partial \theta}\right)^2 - z\frac{\partial^2 u}{\partial \theta^2}, \tag{5.1}$$

where R is the mean radius of the cylindrical shell, u and v are the radial and circumferential displacements of a point on the middle surface, respectively, z and θ are the radial and angular coordinates of the cylinder, respectively, see Fig. 5.1.

The cylinder is reduced to a ring in the well known work of Evensen [124], who found, by assuming the inextensibility condition of the ring's centroidal axis, that

$$\epsilon_{\theta\theta}|_{z=0} = \frac{1}{R}\left[\frac{\partial v}{\partial \theta} + u\right] + \frac{1}{2R^2}\left(\frac{\partial u}{\partial \theta}\right)^2 = 0. \tag{5.2}$$

Therefore, the strain energy during flexural vibrations comes up only from the bending of

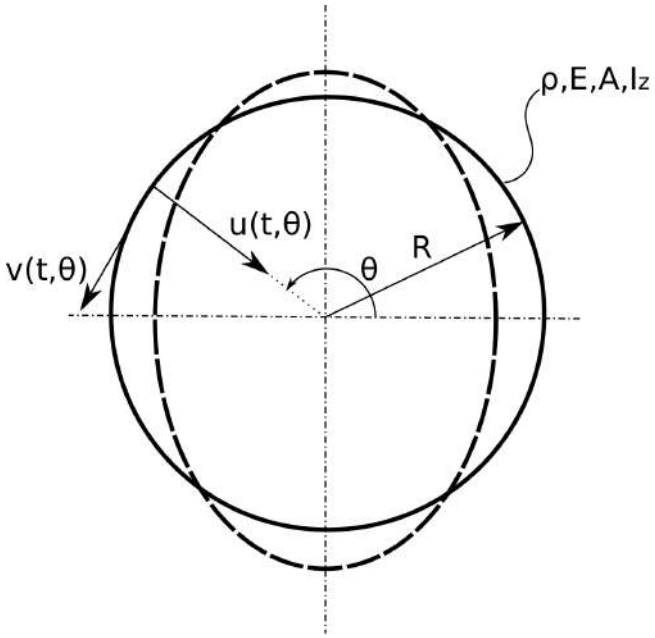

Figure 5.1: Ring in-plane displacements

the ring's axis without radial expansion, it is then computed as

$$U_d = \frac{EI}{2R^3} \int_0^{2\pi} \left(\frac{\partial^2 u}{\partial \theta^2} \right)^2 d\theta. \tag{5.3}$$

The nonlinear strain behavior here is due to the nonlinear condition (5.2). Therefore the relation between u and v is nonlinear, so if we assume

$$u(t,\theta) = q_{1n}(t)\cos(n\theta) + q_{2n}(t)\sin(n\theta),$$

and use the inextensibility condition (5.2), we can not get to an expression for v which satisfies the continuity of a closed circular ring. Thus, a nonlinear term is added to give

$$u(t,\theta) = q_{1n}(t)\cos(n\theta) + q_{2n}(t)\sin(n\theta) - \frac{n\gamma}{4R}\left[q_{1n}^2(t) + q_{2n}^2(t)\right], \qquad (n \geq 2), \tag{5.4}$$

where in this case $\gamma = n$.

Evensen showed in the same paper that his analysis would match the experimental results more precisely if he used a modified version of the inextensibility condition, that is

$$\epsilon_{\theta\theta} = \frac{1}{R}\left[\frac{\partial v}{\partial \theta} + u\right] + \frac{1}{2R^2}\left[\left(v - \frac{\partial u}{\partial \theta}\right)^2 + \left(\frac{\partial v}{\partial \theta} + u\right)^2\right] = 0, \tag{5.5}$$

but in this case the radial displacement u should differ from (5.4) by setting γ to be

$$\gamma = n\left(1 - \frac{1}{n^2}\right)^2. \tag{5.6}$$

This model describes the nonlinear vibrations of the ring due to nonlinear strain theory as having spring-softening stiffness (Duffing) behavior, which coincides with previous studies [122]. This comes, however, in contrast with Nitzan's assumption [117, 118].

Afterwards, Natsiavas [125] used a similar expression for the circumferential strain, that is

$$\epsilon_{\theta\theta} = \frac{1}{R}\left[\frac{\partial v}{\partial \theta} + u\right] + \frac{1}{2R^2}\left(v - \frac{\partial u}{\partial \theta}\right)^2 + \frac{z}{R^2}\left(\frac{\partial v}{\partial \theta} - \frac{\partial^2 u}{\partial \theta^2}\right), \tag{5.7}$$

and using the same u expression proposed by Evensen [124] but with the modified definition of γ in (5.6). The same expression was also used by Rao [112] but after excluding the nonlinear terms, thereby complying with his linear model. The inextensibility condition puts a constraint on the tangential and radial strains, which leads to the determination of the v expression given u. The inextensibilty condition is then deduced by setting (5.7) to zero at the ring's axis (i.e. $z = 0$), this leads to

$$\frac{1}{R}\left[\frac{\partial v}{\partial \theta} + u\right] + \frac{1}{2R^2}\left(v - \frac{\partial u}{\partial \theta}\right)^2 = 0, \quad \epsilon_{\theta\theta} = \frac{z}{R^2}\left(\frac{\partial v}{\partial \theta} - \frac{\partial^2 u}{\partial \theta^2}\right) \tag{5.8}$$

To deduce the strain energy for this case, it will include more terms as in (5.3), this means

$$U_d = \frac{EI}{2R^3}\int_0^{2\pi}\left(\frac{\partial v}{\partial \theta} - \frac{\partial^2 u}{\partial \theta^2}\right)^2 d\theta, \tag{5.9}$$

then by following Natsiavas choice for the $v - u$ transformation we get

$$U_d = \frac{EI}{2R^3}\int_0^{2\pi}\left[u + \frac{\partial^2 u}{\partial \theta^2} + \frac{1}{2R}\left(\frac{\partial u}{\partial \theta}\right)^2\right]^2 d\theta. \tag{5.10}$$

This relation for strain energy was used by Polunin and Shaw [78] but with a negative sign before the last term. However, the authors used Evensen's u relation (5.4) with the unmodified $\gamma = n$, which led them to the following expression for $n = 2$

$$u(t,\theta) = q_1(t)\cos(2\theta) + q_2(t)\sin(2\theta) - \frac{1}{R}\left[q_1^2(t) + q_2^2(t)\right]. \tag{5.11}$$

However, here we recommend a modification to u to comply with Natsiavas' work, and

thereby using the definition of γ in (5.6), this gives

$$u(t,\theta) = q_1(t)\cos(2\theta) + q_2(t)\sin(2\theta) - \frac{9}{16R}\left[q_1^2(t) + q_2^2(t)\right], \tag{5.12}$$

$$v(t,\theta) = \frac{1}{2}\left[-q_1(t)\sin(2\theta) + q_2\cos(2\theta)\right] + \frac{9}{64R}\left[(q_1^2(t) - q_2^2(t))\sin(4\theta) - 2q_1(t)q_2(t)\cos(4\theta)\right]. \tag{5.13}$$

On the other hand, assuming the electrodes to cover approximately the whole ring, the total electrostatic potential energy is given by

$$U_e = \frac{\epsilon_e R b}{2d}\left[V_{dc} + V_{ac}(t,\theta)\right]^2 \int_0^{2\pi} \left(1 + \frac{u}{d} + \frac{u^2}{d^2} + \frac{u^3}{d^3} + \frac{u^4}{d^4}\right) d\theta, \tag{5.14}$$

while the system's kinetic energy is given by

$$T = \int_{-b/2}^{b/2}\int_0^{2\pi}\int_{R-h/2}^{R+h/2} \frac{\rho r}{2}\left[(\dot{u} - \Omega v)^2 + (\dot{v} + \Omega(u+r))^2\right] dr d\theta dz, \tag{5.15}$$

where b is the ring's thickness, h the ring's width, ρ the density, R the ring's nominal radius, ϵ_e the electric permittivity, V_{ac}, V_{dc} the applied alternating and direct voltages respectively, d the gap between the ring and the electrode, and Ω the rotation of the ring's reference frame, which is to be measured.

5.3 Equations of motion

We start by analyzing the system using Lagrange's equations

$$\frac{\partial}{\partial t}\left(\frac{\partial L}{\partial \dot{q}_i}\right) - \frac{\partial L}{\partial q_i} = 0, \tag{5.16}$$

where $L = T - (U_d - U_e)$, and $q_i,\ i \in 1,2$ represents each degree of freedom. Through the analysis, the forced excitation is assumed to be

$$V_{ac}(t,\theta) = V_1(t)\sin(2\theta) + V_2(t)\cos(2\theta). \tag{5.17}$$

Then by normalizing with respect to the system's mass and ignoring terms higher than the

third order we get

$$\ddot{q}_1 + \left(\delta_1(1 - a_1 q_1^2 - a_2 q_2^2) + a_3 q_2 \dot{q}_2 + a_6 q_1 \dot{q}_1\right) \dot{q}_1 + \left(\omega_1^2(1 - a_1 q_1^2 - a_2 q_2^2) + a_4 q_1^2 + a_5 q_2^2 + a_7 \dot{q}_2^2 + a_8 q_2 \ddot{q}_2\right) q_1 - a_9(1 - a_1 q_1^2 - a_2 q_2^2)\dot{q}_2 = f_{a1} V_1(t) + f_{a2} V_1(t) q_1^2 + f_{a3} V_1(t) q_2^2 + f_{a4} V_2(t) q_1 q_2, \tag{5.18a}$$

$$\ddot{q}_2 + \left(\delta_2(1 - b_1 q_2^2 - b_2 q_1^2) + b_3 q_1 \dot{q}_1 + b_6 q_2 \dot{q}_2\right) \dot{q}_2 + \left(\omega_2^2(1 - b_1 q_2^2 - b_2 q_1^2) + b_4 q_2^2 + b_5 q_1^2 + b_7 \dot{q}_1^2 + b_8 q_1 \ddot{q}_1\right) q_2 - b_9(1 - b_1 q_2^2 - b_2 q_1^2)\dot{q}_1 = f_{b1} V_2(t) + f_{b2} V_2(t) q_2^2 + f_{b3} V_2(t) q_1^2 + f_{b4} V_1(t) q_1 q_2, \tag{5.18b}$$

with the coefficients for the given axis-symmetric ring-gyroscope mentioned in Table 5.1. In the described system we assume experimentally determined damping coefficients δ_1, δ_2. Moreover, we obtain repeated natural frequencies, or a degenerate eigenfrequency, that is

$$\omega_1^2 = \omega_2^2 = \frac{1}{5\rho h}\left(\frac{3Eh^3}{R^4} - \frac{4V_{dc}^2 \epsilon}{d^3}\right) \tag{5.19}$$

due to the assumed geometric axis-symmetry, which can differ from reality due to manufacturing limitations.

5.4 Autonomous nonlinear system

The nonlinear model (5.18) comprises a lot of terms, while most of them correspond to the coupling between both degrees of freedom. However, by investigating them thoroughly it was found that not all of them are decisive in determining the system's behavior. We start by giving some insights about the system. First, we consider only the autonomous case for the rest of this section, that is,

$$f_{ij} = 0, \quad i \in \{a, b\},\ j \in \{1, 2, 3, 4\}. \tag{5.20}$$

By observing the equations of motion of the autonomous system we can differentiate between the intrinsic terms for each mode, which have variables of a single mode, and coupling terms, which include variables of both modes. The former ones are represented by the terms including the coefficients a_i or b_i, where $i \in \{4, 6\}$, while the latter are represented by the terms having the coefficients a_j or b_j, where $j \in \{3, 5, 7, 8\}$. The terms $(1 - a_1 q_1^2 - a_2 q_2^2)$ (or the corresponding ones with b coefficients) represent the expansion up to the second order of $1/(1 + a_1 q_1^2 + a_2 q_2^2)$, since the denominator was originally multiplied by the inertia variables $\ddot{q}_1$ and $\ddot{q}_2$. Thus, a_1, b_1, a_2 and b_2 represent the nonlinear inertia terms.

$a_1 = b_1$	$\frac{2673}{1280R^2}$
$a_2 = b_2$	$\frac{81}{1280R^2}$
$a_3 = b_3$	$\frac{81}{640R^2}$
$a_4 = b_4$	$\frac{1}{320h\rho}\left[(59E_0h^3)/R^6 - (384V_{dc}^2\epsilon_0)/d^5\right]$
$a_5 = b_5$	$\frac{1}{320h\rho}\left[(59E_0h^3)/R^6 - (384V_{dc}^2\epsilon_0)/d^5\right]$
$a_6 = b_6$	$\frac{2673}{1280R^2}$
$a_7 = b_7$	$\frac{2511}{1280R^2}$
$a_8 = b_8$	$\frac{81}{40R^2}$
$a_9 = -b_9$	$\frac{8}{5}\Omega$
$f_{a1} = f_{b1}$	$\frac{4V_{dc}\epsilon_0}{5d^2h\rho}$
f_{a2}, f_{b2}	$\frac{9V_{dc}\epsilon_0}{5d^4h\rho} - \frac{4V_{dc}\epsilon_0 a_1}{5d^2h\rho}, \quad \frac{9V_{dc}\epsilon_0}{5d^4h\rho} - \frac{4V_{dc}\epsilon_0 b_1}{5d^2h\rho}$
f_{a3}, f_{b3}	$\frac{3V_{dc}\epsilon_0}{5d^4h\rho} - \frac{4V_{dc}\epsilon_0 a_2}{5d^2h\rho}, \quad \frac{3V_{dc}\epsilon_0}{5d^4h\rho} - \frac{4V_{dc}\epsilon_0 b_2}{5d^2h\rho}$
$f_{a4} = f_{b4}$	$\frac{6V_{dc}\epsilon_0}{5d^4h\rho}$

Table 5.1: Coefficients of (5.18)

In order to study the system's qualitative dynamic behavior, it is then converted into a four-degree-of-freedom first order system of differential equations while ignoring the inertia coupling terms, this yields

$$\dot{z}_1 = z_2, \tag{5.21a}$$

$$\dot{z}_2 = \left(-\delta_1(1 - a_1z_1^2 - a_2z_3^2) - a_3z_3z_4 - a_6z_1z_2\right) z_2 - \left(\omega_1^2(1 - a_1z_1^2 - a_2z_3^2) + a_4z_1^2 + a_5z_3^2 + a_7z_4^2\right) z_1 + a_9(1 - a_1z_1^2 - a_2z_3^2)z_4, \tag{5.21b}$$

$$\dot{z}_3 = z_4, \tag{5.21c}$$

$$\dot{z}_4 = \left(-\delta_2(1 - b_1 z_3^2 - b_2 z_1^2) - b_3 z_1 z_2 - b_6 z_3 z_4\right) z_4 - \left(\omega_2^2(1 - b_1 z_3^2 - b_2 z_1^2) + b_4 z_3^2 + b_5 z_1^2 + b_7 z_2^2\right) z_3 + b_9(1 - b_1 z_3^2 - b_2 z_1^2) z_2, \tag{5.21d}$$

where $z_1 = q_1, z_2 = \dot{q}_1, z_3 = q_2$ and $z_4 = \dot{q}_2$, or in compact form

$$\dot{\boldsymbol{z}} = \boldsymbol{f}(\boldsymbol{z}). \tag{5.22}$$

The system (5.22) forms a four dimensional phase space, which should be carefully considered in order to understand the system's dynamics. However, since a four dimensional space could not be presented graphically, the dynamic behavior will be described by investigating the stability of the fixed points, as well by observing the projections of some trajectories on two dimensional planes. To determine the system's stationary points we set $\dot{\boldsymbol{z}} = \boldsymbol{0}$ and obtain nine different fixed points which are listed in Table (5.2), where

$$\chi_1 = \frac{\omega_1}{\sqrt{-a_4 + a_1\omega_1^2}}, \tag{5.23a}$$

$$\chi_2 = \frac{\omega_2}{\sqrt{-b_4 + b_1\omega_2^2}}, \tag{5.23b}$$

$$\psi_1 = \frac{\sqrt{-b_4\omega_1^2 + \omega_2^2(a_5 + \omega_1^2(b_1 - a_2))}}{\sqrt{a_4 b_4 - a_5 b_5 + (a_2 b_5 - a_1 b_4)\omega_1^2 + \omega_2^2(a_5 b_2 - a_4 b_1 + \omega_1^2(a_1 b_1 - a_2 b_2))}}, \tag{5.23c}$$

$$\psi_2 = \frac{\sqrt{b_5\omega_1^2 - \omega_2^2(a_4 + \omega_1^2(b_2 - a_1))}}{\sqrt{a_4 b_4 - a_5 b_5 + (a_2 b_5 - a_1 b_4)\omega_1^2 + \omega_2^2(a_5 b_2 - a_4 b_1 + \omega_1^2(a_1 b_1 - a_2 b_2))}}. \tag{5.23d}$$

However, by observing the geometry-induced similarities in theses coefficients we find that

$$a_1 = a_6 = 33\, a_2 = \frac{33}{2} a_3, a_5 = a_4, \tag{5.24a}$$

$$b_1 = b_6 = 33\, b_2 = \frac{33}{2} b_3, b_5 = b_4, \tag{5.24b}$$

In addition, due to the assumed axis-symmetrical geometry of the micro-ring we have

$$a_i = b_i,\ i = 1, ..., 8,\ a_9 = -b_9,\ \omega_1 = \omega_2 = \omega, \tag{5.25}$$

these geometric properties allow the expressions (5.23) to be reduced to

$$\chi_1 = \chi_2 = \frac{\omega}{\sqrt{-a_4 + 33a_2\omega^2}}, \tag{5.26a}$$

$$\psi_1 = \psi_2 = \frac{\sqrt{a_2\omega^4}}{\sqrt{2}\sqrt{a_2\omega^2(-a_4 + 17a_2\omega^2)}}, \tag{5.26b}$$

$$\omega = \sqrt{\frac{1}{5\rho h}\left(\frac{3Eh^3}{R^4} - \frac{4V_{dc}^2\epsilon}{d^3}\right)}. \tag{5.26c}$$

Here it is important to differentiate first between constant parameters due to geometric or material properties on one side, and other controllable ones. In this sense, the two parameters, the applied direct voltage V_{dc} and the capacitive gap between the ring and the electrode d, are regarded as controllable parameters, while holding the rest of the parameter values fixed. By observing equations (5.26) we find three critical values at which the fixed points change from real into imaginary values, i.e. they simply vanish. For the fixed points with the value $\chi_{1,2}$ in (5.26a), the terms under the square root can render a negative value, thus imaginary fixed point, if

$$a_4 > 33a_2\omega^2 \tag{5.27}$$

using the geometrical values in Table (5.1), this implies

$$\begin{cases} V_{dc}^2 & > \dfrac{6839}{12(891 - 640(R/d)^2)}\dfrac{Ed^3h^3}{\epsilon_0 R^4}, \text{for } d > \dfrac{8\sqrt{10}R}{9\sqrt{11}}, \\ V_{dc}^2 & < \dfrac{-6839}{12(640(R/d)^2 - 891)}\dfrac{Ed^3h^3}{\epsilon_0 R^4}, \text{for } d < \dfrac{8\sqrt{10}R}{9\sqrt{11}}, \end{cases} \tag{5.28}$$

where the second case is physically impossible because this implies a negative V_{dc}.

Similarly for the value of $\psi_{1,2}$ in (5.26b) we obtain imaginary fixed points if

$$a_4 > 17a_2\omega^2 \tag{5.29}$$

this implies

$$\begin{cases} V_{dc}^2 & > \dfrac{2951}{12(459 - 640(R/d)^2)}\dfrac{Ed^3h^3}{\epsilon_0 R^4}, \text{for } d > \dfrac{8\sqrt{10}R}{3\sqrt{51}}, \\ V_{dc}^2 & < \dfrac{-2951}{12(640(R/d)^2 - 459)}\dfrac{Ed^3h^3}{\epsilon_0 R^4}, \text{for } d < \dfrac{8\sqrt{10}R}{3\sqrt{51}}, \end{cases} \tag{5.30}$$

where the second case is also physically impossible for the previously mentioned reason.

In (5.26c) we observe as well that the system's eigenfrequency could have an imaginary

	z_1^*	z_2^*	z_3^*	z_4^*
S_0	0	0	0	0
S_1	0	0	$-\chi_2$	0
S_2	0	0	χ_2	0
S_3	$-\chi_1$	0	0	0
S_4	χ_1	0	0	0
S_5	$-\psi_1$	0	$-\psi_2$	0
S_6	$-\psi_1$	0	ψ_2	0
S_7	ψ_1	0	$-\psi_2$	0
S_8	ψ_1	0	ψ_2	0

Table 5.2: Fixed points of system (5.21)

value for a case of a relatively large V_{dc}^2/d^3, this means if

$$V_{dc}^2 > \frac{3}{4}\frac{Ed^3h^3}{\epsilon_0 R^4}. \tag{5.31}$$

By comparing the three conditions (5.28), (5.30) and (5.31) we could obviously detect that the critical value of the third condition is always smaller than the critical values of the first two, and thereby will be satisfied for smaller value of V_{dc}. This implies that the first two conditions can not influence the corresponding fixed points, since the third condition would have been already satisfied and would cause all nontrivial fixed points to turn into imaginary values, due to the presence of ω in all fixed points expressions. In summary, we do have for this system only one possible bifurcation value, which is

$$V_{dc}^2 = \frac{3}{4}\frac{Ed^3h^3}{\epsilon_0 R^4}. \tag{5.32}$$

In order to visualize these results, a numeric example is used throughout this chapter. This is based on the experimental work of Gallacher and his team [65]. The parameter values in their work were modified slightly and used for the linearly modeled micro-ring gyroscope in the previous chapter. These values will be used here, which are $h = 175 \times 10^{-6}m,\ R = 4mm,\ d = 3 \times 10^{-6}m$ and the material properties of silicon are taken to be $E_0 = 1.9 \times 10^{11}N/m^2,\ \rho = 2300kg/m^3$. Using these values, we calculate the values of χ and ψ while varying V_{dc}. In this case the bifurcation limit is found to be $V_{dc} = 95.4V$.

In figures (5.2, 5.3) a bifurcation diagram for the fixed points S_1, S_2 in Fig. 5.2 and S_7 in

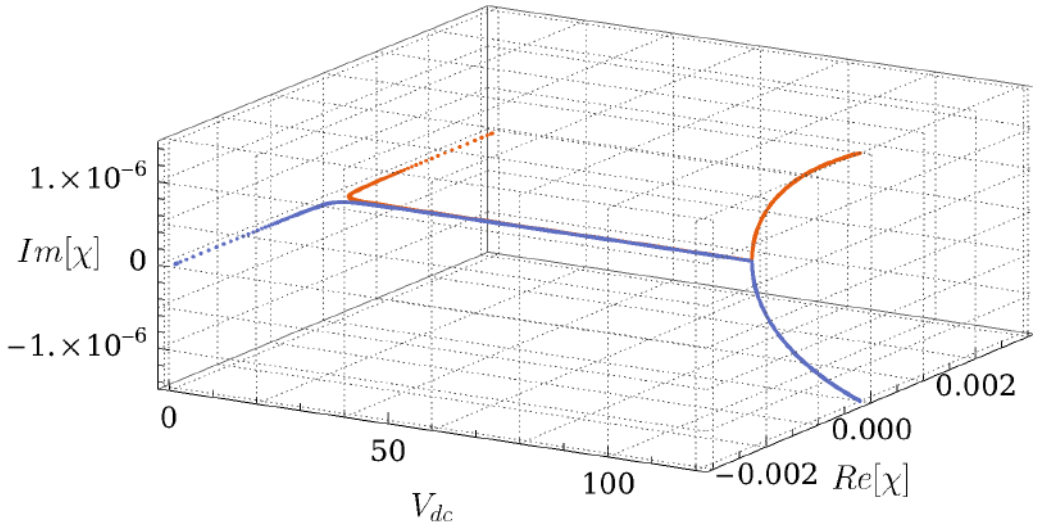

Figure 5.2: Bifurcation of the fixed points pair (blue and orange) S_1, S_2 or $S3, S4$

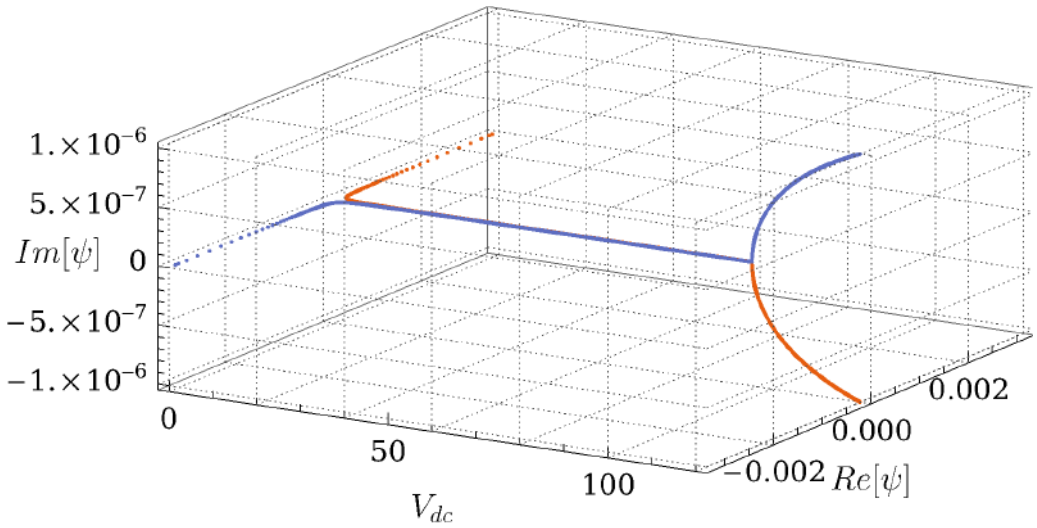

Figure 5.3: Bifurcation of the fixed point $S_7 = (0, \psi, 0, -\psi)$

Fig. 5.3. However, the transition depicted in these diagrams applies for all non trivial fixed points (see Table 5.2), and at the same bifurcation value, according to the condition (5.31). Although a subcritical pitchfork bifurcation (in four-dimensional space) occurs at this value, but the represented figures do not resemble the conventional pitchfork bifurcation diagram. In theses figure we represent the real and imaginary parts of χ and ψ in Fig. 5.2 and Fig. 5.3 respectively on two axes, while displaying the bifurcation parameter V_{dc} on the third axis. It can be concluded from these figures that all the nontrivial fixed points have real values up to the bifurcation value (5.32), afterwards they change in pure imaginary values, i.e. they vanish. Typical values before and after the bifurcation values are represented in Table 5.3.

	Before Bifurcation, $V_{dc} = 90V$				After Bifurcation, $V_{dc} = 100V$			
	z_1^*	z_2^*	z_3^*	z_4^*	z_1^*	z_2^*	z_3^*	z_4^*
S_0	0	0	0	0	0	0	0	0
S_1	0	0	-8.6×10^{-7}	0	0	0	$-7.3 \times 10^{-7}i$	0
S_2	0	0	8.6×10^{-7}	0	0	0	$7.3 \times 10^{-7}i$	0
S_3	-8.6×10^{-7}	0	0	0	$-7.3 \times 10^{-7}i$	0	0	0
S_4	8.6×10^{-7}	0	0	0	$7.3 \times 10^{-7}i$	0	0	0
S_5	-6.1×10^{-7}	0	-6.1×10^{-7}	0	$5.2 \times 10^{-7}i$	0	$5.2 \times 10^{-7}i$	0
S_6	-6.1×10^{-7}	0	6.1×10^{-7}	0	$5.2 \times 10^{-7}i$	0	$-5.2 \times 10^{-7}i$	0
S_7	6.1×10^{-7}	0	-6.1×10^{-7}	0	$-5.2 \times 10^{-7}i$	0	$5.2 \times 10^{-7}i$	0
S_8	6.1×10^{-7}	0	6.1×10^{-7}	0	$-5.2 \times 10^{-7}i$	0	$-5.2 \times 10^{-7}i$	0

Table 5.3: Fixed points of system (5.21), where $h = 175 \times 10^{-6}m$, $R = 4mm$, $d = 3 \times 10^{-6}m$, $E_0 = 1.9 \times 10^{11} N/m^2$, $\rho = 2300 kg/m^3$ and the bifurcation value is $V_{dc} = 95.4V$

5.4.1 Stability of fixed points

As shown in Table 5.2 and Table 5.3 the system under study possesses nine fixed points before the bifurcation point and only the trivial fixed point after it. Here the stability of each fixed point is studied. The stability of each fixed point will be investigated by first perturbing around the fixed point by a small change in system states, that is

$$\boldsymbol{z} = \boldsymbol{z}^* + \boldsymbol{\delta z}, \tag{5.33}$$

this gives

$$\frac{d(\boldsymbol{z}^* + \boldsymbol{\delta z})}{dt} = \boldsymbol{f}(\boldsymbol{z}^* + \boldsymbol{\delta z}) \tag{5.34}$$

then considering $\boldsymbol{z}^*$ to be constant and expanding about it we get

$$\boldsymbol{\delta \dot{z}} = D(\boldsymbol{f}(\boldsymbol{z}^*))\boldsymbol{z} + \tilde{\boldsymbol{f}}(\boldsymbol{z}), \tag{5.35}$$

where $D(\boldsymbol{f}(\boldsymbol{z}^*))$ is the Jacobian matrix of the system at the fixed point $\boldsymbol{z}^*$. The linearized system ,

$$\boldsymbol{\delta}\dot{\boldsymbol{z}} = D(\boldsymbol{f}(\boldsymbol{z}^*))\boldsymbol{z}, \tag{5.36}$$

is then studied to determine the stability of (5.22) around the fixed point $\boldsymbol{z}^*$, where the invariant manifolds of the nonlinear system (5.22) are tangent to the eigenspace of the linearized system. The stability of the linearized system determines the stability of the fixed point also in the original nonlinear system provided being a non-hyperbolic fixed point [84, 99].

In order to determine the stability of the fixed point, the eigenvalues of the Jacobian matrix are then calculated. According to the theory of asymptotic stability [98], if all eigenvalues have negative real parts, then the fixed point is asymptotically stable, also if only one eigenvalue has a positive real part then the fixed point is unstable.

Starting with the trivial fixed point (S_0), the Jacobian matrix is calculated to give

$$D(\boldsymbol{f}(\boldsymbol{z}^*_{\boldsymbol{S_0}})) = \begin{bmatrix} 0 & 1 & 0 & 0 \\ -\omega^2 & -\delta_1 & 0 & a_9 \\ 0 & 0 & 0 & 1 \\ 0 & b_9 & -\omega^2 & -\delta_2 \end{bmatrix}, \tag{5.37}$$

the characteristic equation then reads

$$\lambda^4 + 2\delta\,\lambda^3 + (\delta^2 + \frac{64\Omega^2}{25} + 2\omega^2)\,\lambda^2 + (2\delta\omega^2)\,\lambda + \omega^4 = 0, \tag{5.38}$$

where the damping coefficients for both degrees of freedom are assumed to be equal, and a_9, b_9 are substituted by their values from Table 5.1.

The stability is then studied according to Hurwitz-Routh's criterion [96]. In Hurwitz representation

$$a_0\lambda^4 + a_1\lambda^3 + a_2\lambda^2 + a_3\lambda + a_4 = 0, \tag{5.39}$$

the criteria yields for a characteristic equation of the fourth order the conditions

$$a_1 > 0, \quad \begin{vmatrix} a1 & a_0 \\ a_3 & a_2 \end{vmatrix} > 0, \quad \begin{vmatrix} a1 & a_0 & 0 \\ a_3 & a_2 & a_1 \\ 0 & a_4 & a_3 \end{vmatrix} > 0, \quad a_4 > 0, \tag{5.40}$$

should the conditions be satisfied, that would be necessary and also sufficient that all the roots of the characteristic equation have negative real parts.

Applying this procedure to (5.38) we obtain the following conditions

$$2\delta > 0, \tag{5.41a}$$
$$2\delta\,\omega^2 > 0, \tag{5.41b}$$
$$\omega^4 > 0, \tag{5.41c}$$
$$\frac{4}{25}\delta^2\omega^2(25\delta^2 + 64\Omega^2) > 0. \tag{5.41d}$$

By observing these conditions we obviously conclude that the trivial fixed point is always stable, unless the eigenfrequency ω could be driven to be negative as discussed before.

The eigenvalues are then calculated to support the previous conclusion. In the case of having no rotation of the reference frame, i.e. $\Omega = 0$, the eigenvalue problem is reduced to a two-degree-of-freedom damped system with the eigenvalues

$$\lambda_{1,2} = \frac{1}{2}\left(-\delta \pm \sqrt{\delta^2 - 4\omega^2}\right) \quad \lambda_{3,4} = \frac{1}{2}\left(-\delta \pm \sqrt{\delta^2 - 4\omega^2}\right), \tag{5.42}$$

while by putting the micro gyroscope into operation, thus having non-zero values of Ω, we get a modified version of these eigenvalues to be

$$\begin{aligned}\lambda_{1,2} &= \frac{1}{10}\left(-5\delta + 8i\Omega \pm \sqrt{25\delta^2 - 100\omega^2 - 80i\zeta\Omega - 64\Omega^2}\right)\\ \lambda_{3,4} &= \frac{1}{10}\left(-5\delta - 8i\Omega \pm \sqrt{25\delta^2 - 100\omega^2 - 80i\zeta\Omega - 64\Omega^2}\right)\end{aligned} \tag{5.43}$$

Applying these results to our numeric example we find the eigenvalues before the bifurcation point at $V_{dc} = 90V$ to be

$$\lambda_{1,2} = -5.324 \pm 25562i,\ \lambda_{3,4} = -5.316 \pm 25522i, \tag{5.44}$$

while in case of tuning $V_{dc} = 100V$ after the bifurcation point we get

$$\lambda_{1,2} = -24200 \pm 20,004i,\ \lambda_{3,4} = 24190 \pm 19.996i. \tag{5.45}$$

The effect of the gyroscopic forces, assuming $\Omega \simeq \omega/1000$, is observed here in the slight modification of the natural frequencies of the first case as well as in the dissimilarity of the effective damping in the real parts of the eigenfrequencies. After the bifurcation limit, the imaginary frequencies lead to positive and negative real parts, i.e. a saddle point, while an

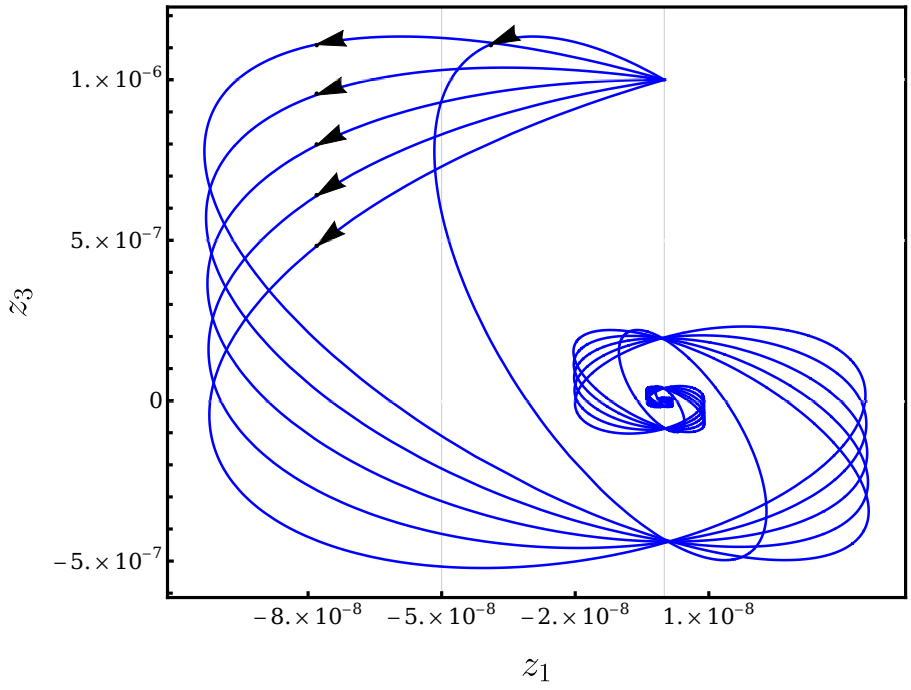

Figure 5.4: A projection of the phase space on the plane $z_1 - z_3$ around the trivial fixed point before the bifurcation point

imaginary part remains existing due to the gyroscopic forces. From these results, we could conclude that before the bifurcation point we have a stable focus (see Fig. 5.4) while after bifurcation it changes into saddle point.

In analyzing the stability of the fixed points S_1-S_4 we find them to have the same characteristic equation and thereby subjected to the same Hurwitz stability conditions. The characteristic equation for these fixed points is then

$$\lambda^4 + \frac{64a_2\omega^6}{a_4 - 33a_2\omega^2} + 2\delta\lambda^3\frac{a_4 - 16a_2\omega^2}{a_4 - 33a_2\omega^2} - \frac{2\delta\lambda\omega^2(a_4^2 - 49a_2a_4\omega^2 + 1056a_2^2\omega^4)}{(a4 - 33a_2\omega^2)^2} + \frac{\lambda^2(25(a_4^2\delta^2 - 2a_4(a_4 + 16a_2\delta^2)\omega^2 + 100a_2a_4\omega^4 - 1122a_2^2\omega^6) + 64a_4(a_4 - 32a_2\omega^2))\Omega^2}{25(a_4 - 33a_2\omega^2)^2} = 0. \tag{5.46}$$

Applying the second condition in (5.40) for (5.46) gives

$$-\frac{2\delta\omega^2(a_4^2 - 49a_2a_4\omega^2 + 1056a_2^2\omega^4)}{(a_4 - 33a_2\omega^2)^2} > 0, \tag{5.47}$$

which clearly shows that it can not be satisfied as long as the eigenfrequency is real, otherwise if it is imaginary, then the fixed point itself will not exist anymore. Hence, it would not be

useful to investigate the satisfaction of the other Hurwitz-conditions for these fixed points.

Furthermore, in analyzing the stability of the fixed points S_5-S_8, they were found to have the same characteristic equation, thus, they will be treated together using Hurwitz stability criterion. The characteristic equation for these fixed points reads

$$\begin{aligned}\lambda^4 + \lambda^3 \frac{2a_4\delta}{a_4 - 17a_2\omega^2} + \lambda^2 \frac{2500a_2a_4\omega^4 - 28050a_2^2\omega^6 + a_4^2(25\delta^2 - 50\omega^2 + 64\Omega^2)}{25(a_4 - 17a_2\omega^2)^2} \\ - \lambda \frac{2a_4\delta\omega^2(a_4 - 33a_2\omega^2)}{(a_4 - 17a_2\omega^2)^2} - \frac{64a_2\omega^6}{a_4 - 17a_2\omega^2} = 0\end{aligned} \tag{5.48}$$

The Hurwitz conditions are then examined for these fixed points. The first and third conditions yield

$$\frac{2a_4\delta}{a_4 - 17a_2\omega^2} > 0, \tag{5.49a}$$

$$-\frac{64a_2\omega^6}{a_4 - 17a_2\omega^2} > 0. \tag{5.49b}$$

For the case of having V_{dc} smaller than the bifurcation value, a_2, a_4 and ω^2 can not be negative. Hence, the two conditions in (5.49) are obviously in pure contradiction. This means that the stability conditions can not be met. This implies that these fixed points as well are always unstable, since these fixed points vanish in the other case when V_{dc} exceeds the bifurcation point.

Summarizing this section, we investigated the fixed points of the autonomous system of the nonlinearly modeled micro-ring gyroscope, and found that the system possesses eight non trivial fixed points in addition to the trivial one. A bifurcation occurs through tuning V_{dc} above a certain value (see (5.32)). Before the bifurcation value, we have a stable trivial solution, while all other solutions are unstable. After the bifurcation value we do have only the unstable trivial solution whose instability is obviously caused by having an imaginary eigenvalue (divergence), and the system as a whole loses stability. Accordingly, this behavior describes a *subcritical pitchfork* bifurcation, where the only persisting fixed point after bifurcation is the trivial one while losing stability.

5.5 Nonlinear resonance of a simplified system

Provided that only the first mode is externally excited, i.e. $V_2(t) = 0$, all forcing terms in the second mode q_2 are eliminated except for a coupled forcing element with the f_{b4} coefficient. In

this sense, the second mode will be mainly excited by the gyroscopic term (coefficient b_9) in a linear fashion, if the nonlinearities were of a smaller order of magnitude under weak excitation. In addition, all the back action terms in the first mode from the second mode were also ignored in the vicinity of a forced primary resonance, that is, if $V_1(t) = Fcos(\omega_f t)$, then $\omega_f \simeq \omega_1$, especially when $\Omega << \omega_1$. Following these assumptions, which were previously considered in [78], the system can be significantly simplified, and the equations (5.18) read

$$\ddot{q}_1 + \delta_1(1 - a_1 q_1^2)\dot{q}_1 + (\omega_1^2(1 - a_1 q_1^2) + a_4 q_1^2 + a_6 \dot{q}_1^2)q_1 = F_0 \left(f_{a1} + f_{a2} q_1^2\right) cos(\omega_f t). \tag{5.50}$$

The normal form method is then used to analyze (5.50) in accordance with [107]. The transformation will be briefly explained for convenience. By adding a detuning parameter

$$\sigma = \omega_1 - \omega_f, \tag{5.51}$$

the system (5.50) is then transformed to a first order system

$$\dot{z}_1 = z_2, \tag{5.52a}$$

$$\dot{z}_2 = -\delta_1 z_5(1 - a_1 z_1^2)z_2 - (\omega_1^2(1 - a_1 z_1^2) + a_4 z_1^2 + a_6 z_2^2)z_1 + \frac{F_0}{2}\left(f_{a1} + f_{a2} z_1^2\right)\left(z_3^2 + z_4^2\right), \tag{5.52b}$$

$$\dot{z}_3 = \frac{i}{2}\left(\omega_f + z_6\right) z_3, \tag{5.52c}$$

$$\dot{z}_4 = \frac{-i}{2}\left(\omega_f + z_6\right) z_3, \tag{5.52d}$$

$$\dot{z}_5 = 0, \quad \dot{z}_6 = 0, \tag{5.52e}$$

where $z_1 = q_1,\ z_2 = \dot{q_1}$, while $z_3 = e^{\frac{i}{2}\omega_f t}, z_4 = e^{\frac{-i}{2}\omega_f t}$ are additional variables to account for the forced periodic excitation, z_5 is a dummy variable to shift the linear damping into nonlinear terms, and z_6 is a dummy variable to account for the detuning parameter. Using the nonlinear transformation and taking the resonance at the system's natural frequency into account we arrive at the normal form (see section 3.1.4)

$$\dot{\boldsymbol{y}} = \boldsymbol{h}(\boldsymbol{y}, t), \tag{5.53}$$

which in turns is transformed again to the polar coordinates to give

$$\dot{r}(t) = \frac{1}{4}\left(2F_0 f_{a1} cos(\phi(t)) - 4\delta r(t) + \frac{1}{\omega_1} F_0 f_{a1} \delta sin(\phi(t))\right), \tag{5.54a}$$

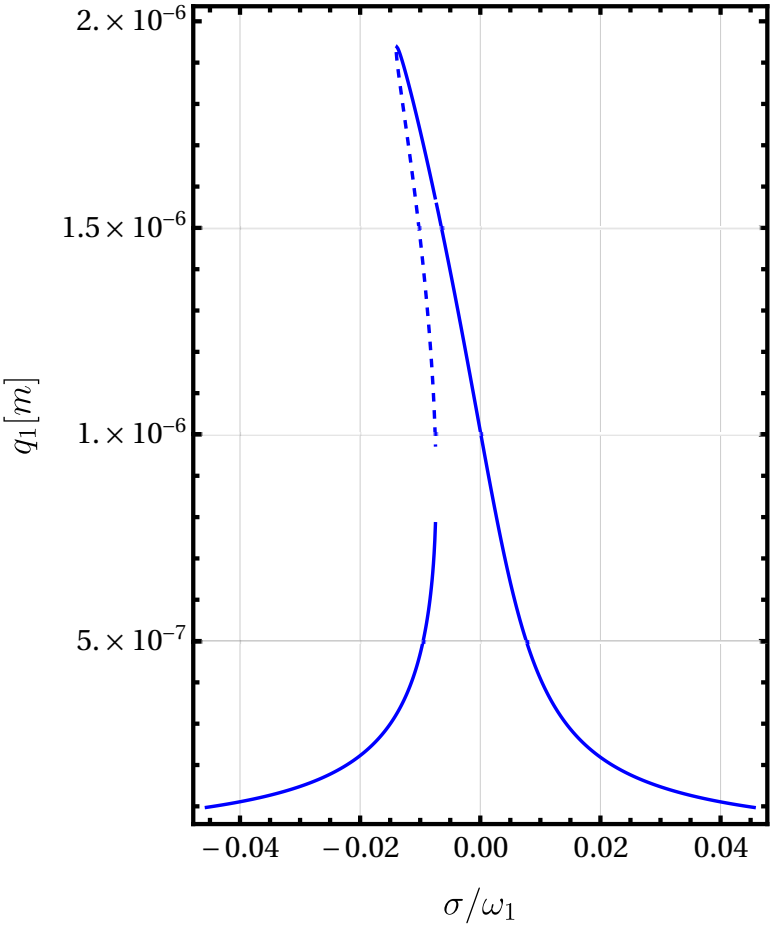

Figure 5.5: Softening nonlinear resonance for the simplified equation of the drive mode (5.50)

$$\dot{\phi}(t) = \frac{1}{8\omega_1^3}\left(-4\omega_1^2(\delta^2 + 2(\omega_f - \omega_1)\omega_1) + (3a_4 - 2a_6\omega_1^2)r(t)^2 + \frac{1}{r(t)}2F_0 f_{a1}\omega_1^2(\delta cos(\phi(t)) - 2\omega_1 sin(\phi(t)))\right). \tag{5.54b}$$

By converting (5.54) nonlinearly back to the original coordinates $\boldsymbol{q}(t)$, we find the displacement of the drive mode to be

$$q_1(t) = -\frac{F(\omega_f - 3\omega_1)cos(\omega_f t)}{8\omega_1^3} - \frac{\delta cos(\omega_f t + \phi(t))r(t)}{2\omega_1^2} + \left(\frac{r(t)}{\omega_1} + \frac{(-3a_4 + 2a_6\omega_1^2)r(t)^3}{16\omega_1^5}\right)\sin(\omega_f t + \phi(t)) - \frac{a_6 - 2a_4\omega_1^2}{32\omega_1^5}r(t)^3\sin(3\omega_f t + 3\phi(t)) \tag{5.55}$$

A softening Duffing response behavior is found as depicted in Fig. 5.5, assuming a silicon

based ring, and using the following geometrical and electrical values

$$R = 4\,mm,\ d = 3\mu m,\ h = 100\mu m,\ V_{dc} = 10V,\ F = 0.5V, \tag{5.56}$$

which comes in accordance with the behavior obtained in [78]. Furthermore, the mathematical expression (5.55) indicates the presence of subharmonic resonances, in addition to the frequency-amplitude dependence.

5.6 Bimodal parametric excitation

Through utilizing the bimodal parametric excitation method used in section 3.1.3, the stability analysis is extended in this section to the nonlinearly modeled micro-ring gyroscope. It was shown in section 3.1.6 that the destabilization effect at any parametric excitation frequency leads as well to an amplification either within the instability regions of the trivial fixed point or just below the instability threshold. Thereby, the *parametric amplification* mechanism is extended from *resonant* to *non-resonant* excitation frequencies. In this sense, it will be only necessary for our nonlinear analysis here to analyze the parametrically excited system and determine the destabilization of its trivial fixed point at any given excitation frequency, in order to prove the amplification capability. The destabilization is measured through calculating the real parts of the system's eigenvalues.

It should be noted also that, except for the linear parametric excitation, the following analysis is performed without modifying the system dynamics, moreover, all the coefficients are based on geometric, elastic and electrostatic properties. In addition, the parameter values used were extracted from a previously experimented micro ring gyroscope.

For the sake of analyzing the stability of the system's solutions without forced excitation, the autonomous version of system (5.18) is used while adding the bimodal excitation method. This is done by adding two additional terms in each equation of motion, one direct (intrinsic) time-dependent term, ξ_{ii}, and cross-coupling time dependent term, $\xi_{ij},\ i \neq j$, each with a corresponding phase shift ζ_{ij}. This gives

$$\begin{aligned}\ddot{q}_1 + \left(\delta_1(1 - a_1q_1^2 - a_2q_2^2) + a_3q_2\dot{q}_2 + a_6q_1\dot{q}_1\right)\dot{q}_1 + \left(\omega_1^2(1 - a_1q_1^2 - a_2q_2^2) + a_4q_1^2 + a_5q_2^2\right. \\ \left. + a_7\dot{q}_2^2 + a_8q_2\ddot{q}_2\right)q_1 - a_9(1 - a_1q_1^2 - a_2q_2^2)\dot{q}_2 + \xi_{11}\cos(\Omega_p t + \zeta_{11})q_1 + \xi_{12}\cos(\Omega_p t + \zeta_{12}) = 0,\end{aligned} \tag{5.57a}$$

$$\ddot{q}_2 + \left(\delta_2(1 - b_1q_2^2 - b_2q_1^2) + b_3q_1\dot{q}_1 + b_6q_2\dot{q}_2\right)\dot{q}_2 + \left(\omega_2^2(1 - b_1q_2^2 - b_2q_1^2) + b_4q_2^2 + b_5q_1^2 + b_7\dot{q}_1^2 + b_8q_1\ddot{q}_1\right)q_2 - b_9(1 - b_1q_2^2 - b_2q_1^2)\dot{q}_1 + \xi_{21}\cos(\Omega_p t + \zeta_{21})q_1 + \xi_{22}\cos(\Omega_p t + \zeta_{22}) = 0. \tag{5.57b}$$

Dealing with equations (5.57) as they are is quiet challenging because of being highly nonlinear and time periodic as well. In order to have better insights and explore the system dynamics the normal form method was used. The method of normal forms has an interesting property in comparison with other perturbational methods, that is, it uses nonlinear coordinate transformation, which leads to a minimal number of nonlinear terms in the normal form coordinates.

The normal form method is described in the literature with different perspectives [105, 84, 100, 104], however, the systematic approach provided in [107] is adopted. Similar to the analysis provided in chapter 4, the system of non-autonomous time-periodic second order nonlinear equations (5.57) is changed into the autonomous first-order nonlinear system

$$\dot{z}_1 = z_2, \tag{5.58a}$$

$$\dot{z}_2 = \left(-\delta_1(z_7 - a_1z_1^2 - a_2z_3^2) - a_3z_3z_4 - a_6z_1z_2\right)z_2 - \left(\omega_1^2(1 - a_1z_1^2 - a_2z_3^2) + a_4z_1^2 + a_5z_3^2 + a_7z_4^2\right)z_1 + a_9(z_7 - a_1z_1^2 - a_2z_3^2)z_4 - \frac{1}{2}\xi_{11}(e^{i\zeta_{11}}z_5 + e^{-i\zeta_{11}}z_6)z_1 - \frac{1}{2}\xi_{12}(e^{i\zeta_{12}}z_5 + e^{-i\zeta_{12}}z_6)z_3, \tag{5.58b}$$

$$\dot{z}_3 = z_4, \tag{5.58c}$$

$$\dot{z}_4 = \left(-\delta_2(z_7 - b_1z_3^2 - b_2z_1^2) - b_3z_1z_2 - b_6z_3z_4\right)z_4 - \left(\omega_2^2(1 - b_1z_3^2 - b_2z_1^2) + b_4z_3^2 + b_5z_1^2 + b_7z_2^2\right)z_3 + b_9(z_7 - b_1z_3^2 - b_2z_1^2)z_2 - \frac{1}{2}\xi_{21}(e^{i\zeta_{21}}z_5 + e^{-i\zeta_{21}}z_6)z_1 - \frac{1}{2}\xi_{22}(e^{i\zeta_{22}}z_5 + e^{-i\zeta_{22}}z_6)z_3, \tag{5.58d}$$

$$\dot{z}_5 = i\Omega_p z_5, \tag{5.58e}$$

$$\dot{z}_6 = -i\Omega_p z_6, \tag{5.58f}$$

$$\dot{z}_7 = 0, \tag{5.58g}$$

where $z_1 = q_1, z_2 = \dot{q}_1, z_3 = q_2, z_4 = \dot{q}_2, z_5 = e^{i\Omega_p t}, z_6 = e^{-i\Omega_p t}$ and $z_7 = 1$ is just a dummy variable, in compact form

$$\dot{\boldsymbol{z}} = \boldsymbol{f}(\boldsymbol{z}). \tag{5.59}$$

Following the same procedure while accounting for the parametric primary resonances, and using $y_5 = z_5 = e^{i\Omega_p t}$, $y_6 = z_6 = e^{-i\Omega_p t}$ and $y_7 = z_7 = 1$, we find the normal form up to the third

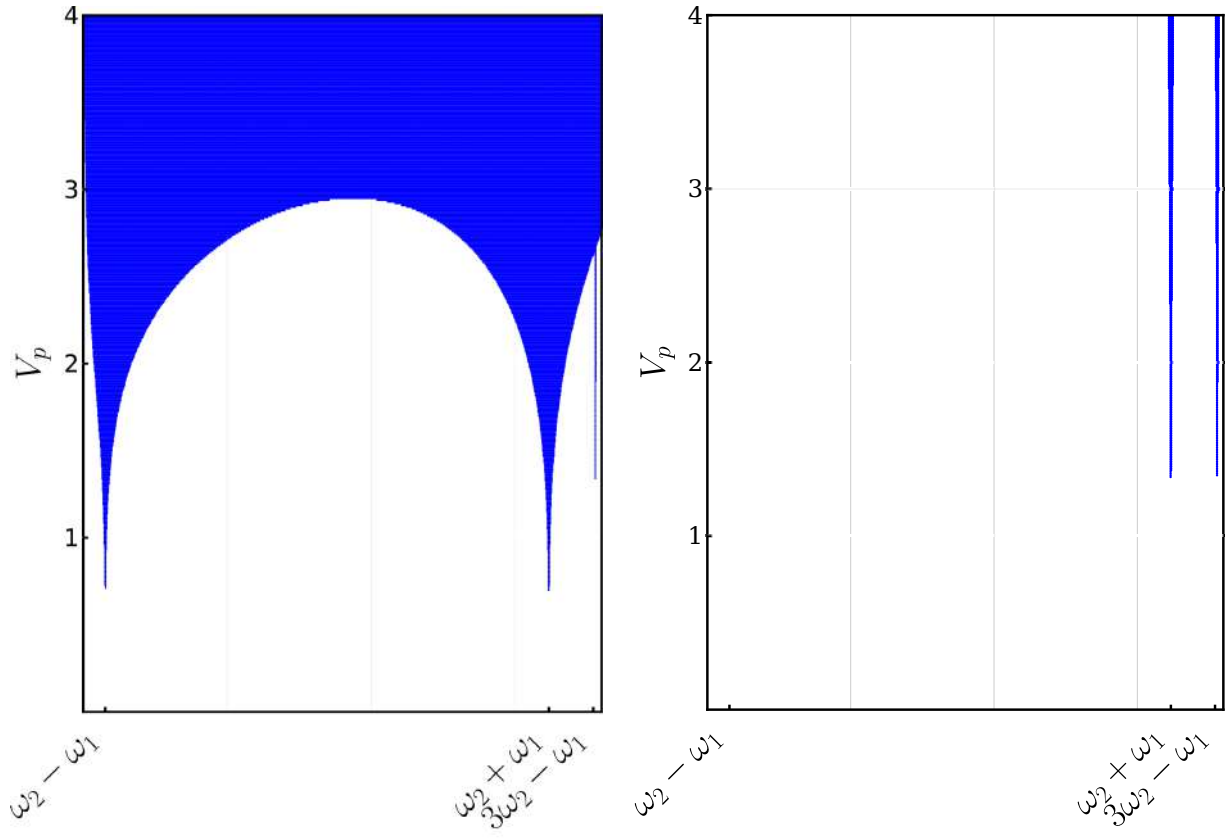

(a) $\zeta_{21} = -\pi/2$ (b) $\zeta_{21} = 0$

Figure 5.6: Stability chart of (5.60)

order to be

$$\dot{y}_1 = A_1 y_1 + A_2(t) y_2 + A_3 y_1^2 y_2 + A_4 y_1 y_3 y_4, \tag{5.60a}$$
$$\dot{y}_2 = B_1 y_2 + B_2(t) y_1 + B_3 y_2^2 y_1 + B_4 y_2 y_3 y_4, \tag{5.60b}$$
$$\dot{y}_3 = C_1 y_3 + C_2(t) y_4 + C_3 y_3^2 y_4 + C_4 y_3 y_1 y_2, \tag{5.60c}$$
$$\dot{y}_4 = D_1 y_4 + D_2(t) y_3 + D_3 y_4^2 y_3 + D_4 y_4 y_1 y_2, \tag{5.60d}$$

where the coefficients A_i, B_i, C_i, D_i are provided in Appendix 5.A. These results are then applied on a realistic micro gyroscope [65], with the parameter values in (5.56), except for $V_{dc} = 1V$. The parametric excitation amplitude is calculated in a similar way to chapter 4 considering an equal amplitude for all excitation terms $\xi_{ij} = \xi = 6 \times 10^6 \, V_p^2$, where V_p is the amplitude of the applied alternating voltage.

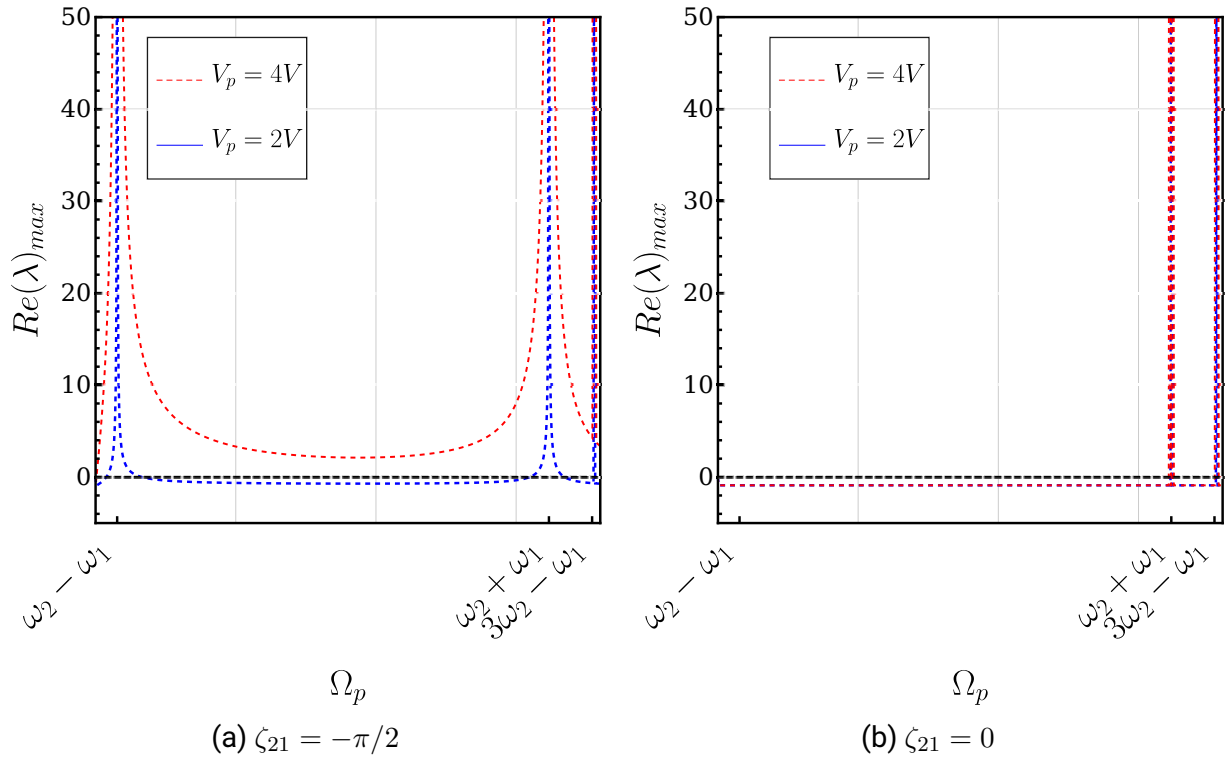

(a) $\zeta_{21} = -\pi/2$ (b) $\zeta_{21} = 0$

Figure 5.7: Maximum real parts of the eigenvalues of system (5.60) at two different voltages, see Fig. (5.6)

In order to determine the stability of this system, the Floquet theory is applied on the Jacobian of the system around the trivial solution. The stability is then determined by finding the eigenvalue with the greatest real part for each excitation frequency Ω_p and voltage V_p. The stability chart is depicted in Fig. (5.6(a)) for the case of having an asynchronous excitation, i.e. $\zeta_{21} = -\pi/2$, while setting all other phases ζ_{ij} to zero. This is to be compared to synchronous excitation case, i.e. all phases are set to zero, in Fig. (5.6(b)).

In order to understand the destabilization shown in the stability charts with respect to the eigenvalues, a section is made at a certain voltage in both figures 5.6(a,b) to depict a third coordinate representing the maximum real part of system's eigenvalues. In Fig 5.7 Lyapunov exponents $Re(\lambda)_{max}$ are depicted with respect to the parametric excitation frequency Ω_p at the voltage values $V_p = 2V, 4V$.

The broadband destabilization is obvious in view of Fig. 5.6(a) and Fig. 5.7(a), where the trivial solution is destabilized at non-resonant frequencies, resulting in positive real parts of some of the eigenvalues which lead to broad instability domain in the stability chart at higher levels of the excitation amplitude. This is in accordance to the previous observations of the linearized system in chapter 4.

However, unlike the linearized system, the destabilization of the trivial solution leads the system's response in this nonlinear system to be influenced by other non trivial solutions, which are to be analyzed afterwards.

5.7 Parametric Resonances

In order to find the nontrivial solutions, or the fixed points of system (5.60), the system should be put in autonomous form. To this end a polar coordinate transformation is used to *neutralize* the time-periodicity of this system using cylindrical coordinates, in which the periodic solution is described by the angular coordinate. This is done by choosing

$$y_1 = \frac{1}{2} e^{\frac{\Omega_p t}{2} + \phi_1(t)} \omega_1 r_1(t), \tag{5.61a}$$

$$y_2 = \frac{1}{2} e^{\frac{\Omega_p t}{2} - \phi_1(t)} \omega_1 r_1(t), \tag{5.61b}$$

$$y_3 = \frac{1}{2} e^{\frac{\Omega_p t}{2} + \phi_2(t)} \omega_2 r_2(t), \tag{5.61c}$$

$$y_4 = \frac{1}{2} e^{\frac{\Omega_p t}{2} - \phi_2(t)} \omega_2 r_2(t). \tag{5.61d}$$

Through this transformation, we could read the relation between r_1 and q_1 as well as between r_2 and q_2. This could be also understood by tracing the different coefficients back to the original system (5.18), see Appendix 5.A. Using this transformation, the normal form equations (5.60) yield

$$\begin{aligned}\dot{r}_1 = {} & \frac{\delta_1}{8}(-4 + a_1 r_1^2 + 2a_2 r_2^2) r_1 - \frac{\xi^2 \Omega_p r_1 \sin(\zeta_{21})}{(\Omega_p^2 - (\omega_2 - \omega_1)^2)(\Omega_p^2 - (\omega_2 + \omega_1)^2)} \\ & + \frac{\xi r_1}{16\omega_1} \left(\frac{4a_9(\omega_1 - \Omega_p)\cos(\zeta_{21} - 2\phi_1))}{(\Omega_p - (\omega_2 + \omega_1))(\Omega_p - (\omega_2 - \omega_1))} + \left(\frac{\delta_1}{\omega_1} - \frac{4b_9\omega_1}{\omega_1^2 - \omega_2^2} + \frac{2\delta_1}{\Omega_p} \right) \cos(2\phi_1) - 4\sin(2\phi_1) \right),\end{aligned} \tag{5.62a}$$

$$\begin{aligned}\dot{r}_2 = {} & \frac{\delta_2}{8}(-4 + b_1 r_2^2 + 2b_2 r_1^2) r_2 - \frac{\xi^2 \Omega_p r_2 \sin(\zeta_{21})}{(\Omega_p^2 - (\omega_2 - \omega_1)^2)(\Omega_p^2 - (\omega_2 + \omega_1)^2)} \\ & + \frac{\xi r_2}{16} \left(\frac{4a_9 \cos(\zeta_{21} - 2\phi_2)}{\omega_1^2 - \omega_2^2} + \frac{1}{\omega_2^2} \left(\delta_2 + \frac{2\delta_2\omega_2}{\Omega_p} + \frac{4b_9\omega_2(\Omega_p - \omega_2)}{(\omega_1 + \omega_2 - \Omega_p)(\omega_1 - \omega_2 + \Omega_p)} \right) \cos(2\phi_2) \right. \\ & \left. - 4\omega_2 \sin(2\phi_2) \right),\end{aligned} \tag{5.62b}$$

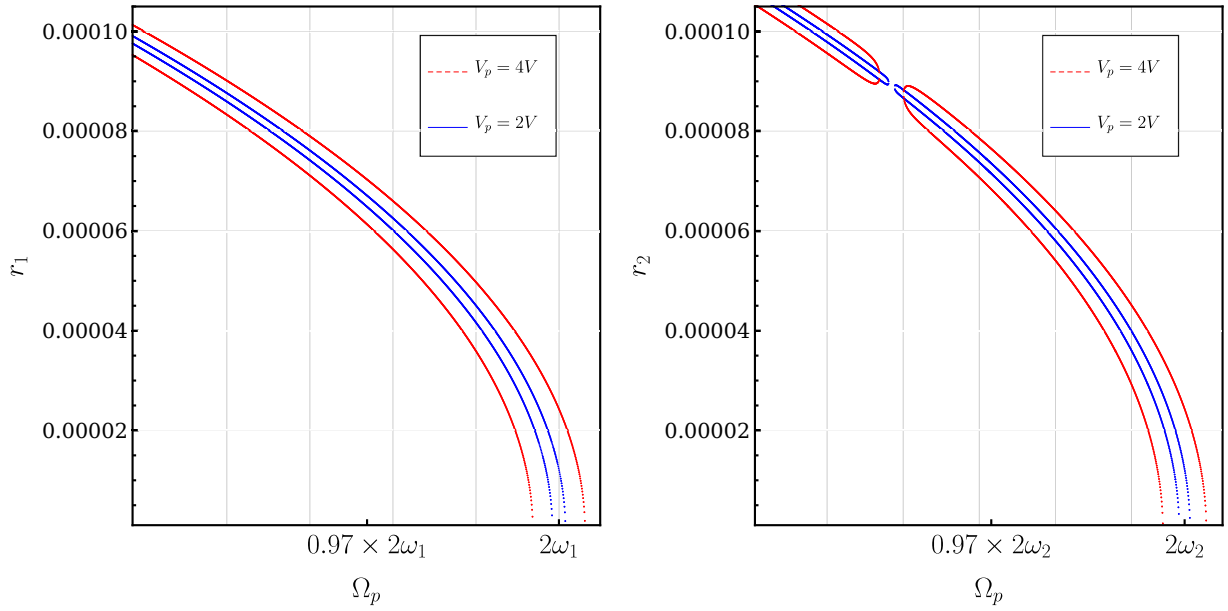

(a) $\Omega_p \simeq 2\omega_1$ (b) $\Omega_p \simeq 2\omega_2$

Figure 5.8: Frequency response curves of the normal form at primary resonances for two voltage values

$$\dot{\phi}_1 = \frac{-\xi^2}{16\omega_1^2}\left(\frac{1}{2\omega_1+\Omega_p} - \frac{4\omega_1(\omega_1^2-\omega_2^2+\Omega_p^2)\cos(\zeta_{21})}{(\Omega_p^2-(\omega_1-\omega_2)^2)(\Omega_p^2-(\omega_1+\omega_2)^2)}\right)$$
$$+\frac{1}{8\omega_1}\left(-\delta_1^2+4\omega_1(2\omega_1-\frac{a_9b_9\omega_1}{\omega_1^2-\omega_2^2}-\Omega_p)+(3a_4+(-3a_1+a_6)\omega_1^2)r_1^2+2(a_5-a_2\omega_1^2+a_7\omega_2^2)r_2^2\right)$$
$$+\frac{\xi}{16\omega_1^2}\left(-4\omega_1\cos(2\phi_1)+\frac{4a_9\omega_1(\omega_1-\Omega_p)\sin(\zeta_{21}-2\phi_1)}{(\Omega_p-\omega_1)^2-\omega_2^2}+(-\delta_1-\frac{4b_9\omega_1^2}{\omega_1^2-\omega_2^2}-\frac{2\delta_1\omega_1}{\Omega_p})\sin(2\phi_1)\right), \tag{5.62c}$$

$$\dot{\phi}_2 = \frac{-\xi^2}{16\omega_2^2}\left(\frac{1}{2\omega_2+\Omega_p} - \frac{4\omega_2(\omega_2^2-\omega_1^2+\Omega_p^2)\cos(\zeta_{21})}{(\Omega_p^2-(\omega_1-\omega_2)^2)(\Omega_p^2-(\omega_1+\omega_2)^2)}\right)$$
$$+\frac{1}{8\omega_2}\left(-\delta_2^2+4\omega_2(2\omega_2+\frac{b_9a_9\omega_2}{\omega_1^2-\omega_2^2}-\Omega_p)+(3b_4+(-3b_1+b_6)\omega_2^2)r_2^2+2(b_5+b_7\omega_1^2-b_2\omega_2^2)r_1^2\right)$$
$$+\frac{\xi}{16\omega_2^2}\left(-4\omega_2\cos(2\phi_2)+\frac{4a_9\omega_2^2\sin(\zeta_{21}-2\phi_2)}{\omega_2^2-\omega_1^2}+(-\delta_2+\frac{4b_9\omega_2(\omega_2-\Omega_p)}{\omega_1^2-(\Omega_p-\omega_2)^2}-\frac{2\delta_2\omega_2}{\Omega_p})\sin(2\phi_2)\right). \tag{5.62d}$$

Calculating the nontrivial fixed points of the normal form in polar coordinates gives the frequency response curves plotted in Fig. (5.8) for the same two V_p voltage values which were used before. The system shows a highly nonlinear softening behavior around the primary parametric resonances $\Omega_p = 2\omega_1$ and $\Omega_p = 2\omega_2$. Moreover, an interesting phenomenon appears

in the response curve of r_2 about the primary parametric resonance of the second mode. At about $0.95 \times 2\omega_2$ an *isolated* branch occurs, or *isola* [126]. Moreover, a clear distinction could be made by comparing Fig. 5.8 with Fig. 5.5, which was calculated in the simplified case under forced excitation. The comparison shows a much more pronounced nonlinear behavior under parametric excitation, which could be related to the excitation method rather than the excitation amplitude. The existence of nontrivial fixed points in a wide range of the subharmonic interval could be beneficial in terms of parametric amplification, if the trivial solution is destabilized. This would be particularly important for microsystems in general including the system under investigation.

5.8 Conclusions

The micro-ring gyroscope is nonlinearly modeled, taking into consideration the nonlinear elasticity following Natsiavas model [125] as well as the nonlinear electromechanical coupling with the electrodes. All coefficients of the dynamical system are defined by geometry and material properties or by excitation parameters. However, only two parameters, the electrode-ring gap d and applied DC voltage V_{dc}, could be used to trigger different dynamic phenomena. It was found that increasing V_{dc} could cause divergence (negative stiffness) and a subcritical pitchfork bifurcation. But for further analyses only the pre-bifurcation value is used, that is, when the trivial solution is stable. The system is first simplified and the drive mode is subjected to forced excitation without any parametric pumping. This yielded a clear Duffing softening behavior in the resonance curve, which comes in accordance with [78]. The system is then analyzed when subjected to the proposed bimodal phase-shifted excitation in the previous chapters. The system exhibits a clear softening behavior, but with extended branches to cover a wide range of the subharmonic frequency range. However, the inclusion of back-couplings from the sense degree of freedom q_2 gives various phenomena to occur in the subharmonic region of the primary parametric resonance frequency, including an isolated branch in the resonance curve of the second (sense) mode.

Appendix

Appendix 5.A Coefficients of system (5.60)

$$A_1 = -\frac{1}{2}\delta_1 - \frac{i\delta_1^2}{8\omega_1} + \frac{i}{16\omega_1^2}\left(\omega_1^3(16 - \frac{8a_9b_9}{\omega_1^2-\omega_2^2}) - \frac{\zeta_{11}^2}{2\omega_1+\Omega_p} + 2e^{-i(\zeta_{12}+\zeta_{21})}\xi_{12}\xi_{21}\omega_1\left(\frac{e^{2i\zeta_{21}}}{(\Omega_p+\omega_1-\omega_2)(\Omega_p+\omega_1+\omega_2)} + \frac{e^{2i\zeta_{12}}}{(\Omega_p-(\omega_1-\omega_2))(\Omega_p-(\omega_1+\omega_2)}\right)\right) \tag{5.63a}$$

$$A_2(t) = -\frac{ie^{i(\zeta_{11}+\Omega_p t)}\xi_{11}}{4\omega_1} + \frac{e^{i\Omega_p t}}{16\omega_1^2}\left(\frac{4b_9e^{i\zeta_{12}}\xi_{12}\omega_1^2}{\omega_1^2-\omega_2^2} + \frac{e^{i\zeta_{11}}\delta_1\xi_{11}(2\omega_1+\Omega_p)}{\Omega_p} + \frac{4a_9e^{i\zeta_{21}}\xi_{21}\omega_1(\omega_1-\Omega_p)}{(\omega_1-\omega_2-\Omega_p)(\omega_1+\omega_2-\Omega_p)}\right) \tag{5.63b}$$

$$A_3 = \frac{1}{2\omega_1^3}\left(3ia_4 + \omega_1(a_1(\delta_1 - 3i\omega_1) + ia_6\omega_1)\right) \tag{5.63c}$$

$$A_4 = \frac{i}{\omega_1\omega_2^2}\left(a_5 + a_2(i\delta_1 - \omega_1)\omega_1 + a_7\omega_2^2\right) \tag{5.63d}$$

$$B_1 = -\frac{1}{2}\delta_1 + \frac{i\delta_1^2}{8\omega_1} - \frac{i}{16\omega_1^2}\left(\omega_1^3(16 - \frac{8a_9b_9}{\omega_1^2+\omega_2^2}) - \frac{\zeta_{11}^2}{2\omega_1+\Omega_p} + 2e^{-i(\zeta_{12}+\zeta_{21})}\xi_{12}\xi_{21}\omega_1\left(\frac{e^{2i\zeta_{12}}}{(\Omega_p+\omega_1-\omega_2)(\Omega_p+\omega_1+\omega_2)} + \frac{e^{2i\zeta_{21}}}{(\Omega_p-(\omega_1-\omega_2))(\Omega_p-(\omega_1+\omega_2)}\right)\right) \tag{5.63e}$$

$$B_2(t) = -\frac{e^{-\Omega_p t}}{16}\left(\frac{4b_9 e^{-i\zeta_{12}}\xi_{12}}{\omega_1^2-\omega_2^2} + \frac{e^{-i\zeta_{11}}\xi_{11}(2\delta_1\omega_1 + 4i\omega_1\Omega_p + \delta_1\Omega_p)}{\omega_1^2\Omega_p} + \frac{4a_9 e^{-i\zeta_{21}}\xi_{21}(\omega_1-\Omega_p)}{\omega_1(\omega_1-\omega_2-\Omega_p)(\omega_1+\omega_2-\Omega_p)}\right) \tag{5.63f}$$

$$B_3 = \frac{1}{2\omega_1^3}\left(-3ia_4 + \omega_1(a_1(\delta_1+3i\omega_1) - ia_6\omega_1)\right) \tag{5.63g}$$

$$B_4 = -\frac{i}{\omega_1\omega_2^2}\left(a_5 + ia_2(\delta_1+i\omega_1)\omega_1 + a_7\omega_2^2\right) \tag{5.63h}$$

$$C_1 = -\frac{1}{2}\delta_2 - \frac{2i\delta_2^2}{16\omega_2} + \frac{i}{16\omega_2^2}\left(\omega_2^3(16 + \frac{8a_9b_9}{\omega_1^2-\omega_2^2}) - \frac{\zeta_{22}^2}{2\omega_2+\Omega_p} + 2\omega_2\left(-\frac{e^{-i(\zeta_{12}-\zeta_{21})}\xi_{12}\xi_{21}}{(\omega_1+\omega_2-\Omega_p)(\omega_1-\omega_2+\Omega_p)} + \frac{e^{i\zeta_{12}-\zeta_{21}}\xi_{12}\xi_{21}}{(\Omega_p-\omega_1+\omega_2)(\Omega_p+\omega_1+\omega_2)}\right)\right) \tag{5.63i}$$

$$C_2(t) = -\frac{ie^{i\zeta_{22}+\Omega_p t}\xi_{22}}{4\omega_2} - \frac{e^{\Omega_p t}}{16\omega_2^2\Omega_p(\omega_1^2-\omega_2^2)(\omega_1+\omega_2-\Omega_p)(\omega_1-\omega_2+\Omega_p)}\left(-4a_9e^{i\zeta_{21}}\xi_{21}\omega_2^2\Omega_p(-\omega_1^2+(\omega_2-\Omega_p)^2) + 4b_9e^{i\zeta_{12}}\xi_{12}\omega_2(\omega_1^2-\omega_2^2)(\omega_2-\Omega_p)\Omega_p - e^{i\zeta_{22}}\delta_2\xi_{22}(\omega_2^2-\omega_1^2)((\omega_2-\Omega_p)^2-\omega_1^2)(2\omega_2+\Omega_p)\right) \tag{5.63j}$$

$$C_3 = \frac{1}{2\omega_2^3}\left(3ib_4 + \omega_2(b_1(\delta_2-3i\omega_2) + ib_6\omega_2)\right) \tag{5.63k}$$

$$C_4 = -\frac{i}{\omega_1^2\omega_2}\left(b_5 + ib_2(-\delta_2+i\omega_2)\omega_2 + b_7\omega_1^2\right) \tag{5.63l}$$

$$D_1 = -\frac{1}{2}\delta_2 + \frac{2i\delta_2^2}{16\omega_2} - \frac{i}{16\omega_2^2}\left(\omega_2^3(16 + \frac{8a_9b_9}{\omega_1^2-\omega_2^2}) - \frac{\zeta_{22}^2}{2\omega_2+\Omega_p} + 2\omega_2\left(-\frac{e^{-i(\zeta_{12}-\zeta_{21})}\xi_{12}\xi_{21}}{(\omega_1+\omega_2-\Omega_p)(\omega_1-\omega_2+\Omega_p)} + \frac{e^{i\zeta_{12}-\zeta_{21}}\xi_{12}\xi_{21}}{(\Omega_p-\omega_1+\omega_2)(\Omega_p+\omega_1+\omega_2)}\right)\right) \tag{5.63m}$$

$$D_2(t) = \frac{e^{-\Omega_p t}}{16}\left(\frac{-4a_9 e^{-i\zeta_{21}}\xi_{21}}{\omega_1^2-\omega_2^2} + \frac{e^{-i\zeta_{22}}\xi_{22}(2\delta_2\omega_2 + 4i\omega_2\Omega_p + \delta_2\Omega_p)}{\omega_2^2\Omega_p} + \frac{b_9 e^{-i\zeta_{12}}\xi_{12}(\omega_2-\Omega_p)}{\omega_2(\omega_2-\omega_1-\Omega_p)(\omega_1+\omega_2-\Omega_p)}\right) \tag{5.63n}$$

$$D_3 = \frac{1}{2\omega_2^3}\left(-3ib_4 + \omega_2(b_1(\delta_2+3i\omega_2) - ib_6\omega_2)\right) \tag{5.63o}$$

$$D_4 = -\frac{i}{\omega_1^2\omega_2}\left(b_5 + ib_2(\delta_2+i\omega_2)\omega_2 + b_7\omega_1^2\right) \tag{5.63p}$$

6 Experimental investigation of a microsystem

In this chapter, the experimental investigations and the accompanying model aim at exploring the behavior of a two-degree-of-freedom system composed of two coupled microcantilevers that is subjected to bimodal parametric excitation. Although different configurations of bimodal parametric excitation were conducted experimentally before, but the implementation of asynchronous parametric excitation could be found in a single publication carried out on an electronic system [36]. Thereby, the conducted experiment in this thesis should be the first one to be carried out on a mechanical system or on a microelectromechanical system to the best of the author's knowledge.

The main goal of this study is to validate some of the theoretical findings discussed in the previous chapters, and especially the broadband destabilization phenomenon under asynchronous parametric excitation. To this end, an experimental setup was implemented at the Technical University of Ilmenau in a collaboration with the team of Prof. Thomas Sattel. The author's contribution in the setup included an electronic circuit to apply the bimodal parametric excitation scheme and to study the effect of the excitation asynchronicity on the stability of the system in view of the theory presented before. Finally, the experimental findings are compared with numerical results calculated through a lumped-parameter model. This comparison gives an insight for explaining and extending the experimental observations.

6.1 General experimental setup

The experimental setup used in these experiments is composed of three major systems. The first system is the mechanical system under study which contains two microcantilevers, whose vibrations are isolated from each other at their resonant frequencies. The second system is composed of an electronic control circuit which was designed and implemented in cooperation

between the two groups of Prof. Hagedorn (Technical University of Darmstadt) and Prof. Thomas Sattel (Technical University of Ilmenau). The third one is the signal generation and acquisition system containing digital oscilloscopes, a laser vibrometer and a computer.

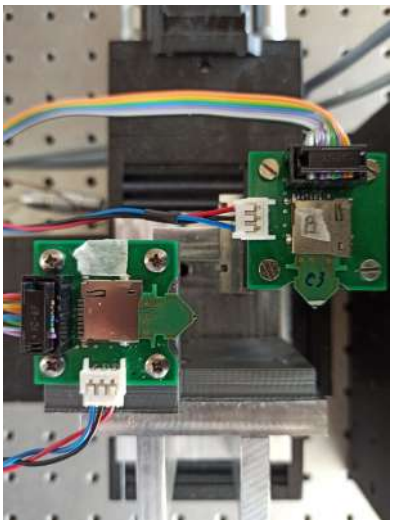

(a) Stage 1

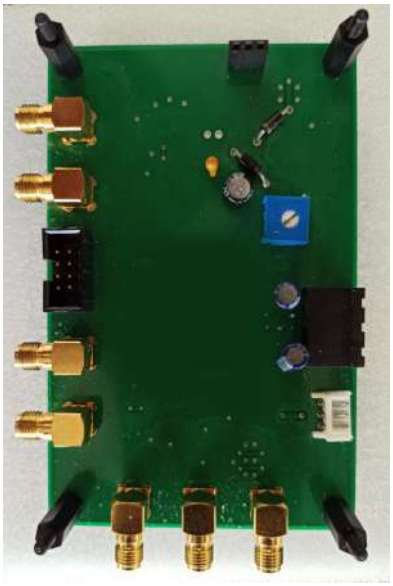

(b) Stage 2

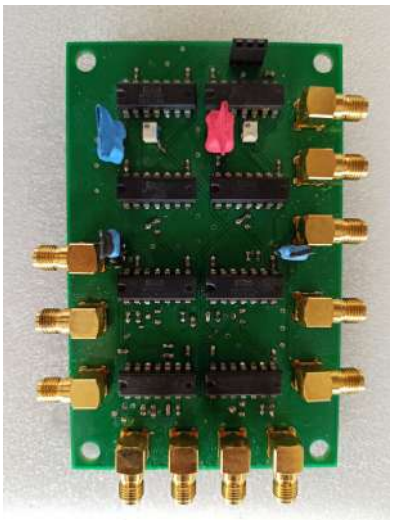

(c) Stage 3

Figure 6.1.1: Pictures of the three-stage electronic circuit boards

6.1.1 Cantilevers

The micro-cantilevers are manufactured by the company nano analytik GmbH and attached to a printed circuit board (PCB) with micro-SD connectivity terminals (see Fig. 6.1.2). They are produced mainly to function as probes in Atomic Force Microscopes. The micro-cantilever has a built-in piezoresistive sensor with a Wheatstone bridge placed at its root, and an electro-thermo-mechanical actuator shown as a zigzag-shaped wire in the figure. The actuator is composed of a conductive aluminum wire attached to a silicon dioxide layer situated above a silicon substrate. Since both materials have different thermal expansion values, this configuration acts as a bimorph actuator controlled through an applied current, which heats up the aluminum wire. However, since this metallic layer is very thin, exceeding a certain voltage limit leads normally to irreversible deformation and distorted dynamic behavior. This property will act as the upper limitation condition for the excitation amplitudes used in these experiments.

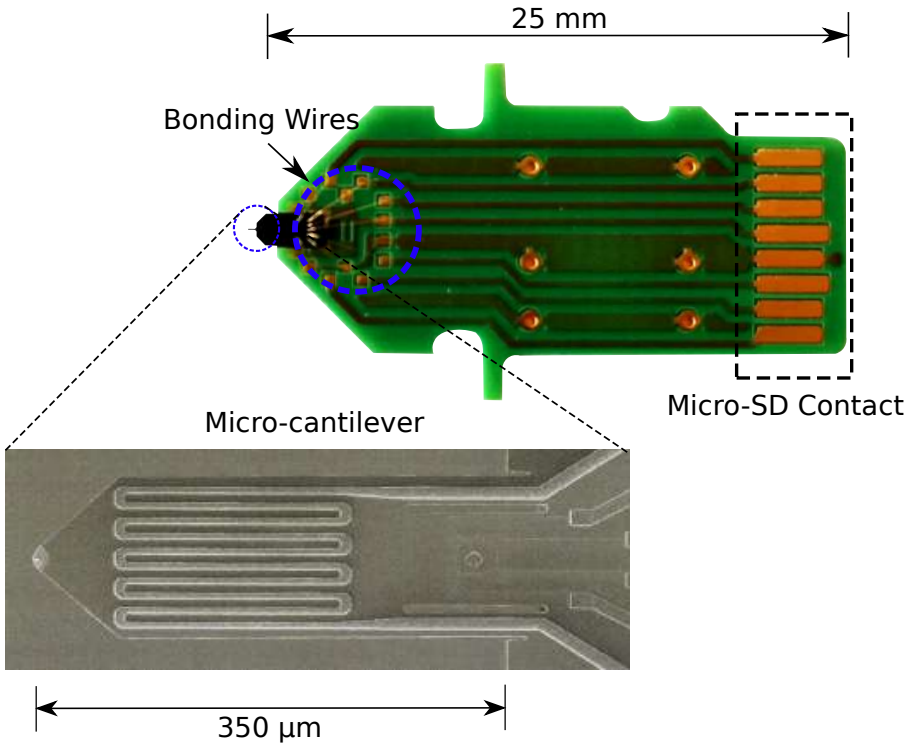

Figure 6.1.2: Microcantilever and its holding Micro-SDCard

6.1.2 Electronic circuitry

The electronic control system is developed in three stages, which are shown in Fig. 6.1.1. The first stage (Stg1) contains a pre-amplifier for the piezo-resistive displacement sensor in addition to being an interface between the cantilevers mounted on the micro-SD card and the rest of the control circuit. The second stage (Stg2) comprises the amplification and filtering modules for the incoming sensor signal, as well as current-voltage converters for excitation signals before being applied on the thermoelectric actuator. Stg2 acts as an mid-stage between Stg1 and the third stage (Stg3). Both the first two stages of the electronic system were developed and assembled by Hans-Georg Pietscher in Ilmenau [127]. A brief description of the electronic circuits for the boards Stg1 and Stg2 is provided in Appendix 6.A.

The third stage (Stg3) represents the contribution of the author and contains the parametric excitation circuitry in addition to added nonlinear feedback signals. This is explained through the schematic drawing in Fig. 6.1.3. In this figure both Stg1 and Stg2 are represented compactly as amplifiers connected directly to either the sensor or the actuator of both cantilevers. However, Stg3 interfaces only with Stg2. The input/output ports of Stg3 could be classified into incoming sensor signals, output excitation signals and control signals. The incoming sensor signals from Stg2 are shown in Fig. 6.1.3 as *S1*, the sensor signal of the first cantilever, and *S2* the sensor

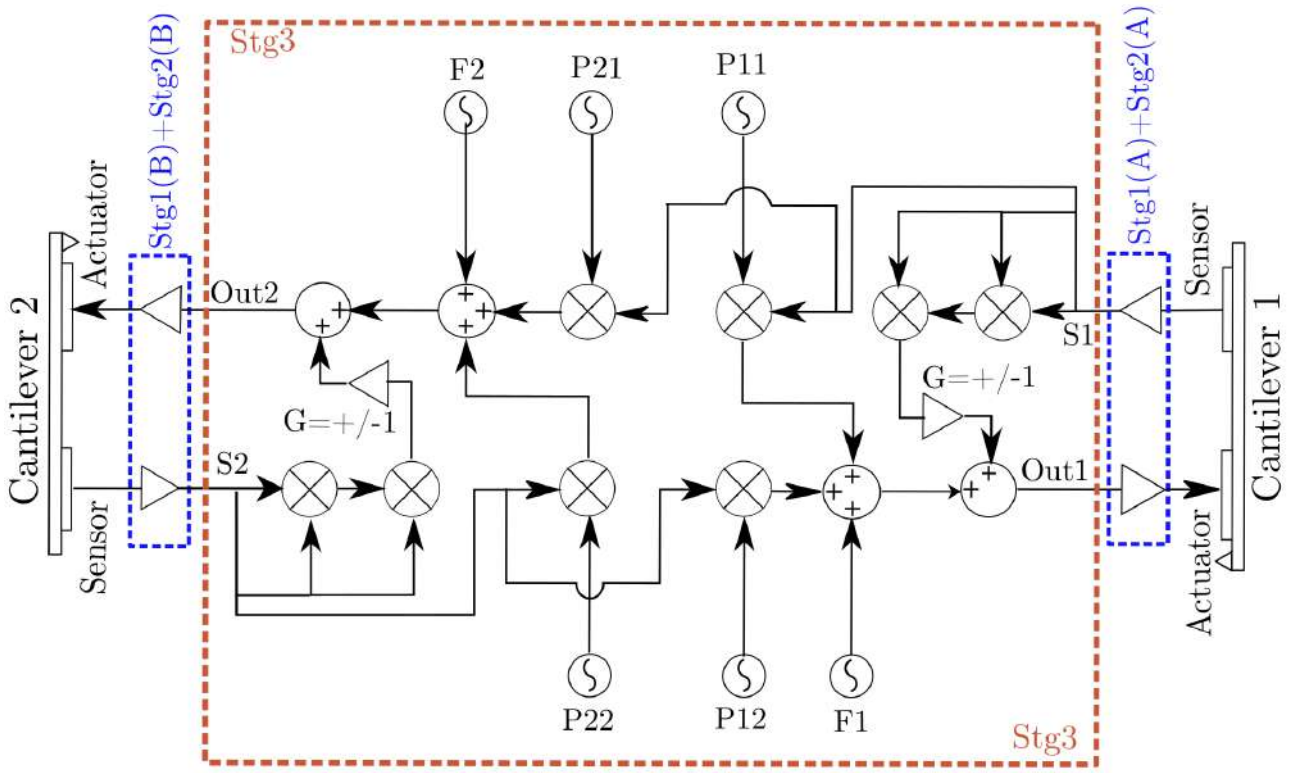

Figure 6.1.3: Schematic of Stg3 in the electronic control system (see Fig. 6.1.1(c)).

signal of the second cantilever. Stg3 can possibly send two kinds of output signals towards Stg2, either signals carrying only parametric excitation or signals carrying parametric excitation in addition to cubic nonlinearities. Throughout this work, only the latter is used and named *Out1* and *Out2*, each corresponds to one of the cantilevers. The control signals come from the oscilloscopes (see Fig. (6.1.4)). They include parametric excitation signals, which are input to Stg3 through the ports *P11*, *P12*, *P21* and *P22*, and the forced excitation signals through the ports *F1* and *F2*.

As can be shown using Fig. (6.1.3), the role of this electronic circuit is to provide two types of signal processing, the parametric excitation coupling and the electronic initiation of nonlinear terms in the two-cantilever dynamical system. The first task is implemented through four multipliers of the type MPY634KP, each one represents a parametric excitation term in the 2×2 parametric excitation matrix of the dynamical system, and each one is supplied with a single control signal, which is named in accordance with the intended parametric excitation term. A circuit diagram explaining the connections of the multipliers is provided in Appendix 6.B.

Putting the mechanical system in addition to the electronic one (Fig. 6.1.3) in a mathematical

form of a two-degree-of-freedom system, we get

$$\underbrace{\boldsymbol{M}\ddot{\boldsymbol{q}} + \boldsymbol{D}\dot{\boldsymbol{q}} + \boldsymbol{K}\boldsymbol{q} + \tilde{\boldsymbol{f}}_{nl}}_{\text{mechanical system}} + \underbrace{\begin{bmatrix} P11 & P12 \\ P21 & P22 \end{bmatrix} \boldsymbol{q} + \begin{Bmatrix} NL1\, q_1^3 \\ NL2\, q_2^3 \end{Bmatrix} = \begin{Bmatrix} F1 \\ F2 \end{Bmatrix}}_{\text{electronic system}}. \tag{6.1}$$

Here we have expanded the parametric excitation matrix and the forced excitation vector to illustrate work principle of the electronic board Stg3, where $\boldsymbol{q}$ is the vector of modal coordinates, D and K are the damping and stiffness matrices respectively, $NL1$ and $NL2$ are the coefficients of the electronically induced nonlinear cubic terms, $\tilde{\boldsymbol{f}}$ represents the system's inherent nonlinear terms, and $F1$ and $F2$ are the forced excitation terms.

In (6.1) the four parametric excitation control signals $P11, P12, P21$ and $P22$ are represented in a 2×2 matrix form, where $P11$ and $P22$ are intrinsic parametric excitation signals, whilst $P12$ and $P21$ are the coupling excitation signals. In view of the schematic diagram, Fig. 6.1.3, equation (6.1) could be explained as follows.

Firstly, as an example of the parametric excitation, the multiplier connected to the port $P12$ takes the sensor signal $S2$, multiplies it by $P12$ signal and inputs it to the forcing output of the first degree of freedom $Out1$, which also receives the output of the multiplier feed by $P11$. The same could be said for $P22$ and $P21$ feeding $Out2$.

Secondly, The electronically induced nonlinearities are implemented through the same type of multipliers, where the sensor signal is multiplied by itself two times through two successive multipliers and added to the parametric excitation signal and the forced excitation signals at the final output $Out1$ or $Out2$. These nonlinearities correspond directly to the electronically induced nonlinear terms $NL1 \times S1^3$ and $NL2 \times S2^3$, where $S1, S2$ are the sensor signals corresponding to $\boldsymbol{q} = q_1, q_2$ in the equation.

Thirdly, the forced excitation terms $F1$ and $F2$ are implemented by using an addition function in the mentioned multipliers. Thus, the multiplier MPY634KP gives an output of two multiplied signals and another added one. Then the output $Out1$, for instance, comprises the four forcing elements, the two parametrically excited signals $P11 \times S1, P12 \times S2$, the forced excitation $F1$ and the induced nonlinearity $S1^3$.

To sum up the signal flow in this circuit, the sensor signals of both cantilevers $S1$ and $S2$ are input to the four multipliers and represented in (6.1) as q_1 and q_2 respectively. The outputs $Out1$ and $Out2$ are summations of the parametric excitation terms, the forced excitation terms

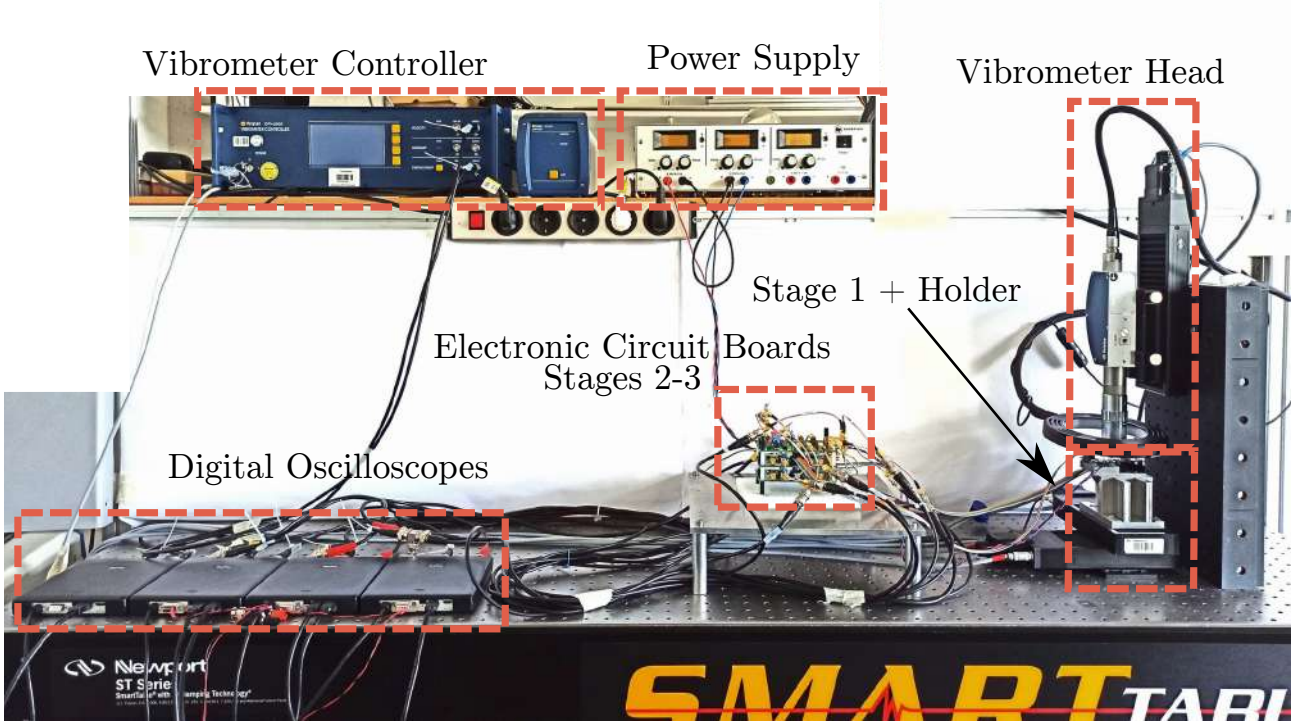

Figure 6.1.4: A picture of the whole measurement system with labels indicating the main components; the electronic system, the vibrometer, and the oscilloscopes.

and the nonlinear terms. That is,

$$Out1 = -P11 \times S1 - P12 \times S2 + F1 - NL1 \times S1^3, \tag{6.2a}$$

$$Out2 = -P21 \times S1 - P22 \times S2 + F2 - NL2 \times S2^3, \tag{6.2b}$$

where other gains and factors are eliminated for brevity. The negative signs before some of the terms in (6.2) are considered to comply with the mathematical formulation in (6.1).

6.1.3 General connection plan

As can be shown in Fig. 6.1.4, the experimental setup can be broken down into the main components mentioned before, the cantilevers, the electronic control system, and the measurement system containing the oscilloscopes and the vibrometer. As explained before, the cantilevers are connected to the electronic circuit via Stg1. The electronic system is interconnected according to the requirements of each experiment, which will be explained in each experiment in detail. Secondly, the four oscilloscopes act as a signal-acquisition and generation system, that is, they interface with the electronic circuit to provide excitation signals or receive measured signals.

On the other hand, the control scripts, written on Matlab (see Appendix 6.D) are used to control these oscilloscopes. Moreover, the oscilloscopes are connected to each other via a synchronization bus, such that they could measure and generate wave signals at the same sample frequency and with synchronized timing. This last configuration step is significantly important in generating different waves with certain phase-shift as will be shown afterwards. In addition, the cantilever vibrations are measured using a laser vibrometer, which sends its signals also to the oscilloscopes. Relying on the Doppler effect, the vibrometer measures the vibration velocities, and in addition the vibrometer used in this work provides a hardware-based time-integration of the velocity signal to provide a displacement signal. More information about the devices used in the experiments is given in Appendix 6.C.

The integration of the vibrometer in the setup is important here for two reasons. Firstly, its signals are not affected by the electronic noise that may appear in the piezoresistive sensor signals, in that way we can differentiate between noise induced outputs and vibration induced ones. Secondly, the vibrometer can provide a calibration relation between sensor supplied voltage and the actual displacement values in nanometers nm. Using the gains of the whole electronic system and the sensor gain, this information could be calculated, but the vibrometer provides a more direct and much more accurate method for the same goal. Since only one vibrometer is available, it points normally to the cantilever C1 in coupled system measurements.

6.2 Characterization of Cantilevers

This experiment involves the dynamic characterization of the used cantilevers, C1 and C2, in the parametric excitation experiments carried out afterwards. The characterization includes the determination of the natural frequency and the quality factor.

6.2.1 Experimental Setting

The experimental setup includes one cantilever, either C1 or C2, connected to a corresponding Stg1 board, which is connected to Stg2. The parametric excitation circuit is excluded here of course, so Stg3 is not connected in this experiment. Stg2 gains its sinusoidal forced excitation input from an oscilloscope's generator, and transfers it after processing to the thermo-actuator on Stg1, which brings the cantilever into oscillation. Stg2 receives the sensor signal again from Stg1, and forwards it after band-pass filtering again to the oscilloscope. The generator signal is supplied by a MatLab code and the sensor signal is again acquired by the computer through the oscilloscope. The cantilever vibrations, are measured through the sensor signal, and in

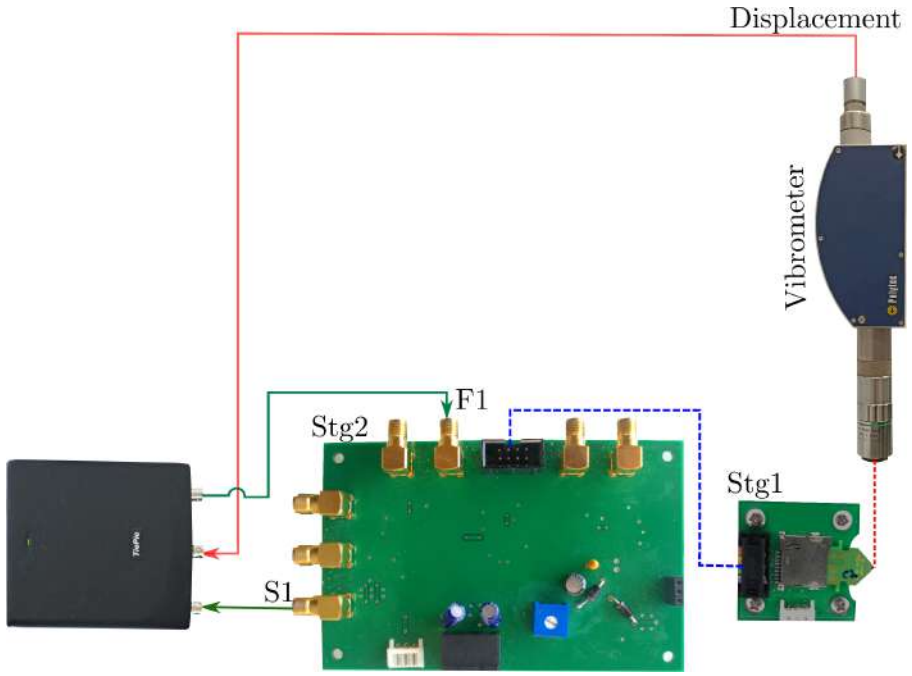

Figure 6.2.1: The connection plan for the characterization experiment

addition through the vibrometer displacement signal.

6.2.2 Measurement procedure

The natural frequency of each cantilever is determined at first approximately using manual tuning of the excitation frequency ω_i using the oscilloscope's manufacturer software. That was only done in order to define a narrow frequency band, within which the frequency response curve would be afterwards determined. Then, the frequency sweep algorithm with the excitation signal $F = 0.5V + 1V \times cos(\omega_f t)$ is used to determine the frequency response curve, where $\omega_f = \omega_i \pm 500\ Hz$, and ω_i is the approximately determined cantilever's natural frequency. In addition, the cantilever is subjected to a step-function excitation at the natural frequency, and then left to exhibit free oscillations. From both experiments the natural frequency and cantilever's quality factor in ambient atmosphere are determined.

6.2.3 Results

The frequency response curves in Fig.(6.2.2) show a purely linear response, where the natural frequencies are found to be $\omega_{C1} = 100.98\ kHz$ and $\omega_{C2} = 101.6\ kHz$, while the quality factors are $Q_{C1} = 572$ and $Q_{C2} = 612$ respectively. To avoid ambiguity, the frequencies will

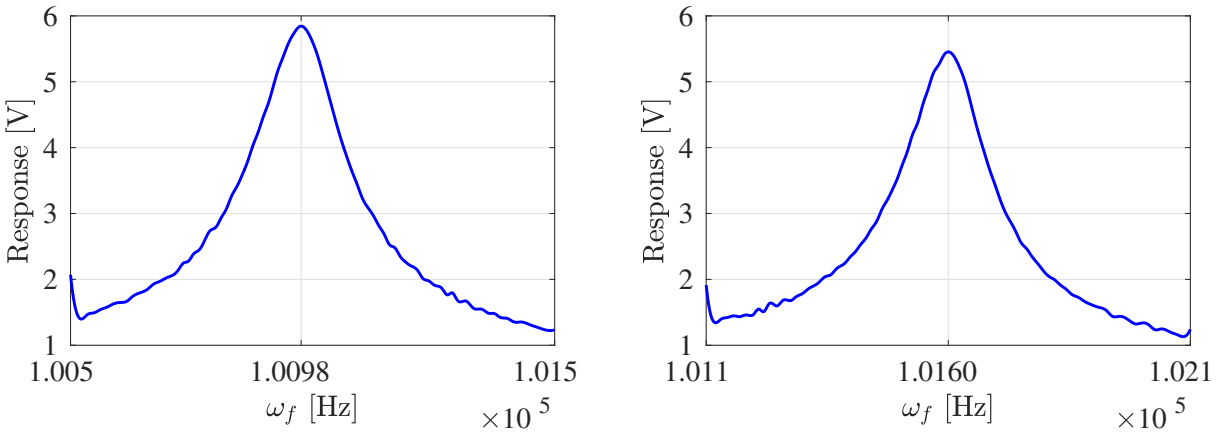

(a) C1 (b) C2

Figure 6.2.2: Frequency response curves of both cantilevers

be always represented in Hz, since this unit is preferable through measurement, however we will keep using ω instead of f. The 2π factor is taken into consideration through the mathematical and numerical calculations. Moreover, the responses of the cantilevers acquired through the piezoresistive sensor were calibrated using the vibrometer signals giving a a relation of $1V$ (sensor response) $\Rightarrow 83\,nm$ (vibration amplitude) for the C1 cantilever and $1V \Rightarrow 59\,nm$ for the C2 cantilever.

6.3 Bimodal parametric excitation

After determining the dynamic properties of both cantilevers through the previous experiment, we are now interested in investigating the effect of bimodal parametric excitation of the two-cantilever-system. In order to do that the third electronic board (Stg3) is then connected to the setup . As explained before in (6.1), there are four excitation signals ($P11, P12, P22$) and ($P21$), whereas the phase shift of the last signal with respect to the former three signals is set to zero or to $-\pi/2$. That is, we carry out two experiments, one with a phase shift and the other without. In each experiment the stability chart is then determined and the effect of adding the phase shift is discussed.

6.3.1 Experimental Setting

As depicted in Fig. (6.3.1), the two cantilevers (mounted on micro-SD cards) are connected to the electronic control system through Stg1 board. Each Stg1 board is connected to the corresponding Stg2 board. Both Stg2 boards are then connected to Stg3 board which is the

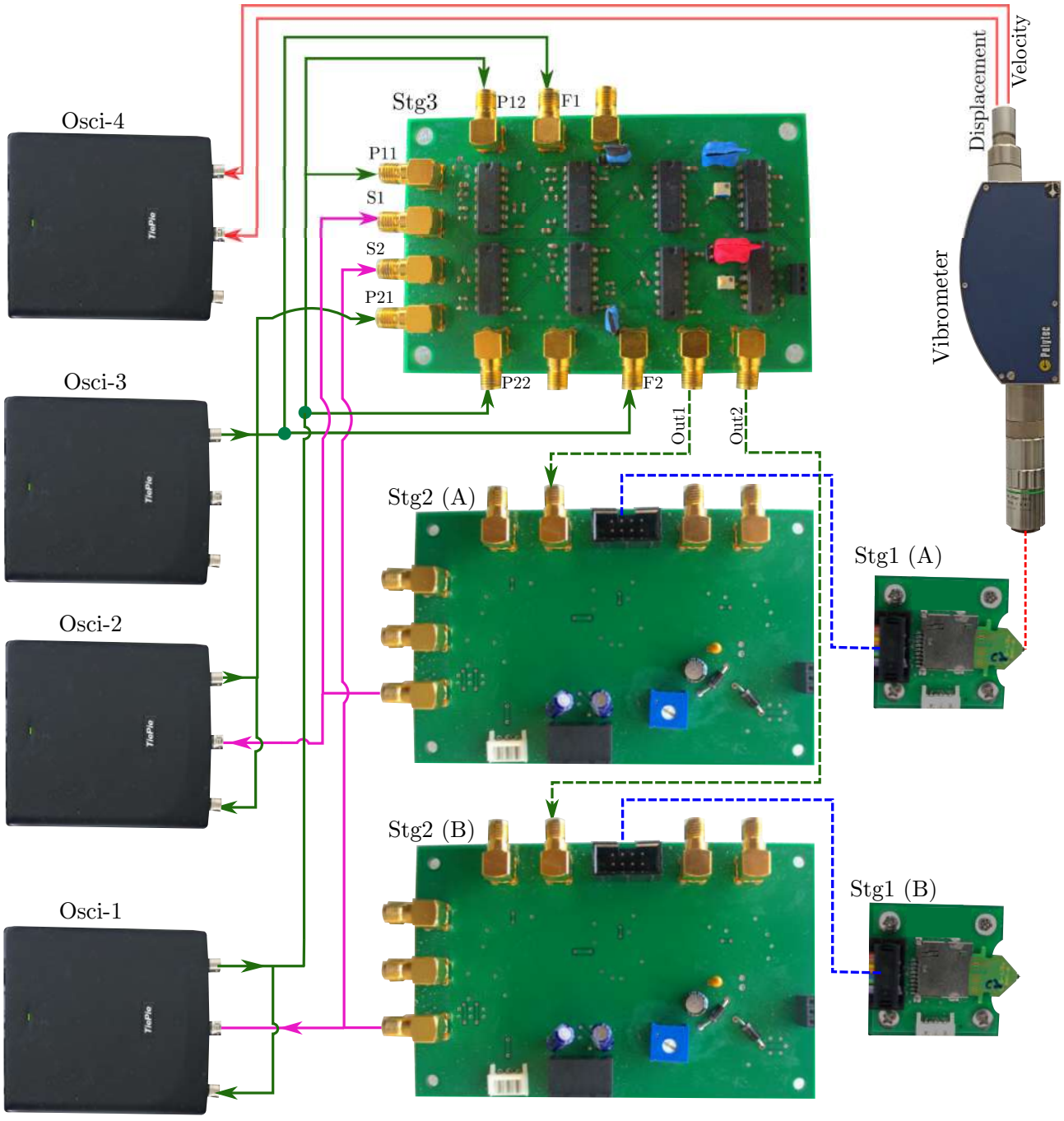

Figure 6.3.1: The connection plan for the bimodal excitation experiment

one responsible for initiating the parametric excitation of the system.

Three signal generators are used. One of them provides the parametric excitation signal to three multipliers on the Stg3 board, which are P_{11}, P_{22} and P_{12}. The last multiplier P_{21} is connected to a different signal generator in order to allow for inducing a phase shift with respect to the other three parametric excitation elements. The third generator is then used to provide both cantilevers with a 0.6 DC voltage. The sensor signals S_1 and S_2 are then captured by the digital oscilloscopes. And finally, the potential difference at the thermoelastic actuator is monitored, for the sake of insuring not having an overload (>2V) leading to failure. The Wheatstone bridge voltage is set at -3 V in order to provide an adequate signal amplitude.

The vibrometer laser is pointed to cantilever C1 in the whole experiment. Unfortunately, the vibrations of the cantilever C2 are only acquired through the piezoresistive sensor, since only one laser vibrometer could be used.

6.3.2 An electro-thermal effect

The mathematical modeling of the electro-thermal coupling mechanism for the investigated cantilever beams is not meant to be discussed here, however, an important feature of this actuation method will be highlighted for the sake of completeness with respect to the design of this experiment, and in order to explain the usage of a DC voltage in all of the described experiments.

Through the design of bimorph electrothermal actuators it is known that the electrothermal force acting on the mechanical system is proportional to the square of the applied voltage [128, 129], that is

$$F_{thermal} = \alpha V(t)^2. \tag{6.3}$$

As a result, since the applied voltage is periodic, we obtain only an actuation at double the excitation frequency. This means in the case of a parametric excitation the parametric force becomes

$$F_p(x,t) = \alpha F_0 \cos^2(\Omega_p t) x(t)^2 = \frac{F_0 \alpha}{2}(1 + \cos(2\Omega_p t)) x(t)^2. \tag{6.4}$$

To overcome this effect and to have only an excitation with Ω_p frequency a forced DC voltage is applied (corresponding to F_1,F_2 in (6.1)), this means

$$F_{tot} = \alpha \left[F_{DC} + F_{AC}(t)x(t)\right]^2 = \alpha \left[F_{DC} + F_0 \cos(\Omega_p t) x(t)\right]^2 \tag{6.5}$$

$$= \alpha \left[F_{DC}^2 + F_0 F_{DC} \cos(\Omega_p t) x(t) + \frac{F_0^2}{2}(1 + cos(2\Omega_p t)) x(t)^2\right]. \tag{6.6}$$

From this equation, two main conclusions are obtained. Firstly, the parametric excitation should have an accompanying DC forced excitation in order to have an effect from this actuation method. And secondly, the last term does not affect our measurements, since it describes a significantly higher frequency term which does not influence the dynamics of the mechanical system under the applied excitation conditions.

6.3.3 Measurement procedure

In accordance with (6.2), the experiment is carried out through applying a parametric excitation at each of $P11, P22$ and $P12$ with

$$Pij = V_p \cos(\Omega_p t), \tag{6.7}$$

while the fourth parametric excitation signal $P21$ has a phase shift ζ, thus

$$P21 = V_p \cos(\Omega_p t + \zeta), \tag{6.8}$$

where $\zeta = 0$ in the case of no phase-shift, or $\zeta = -\pi/2$, which is the only phase-shift considered in this work. This particular phase-shift value was shown before to lead to the aimed result of having a broadband destabilization of the trivial solution, see chapter 3.

In addition, the direct forcing component $F1$ and $F2$ are set to a constant voltage of 0.6 V. Although this does not contribute to the system dynamics, it is necessary to activate the parametric excitation in general. This corresponds to the quadratic effect induced by thermo-elastic excitation process explained in the previous section.

Before starting the experiment, the gains of Stg2 boards were adjusted, such that the threshold of instability for each cantilever alone at the double of the eigenfrequency is equal to approximately 3 V. This value was chosen in accordance with the maximum voltage the thermo-elastic actuator can sustain.

The measurement procedure involves discretizing the two-dimensional parameter space of excitation amplitude V_p and frequency Ω_p into a grid involving the three combination resonance frequencies $2\omega_{C1}, \omega_{C1} + \omega_{C2}$ and $2\omega_{C2}$ and up to a maximum excitation voltage of 4V, with an exception of the summation combination frequency for the phase-shifted excitation case. The difference combination resonance frequency is investigated alone, since it lies in a far away frequency range.

The measurement is then carried out by choosing values of the pair (V_p, Ω_p) inside the measurement grid, while the response is evaluated to give a resonance, i.e. instability, or no

resonance. Through this binary assessment the stability chart is constructed, and the borders of stability are found, giving the expected Arnold's tongues shape.

6.3.4 The stability chart

As shown in figures 6.4.3 and 6.4.4, the Arnold's tongues are found for the system with and without a phase-shift. The bimodal parametric excitation is applied on the cantilevers at frequency-amplitude pairs with a spacing of 10 Hz in frequency and 0.1 V in the excitation amplitude. Then, only the instability points are shown in the figures. A fitted curve is then computed to estimate the instability borderlines.

Fig. 6.4.3 shows different available maximum excitation amplitudes among different instability regions. This can be explained that the maximum attainable excitation amplitude for each instability tongue corresponds to the same maximum voltage applied on the thermoelastic actuator. The voltage applied on the actuator, however, is a product of the excitation amplitude and the sensor's feedback signal since it is a parametric excitation signal. Therefore, the maximum attainable voltage on the actuator (2 V) corresponds differently to different excitation amplitudes, which causes, as shown, different limitation values for the measured instability tongues.

Moreover, the instability regions are found at the primary resonance frequencies $\Omega_p = 2\omega_i,\ i = C1, C2$ and at the summation frequency $\Omega_p = \omega_{C2} + \omega_{C1}$ under synchronous excitation ($\zeta = 0$). While under asynchronous excitation ($\zeta = -\pi/2$) an instability tongue is also observed at the difference combination frequency $\Omega_p = \omega_{C2} - \omega_{C1}$.

The instability tongues for the synchronous case show also a frequency and amplitude shifting in comparison with those for $\zeta = -\pi/2$. A particular feature is the high amplitude shift for the tongue of summation combination resonance as shown in the figure. In addition, since the maximum available voltage that could be applied on the thermoelastic actuator without failure put a large constraint on the attainable results, the broadband destabilization feature could not be observed.

Thus, an alternative goal was put, which is to observe other features which could be enough to validate a mathematical model that predicts the broadband phenomenon. To this end, an additional analysis is carried out on measured instability tongues, which is to investigate the change in the topology of the stability chart in the two cases under study. To study the change in the geometry of each instability tongue, the instability tongue for each resonance case is then compared in both cases, with and without phase-shift. But since the instability tongues showed a substantial shifting in amplitude and frequency, they were centered with respect to

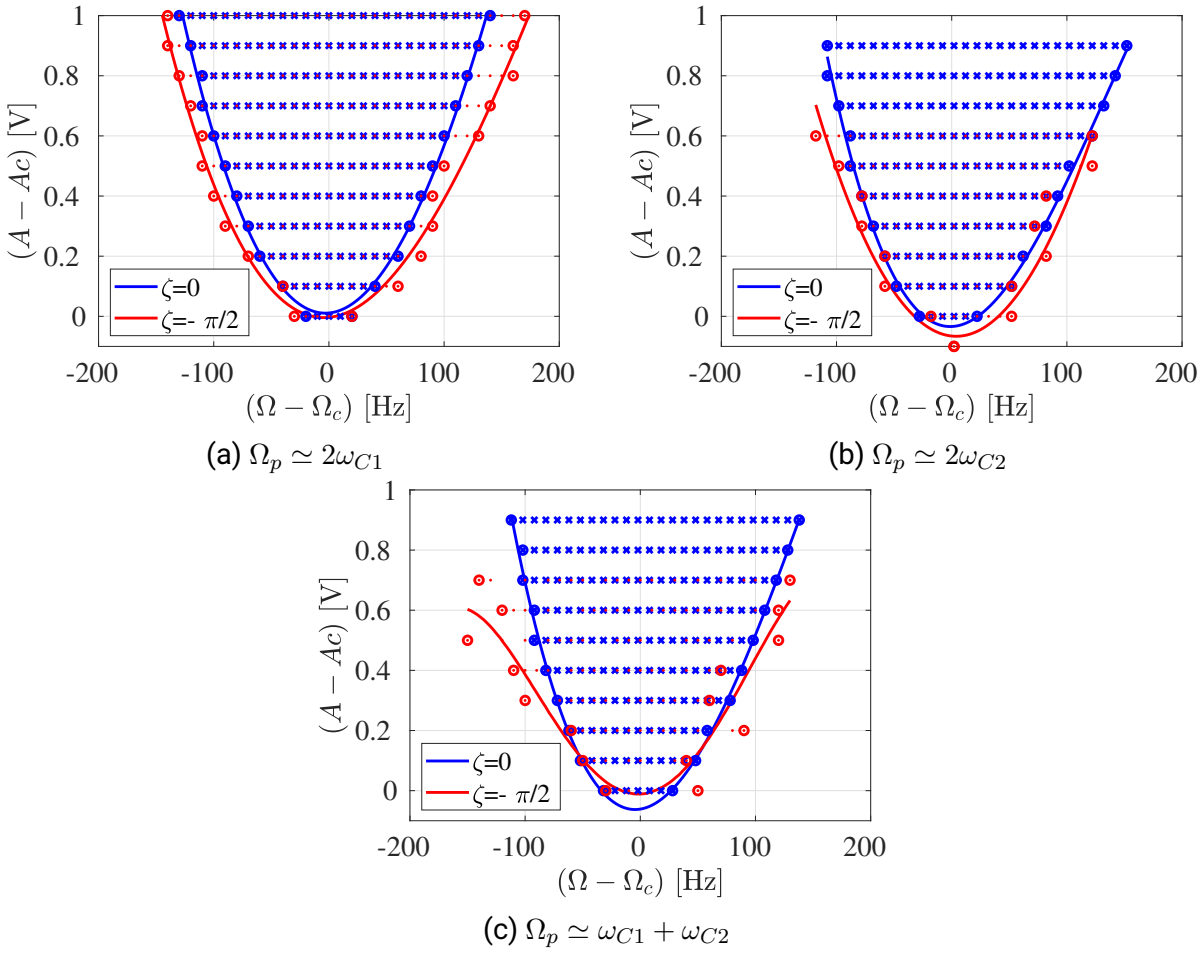

(a) $\Omega_p \simeq 2\omega_{C1}$ (b) $\Omega_p \simeq 2\omega_{C2}$

(c) $\Omega_p \simeq \omega_{C1} + \omega_{C2}$

Figure 6.3.2: Comparison between the instability tongues for $\zeta = 0$ and $\zeta = -\pi/2$

each other by shifting one of them in frequency and amplitude to a common centre (Ω_c, A_c). As depicted in Fig. 6.3.2 we can see obviously an increase of the tongues' widths in the case of having a phase-shift. It must be noted however, that they are not that significant, since all the experiments are done at low excitation levels. And returning to theory, this increase in width effect occurs nonlinearly with respect to the excitation amplitude. This will be discussed again later with respect to the model-based numerical results.

6.3.5 Experimental determination of the logarithmic increment

The change in system's Lyapunov exponents inside the instability tongues is intended to be measured in order to validate the previous theoretical findings for the theory of parametric excitation [37, 80]. By linearizing the investigated system around the trivial solution the

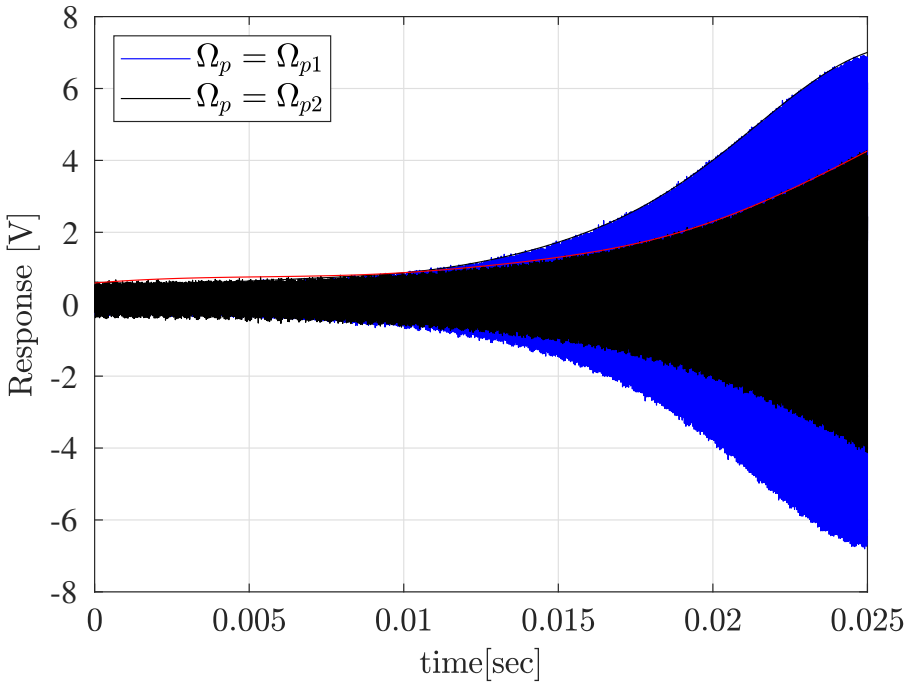

Figure 6.3.3: Divergent responses with different system exponents $Re(\lambda_1), Re(\lambda_2) > 0$ at different parametric excitation frequencies Ω_{p1}, Ω_{p2}.

system's Lyapunov exponent can be described by

$$Re(\lambda) = -\zeta_d \omega_i, \tag{6.9}$$

where $i = C1, C2$, and ζ_d is the damping ratio of the linearized system, which carries a negative value in case of instability. Therefore, for the sake of measuring $Re(\lambda)$, the damping ratio ζ_d is determined through the method of logarithmic decrement known from the theory of linear vibrations [130]. However, in this case it would be more proper to call it the *logarithmic increment*. In all cases, by measuring the response amplitudes $x(t_1)$ and $x(t_2)$, when $t_2 - t_1 = T$, and $T = 2\pi/\sqrt{1-\zeta_d^2}\omega_i$, we get

$$\frac{x(t_1)}{x(t_2)} = e^{\zeta_d \omega_i T} \frac{\cos(\sqrt{1-\zeta_d^2}\omega_i t - \phi)}{\cos(\sqrt{1-\zeta_d^2}\omega_i t - \phi + 2\pi)} \tag{6.10}$$

$$= e^{\zeta_d \omega_i T} = e^{\frac{2\pi\zeta_d}{\sqrt{1-\zeta_d^2}}}, \tag{6.11}$$

then

$$\delta_{inc} = ln\frac{x(t_1)}{x(t_2)} = \frac{2\pi\zeta_d}{\sqrt{1-\zeta_d^2}}, \tag{6.12}$$

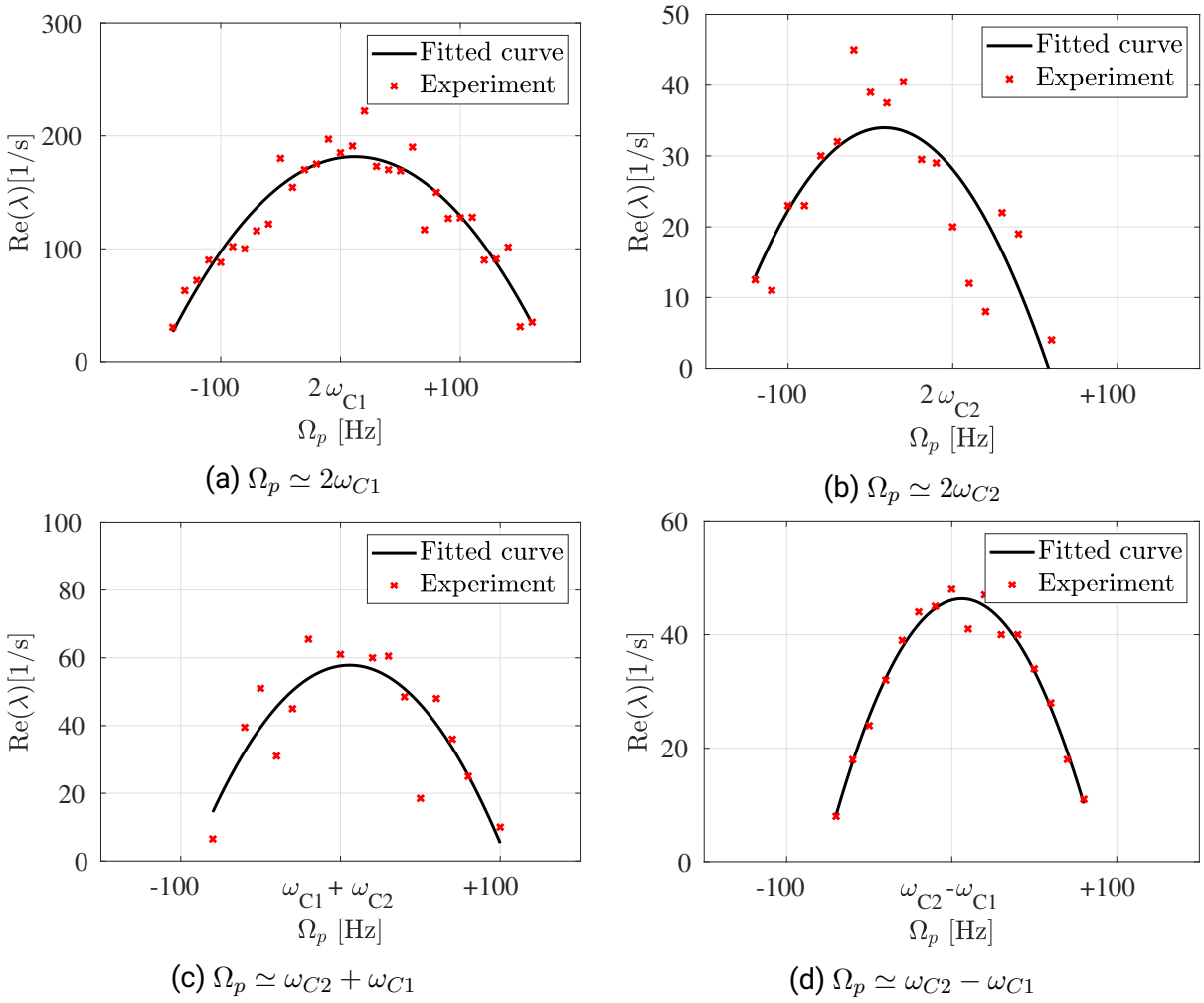

(a) $\Omega_p \simeq 2\omega_{C1}$

(b) $\Omega_p \simeq 2\omega_{C2}$

(c) $\Omega_p \simeq \omega_{C2} + \omega_{C1}$

(d) $\Omega_p \simeq \omega_{C2} - \omega_{C1}$

Figure 6.3.4: Measured values of $Re(\lambda)$ inside the instability tongues

where in this case both ζ_d and δ_{inc} have negative values.

An example of two different time histories at two different parametric excitation frequencies inside an instability tongue is shown in Fig. 6.3.3. As an example, from these two time histories two different values of $Re(\lambda)$ are calculated corresponding to two excitation frequencies Ω_p. By plotting the values of $Re(\lambda)$ against excitation frequencies inside each instability tongue, Fig. 6.3.4 is then obtained. From this figure, it could be shown that the change of $Re(\lambda)$ around the resonance frequency follows a near-parabolic shape, which coincides with the previous theoretical findings, for instance in Fig. 3.2 in chapter 3.

6.4 Lumped-parameter model and discussion

The two-cantilever system is modeled as a two-degree-of-freedom lumped parameter system for the sake of having more insights about the experimental results. Each degree of freedom is a single mode, corresponding to the cantilever's first mode of vibration, which is normally exhibited through measurement. However, this model is phenomenological, which means it is meant to be a qualitative description of the cantilever motion, since a precise calibration of system's coefficients is not yet available due to the complexity of the electro-thermomechanical coupling [129]. Furthermore, as shown here, a qualitative comparison will be sufficient to discuss the experimental results through the presented model. Moreover, although the electronically induced nonlinearities (see (6.2)) are still present, they were of little influence on the measured system behavior, thus, they were excluded from the model. And finally, the experiment carried out on the coupled system involved time-invariant F_1 and F_2, which have no dynamic effect and could be safely excluded as well. This leaves us with a linear system of differential equations with displacement-proportional time-varying coefficients.

According to the previous arguments, (6.1) is then rewritten to be

$$m_1\ddot{x_1} + c_1\dot{x_1} + k_1x_1 + \epsilon_{11}x_1\cos(\Omega_p t) + \epsilon_{12}x_2\cos(\Omega_p t) = 0, \tag{6.13a}$$

$$m_2\ddot{x_2} + c_2\dot{x_2} + k_2x_2 + \epsilon_{21}x_1\cos(\Omega_p t + \zeta) + \epsilon_{22}x_2\cos(\Omega_p t) = 0, \tag{6.13b}$$

where m_i represents the modal masses, k_i the modal stiffness coefficients, c_i the modal damping coefficients, ϵ_{ij} the parametric excitation amplitudes and ζ a phase shift. By normalizing with respect to the modal mass we get

$$\ddot{x_1} + 2\delta_1\omega_{C1}\dot{x_1} + \omega_{C1}^2x_1 + \xi_{11}x_1\cos(\Omega_p t) + \xi_{12}x_2\cos(\Omega_p t) = 0, \tag{6.14a}$$

$$\ddot{x_2} + 2\delta_2\omega_{C2}\dot{x_2} + \omega_{C2}^2x_2 + \xi_{21}x_1\cos(\Omega_p t + \zeta) + \xi_{22}x_2\cos(\Omega_p t) = 0. \tag{6.14b}$$

Using the characterization measurement data acquired for each cantilever (see section 6.2) we can supply the model with δ_1, δ_2 and ω_{C1}, ω_{C2}. However the forcing elements ξ_{ij} could not be measured or calibrated. However, according to the manufacturer's data sheet a rough estimation could be made. The force sensitivity is of the order of V/mN which gives a net force of about $\sim 10^{-3}N$ in the range of the applied voltage and since the modal mass is of the order of nanograms, i.e. $\sim 10^{-12}kg$, the normalized excitation amplitude $\xi = \epsilon/m$ could be of the order of $\sim 10^8 - 10^9$.

The phase-shift ζ represents the most important parameter in the discussed experiments and therefore in this explanatory model. It will carry through our calculations only two values,

either zero or $-\pi/2$, which resembles the experiments carried out and discussed in section 6.3. The parametric excitation signals in the experiment explained in section 6.3 were all of the same amplitude, thus, in this affirming model we assume that they are all equal, i.e. $\xi_{ij} = \xi$

Therefore, the stability charts of (6.14) in the parameter space Ω_p-ξ are calculated for the two different cases, synchronous ($\zeta = 0$) and asynchronous ($\zeta = -\pi/2$). The calculation was carried out numerically using Floquet theory [41, 80]. The results are then shown in Fig. 6.4.1. These results are very similar to what was shown before for other parameter values (see sections 3.1.3 and 5.6). The stability chart shown for the case of synchronous parametric excitation represents a common one for coupled parametrically excited systems [37], however having a phase shift of $\pi/2$ leads to a broadband destabilization. This is explained by observing the merged instability region in Fig. 6.4.2 above approximately $\xi = 3 \times 10^{10} N/m.kg$. In this region, the system is unstable for a broad band of excitation frequencies.

If the system is nonlinear, the system could have other nontrivial stable solutions inside the instability regions of the trivial solution, otherwise the system's behavior will be unbounded. This phenomenon becomes particularly useful for microsystems, since the nontrivial stable solution provides an amplification of the response. Otherwise, even for linear systems, a parametric amplification is achieved by choosing the parameters which corresponds to be just below the instability region. For this case, the system Lyapunov exponents are significantly increased near the border of instability, and thereby the system's response is amplified. These aspects were discussed in section 3.1.6.

The discussed experiment in this chapter aimed, therefore, first to validate this broadband destabilization or amplification. However, the cantilevers' actuators fell short of reaching the required excitation amplitudes. Due to this limitation, the parametric excitation amplitude ξ could not exceed $2.3 \times 10^9 N/m.kg$, which is shown in Figs. 6.4.2 and 6.4.1.

This model, however, could be validated through other common features between theory and experiment. Having done that, the prediction of the model beyond the measurement constraints could be considered at least to be feasible, and thus could be attained as soon as the practical constraints allow. In this way, the model serves as an extension of the measured observations towards currently unattainable ones. In other words, the broadband destabilization is predicted by the model but yet experimentally unattainable under the available measurement conditions. However, since the model predicts its existence, our main goal here is to validate this model for the sake of asserting the model's prediction.

According to this argument, we concentrate on the stability chart below the maximum possible excitation amplitude. Therefore, the experimentally feasible parameter space is enlarged in Figs. 6.4.3 and 6.4.4. In these figures both experimental and numerically calculated results are

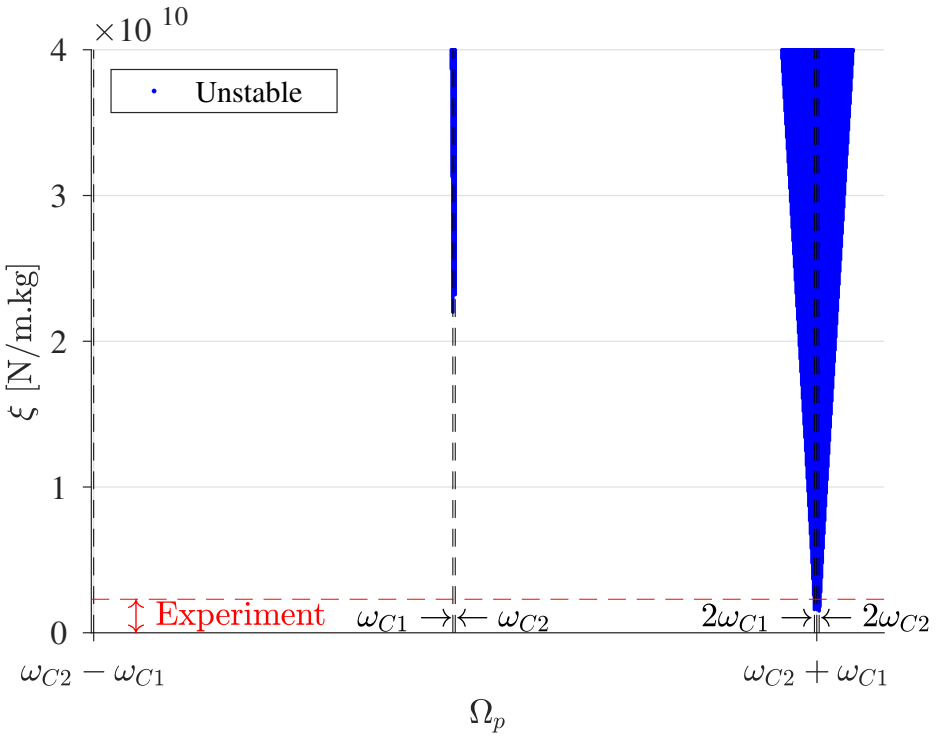

Figure 6.4.1: Calculated stability chart for the model (6.14), where $\omega_{C1} = 100.98kHz, \omega_{C2} = 101.6kHz$ and $\zeta = 0$.

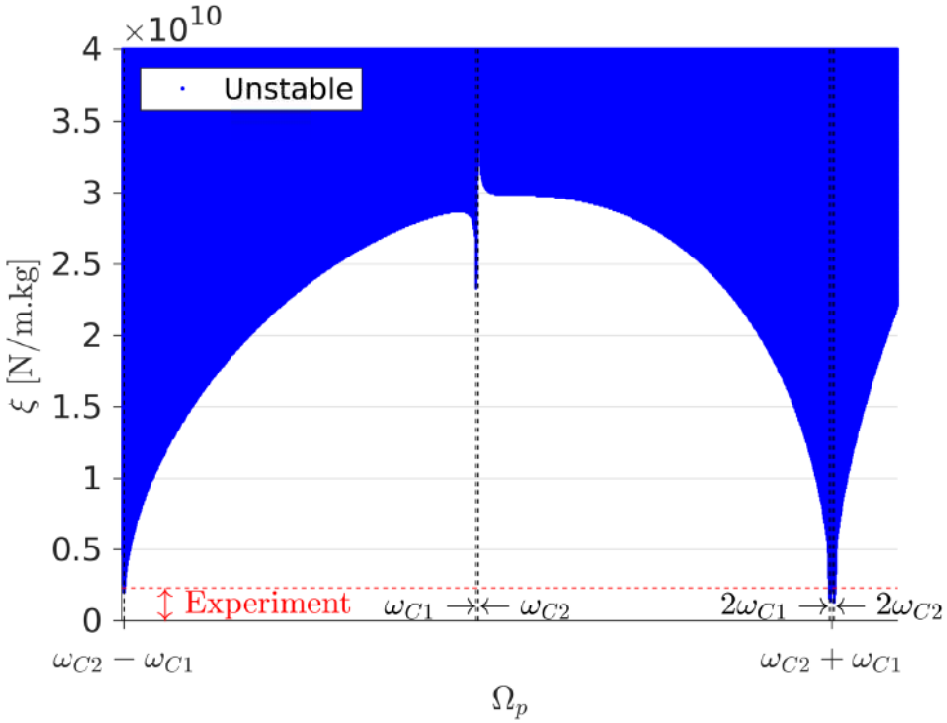

Figure 6.4.2: Calculated stability chart for the model (6.14), where $\omega_{C1} = 100.98kHz, \omega_{C2} = 101.6kHz$ and $\zeta = -\pi/2$.

depicted.

Before discussing the matching between model and experiment, several observations are made between Fig. 6.4.3(c,d) and Fig. 6.4.4(c,d) to discuss the role of the phase shift ζ in changing the stability chart at these low excitation amplitudes. Firstly, the difference combination resonance appears only in the phase-shifted excitation. This observation was made theoretically before in previous works [36, 37]. Secondly, the instability tongue corresponding to the summation combination resonance frequency is shifted upwards in the case of the phase-shift. Thirdly, the instability tongues of the parametric primary resonances are slightly shifted in frequency for the asynchronous excitation case.

Additionally, another subtle observation could be made about the width of the instability tongues. By returning to the full picture of the stability charts in Figs. 6.4.1 and 6.4.2, a nonlinear gradual increase in the instability tongues could be observed up to the excitation amplitude where they merge to give the broadband instability region. This increase of the instability tongues' widths could be observed as well at low excitation levels. In Fig. 6.4.5 a comparison between the instability tongues of both cases is depicted. Since the tongues are shifted in amplitude and frequency, those of the phase-shifted excitation case are then centered with respect to the in-phase excitation case for the sake of comparison. By doing that, we observe a slight increase in the instability tongue's width in each case, significantly appearing in the summation resonance instability. These model-based results come inline with the experimental observations discussed in section 6.3.

These discussed features could be observed in the experimentally obtained stability charts. In comparing the a and b plots with the corresponding c and d plots in each of the figures 6.4.4 and 6.4.3, we can see a high topological similarity between model and experiment. The amplitude-shift of the summation resonance instability tongue could be observed as well in the experiment, and was checked for reproducibility in several other experiments with other cantilevers. The model could also explain the reason behind the appearance of the difference combination resonance in experiment when only a phase-shifted excitation is applied.

In summary, in addition to the topological similarity between the parameter spaces in the model and the experiment, three distinct features are found to exist in both of them. In comparing the synchronous and the asynchronous excitation cases, the features are then the amplitude-shift of the summation resonance tongue, the existence of difference combination resonances, and the relative slight increase of instability tongues' widths, all of them occurring under asynchronous excitation. Since they are distinct observations in both model and experiment, we could then affirm the validity of the presented model.

Therefore, the model is validated and predicts the broadband destabilization at higher

excitation amplitudes than the attainable ones. Thus, the improvement of the excitation method in further investigation is recommended for the realization of the broadband instability effect.

6.5 Conclusions

In this chapter, the stability of the trivial solution of a coupled two-microcantilever system is experimentally investigated. The main aim of this study is to validate the previous theoretical findings discussed in the previous chapters. These findings included some interesting and novel phenomena for the microsystems' technology in general. A chief phenomenon is the broadband destabilization of the system which could be utilized to form a broadband parametric amplification. To this end, an electronic control circuit was built to induce a bimodal parametric excitation mechanism in a system of two microcantilevers. The cantilevers were only coupled through the parametric excitation. Although the broadband destabilization phenomenon could not be observed experimentally, a mathematical model predicting the aimed broadband effect could be validated through the experimental results. In this way, the model serves to be as an extension of the currently available experimental findings.

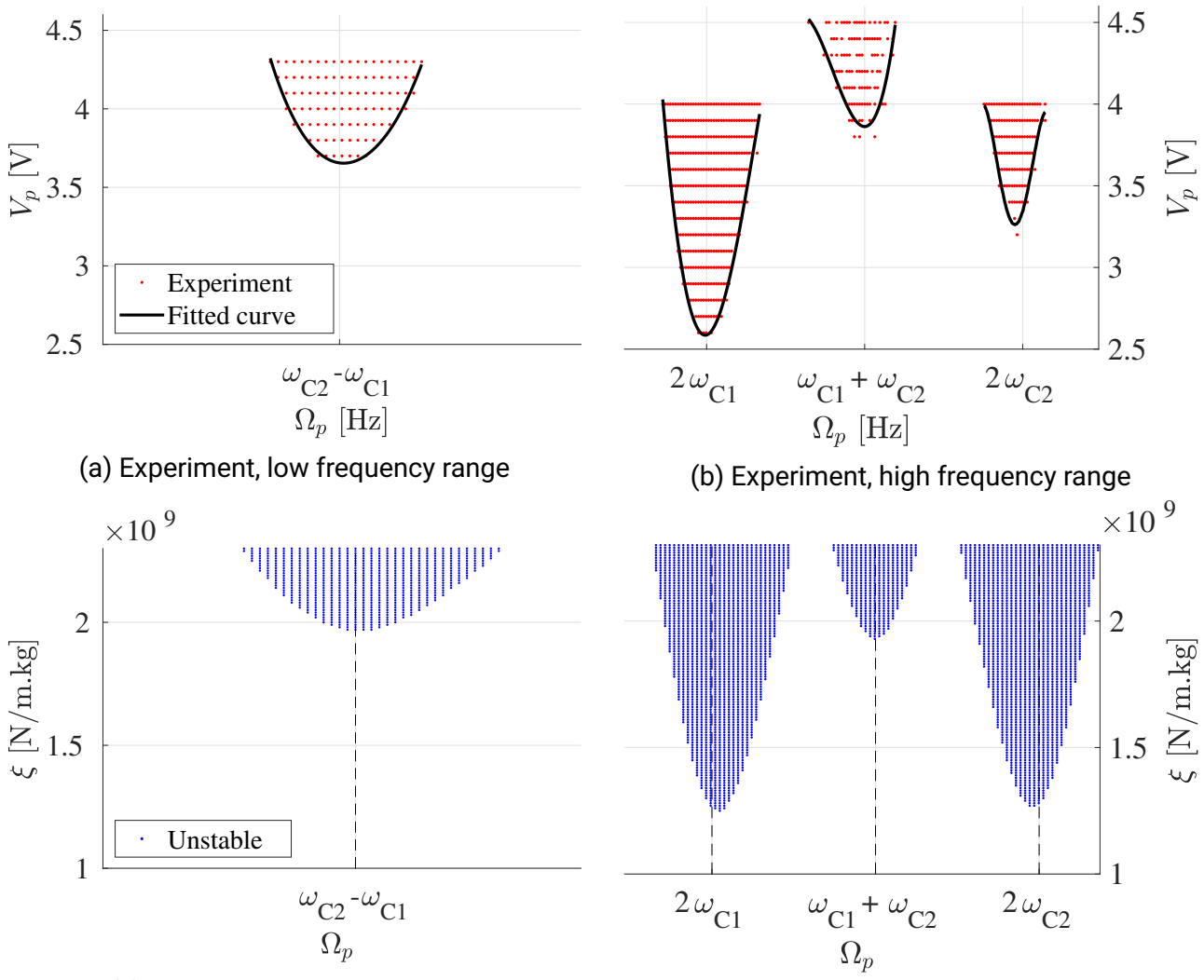

(a) Experiment, low frequency range

(b) Experiment, high frequency range

(c) Model, low frequency range

(d) Model, high frequency range

Figure 6.4.3: Stability chart of the bimodal parametrically excited system with a phase shift $\zeta = -\pi/2$, where $\omega_{C1} = 100.98\ kHz, \omega_{C2} = 101.6\ kHz$

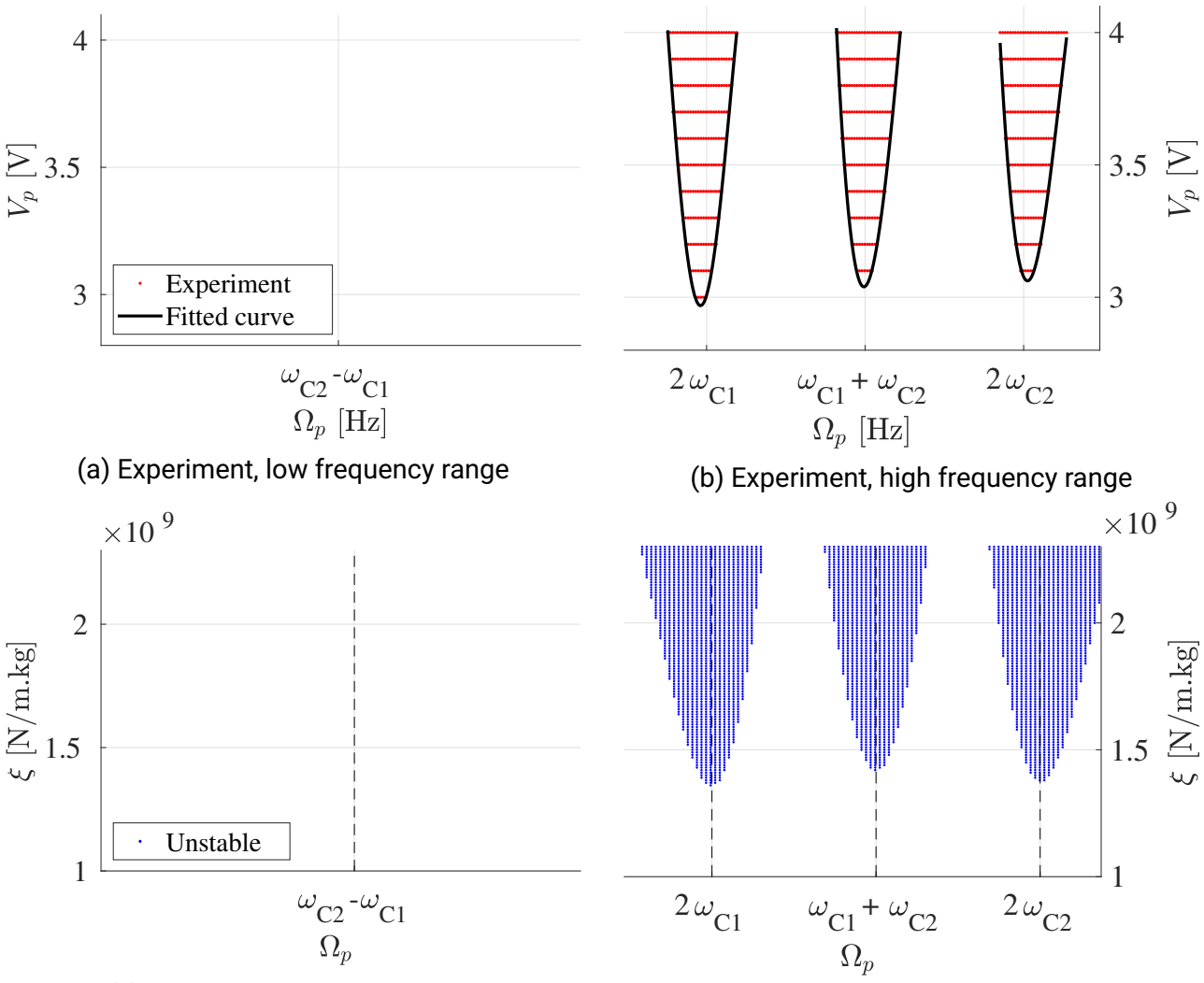

(a) Experiment, low frequency range

(b) Experiment, high frequency range

(c) Model, low frequency range

(d) Model, high frequency range

Figure 6.4.4: Stability chart of the bimodal parametrically excited system without a phase shift, i.e. $\zeta = 0$, where $\omega_{C1} = 100.98\ kHz$, $\omega_{C2} = 101.6\ kHz$

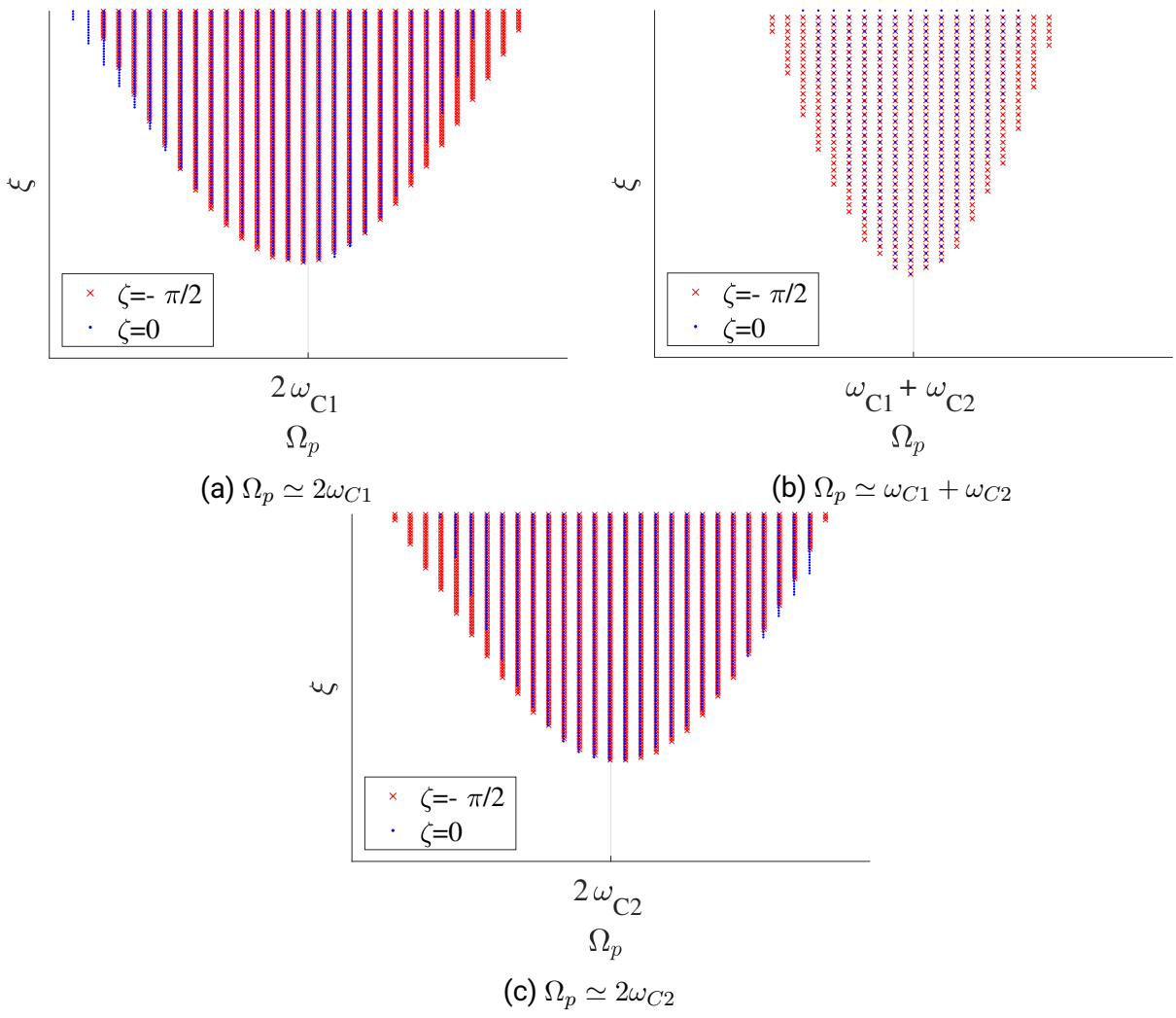

(a) $\Omega_p \simeq 2\omega_{C1}$

(b) $\Omega_p \simeq \omega_{C1} + \omega_{C2}$

(c) $\Omega_p \simeq 2\omega_{C2}$

Figure 6.4.5: Comparing the instability tongues between the synchronous ($\zeta = 0$) and asynchronous ($\zeta = -\pi/2$) excitation cases

Appendix

Appendix 6.A Circuit diagram: Stages 1-2

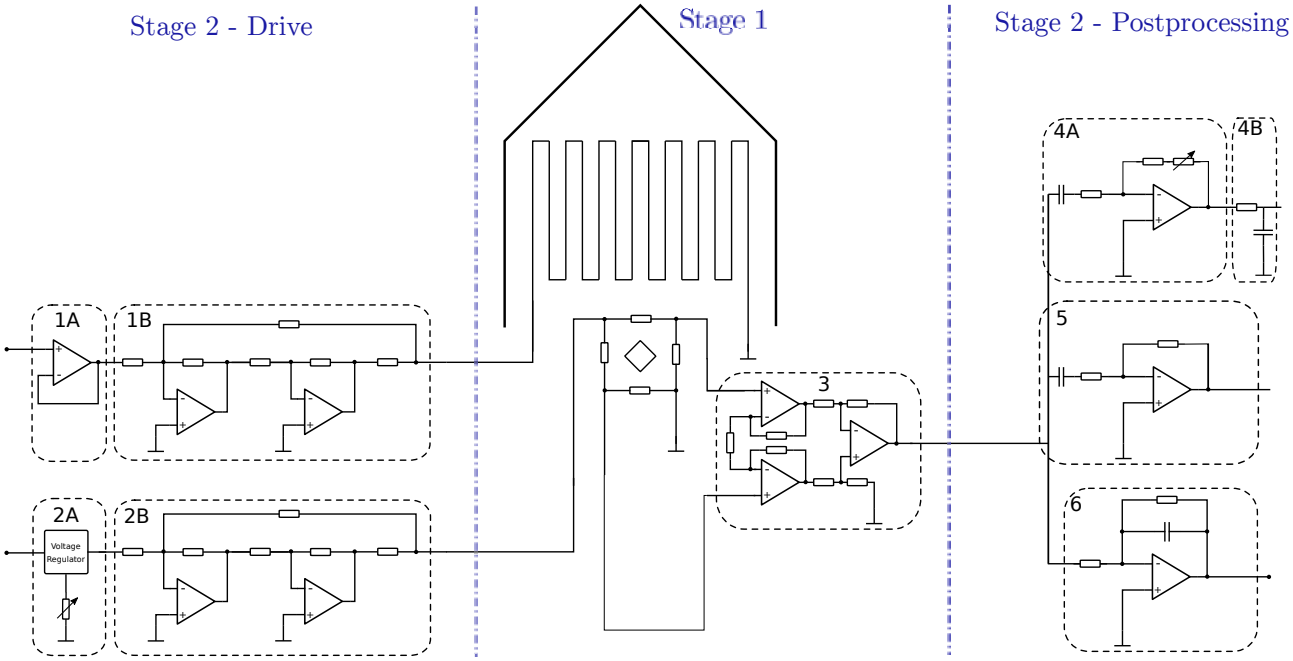

Figure 6.A.1: Circuit diagram for stages 1 and 2 in the electronic system (see Fig. 6.1.1(a,b)), modified from [127].

Fig. 6.A.1 shows the circuit diagram for Stg1 and Stg2 boards. The figure shows six different electronic modules numbered from 1A,1B to 6, which will be explained. In Stg1 a low-noise instrumentation amplifier (module 3) of the type INA849 is implemented, which is supplied with the sensor signal from the Wheatstone bridge placed on the cantilever. The output of this amplifier is then transferred through a ribbon cable to Stg2 for further signal processing. The cable carries, in addition, the excitation signal and the bridge voltage. This voltage is set to -3V for all the experiments reported here, in order to provide a suitable control of the parametric resonances. Both signals are supplied from Stg2.

The main hardware processing of excitation and sensor signals is carried out on Stg2. As shown in Fig. (6.A.1), Stg2 circuit is positioned in the midway between Stg1 (cantilever pre-amplifier) and Stg3 (parametric excitation). The signals directed towards Stg1 include: the voltage supply for the sensor bridge after passing through a voltage-current converter using the operational amplifier OPA2211 (module 2B), in addition to the thermoactuator excitation signal after passing also through a voltage-current converter using LM7372 (module 1B). The pre-amplified sensor signal coming from Stg1 is then treated on Stg2 in three parallel paths. One path includes a low-pass filter using OPA2211 (module 6), the second includes a high-pass filter using THS4022 (module 5) and the last one includes a low- and high-pass filters using THS4022 (module 4). All of the experiments carried out in this work use the last output, in order to filter the signals between 1.59 kHz and 1.59 MHz.

Appendix 6.B Circuit diagram: Stage 3

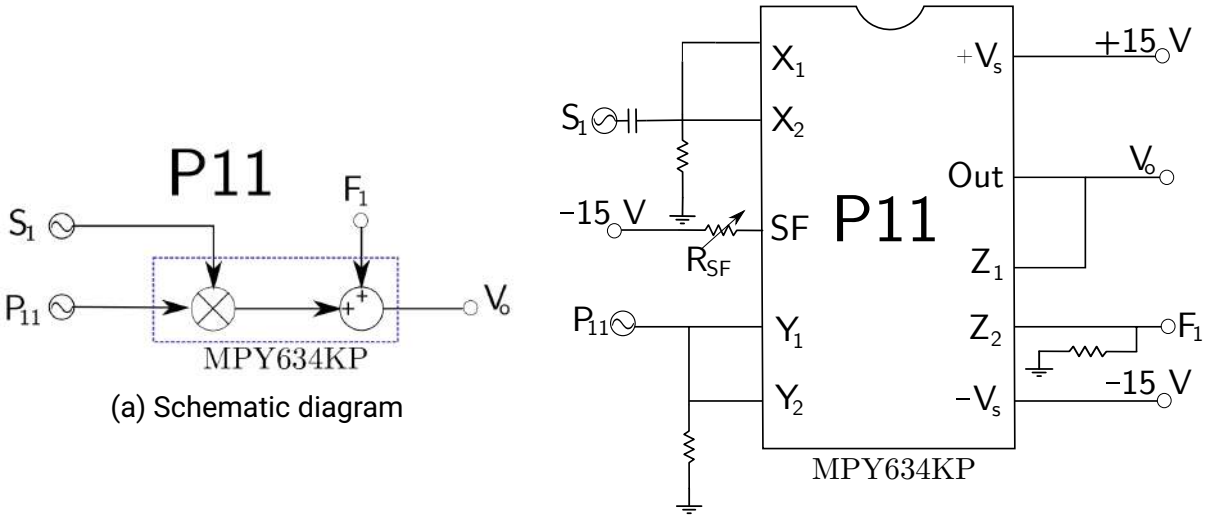

(a) Schematic diagram

(b) Circuit diagram

Figure 6.B.1: Schematic and circuit diagrams of a multiplication module in Stage 3 board

As explained in section 6.1.2, the electronic circuit of Stage 3 board is composed of several multiplication modules (see Fig. 6.1.3). In order to show the circuitry of this electronic board, the circuit diagram of one multiplier is depicted in Fig. 6.B.1. This diagram is typical for all other multiplication modules in the electronic board with slight variations. This should give enough detail about the design of this board.

As shown in the figure the multiplier MPY634KP takes four main multiplication input signals, along with an addition-signal, and gives a single output V_o. The output signal is then calculated

according to

$$V_0 = \frac{(X_1 - X_2)(Y_1 - Y_2)}{SF} + Z_2, \tag{6.15}$$

where X_1, X_2, Y_1, Y_2 are the multiplication input signals, SF is a scaling factor, and Z_2 is an added signal to the whole sum. The scaling factor could be controlled by attaching the corresponding resistance of the value

$$R_{SF} = 5.4k\Omega \left(\frac{SF}{10 - SF} \right). \tag{6.16}$$

In the presented multiplication module of $P11$ in Fig. 6.B.1, X_2 port is connected to S_1 signal, Y_1 port to P_{11} signal, and Z_2 to F_1. Neglecting the scaling factor for now, we get

$$V_o = -P_{11} \times S_1 + F_1, \tag{6.17}$$

which represents a part of the total output to actuator 1 $Out1$ in (6.2). The negative sign used before the first term is to comply with the mathematical model (6.1).

The inputs are attached to pull-down resistors to eliminate floating values at the multiplier inputs. Moreover, a capacitor is connected to the input of the sensor signal to filter out DC signals. To add the output of two multipliers according to Fig. 6.1.3, taking for instance P_{11} and P_{12} as an example, the output signal of the multiplier P_{11} is connected to the addition input port Z_2 in the multiplier of P_{12}. The same case happens for successive multiplication operations, for instance for $S1^3$, but using the multiplication input ports instead (see (6.2)).

Appendix 6.C Devices

The main devices used through the experiments are:

- Four Oscilloscopes TiePie Handyscope HS5 each with two input channels of 250 MHz maximum bandwidth and 1 output signal generator with output frequency of up to 40 MHz and output voltage of up to +/- 12 V. That means they provide eight input channels and four generators in general.
- Laser Vibrometer PolyTec OFV-5000 with frequency range of 0-24 MHz and maximum velocity of 10 m/s connected to a microscopic lens 20X of aperture f/200.
- OWIS Positioning system with linear piezo-tables, in which the holders of stage 1 boards are fixed, and another vertical table holding the laser head of the vibrometer.

Appendix 6.D Software

The control of the whole measurement system is performed by a program composed of a set of Matlab scripts based on Object-Oriented Programming (OOP). This program includes several functions which are the control of the piezo-positioning system, the vibrometer and the oscilloscopes. It was developed by the team of researchers at the Mechatronics department in TU Ilmenau. The measurement scripts are based on their template and modified by the author for the purposes of the explained experiments in this chapter. The main scripts used for these experiments are the following:

- A script for carrying out stepped sweep in the frequency-amplitude parameter space.
- A script for applying linear frequency sweep to determine the natural frequencies of the cantilevers.
- A script for measuring the gain values of Stg2.
- A script for measuring the vibration decay in a free vibration experiment.
- A script to determine the logarithmic increments at each frequency for a given amplitude.

7 Conclusions and outlook

Parametric excitation is discussed in the literature in various forms: in single-degree-of-freedom systems, typically the Mathieu equation, or multi-degree-of-freedom systems, also either including synchronous or asynchronous parametric excitations, and as well as for the cases of resonance or anti-resonance. However, much less attention is given to parametrically excited nonlinear systems, not to mention the asynchronous parametric excitation, which refers to having out-of-phase coupling parametric excitation terms. Additionally, this type of excitation turned out to be of particular importance to nonlinear micro and nanosystems, however, they were not considered before for this type of excitation. In terms of experiments, previous studies did not consider asynchronous parametric excitation in mechanical systems. These open questions lead the motivation to write this thesis, in which the aspects mentioned are approached throughout the thesis in a systematic way, from the simplest systems to time-periodic nonlinear ones.

The results of this work can be classified into three major domains. In the first domain, a theoretical study is carried out on time-periodic nonlinear systems, while considering an example of a two-degree-of-freedom system. This class of systems manifests the major types of destabilization, namely, nonlinearities, time-periodicity, and coupling of system's degrees of freedom. In addition, these systems gain their importance not only in the theory of dynamical systems, but also because they are typically present in many micro and nanosystems. The second domain is concerned with the implementation of the theoretical findings in micro-ring gyroscopes, as an example of microsystems, with an emphasis on the effect of the broadband amplification effect. Finally, the experimental realization represents the third domain, through which an experimental study is carried out on a system of two cantilevers for the sake of validating the discussed theoretical findings, and observing phenomena which were not before experimentally considered. The results in each of these three domains are discussed in detail as follows.

In the first domain of contribution, a theoretical study on linear and nonlinear time-periodic systems is presented. Through this study, the stability of system's solutions is shown to depend

heavily on the synchronicity of the parametric excitation terms. Specifically, if the coupling terms of the parametric excitation matrix are out of phase, an interesting effect is observed; the destabilization effect in a broad band of parametric excitation frequencies. This means, in contrast with the common utilization of parametric amplification at resonant frequencies, this type of excitation offers a destabilization effect at non-resonant frequencies. This result was discussed before in the literature and named the "total instability" effect, but neither was it validated experimentally nor was it covered thoroughly for nonlinear systems. Through this work, this phenomenon is discussed again for linear systems while giving some additional insights. A stability chart is produced and found to appear topologically similar through analyzing different systems incorporating this type of excitation. Since particular attention is given in this work to small-scaled systems, a special case is considered through the discussion where the natural frequencies are relatively large, in hundreds of kHz, while the difference between them accounts to a smaller order of magnitude, hundreds or thousands of Hz. In this case, a vast separation between summation and difference frequencies exists, which makes the mentioned phenomenon more pronounced in microsystems under asynchronous parametric excitation.

Furthermore, the discussion is then extended to forced parametrically excited systems for the sake of elaborating on the effect of parametric amplification which plays an important role in micro and nanosystems. Non-resonant parametric amplification has been known to resemble an increase in the response amplitude at resonance frequencies near the border of instability. This is precisely what differentiates it from the case of a parametric resonance, where the trivial solution is strictly unstable. This distinction in the literature expresses itself in the selection of the parametric excitation amplitude either to be just below the onset of instability for the case of non-resonant parametric amplification, or to cause instability for the case of a parametric resonance. In order to explain this, the system is analyzed analytically using the multiple scales method in order to discuss the mechanism of non-resonant parametric amplification mathematically. The analysis was carried out up to the second order approximation. Through the analysis, the amplitudes of first order correction terms showed a significant dependence on the parametric excitation. Specifically speaking, the amplification of the amplitudes of these terms was directly related to the destabilization of the trivial solution. This means, for the asynchronous parametric excitation, an amplification in these amplitudes is observed at non-resonant frequencies in addition to the resonant ones leading to a broadband parametric amplification.

The previous results are inline with the experimental studies conducted near the border of instability, where the amplification gains were significantly increased. Nevertheless, up to this

analysis step, it is still unclear how these correction terms could induce these amplification gains despite being of a lower order of magnitude. This could be clarified by carrying out the analysis up to the second order of approximation. Through this analysis the Lyapunov exponents of the system's homogeneous solution were deduced and found to be identical to those in the case of unforced parametrically excited systems. Thus, only near the instability border the homogeneous solution does start to have a significantly slow attenuating envelope, which in short times could be of the same order of magnitude as the particular solution, i.e. the forced response. However, the initial conditions of the homogeneous solution will also be influenced by the perturbations induced through the correction terms, which induce a broadband amplification effect as mentioned previously. In this way, the experimentally observed parametric amplification could be explained by having a slow attenuated homogeneous solution allowing a greater influence of the correction terms carrying the broadband effect, and then added to the particular forced response. A direct time integration is carried out also at different parametric excitation amplitudes around the stability border to investigate this correspondence between the amplification of the response and the destabilization of the trivial solution, and it was proved to be existing. Moreover, this could explain the reason behind having this parametric amplification only near the onset of instability, since it only takes place when the envelope of the homogeneous solution turns to be relatively slow.

An amplification of the response within the instability area requires the inclusion of nonlinear terms, through which the trivial solution is destabilized. Thus, by adding nonlinear stiffness and damping terms the system is analyzed again and other phenomena could be observed. The system stability and the permissible nontrivial solutions were studied at resonant and non-resonant frequencies. At non-resonant frequencies, the trivial solution gives the same results as before in the case of the linear system. Furthermore, at the primary parametric resonance frequency, the nontrivial steady state solutions, i.e. limit cycles, were found to be mostly determined by the linear damping and the detuned parametric excitation frequency, which are considered in this case to be the system's bifurcation parameters. A significant distinction is then made between having large excitation amplitude and having a small one. In each case the system shows nontrivial solutions for different limited ranges of linear damping when the excitation frequency is tuned at the parametric resonance frequency. However, by the detuning of the excitation frequency another unstable solution appears. In this case, the variation of linear damping shows an interesting phenomenon, an isolated nontrivial solution in a certain domain of the linear damping. This isolated solution leads to an abrupt increase or decrease of the system's response through varying the system's damping. Such a result can be of particular importance if this system's damping could be controlled, such as through electronic

resistance. In this way a high sensitivity could be then obtained at the bifurcation limit, and a bifurcation control scheme could be useful for micro or nano-applications. Although at primary resonance frequencies the system shows an uncoupling between the two degrees of freedom, if their natural frequencies were notably similar, an internal resonance takes place, which couples both degrees of freedom. In addition, through this coupling the phase space is found to be rather complex, since numerous nontrivial solutions could be calculated. This is observed by depicting the resonance curves around the primary resonance frequency.

At combination resonance frequencies the system exhibits multiple steady-state solutions, where both degrees of freedom are again coupled. However, the phase-shift between the coupling parametric excitation terms, or the asynchronicity, changes the system's behavior substantially. At the summation frequency a synchronous excitation shows a common hardening resonance curve, where stable and unstable limit cycles exist. However, an asynchronous excitation causes the existence of only stable limit cycle in the vicinity of the summation combination frequency. By repeating the analysis at the difference resonance frequency, nontrivial solutions do not occur under synchronous parametric excitation, while the trivial fixed point was shown before to be stable. However, if the parametric excitation turns to be asynchronous the stability of the trivial fixed point is lost, causing a parametric resonance, and a nontrivial steady state solution is found instead in the form of a stable limit cycle.

The second domain of contribution in this work involves the implementation of the theoretical findings in a microsystem. The main application considered is the micro-ring gyroscope, for which the parametric excitation is shown in the literature to be of significant importance. For the linearly modeled gyroscope the broadband destabilization effect is investigated. Since the system could be reduced to a two-degree-of-freedom system, all the results from the linear theory of parametrically excited systems, including the broadband destabilization effect, could be transferred easily to the analysis of the micro gyroscope. Moreover, it was emphasized how applying this method of excitation could lead to enhancing both the sensitivity and the accuracy. In addition, another characteristic also applies to this system, which is the capability of tuning the excitation frequency without experiencing abrupt change in amplification. The applicability of this characteristic relies on the fact that the amplification could be attained at a broad frequency band.

By modeling the micro-gyroscope nonlinearly a better understanding could be attained. An autonomous version of the system is first investigated through canceling all excitation terms. By doing that nine fixed points are found including the trivial fixed point. A subcritical pitchfork bifurcation is detected through varying the direct voltage applied on the gyroscope. At a certain voltage amplitude, the system's eigenfrequency turns to be imaginary leading to divergence.

After bifurcation only the trivial solution persists, while all nontrivial solutions vanish. However, due to divergence, the trivial solution also turns into a saddle point. Before the bifurcation point, stability could only be found at the trivial fixed point. All other nontrivial points are found to be unstable. A nonautonomous case is studied next, by considering a small excitation. At this excitation level the back action of the sense mode on the drive mode could be neglected. Thus, the drive mode is studied uncoupled from the sense mode. Using the method of normal forms, a softening nonlinear effect is exhibited which confirms results from a previous study.

Moreover, by applying the bimodal excitation method, both degrees of freedom are then coupled through different nonlinear terms. Using the method of normal forms, the system is analyzed by tuning around the primary resonance frequencies. Through this analysis the resonance curves for both degrees of freedom at their parametric resonance frequencies are obtained which indicate limit cycles. Both the drive and sense modes showed again a softening behavior. Moreover, the sense mode could exhibit an isolated resonance curve, which is more obvious at higher excitation amplitudes.

In the third domain of contribution, the same two-degree-of-freedom system discussed through this work was realized experimentally. The system is implemented using two microcantilevers coupled only through the parametric excitation. Linearity is assumed for the behavior of these cantilevers, while the system's nonlinearities were found to have a minimal influence on the system dynamics as long as the trivial solution is stable or near stability. This is found to be useful, since it allowed the first experimental investigation of the bimodal excitation scheme to be without other nonlinear effects.

The bimodal parametric excitation mechanism is implemented through an electronic circuit. The circuit contained additional nonlinearities for the sake of limiting the response amplitude when the trivial solution is destabilized at resonances. This circuit was supplemented by a pre-amplification circuit designed by our collaborators. Both two electronic circuits were connected to the two uncoupled microcantilevers and set for experimental study at the Technical University of Ilmenau. The experimental study could yield the desired results and validate the corresponding mathematical model. However, a limitation in the excitation amplitudes was experienced, which could not allow the system to exhibit the broadband destabilization effect. Still, this did not hinder the validation of the mathematical model, since three features of the system were found in the experimental results to be inline with the model-based results. The first observation is that, the instability tongue at the summation combination frequency is shifted to higher values of excitation amplitudes under asynchronous excitation. A second common feature is found, that is an increase of the instability tongues' widths by imposing asynchronous parametric excitation. And lastly that the difference combination frequency

could only be exhibited in the asynchronous excitation case for both model and experiment. In addition to these features, the topology of the stability chart in both theory and experiment showed an obvious similarity under the allowed excitation amplitudes.

In conclusion, this is the first experiment to be carried out for asynchronous parametric excitation at all resonant frequencies. Nevertheless, a single study was found on this type of excitation, where only the summation combination resonance was considered [36]. However, it could not be applied on mechanical systems due to practical limitations [38]. This makes this study to be the first realization of the discussed asynchronous parametric excitation in mechanical systems. Moreover, although the experimental realization of the difference combination resonance was known to be hardly attainable in mechanical systems, it could be experienced readily through this work. This may be attributed to the relatively low damping and high attainable response amplitudes in microsystems in comparison to macro-scaled ones.

To summarize these conclusions, this work was mainly focused on nonlinear time-periodic systems, although a few other linear and time-invariant systems were also investigated. The important results found are as follows:

- The stability chart is constructed for linear and nonlinear dynamical systems with phase-shifted coupled parametric excitation terms.
- The direct relation between the amplification of the system's response and the destabilization of the trivial solution could be explained analytically.
- Nonlinear time-periodic systems were investigated in some detail offering new insights regarding the existence of limit cycles among other aspects.
- The broadband destabilization effect is found to be significant for the performance of micro-ring gyroscopes.
- The nonlinearly modeled micro-ring gyroscope exhibits significant nonlinear effects, such as the softening behavior, and a subcritical pitchfork bifurcation at large direct voltage.
- The mathematical model of the bimodal parametrically excited system is validated experimentally.

This work suggests some open questions to be addressed by future studies. First, the study of the nonlinear time-periodic system still needs more investigation due to its rich and complex dynamics. Specifically, the stability analysis for nontrivial solutions would allow more understanding of the behavior, especially when the corresponding solutions in the phase space could be calculated. A particular study about the stability of these solutions at non-resonant frequencies would be of major importance. That is particularly important for micro and nanosystems, since higher parametric amplification values could be attained through optimization of controllable

system parameters.

Secondly, perturbing nonlinear systems with circulatory forces could be informative about their influence on the stability of system's trivial and nontrivial solutions. A particular question about the effect of time-dependency of these forces could be of special interest, since it forms then an asynchronous parametric excitation.

Thirdly, although the broadband destabilization effect could not be attained experimentally due to a practical limitation, the validated mathematical model anticipates its existence. Thus, it is suggested to modify the excitation method in order to increase its amplitude to allow for exhibiting this phenomenon experimentally.

Lastly and more generally, this work shows how much potential there still is in the theory of time-periodic systems that could be implemented in nonlinear micro and nanosystems for enhancing their performance.

Bibliography

[1] Jon McGinnis. Arabic and Islamic Natural Philosophy and Natural Science. In Edward N Zalta, editor, *The Stanford Encyclopedia of Philosophy*. Metaphysics Research Lab, Stanford University, Spring edition, 2022.

[2] René Dugas. *A history of mechanics*. Dover Publications, 1988.

[3] Mohammad I. Younis. *MEMS Linear and Nonlinear Statics and Dynamics*. Springer US, Boston, MA, 2011.

[4] Jeffrey F. Rhoads, Steven W. Shaw, and Kimberly L. Turner. Nonlinear dynamics and its applications in micro-and nanoresonators. *Journal of Dynamic Systems, Measurement and Control, Transactions of the ASME*, 132(3):1–14, may 2010.

[5] J. A. Richards. *Analysis of Periodically Time-Varying Systems*. Springer Berlin Heidelberg, 1983.

[6] Giulia Bevilacqua, Xingchen Shao, John R. Saylor, Joshua B. Bostwick, and Pasquale Ciarletta. Faraday waves in soft elastic solids. *Proceedings of the Royal Society A*, 476(2241), sep 2020.

[7] Kenneth R. Meyer and Dieter S. Schmidt. Hill's lunar equations and the three-body problem. *Journal of Differential Equations*, 44(2):263–272, may 1982.

[8] V V Bolotin. *Dynamic stability of elastic systems*. Holden-Day, Inc., 1964.

[9] M. J.O. Strutt. Zur Wellenmechanik des Atomgitters [On the wave mechanics of the atomic lattice]. *Annalen der Physik*, 391(10):319–324, jan 1928.

[10] Felix Bloch. Über die Quantenmechanik der Elektronen in Kristallgittern [On the quantum mechanics of electrons in crystal lattices]. *Zeitschrift für Physik*, 52(7):555–600, jul 1929.

[11] E. Mettler. Allgemeine Theorie der Stabilität erzwungener Schwingungen elastischer Körper [General theory of stability of forced vibrations of elastic bodies]. *Ingenieur-Archiv*, 17(6):418–449, 1949.

[12] Norbert. Eicher. *Einführung in die Berechnung parametererregter Schwingungen [Introduction to the computation of parameter-excited vibrations]*. TUB-Dokumentation Weiterbildung. Technische Uni Berlin, Berlin, 1981.

[13] Matthew Cartmell. *Introduction to linear, parametric, and nonlinear vibrations*. Springer Dordrecht, 1990.

[14] Vladimir A. Yakubovich and V. M. Starzhinskii. *Linear differential equations with periodic coefficients*. Wiley London, 1975.

[15] Peter Hagedorn. Kombinationsresonanz und Instabilitätsbereiche zweiter Art bei parametererregten Schwingungen mit nichtlinearer Dämpfung [Combination resonance and secondary instability regions in parameterically excited oscillations with nonlinear damping]. *Ingenieur-Archiv*, 38(2):80–96, 1969.

[16] Alexei A. Mailybaev. On stability domains of nonconservative systems under small parametric excitation. *Acta Mechanica 2002 154:1*, 154(1):11–30, 2002.

[17] S. C. Sinha and E. A. Butcher. Symbolic computation of fundamental solution matrices for linear time-periodic dynamical systems. *Journal of Sound and Vibration*, 206(1):61–85, sep 1997.

[18] Norbert Eicher. *Ein Iterationsverfahren Zur Berechnung Des Stabilitaetsverhaltens Zeitvarianter Schwingungssysteme [An iteration method for the computation of the stability behavior of time-Variant oscillatory systems]*. VDI Verlag, Duesseldorf, 1984.

[19] Derek J. Daniel. Exact solutions of Mathieu's equation. *Progress of Theoretical and Experimental Physics*, 2020(4):43–44, apr 2020.

[20] Aleš Tondl. *On the interaction between self-excited and parametric vibrations*. National Research Institute for Machine Design Běchovice, Prague, 1978.

[21] A. Tondl and H. Ecker. On the problem of self-excited vibration quenching by means of parametric excitation. *Archive of Applied Mechanics*, 72(11):923–932, 2003.

[22] S. Fatimah and F. Verhulst. Suppressing flow-induced vibrations by parametric excitation. *Nonlinear Dynamics*, 31(3):275–298, 2003.

[23] Fadi Dohnal. Suppressing self-excited vibrations by synchronous and time-periodic stiffness and damping variation. *Journal of Sound and Vibration*, 306(1-2):136–152, sep 2007.

[24] Fadi Dohnal and Ferdinand Verhulst. Averaging in vibration suppression by parametric stiffness excitation. *Nonlinear Dynamics*, 54(3):231–248, jan 2008.

[25] Aleš Tondl. To the problem of quenching self-excited vibrations. *Acta Tech CSAV*, 43(1):109–116, 1998.

[26] F. Dohnal. Experimental studies on damping by parametric excitation using electromagnets. *Proceedings of the Institution of Mechanical Engineers, Part C: Journal of Mechanical Engineering Science*, 226(8):2015–2027, aug 2012.

[27] Erich Schmidt, Wolfgang Paradeiser, Fadi Dohnal, and Horst Ecker. Design of an electromagnetic actuator for parametric stiffness excitation. *COMPEL - The International Journal for Computation and Mathematics in Electrical and Electronic Engineering*, 26(3):800–813, 2007.

[28] T. Pumhössel and H. Springer. Active damping of vibrations of a lightweight beam structure - Experimental results. *Motion and Vibration Control - Selected Papers from MOVIC 2008*, pages 253–262, 2009.

[29] Pradyumna Kumar Sahoo and S. Chatterjee. High-frequency vibrational control of principal parametric resonance of a nonlinear cantilever beam: Theory and experiment. *Journal of Sound and Vibration*, 505:116138, aug 2021.

[30] Jerzy Warminski and Krzysztof Kecik. Instabilities in the main parametric resonance area of a mechanical system with a pendulum. *Journal of Sound and Vibration*, 322(3):612–628, may 2009.

[31] Fabrizio Pinto. Parametric resonance: An introductory Experiment The pumping of a swing from the standing position. *American Journal of Physics*, 31:215, 1993.

[32] Kimberly L. Turner, Scott A. Miller, Peter G. Hartwell, Noel C. MacDonald, Steven H. Strogatz, and Scott G. Adams. Five parametric resonances in a microelectromechanical system. *Nature*, 396(6707):149–152, nov 1998.

[33] Bahareh Zaghari, Emiliano Rustighi, and Maryam Ghandchi Tehrani. Dynamic response of a nonlinear parametrically excited system subject to harmonic base excitation . *Journal of Physics: Conference Series*, 744, 2016.

[34] Jeffrey F. Rhoads, Nicholas J. Miller, Steven W. Shaw, and Brian F. Feeny. Mechanical domain parametric amplification. *Journal of Vibration and Acoustics, Transactions of the ASME*, 130(6), dec 2008.

[35] Lamberto Cesari. Sulla stabilità delle soluzioni delle equazioni differenziali lineari [On the stability of solutions of linear differential equations]. *Annali della Scuola Normale Superiore di Pisa-Classe di Scienze*, 8(2):131–148, 1939.

[36] Hans Schmieg. *Kombinationsresonanz bei Systemen mit Allgemeiner Harmonischer Erregermatrix [Combination resonance in systems with general harmonic excitation matrix]*. PhD thesis, Universität Fridericiana Karlsruhe, 1976.

[37] Artem Karev and Peter Hagedorn. Global stability effects of parametric excitation. *Journal of Sound and Vibration*, 448:34–52, 2019.

[38] Artem Karev. *Asynchronous Parametric Excitation in Dynamical Systems*. Ph.d. thesis, Technische Universität Darmstadt, 2021.

[39] Fadi Dohnal. Vibration suppression of self-excited oscillations by parametric inertia excitation. *PAMM*, 5(1):153–154, dec 2005.

[40] Artem Karev, Daniel Hochlenert, and Peter Hagedorn. Asynchronous parametric excitation, total instability and its occurrence in engineering structures. *Journal of Sound and Vibration*, 428:1–12, aug 2018.

[41] Ali Hasan Nayfeh and Dean T. Mook. *Nonlinear Oscillations*. Wiley, may 1995.

[42] Bahareh Zaghari, Till Kniffka, Cameron Levett, and Emiliano Rustighi. Parametrically Excited Nonlinear Two-Degree-of-Freedom Electromechanical Systems. *Journal of Physics: Conf. Series*, 1264, 2019.

[43] S. Lucyszyn. Review of radio frequency microelectromechanical systems technology. *IEE Proceedings: Science, Measurement and Technology*, 151(2):93–103, mar 2004.

[44] Xinmiao Liu, Weixin Liu, Zhihao Ren, Yiming Ma, Bowei Dong, Guangya Zhou, and Chengkuo Lee. Progress of optomechanical micro/nano sensors: a review. *International Journal of Optomechatronics*, 15(1):120–159, 2021.

[45] Derek K. Shaeffer. MEMS inertial sensors: A tutorial overview. *IEEE Communications Magazine*, 51(4):100–109, 2013.

[46] Amy C.Richards Grayson, Rebecca S. Shawgo, Audrey M. Johnson, Nolan T. Flynn, Yawen Li, Michael J. Cima, and Robert Langer. A BioMEMS review: MEMS technology for physiologically integrated devices. *Proceedings of the IEEE*, 92(1):6–21, 2004.

[47] Nader Jalili and Karthik Laxminarayana. A review of atomic force microscopy imaging systems: application to molecular metrology and biological sciences. *Mechatronics*, 14(8):907–945, oct 2004.

[48] Andreas J. Heinrich, William D. Oliver, Lieven M.K. Vandersypen, Arzhang Ardavan, Roberta Sessoli, Daniel Loss, Ania Bleszynski Jayich, Joaquin Fernandez-Rossier, Arne Laucht, and Andrea Morello. Quantum-coherent nanoscience. *Nature Nanotechnology*, 16(12):1318–1329, nov 2021.

[49] Adrian Cho. The first quantum machine. *Science*, 330(6011):1604, dec 2010.

[50] R. D. Delaney, M. D. Urmey, S. Mittal, B. M. Brubaker, J. M. Kindem, P. S. Burns, C. A. Regal, and K. W. Lehnert. Superconducting-qubit readout via low-backaction electro-optic transduction. *Nature*, 606(7914):489–493, jun 2022.

[51] Richard B. Hetnarski and M. Reza. Eslami. *Thermal stresses : advanced theory and applications*. Springer, 2008.

[52] Peng Wang, Ya Bing Liu, Donglin Wang, Huan Liu, Weiguo Liu, and Hui Kai Xie. Stability Study of an Electrothermally-Actuated MEMS Mirror with Al/SiO2 Bimorphs. *Micromachines*, 10(10), oct 2019.

[53] K. L. Ekinci and M. L. Roukes. Nanoelectromechanical systems. *Review of Scientific Instruments*, 76(6):061101, may 2005.

[54] Shirin Ghaffari, Saurabh A. Chandorkar, Shasha Wang, Eldwin J. Ng, Chae H. Ahn, Vu Hong, Yushi Yang, and Thomas W. Kenny. Quantum Limit of Quality Factor in Silicon Micro and Nano Mechanical Resonators. *Scientific Reports*, 3(1):1–7, nov 2013.

[55] A. Z. Hajjaj, N. Jaber, S. Ilyas, F. K. Alfosail, and M. I. Younis. Linear and nonlinear dynamics of micro and nano-resonators: Review of recent advances. *International Journal of Non-Linear Mechanics*, 119:103328, mar 2020.

[56] M. D. LaHaye, O. Buu, B. Camarota, and K. C. Schwab. Approaching the Quantum Limit of a Nanomechanical Resonator. *Science*, 304(5667):74–77, apr 2004.

[57] F. Pistolesi, A. N. Cleland, and A. Bachtold. Proposal for a Nanomechanical Qubit. *Physical Review X*, 11(3):031027, sep 2021.

[58] Jeffrey F. Rhoads, Congzhong Guo, and Gary K. Fedder. Parametrically Excited Micro- and Nanosystems. In *Resonant MEMS: Principles, Modeling, Implementation, and Applications*, pages 73–95. Wiley-VCH Verlag, aug 2015.

[59] F. Massel, T. T. Heikkilä, J. M. Pirkkalainen, S. U. Cho, H. Saloniemi, P. J. Hakonen, and M. A. Sillanpää. Microwave amplification with nanomechanical resonators. *Nature*, 480(7377):351–354, dec 2011.

[60] D. Rugar and P. Grütter. Mechanical parametric amplification and thermomechanical noise squeezing. *Physical Review Letters*, 67(6):699–702, aug 1991.

[61] Wenhua Zhang, Rajashree Baskaran, and Kimberly L. Turner. Effect of cubic nonlinearity on auto-parametrically amplified resonant MEMS mass sensor. *Sensors and Actuators, A: Physical*, 102(1-2):139–150, dec 2002.

[62] Laura A. Oropeza-Ramos, Christopher B. Burgner, and Kimberly L. Turner. Inherently Robust micro gyroscope actuated by parametric resonance. In *Proceedings of the IEEE International Conference on Micro Electro Mechanical Systems (MEMS)*, pages 872–875, 2008.

[63] Laura A. Oropeza-Ramos, Christopher B. Burgner, and Kimberly L. Turner. Robust micro-rate sensor actuated by parametric resonance. *Sensors and Actuators, A: Physical*, 152(1):80–87, may 2009.

[64] B. J. Gallacher, J. S. Burdess, and K. M. Harish. A control scheme for a MEMS electrostatic resonant gyroscope excited using combined parametric excitation and harmonic forcing. *Journal of Micromechanics and Microengineering*, 16(2):320–331, feb 2006.

[65] K. M. Harish, B. J. Gallacher, J. S. Burdess, and J. A. Neasham. Experimental investigation of parametric and externally forced motion in resonant MEMS sensors. *Journal of Micromechanics and Microengineering*, 19(1):015021, jan 2009.

[66] Caglar Ataman and Hakan Urey. Modeling and characterization of comb-actuated resonant microscanners. *Journal of Micromechanics and Microengineering*, 16(1):9–16, jan 2006.

[67] Gyan Prakash, Arvind Raman, Jeffrey Rhoads, and Ronald G. Reifenberger. Parametric noise squeezing and parametric resonance of microcantilevers in air and liquid environments. *Review of Scientific Instruments*, 83(6):065109, jun 2012.

[68] Vladislav Apostolyuk. *Coriolis vibratory gyroscopes: Theory and design*. Springer International Publishing, jan 2016.

[69] Vittorio M.N. Passaro, Antonello Cuccovillo, Lorenzo Vaiani, Martino De Carlo, and Carlo Edoardo Campanella. Gyroscope technology and applications: A review in the industrial perspective. *Sensors*, 17(10):2284, oct 2017.

[70] Farrokh Ayazi and Khalil Najafi. A HARPSS polysilicon vibrating ring gyroscope. *Journal of Microelectromechanical Systems*, 10(2):169–179, jun 2001.

[71] Z. X. Hu, B. J. Gallacher, K. M. Harish, and J. S. Burdess. A parametrically amplified MEMS gyroscope. *International Conference and Exhibition on Device Packaging 2010, Held in Conjunction with the Global Business Council, GBC 2010 Spring Conference*, 2(2):1081–1099, jun 2010.

[72] Sungjin Yoon, Usung Park, Jaewook Rhim, and Sang Sik Yang. Tactical grade MEMS vibrating ring gyroscope with high shock reliability. *Microelectronic Engineering*, 142:22–29, jul 2015.

[73] Haoran Wen. *Toward Inertial-Navigation-on-Chip*. Springer Theses. Springer International Publishing, Cham, 2019.

[74] Mrigank Sharma, Elie Hanna Sarraf, Rajashree Baskaran, and Edmond Cretu. Parametric resonance: Amplification and damping in MEMS gyroscopes. *Sensors and Actuators, A: Physical*, 177:79–86, apr 2012.

[75] C. H. Ahn, S. Nitzan, E. J. Ng, V. A. Hong, Y. Yang, T. Kimbrell, D. A. Horsley, and T. W. Kenny. Encapsulated high frequency (235 kHz), high-Q (100 k) disk resonator gyroscope with electrostatic parametric pump. *Applied Physics Letters*, 105(24):243504, dec 2014.

[76] Sarah H. Nitzan, Valentina Zega, Mo Li, Chae H. Ahn, Alberto Corigliano, Thomas W. Kenny, and David A. Horsley. Self-induced parametric amplification arising from nonlinear elastic coupling in a micromechanical resonating disk gyroscope. *Scientific Reports*, 5(1):1–6, mar 2015.

[77] Xin Zhou, Chun Zhao, Dingbang Xiao, Jiangkun Sun, Guillermo Sobreviela, Dustin D. Gerrard, Yunhan Chen, Ian Flader, Thomas W. Kenny, Xuezhong Wu, and Ashwin A. Seshia. Dynamic modulation of modal coupling in microelectromechanical gyroscopic ring resonators. *Nature Communications*, 10(1), dec 2019.

[78] Pavel M. Polunin and Steven W. Shaw. Self-induced parametric amplification in ring resonating gyroscopes. *International Journal of Non-Linear Mechanics*, 94:300–308, sep 2017.

[79] Ahmed A. Barakat and Peter Hagedorn. On a simple nonlinear system with circulatory forces. *PAMM*, 19(1), nov 2019.

[80] Ahmed A. Barakat and Peter Hagedorn. Broadband parametric amplification for micro-ring gyroscopes. *Sensors and Actuators A: Physical*, 332:113130, 2021.

[81] Ahmed A. Barakat, Eva M. Weig, and Peter Hagedorn. Non-trivial solutions and their stability in a two-degree-of-freedom Mathieu-Duffing system, 2022.

[82] Ahmed A. Barakat, Roberta Lima, Rubens Sampaio, and Peter Hagedorn. Bimodal parametric excitation of a micro-ring gyroscope. *PAMM*, 20(1):e202000153, jan 2021.

[83] Ahmed A. Barakat and Peter Hagedorn. Broadband Micro-gyroscope Signal Amplification for Enhanced Measurement Sensitivity. *Lecture Notes in Civil Engineering*, 253:865–873, 2023.

[84] Stephen Wiggins. *Introduction to Applied Nonlinear Dynamical Systems and Chaos*, volume 2 of *Texts in Applied Mathematics*. Springer-Verlag, New York, 2003.

[85] Oleg N. Kirillov. *Nonconservative Stability Problems of Modern Physics*. De Gruyter, Berlin, Boston, jan 2013.

[86] Lawrence Perko. *Differential Equations and Dynamical Systems*. Springer New York, New York, NY, 2001.

[87] Peter Hagedorn and Daniel Hochlenert. *Technische Schwingungslehre: Schwingungen linearer diskreter mechanischer Systeme [Engineering vibration theory: vibrations of linear discrete mechanical systems]*. Verlag Europa-Lehrmittel, 2015.

[88] V V Bolotin. *Nonconservative Problems of the Theory of Elastic Stability*. Pergamon Press, 1963.

[89] Ali Hasan Nayfeh. *Perturbation Methods*. Wiley, aug 2000.

[90] Ivana Kovacic and Michael J. Brennan. *The Duffing Equation: Nonlinear Oscillators and their Behaviour*. John Wiley and Sons, mar 2011.

[91] H. Ziegler. Die Stabilitätskriterien der Elastomechanik [The stability criteria of elastomechanics]. *Ingenieur-Archiv*, 20(1):49–56, 1952.

[92] Peter Hagedorn, Eduard Heffel, Peter Lancaster, Peter C. Müller, and Santosh Kapuria. Some recent results on MDGKN-systems. *Zeitschrift fur Angewandte Mathematik und Mechanik*, 95(7):695–702, jul 2015.

[93] Peter Hagedorn, Manuel Eckstein, Eduard Heffel, and Andreas Wagner. Self-excited vibrations and damping in circulatory systems. *Journal of Applied Mechanics, Transactions ASME*, 81(10):101009, aug 2014.

[94] Oleg N. Kirillov. Destabilization paradox due to breaking the Hamiltonian and reversible symmetry. *International Journal of Non-Linear Mechanics*, 42(1):71–87, jan 2007.

[95] David R. Merkin. *Introduction to the Theory of Stability*. Springer New York, New York, NY, 1996.

[96] Peter Hagedorn. *Non-linear oscillations*. Oxford University Press, Oxford, 1988.

[97] L Ya Adrianova. *Introduction to linear systems of differential equations*. American Mathematical Society, 1995.

[98] Luis Manuel Braga da Costa Campos. *Non-Linear Differential Equations and Dynamical Systems*. Springer Berlin Heidelberg, 2019.

[99] Ali H. Nayfeh and Balakumar Balachandran. *Applied Nonlinear Dynamics*. Wiley, mar 1995.

[100] Yuri A. Kuznetsov. *Elements of Applied Bifurcation Theory*, volume 112 of *Applied Mathematical Sciences*. Springer New York, New York, NY, 2004.

[101] Carmen. Chicone. *Ordinary differential equations with applications*. Springer, 2006.

[102] F. Dohnal. General parametric stiffness excitation – anti-resonance frequency and symmetry. *Acta Mechanica*, 196(1):15–31, sep 2007.

[103] Ivana Kovacic, Richard Rand, and Si Mohamed Sah. Mathieu's equation and its generalizations: Overview of stability charts and their features. *Applied Mechanics Reviews*, 70(2), mar 2018.

[104] John Guckenheimer, Philip Holmes, and M. Slemrod. *Nonlinear Oscillations Dynamical Systems, and Bifurcations of Vector Fields*. Applied Mathematical Sciences. Springer New York, New York, NY, 1984.

[105] Ali Hasan Nayfeh. *The Method of Normal Forms, Second Edition*. Wiley-VCH Verlag GmbH, Weinheim, Germany, jul 2011.

[106] J Murdock. *Normal forms and unfoldings for local dynamical systems*. Springer Monographs in Mathematics. Springer New York, New York, NY, 2003.

[107] D Hochlenert. Normalformen und Einzugsbereiche nichtlinearer dynamischer Systeme. *[Normalforms and basins of attraction of nonlinear dynamical systems], Habilitationsschrift, TU Berlin*, 2012.

[108] Gyan Prakash, Arvind Raman, Jeffrey Rhoads, and Ronald G. Reifenberger. Parametric noise squeezing and parametric resonance of microcantilevers in air and liquid environments. *Review of Scientific Instruments*, 83(6):065109, jun 2012.

[109] A. H. Nayfeh, C. Chin, and D. T. Mook. Parametrically Excited Nonlinear Two-Degree-of-Freedom Systems with Repeated Natural Frequencies. *Shock and Vibration*, 2(1):43–57, 1995.

[110] A. H. Nayfeh and L. D. Zavodney. The response of two-degree-of-freedom systems with quadratic non-linearities to a combination parametric resonance. *Journal of Sound and Vibration*, 107(2):329–350, jun 1986.

[111] Waqas Amin Gill, Ian Howard, Ilyas Mazhar, and Kristoffer McKee. A Review of MEMS Vibrating Gyroscopes and Their Reliability Issues in Harsh Environments. *Sensors*, 22(19):7405, sep 2022.

[112] Singiresu S. Rao. *Vibration of Continuous Systems*. John Wiley and Sons, Inc., dec 2007.

[113] J. N. Reddy. *Energy Principles and Variational Methods*. John Wiley and Sons, Incorporated, 2020.

[114] Augustus Edward Hough Love. *A Treatise on the Mathematical Theory of Elasticity*. Cambridge University Press, 1944.

[115] K. Tanaka, Y. Mochida, M. Sugimoto, K. Moriya, T. Hasegawa, K. Atsuchi, and K. Ohwada. *A micromachined vibrating ring gyroscope*. PhD thesis, University of Michigan, 1995.

[116] Zhongxu Hu, Barry J. Gallacher, Kiran M. Harish, and James S. Burdess. An experimental study of high gain parametric amplification in MEMS. *Sensors and Actuators, A: Physical*, 162(2):145–154, aug 2010.

[117] S. Nitzan, T. H. Su, C. Ahn, E. Ng, V. Hong, Y. Yang, T. Kenny, and D. A. Horsley. Impact of gyroscope operation above the critical bifurcation threshold on scale factor and bias instability. In *Proceedings of the 2014 IEEE 27th International Conference on Micro Electro Mechanical Systems (MEMS)*, pages 749–752. Institute of Electrical and Electronics Engineers Inc., 2014.

[118] Sarah H. Nitzan, Parsa Taheri-Tehrani, Martial Defoort, Soner Sonmezoglu, and David A. Horsley. Countering the Effects of Nonlinearity in Rate-Integrating Gyroscopes. *IEEE Sensors Journal*, 16(10):3556–3563, may 2016.

[119] Dong Dong Liang, Xiao Dong Yang, Wei Zhang, Yuan Ren, and Tianzhi Yang. Linear, nonlinear dynamics, and sensitivity analysis of a vibratory ring gyroscope. *Theoretical and Applied Mechanics Letters*, 8(6):393–403, dec 2018.

[120] Sang Won Yoon, Sangwoo Lee, and Khalil Najafi. Vibration sensitivity analysis of MEMS vibratory ring gyroscopes. *Sensors and Actuators, A: Physical*, 171(2):163–177, nov 2011.

[121] Qingsong Li, Dingbang Xiao, Yi Xu, Ming Zhuo, Xin Zhou, Yongmeng Zhang, Lei Yu, and Xuezhong Wu. Nonlinearity Reduction in Disk Resonator Gyroscopes Based on the Vibration Amplification Effect. *IEEE Transactions on Industrial Electronics*, 67(8):6946–6954, aug 2020.

[122] Marco Amabili and Michael P. Païdoussis. Review of studies on geometrically nonlinear vibrations and dynamics of circular cylindrical shells and panels, with and without fluid-structure interaction. *Applied Mechanics Reviews*, 56(4):349–356, jul 2003.

[123] HU-NAN CHU. Influence of Large Amplitudes on Flexural Vibrations of a Thin Circular Cylindrical Shell. *Journal of the Aerospace Sciences*, 28(8):602–609, aug 1961.

[124] D. A. Evensen. Nonlines flexural vibrations of thin circular rings. *Journal of Applied Mechanics, Transactions ASME*, 33(3):553–560, sep 1964.

[125] S. Natsiavas. Dynamics and stability of non-linear free vibration of thin rotating rings. *International Journal of Non-Linear Mechanics*, 29(1):31–48, jan 1994.

[126] Thibaut Detroux, Jean Philippe Noël, Lawrence N. Virgin, and Gaëtan Kerschen. Experimental study of isolas in nonlinear systems featuring modal interactions. *PLOS ONE*, 13(3):e0194452, mar 2018.

[127] Hans-Georg Pietscher. *Parameterregelung einer aktiven Cantilever-Messonde zur Sensitivitätssteigerung in der Rasterkraftmikroskopie [Parametric control of an active cantilever probe for sensitivity enhancement in atomic force microscopy] . MSc thesis*. Technische Universität Ilmenau, 2022.

[128] Dan O. Popa, Byoung Hun Kang, John T. Wen, Harry E. Stephanou, George Skidmore, and Aaron Geisberger. Dynamic modeling and input shaping of thermal bimorph MEMS actuators. *Proceedings - IEEE International Conference on Robotics and Automation*, 1:1470–1475, 2003.

[129] Dennis Roeser, Stefanie Gutschmidt, Thomas Sattel, and Ivo W. Rangelow. Tip Motion - Sensor Signal Relation for a Composite SPMCantilever. *Journal of Microelectromechanical Systems*, 25(1):78–90, feb 2016.

[130] Leonard Meirovitch. *Fundamentals of vibrations*. Waveland Press, 2010.